U.PORTO
FACULDADE DE CIÊNCIAS
UNIVERSIDADE DO PORTO

PhD

PhD

3rd
CYCLE

FCUP
2024

U.PORTO

Towards a New Generation of Stellar Models: Impact of Physical Ingredients on the Accuracy of Stellar Parameters Inferences

Nuno Moedas

FC

U.PORTO
FACULDADE DE CIÊNCIAS
UNIVERSIDADE DO PORTO

PhD

Toward a New Generation of Stellar Models: Impact of Physical Ingredients on the Accuracy of stellar Parameters Inferences

Nuno Moedas
Programa Doutoral em Astronomia
Departamento de Física e Astronomia
Faculty of Sciences of the University of Porto
2024

PhD

Toward a New Generation of Stellar Models: Impact of Physical Ingredients on the Accuracy of stellar Parameters Inferences

Nuno Moedas

Thesis carried out as part of Programa Doutoral em Astronomia

Departamento de Física e Astronomia

2024

Supervisor
Diego Bossini, Doutor, Università di Padova;

Co-supervisor
Morgan Deal, Doutor, Université de Montpellier

All the corrections determined by the jury, and only those, were made.

The Supervisor, Diego Bossini

Diego Bossini

Porto, 29 / 11 / 2024

Note: This page should only be included **in the final version after defence and only if the jury approves the thesis with a recommendation for the student to correct errors, inaccuracies or formal inaccuracies** identified and expressly mentioned during the tests. **This page must be deleted from the version to be submitted as part of the thesis submission prior to the defence.**

Acknowledgements

A very big thank you to my supervisors, Diego Bossini and Morgan Deal, for all the help and support they gave me during the four years of my Ph.D. This achievement was only possible because of them. Thanks to my colleagues for the discussions we had during these years. I would also like to thank all my friends who have supported me during my time at university. Additionally, I want to thank my family—my mom, dad, and especially my brother and sister—for all they have done for me, which helped me achieve what I have today."

Abstract

The chemical composition is a key component in stellar models and has a strong influence on stellar evolution. However, the composition is not static and changes with time due to nuclear reactions in the core of the star and chemical transport mechanisms. One of the most important transport mechanisms considered in stellar modeling is atomic diffusion. This can be broken down into two main competing sub-processes, gravitational settling and radiative acceleration. Studies have shown that both processes need to be included in stellar models to better characterize stars. However, there are two major drawbacks when it comes to F-type stars. First, atomic diffusion is usually not taken into account in models of these and more massive stars since it produces unrealistic variations of the surface chemical abundances compared to observations of non-chemically peculiar stars. Second, the main methods for calculating radiative accelerations are expensive and do not allow the computation of a large number of stellar models needed to characterize stars.

In this work, I aim to assess the impact and efficiency of transport processes of chemical elements in stellar models on the characterization of stars. To start, I showed how to avoid unrealistic variations of the surface abundances using a calibrated turbulent mixing coefficient. Secondly, I tested an efficient method to compute radiative accelerations. Finally, I applied these tools to characterize asteroseismic targets, including the 94 Ceti, a triple system with a planet. Both methods allow to improve the prediction of chemical abundances in stellar models. Regarding stellar characterization, they both give differences up to 5%, 2%, and 20% for mass, radius, and age, respectively, compared to standard methods. This work shows that, in order to reduce the uncertainties in stellar models, a full treatment of atomic diffusion should always be considered.

Keywords: Asteroseismology – Diffusion-Turbulence – Stars: Abundances – Stars: Evolution

Resumo

A composição química é uma componente fundamental nos modelos estelares e tem uma forte influência na evolução estelar. No entanto, a composição não é fixa e muda com o tempo devido a reacções nucleares no núcleo da estrela e a mecanismos de transporte químico. Um dos mecanismos de transporte mais importantes considerados na modelação estelar é a difusão atómica. Este pode ser dividido em dois sub-processos principais em competição, a "gravitational settling" e a "radiative acceleration". Estudos demonstraram que ambos os processos devem ser incluídos nos modelos estelares para melhor caraterizar as estrelas. No entanto, existem dois grandes inconvenientes quando se trata de estrelas do tipo F. Em primeiro lugar, a difusão atómica não é normalmente tida em conta nos modelos destas estrelas e de estrelas mais massivas, uma vez que produz variações irrealistas das abundâncias químicas à superfície, em comparação com observações de estrelas não quimicamente peculiares. Em segundo lugar, os principais métodos de cálculo das "radiative acceleration" são dispendiosos e não permitem o cálculo de um grande número de modelos estelares necessários para caraterizar as estrelas.

Neste trabalho, o meu objetivo é avaliar o impacto e a eficiência dos processos de transporte de elementos químicos em modelos estelares na caraterização das estrelas. Para começar, mostrei como evitar variações irrealistas das abundâncias superficiais usando um coeficiente de "turbulent mixing" calibrado. Em segundo lugar, testei um método eficiente para calcular "radiative acceleration". Finalmente, apliquei estas ferramentas para caraterizar alvos asterossísmicos, incluindo o 94 Ceti, um sistema triplo com um planeta. Ambos os métodos permitem melhorar a previsão das abundâncias químicas em modelos estelares. Relativamente à caraterização estelar, ambos dão diferenças de até 5%, 2% e 20% para a massa, raio e idade, respetivamente, em comparação com os métodos padrão. Este trabalho mostra que, para reduzir as incertezas nos modelos estelares, deve ser sempre considerado um tratamento completo da difusão atómica.

Contents

List of Figures

List of Tables

Physical Constants

Boltzmann Constant	k_{B}	$= 1.3806504 \times 10^{-16}\mathrm{erg\ K^{-1}}$
Gas Constant	R_g	$= 8.314511 \times 10^{7}\ \mathrm{erg\ K^{-1}mole^{-1}}$
Gravitational Constant	G	$= 6.67428 \times 10^{-8}\ \mathrm{cm^3g^{-1}s^{-2}}$
Mass of a proton	m_p	$= 1.67262192 \times 10^{-30}\ \mathrm{g}$
Radiative Density Constant	a	$= 7.57 \times 10^{-15}\ \mathrm{erg\ cm^{-3}K^{-4}}$
Stefan-Boltzmann Constant	σ_{SB}	$= 5.67040 \times 10^{-5}\mathrm{erg\ cm^{-2}K^{-4}s}$
Speed of light	c	$= 2.99792458 \times 10^{10}\ \mathrm{cm\ s^{-1}}$
Solar Luminosity	$\mathrm{L}_\odot$	$= 3.8418 \times 10^{33}\ \mathrm{erg\ s^{-1}}$
Solar Mass	$\mathrm{M}_\odot$	$= 1.9892 \times 10^{33}\ \mathrm{g}$
Solar Radius	$\mathrm{R}_\odot$	$= 6.9598 \times 10^{10}\ \mathrm{cm}$
Large Frequency of the Sun	$\Delta\nu_\odot$	$= 135.1\ \mu\mathrm{Hz}$
Frequency of Maximum Power of the Sun	$\nu_{\mathrm{max},\odot}$	$= 3090.0\ \mu\mathrm{Hz}$

Glossary

PMS	Pre Main Sequence
MS	Main Sequence
ZAMS	Zero Age Main Sequence
TAMS	Terminal Age Main Sequence
SG	Sub Giant
RGB	Red Giant Branch
HB	Horizontal Branch
AGB	Asymptotic Giant Branch
PN	Planetary Nebula
WD	White Dwarf
EoS	Equation of State
SVP	Single-Valued Parameters

Statement of Collaboration

Part of this thesis has been written with the contribution of many collaborators. I highlight the contribution of Diego Bossini, Morgan Deal, Margarida Cunha for writing chapters 7, 8, and 9 that are part of Moedas et al. (2022, 2024). For the seismic data and planetary analysis in chapter 10.4, I thank Rafael Garcia and Olivier Demangeon for their collaboration.

Introduction

The stars are the light to the mysteries of our Universe. They are the home of exoplanets, they modify the chemical composition of the galaxy by transforming the light elements into all the different elements that can be observed. Therefore, the precise determination of the fundamental properties of stars, in particular their age and mass, is a crucial step in characterizing them and their environment. As consequence, many disciplines of astrophysics that can benefit from the knowledge of these fundamental properties must rely on correct stellar modeling (Lebreton & Goupil, 2014).

In recent years, large-scale spectroscopic (such as APOGEE, Ahumada et al. 2020, ESPRESSO Cupani et al. 2017) and photometric (such as 2MASS, Cutri et al. 2003 Sloan Digital Sky Survey, SDSS, Szalay 1998 and Gaia, Gaia Collaboration et al. 2018) observations of stars have been complemented by new asteroseismic surveys, mainly based on the CoRoT/ESA (Baglin et al., 2006) and *Kepler*/NASA (Borucki et al., 2010) space telescopes. In fact, the development of asteroseismology, the field of astronomy that studies the natural oscillations of stars, has brought new constraints directly related to the interior of stars that can help us break the degeneracy in stellar fundamental properties (Chaplin et al., 2011, Chaplin & Miglio, 2013). The information we have access to (especially asteroseismic data) has increased dramatically with the TESS (Transiting Exoplanet Survey Satellite/NASA; Ricker 2016) mission. It has observed hundreds of thousands of stars (mostly cool, main-sequence stars), monitoring nearly 85% of the sky. In the near future, ESA's PLATO (PLAnetary Transits and Oscillation of stars; Rauer et al. 2014, 2024) telescope promises to be a mission that will provide precise, high-quality information that will create new opportunities to test stellar physics in more detail.

However, current stellar models are unable to achieve the accuracy requirements for the interpretation of the data of future missions (e.g., PLATO requires 15% for the mass, 2% for the radius, and 10% for the age for solar-type oscillators, in order to characterize Earth-like planets). This is due either to an implementation of incomplete physics or to

our poor knowledge of how to constrain certain parameters. It is therefore necessary to find and quantify the inaccuracies in stellar models, and improve the tools use for building and optimizing the models by implementing the latest and most complete stellar physics.

One source of uncertainty is linked to the modeling of chemical transport mechanisms acting inside stars. These processes can be either microscopic or macroscopic and can compete with each other, leading to a redistribution of the chemical elements inside a star, which affects its internal structure, evolution, and abundance profiles. Atomic diffusion is one of these processes. This microscopic transport process is mainly driven by pressure, temperature, and chemical gradients, redistributing the elements throughout the stellar interior (Michaud et al., 2015). Valle et al. (2014, 2015) tested the impact of diffusion on stellar properties and found that neglecting it can lead to uncertainties of 4.5%, 2.2%, and 20% on mass, radius, and age. Using data from Kepler, Nsamba et al. (2018) found a systematic difference of 16% in the ages inferred from grids with and without diffusion on a sample of stars with masses of less than $M = 1.2$ $M_{\odot}$. Furthermore, in a model-based controlled study performed in the context of PLATO, Cunha et al. (2021) found that atomic diffusion can impact the accuracy of the inferred age by approximately 10% for a 1.0 $M_{\odot}$ star close to the end of the main sequence. These results highlight the need to enhance our understanding and modeling of atomic diffusion and other chemical transport mechanisms.

Atomic diffusion can be decomposed into two main competing subprocesses: One is gravitational settling, which brings the elements from the stellar surface into the deep interior, except for hydrogen, which is transported from the interior to the surface. The other is the radiative acceleration that pushes some elements —mainly the heavy ones— toward the surface of stars due to a transfer of momentum between photons and ions. Several studies have shown that the efficiency of the processes depends on the stellar fundamental properties, which translate into an increase in the efficiency with mass and a decrease with metallicity (see e.g. Deal et al., 2018, and references therein). Nevertheless, the works of Chaboyer et al. (2001) and Salaris & Weiss (2001) prove that gravitational settling is sufficient to predict the surface abundances of low-mass stars. The effects of radiative accelerations become important for more massive stars with a small surface convective zone (e.g. for solar-metallicity stars with an effective temperature of higher than $\sim$ 6000 K, Michaud et al. 2015). Moreover, Rehm et al. (2024) show that radiative

accelerations are necessary to excite seismic modes missing in stellar models. Nevertheless, for stars more massive than the Sun, atomic diffusion alone causes variations on the surface abundances that are larger than those observed in clusters (e.g. Gruyters et al., 2014, 2016, Semenova et al., 2020). This indicates a need for additional chemical transport mechanisms, including radiative accelerations. However, radiative acceleration is highly computationally demanding and is therefore often neglected in stellar models (Weiss & Schlattl, 2008, Bressan et al., 2012, Hidalgo et al., 2018, Pietrinferni et al., 2021).

Some works (e.g. Eggenberger et al., 2010, Vick et al., 2010, Deal et al., 2020, Dumont et al., 2020, and references therein) demonstrated the necessity to include other chemical-transport processes in competition with atomic diffusion. Nevertheless, the identification and accurate modeling of the different processes are still ongoing. The processes that can be considered are either diffusive or advective. If we assume that all of them are fully diffusive, we can parameterize their effects by considering a turbulent mixing coefficient, which can be constrained using the surface abundances of stars in cluster (Gruyters et al., 2013, 2016, Semenova et al., 2020). This was performed in F-type stars by Verma & Silva Aguirre (2019), where the authors used the glitch induced by the helium second ionization region to calibrate the turbulent mixing coefficient that best reproduces the helium surface abundances. Eggenberger et al. (2022) also showed that the effect of the rotation-induced mixing in the Sun could be parameterized with a simple turbulent diffusion coefficient expression.

In this thesis, I explore how the chemical transport mechanisms affect the stellar characterization of F-type main-sequence stars. I investigate the effects of atomic diffusion (with radiative accelerations) for solar-like oscillating stars and quantify the variation in [Fe/H] from the main sequence to the red giant branch bump. I focus on F-type stars, which are the most impacted by atomic diffusion due to the shallow convective envelope. I explore two possible ways to add atomic diffusion avoiding the surface over-variations that it creates, with the consideration of a more efficient way to compute radiative accelerations.

This thesis is organized as follows:

In Part I, I present an overview of astronomy. It focuses on the foundations of stellar structure, evolution, and chemical evolution theory, the theory behind asteroseismology, and the observation techniques in astronomy.

- In Chapter 1, I give an overview of the basic physics theory behind stars, including

a brief description of the life evolution of low-mass stars, i.e. main subject of this work.

- In Chapter 2, I give a brief introduction of asteroseismology theory.
- In Chapter 3, I present the observation methods to obtain data from stars.
- In Chapter 4, I summarise the theory of the chemical transport mechanisms inside stars.

In Part II, I present the tools necessary to develop the work.

- In Chapter 5, I show the different codes I use: the code for the computation of the stellar modes (MESA), the code for the calculation of the seismic frequencies (GYRE), and the optimization code (AIMS)
- In Chapter 6, I present sample of stars used in this work.

In Part III, I present the original results of the work.

- In Chapter 7, I investigate the impact of atomic diffusion on stellar models including radiative accelerations
- In Chapter 8, I quantify the effects of turbulent mixing in stellar models and calibrate it to reproduce the effects of radiative accelerations.
- In Chapter 9, I test the impact of turbulent mixing for the characterization of real stars.
- In Chapter 10, I implement the Sigle-Valued Parameters (SVP) method in the stellar models and use it to characterize a sample of stars.

Part I

Background

Chapter 1

Stellar Physics

This chapter is based on the notes of stellar structure and evolution by Mário João P. F. G. Monteiro of the Faculdade de Ciências da Universidade do Porto, and the book of Kippenhahn & Weigert (1990).

My focus in this chapter and in the rest of the manuscript is on low-mass stars, with masses between $\sim 0.6\,M_\odot$ and $\sim 1.6\,M_\odot$. These stars help us understand the evolution of solar-like stars and the evolution and formation of planetary systems. In particular, I will focus in the next chapters on solar-metallicity F-type stars, which are usually stars with masses $\gtrsim 1.15\,M_\odot$ and $\lesssim 1.6\,M_\odot$, or more specifically stars with an effective temperature of $6000\,K \leqslant T_{\rm eff} \leqslant 7500\,K$. This is important as these stars start to present a different stellar structure that influences their stellar and chemical evolution. Regardless, each star is different, evolving and behaving differently depending on its mass and chemical composition. But, all stars are ruled by the same basic physics. They have the same stellar structure equations, the same processes of transport of energy, and their main source of energy is nuclear reactions. In this chapter, I will look at the basic physics that governs stars.

1.1 Stellar structure equations

The stars follow four basic equations of stellar structure, assuming an isolated evolution (no consideration of binary interaction and accretion), a spherical symmetry, and no rotation and magnetic field. These are (in the Eulerian framework) the mass conservation equation

$$\frac{dm}{dr} = 4\pi r^2 \rho, \tag{1.1}$$

the hydrostatic equilibrium equation

$$\frac{dP}{dr} = -\frac{Gm}{r^2}\rho, \tag{1.2}$$

the energy transport equation

$$\frac{dT}{dr} = -\frac{GmT\rho}{r^2 P}\nabla \text{ with } \nabla = \frac{d\ln T}{d\ln P}, \tag{1.3}$$

and the energy conservation equation

$$\frac{dL}{dr} = 4\pi r^2 \rho(\epsilon_n - \epsilon_\nu + \epsilon_g). \tag{1.4}$$

In these equations, r and m are the radial and mass coordinates, respectively, relative to the center of the star. P, L, T and ρ are the local pressure, luminosity, temperature and density, ϵ_n is the energy produced by nuclear reactions, ϵ_ν is the energy lost by neutrinos, ϵ_g is the work done on the gas during any expansion or contraction of the star, G is the gravitational constant and ∇ is the thermal gradient. The first two equations describe the mass profile of the star, the other two describe the thermal profile of the star. All the equations have a time dependence, due to the changes in chemical composition and mean molecular weight (μ) caused, for example, by the nuclear reactions.

1.2 Continuity equation

The equation 1.1 represents the mass contained in a sphere of radius r. For a star of stellar radius R we know that the total mass is

$$M = \int_0^R 4\pi r^2 \rho \, \mathrm{d}r. \tag{1.5}$$

Nonetheless, this assumes that there is no change in mass during the evolution. So if there is some variation, for example, due to mass loss, we can define that the mass contained in a sphere or radius r at a given time t is

$$\mathrm{d}m = 4\pi r^2 \rho \, \mathrm{d}r - 4\pi r^2 \rho v \, \mathrm{d}t. \tag{1.6}$$

The first term represents the mass conservation equation and the second term is the flow of mass with a radial velocity v (outflow if $v > 0$, inflow/accretion if $v < 0$). The change in mass with time is described as

$$\frac{dm}{dt} = -4\pi r^2 \rho v. \tag{1.7}$$

If we differentiate eq. 1.1 with respect to t or the eq. 1.7 with respect to r we obtain

$$\frac{d\rho}{dt} = -\frac{1}{r^2}\frac{d}{dr}(r^2\rho v). \tag{1.8}$$

This is the continuity equation of hydrodynamic for the spherical symmetry.

1.3 Hydrostatic equilibrium

The hydrostatic equilibrium equation (eq. 1.2) is a special case of the momentum equation

$$\frac{dP}{dr} = -\frac{Gm}{r^2}\rho - \rho\frac{dv}{dt}, \tag{1.9}$$

when no significant changes in time ($\frac{\partial}{\partial t} = 0$) is considered. This is the simplest case where only pressure and gravitational forces are taken into account (electromagnetic force and rotation are not considered). In this case, the star has a radial acceleration if there is no equilibrium between the pressure and gravity forces.

In the extreme case where only one of the two forces is present, we can estimate the time of collapse where only gravity is present. This is the free fall time scale ($\tau_{\rm ff}$), which can be estimated as

$$\tau_{\rm ff} \approx \sqrt{\frac{R}{g}}, \tag{1.10}$$

where g is the gravitational acceleration, $g = \frac{Gm}{r^2}$. For the opposite case, where only pressure exists, the explosion time scale can be estimated as

$$\tau_{\rm exp} \approx R\sqrt{\frac{\bar{\rho}}{\bar{P}}}, \tag{1.11}$$

where $\bar{\rho}$ and $\bar{P}$ are the mean values of density and pressure.

In the case of a small perturbation, the pressure and gravity terms are equal and $\tau_{\rm ff} \approx \tau_{\rm exp}$. This is the so-called hydrostatic equilibrium time scale $\tau_{\rm hydro}$, the time it takes to regain equilibrium. This can be shown to be

$$\tau_{\rm hydro} = \sqrt{\frac{3}{2\pi}\frac{1}{G\bar{\rho}}}. \tag{1.12}$$

The $\tau_{\rm hydro}$ for the different stars is much smaller than the timescale of the structural changes in the star. For the Sun, $\tau_{\rm hydro}$ is about 27 minutes, which is much smaller compared to a significant change in stellar structure that takes millions of years. This suggests that most stars are in a state of constant equilibrium.

In the case where rotation is considered, stars can lose their spherical symmetry and this adds an extra term to the angular momentum transport, rewriting the momentum equation as

$$\rho\frac{\partial}{\partial t} + \rho(v\cdot\nabla)v = -\nabla P - \rho\nabla\phi. \tag{1.13}$$

where ϕ is the gravitational potential, ∇ is the operator containing the partial derivatives in spherical coordinates, and v is the velocity vector. The term $(v\cdot\nabla)v$ can be defined as the potential field driven by the stellar rotation ($\phi_{\rm rot}$). If the star is in equilibrium, the time derivative is zero ($\frac{\partial}{\partial t} = 0$), which leads to

$$\rho\nabla\phi_{\rm rot} = -\nabla P - \rho\nabla\phi. \tag{1.14}$$

In this work, I only look at slow-rotating stars where spherical symmetry approximation is valid.

1.4 Energy transport

In stars, there is a constant flow of energy from the deep interior, where it is produced (see section 1.5 for more details), to the stellar surface, where it is radiated into space. The energy transport is described by eq. 1.3. However, the temperature gradient $\nabla = \frac{\partial \ln T}{\partial \ln P}$ is different depending on how the energy is transported. In the stellar interior, there are three main mechanisms of energy transport, which are

- **Radiative Transport**; energy is transported by photons;
- **Convective Transport**: energy is transported by the motion of matter;
- **Conductive Transport**: energy transported by collisions of electrons and particles.

These three processes can exist simultaneously inside stars. The last one, the transport of energy by conduction, is the main mechanism when the matter reaches a degenerate state, which is the case in white dwarfs and in the core of some red giants. However, we do not study this process in this manuscript, as it is not present in Main-Sequence (MS) stars, which are the main focus of this work. In the next two subsections, we will describe radiative and convective transport, one or the other being dominant depending on the physical conditions of the stellar layers.

1.4.1 Radiative transport

Radiative transport is characterized by a constant flux of photons from the hotter to the cooler layers of the star. In an optically thick medium, the mean energy flux in a given region can be described, within the diffusion approximation framework*, by

$$F_{\rm rad} = -\frac{4acT^3}{3\kappa\rho}\frac{\partial T}{\partial r}, \tag{1.15}$$

where a is the radiative density constant, c is the speed of light, and κ is the Rosseland mean opacity. The flux can be related to the local luminosity by $l = 4\pi r^2 F_{\rm rad}$, which allows writing eq. 1.15 as

$$\frac{\partial T}{\partial r} = -\frac{3\kappa\rho l}{16\pi r^2 acT^3}. \tag{1.16}$$

This equation is the energy transport equation in a radiative medium, where we can define the temperature gradient ∇ as

$$\nabla_{\rm rad} = -\frac{3}{16\pi acG}\frac{\kappa l P}{mT^4}. \tag{1.17}$$

In regions where the dominant energy transport process is radiation, the true temperature gradient follows the radiative temperature gradient $\nabla = \nabla_{\rm rad}$. However, for regions of higher opacity κ and/or higher energy production (regions of higher local luminosity), this gradient increases to unrealistic values. This creates unstable regions where the energy cannot be transported by radiation and enters a regime of instability. As a result, convection becomes the dominant energy transport process.

1.4.2 Convective transport

In the regime where the radiation is inefficient to transport the energy internally, a dynamical instability regime appears and favors a macroscopic motion of the matter that characterizes convection. Different theories and methods try to explain the transport in this region. From 3D-hydrodynamic simulations (Salaris & Cassisi, 2015), Scale-Free Convection (SFC) theory (Pasetto et al., 2015), try to model the convective region. I considered the Mixing Length Theory (MLT) in this manuscript. The different prescriptions can influence the determination of thermal gradients, and pressure profile convective motion of the models. But first, we need to define the region where the convective motion takes place.

*The medium is optically thick, leading to larger scatter and absorption of the photons

Let us consider a portion of matter (a blob) that exchanges a portion of energy. This leads to the blob (identified by "b") having a different temperature and density than its surroundings (identified by "s") which leads to a displacement (movement of the blob) Δr of the matter. The density variation $\Delta\rho$ can be described as

$$\Delta\rho = \left[\frac{\partial\rho_{\rm b}}{\partial r} - \frac{\partial\rho_{\rm s}}{\partial r}\right]\Delta r. \tag{1.18}$$

After the displacement, the density variation induces a buoyancy force $F_\rho = -g\Delta\rho$. If $\Delta\rho > 0$ the blob returns to its original position and the equilibrium is restored. But if $\Delta\rho < 0$ we enter an unstable configuration and the blob continues to rise inside the star.

To understand how this happens, we can see how the density varies with the other thermodynamic variables

$$\frac{\mathrm{d}\rho}{\rho} = \alpha\frac{\mathrm{d}P}{P} - \delta\frac{\mathrm{d}T}{T} + \varphi\frac{\mathrm{d}\mu}{\mu}, \tag{1.19}$$

where $\alpha := \left(\frac{\partial\ln\rho}{\partial\ln P}\right)$, $\delta := -\left(\frac{\partial\ln\rho}{\partial\ln T}\right)$ and $\varphi := \left(\frac{\partial\ln\rho}{\partial\ln\mu}\right)$, are expansion coefficients, and μ is the mean molecular weight. From this relation we have

$$\frac{1}{\rho}\frac{\mathrm{d}\rho}{\mathrm{d}r} = \frac{1}{P}\frac{\mathrm{d}P}{\mathrm{d}r}\left(\alpha - \delta\frac{\mathrm{d}\ln T}{\mathrm{d}\ln P} + \varphi\frac{\mathrm{d}\ln\mu}{\mathrm{d}\ln P}\right) = \frac{1}{P}\frac{\mathrm{d}P}{\mathrm{d}r}\left(\alpha - \delta\nabla + \varphi\nabla_\mu\right) \leq 0. \tag{1.20}$$

If the displacement of the blob is slow, this allows the pressure inside the blob to be in equilibrium with its surroundings $P_b = P_s$. Then we have

$$\frac{\Delta\rho}{\rho} \leq 0 \Rightarrow \frac{\Delta r}{P}\frac{\mathrm{d}P}{\mathrm{d}r}\left[\left(\alpha - \delta\nabla + \varphi\nabla_\mu\right)_{\rm b} - \left(\alpha - \delta\nabla + \varphi\nabla_\mu\right)_{\rm s}\right]. \tag{1.21}$$

The chemical composition of the blob does not change (under the assumption of no mass exchange with the surroundings), so $\nabla_{\mu,\rm b} = 0$. This leads to a state of stability

$$\nabla \geq \nabla_{\mathbf{b}} + \frac{\varphi}{\delta}\nabla_\mu. \tag{1.22}$$

In the case of stable layers, the energy is transported by radiation only, so ∇ is equal to $\nabla_{\rm rad}$. Assuming that the blob gradient changes adiabatically $\nabla_{\mathbf{b}} = \nabla_{\mathbf{ad}}$*; the region is stable if

$$\nabla_{\rm rad} \geq \nabla_{\rm ad} + \frac{\varphi}{\delta}\nabla_\mu, \tag{1.23}$$

which is the Ledoux criterion (Ledoux, 1947), for stability. For regions of homogeneous composition, we can simplify this criterion (the Schwartzschild criterion, Schwarzschild

*$\nabla_{\mathbf{ad}} \equiv \left(\frac{\partial\ln T}{\partial\ln P}\right)_S = \frac{\delta}{c_P}\frac{P}{\rho T}$ where c_P is the specific heat at constant pressure

1958) as

$$\nabla_{\rm rad} \geq \nabla_{\rm ad}. \tag{1.24}$$

Both cases show that when the radiative gradient is much higher than the others, it leads to an instability that creates a convective zone. Note that eq. 1.23 and 1.24 are local criteria that allow us to evaluate the stability only with the local P, T, and ρ. However, they are not sufficient because the convective motion is not only dependent on the local force acting in the layer, but also on the neighboring layers (momentum transfer, inertia, continuity equation). Nevertheless, the thermal gradient can be approximated to $\nabla_{\rm rad}$ in stable regions, and to $\nabla_{\rm ad}$ in unstable regions*.

1.4.2.1 Mixing length theory

Now, in order to characterize the convective regions of the star, we need to know what is the contribution of convection to the transport of energy. The total flux is

$$F_{\rm t} = F_{\rm conv} + F_{\rm rad} = \frac{4acG}{3}\frac{T^4 m}{\kappa P r^2}\nabla_{\rm rad}. \tag{1.25}$$

The radiation still has some contributions as defined in eq. 1.15. Only the convective flux needs to be determined. Consider that the blob has a temperature difference ΔT from its surroundings. It moves radially with a mean velocity v and the pressure is in equilibrium. The convective flux can be written as

$$F_{\rm conv} = \rho v c_p \Delta T, \tag{1.26}$$

where $c_p = \frac{\partial q}{\partial T}$ is the specific heat and q is the heat per unit mass. Similarly to density, we can write the temperature difference as

$$\frac{\Delta T}{T} = \frac{\ell_m}{2H_P}(\nabla - \nabla_b), \tag{1.27}$$

where ℓ_m is the distance the blob moves and H_P is the pressure scale height, defined as

$$\frac{1}{H_P} = -\frac{d\ln P}{dr} = \frac{\rho g}{P}. \tag{1.28}$$

If we assume the blob to have a constant pressure and element abundance ($\Delta P = \Delta\mu = 0$), from eq. 1.19 we have $\frac{\Delta\rho}{\rho} = \delta\frac{\Delta T}{T}$. To determine the flux we still need to determine the mean velocity v. We can look at the work per unit mass (W) that the buoyancy force

*There is convective super-adiabatic regions when $\nabla > \nabla_{\rm ad}$

produces in a given distance ℓ_m,

$$W = (-g\Delta\rho)\frac{\ell_m}{2\rho} = \delta\frac{g}{2T}\ell_m\Delta T. \tag{1.29}$$

Considering that half of the work is converted to kinetic energy we derive that

$$v = g\delta(\nabla - \nabla_b)\frac{\ell_m^2}{8H_P}. \tag{1.30}$$

We found that the convective flux can be written as

$$F_{\text{conv}} = \rho c_P T\sqrt{g\delta}\frac{\ell_m^2}{4\sqrt{2}}H_P^{-3/2}(\nabla - \nabla_b)^{3/2}. \tag{1.31}$$

Replacing the F_{rad} (eq. 1.15) and F_{conv} (eq. 1.31) in eq. 1.25 we can derive the following expression

$$(\nabla - \nabla_b)^{3/2} = \frac{8}{9}\text{U}(\nabla_{\text{rad}} - \nabla_{\text{ad}}), \tag{1.32}$$

where

$$\text{U} = \frac{3acT^3}{c_P\rho^2\kappa\ell_m^2}\sqrt{\frac{8H_P}{g\delta}}. \tag{1.33}$$

In the last two equations, we still do not define ∇_b and ℓ_m. ℓ_m is the mean mixing distance (mixing length), which is usually unknown since we are representing a 3-dimensional value in 1 dimension. To estimate the flux, the mixing length parameter is parameterized as $\ell_m = \alpha_{\text{MLT}}H_P$, where α_{MLT} is the mixing length parameter that represents the unknown effects of convection.

To know the convective flux we need to know how the temperature varies in the blob, which is described by ∇_b. In the limit where there is no energy exchange with the surrounding, we have $\nabla_b = \nabla_{\text{ad}}$. However, the blob can lose some energy to its surroundings. The energy exchanged is equal to the blob's luminosity (L_b), spread across its entire surface area (S_b). We have

$$L_b = \frac{2S_b}{d_b}\frac{4acT^3}{3\kappa\rho}, \tag{1.34}$$

where d_b is the diameter of the blob. The temperature change of the blob is described by the adiabatic term and the L_b term, where

$$\frac{dT_b}{dr} = \left(\frac{dT}{dr}\right)_{\text{ad}} - \frac{L_b}{\rho V_b c_P v}, \tag{1.35}$$

where V_b is the volume of the blob. For a spherical blob we have $\frac{S_b}{d_b V_b} = \frac{9}{8\ell_m^2}$, and we obtain

$$(\nabla_b - \nabla_{\text{ad}}) = 2\text{U}\sqrt{\nabla - \nabla_{\text{b}}}^{1/2}. \tag{1.36}$$

We can define the convective efficiency coefficient $\Gamma = \frac{(\nabla - \nabla_b)^{1/2}}{2U}$, and replacing in eq. 1.32 and 1.36 we get

$$\Gamma = \frac{\nabla - \nabla_b}{\nabla_b - \nabla_{\text{ad}}}, \tag{1.37}$$

$$\Gamma = \frac{9}{4}\frac{\nabla_{\text{rad}} - \nabla_b}{\nabla - \nabla_b}. \tag{1.38}$$

In extreme cases we can identify two limits:

- $\Gamma \to \infty$ when the convective flux is much higher than the radiative flux, it is an efficient convection, $\nabla = \nabla_b \to \nabla_{\text{ad}}$;
- $\Gamma \to 0$ when the radiative flux is much higher than the convective flux, it is an inefficient convection $\nabla = \nabla_b \to \nabla_{\text{rad}}$.

1.5 Energy production

As we have seen, there is a constant flow of energy from the interior to the surface of the star, where it is emitted into space. So the star is constantly losing energy. Therefore, it needs a source of energy to maintain its equilibrium.

To describe the production, let's consider a spherical mass shell of radius r. The energy crossing the inner surface of the shell per second is L_r and the energy leaving the shell is $L_r + dL_r$. The energy variation dL_r is caused by nuclear reactions, by cooling, or by the compression or expansion of the mass shell. Considering that this energy produced per unit of mass is ϵ, we have that

$$\mathrm{d}L_r = \epsilon \mathrm{d}m, \tag{1.39}$$

considering the conservation of mass equation (eq. 1.1), we can write the equation as

$$\frac{\mathrm{d}L_r}{\mathrm{d}r} = 4\pi r^2 \rho \epsilon, \tag{1.40}$$

which is the energy conservation equation we presented earlier (eq. 1.4). In the case of a star, ϵ is the combination of three main "sources" of energy

$$\epsilon = \epsilon_n - \epsilon_\nu + \epsilon_g. \tag{1.41}$$

ϵ_g is the work done by the gas during an expansion or contraction. From this method, there is the production of energy during a contraction, but it is not efficient enough to maintain the equilibrium of the star. The main source of energy comes from the nuclear

reactions producing energy ϵ_n by fusing lighter elements to create heavier ones. However, some of the energy is converted into neutrinos ϵ_ν, which are by-products of the nuclear reactions. This loss of energy to neutrinos is usually taken into account in the energy of the nuclear reactions. Also, the star only produces energy by nuclear reaction in its core (where P and T are high enough to ignite the reactions), so only a fraction of the elements are available for energy production.

In nuclear reactions, there is a change in the abundance of the elements from the conversion of an element i to an element j. The variation of the mass fraction X_i of an element i induced by nuclear reactions is

$$\rho \frac{\partial X_i}{\partial t} = A_i m_p \left[\sum_j (r_{ji} - r_{ij}) \right], \tag{1.42}$$

where r_{ij} is the rate of transformation of the element i into j, A_i is the atomic mass of the element i, and m_p is the mass of a proton.

In low-mass stars, nuclear fusion primarily involves hydrogen burning (during the main sequence) and helium burning (in the horizontal branch). The fusion of heavier elements, such as carbon and oxygen, generally occurs only in intermediate-mass and more massive stars.

1.5.1 Hydrogen fusion

The fusion of hydrogen is the first reaction that can take place inside a star. The burning of this element is the main source of energy during the longest phase of evolution, the MS. To convert hydrogen into helium, there are two main channels of reactions that can occur, the PP-chain and the CNO cycle. In both cases, four hydrogen nuclei (^{1}H) fuse to form one helium nucleus (^{4}He).

The PP-chain (proton-proton chain) directly fuses the four nuclei of ^{1}H. There are three alternatives to the PP-chain. Figure 1.1 is a scheme of the pp-chain reactions of all possible channels. The preferred channel depends on the temperature at which they occur: as the temperature increases, the preferred chain of reactions goes from PP1 to PP3.

The CNO cycle is the other main series of reactions for hydrogen fusion. It uses the different isotopes of carbon C, nitrogen N, and oxygen O as catalysts. Figure 1.2 is a scheme of the reaction chain of this cycle. It has two main cycles, one using ^{12}C (CNO-I), the other using ^{16}O (CNO-II). This depends on the reaction performed by ^{15}N, which has a high probability of forming ^{12}C. Regardless of the reaction chain, the abundance of

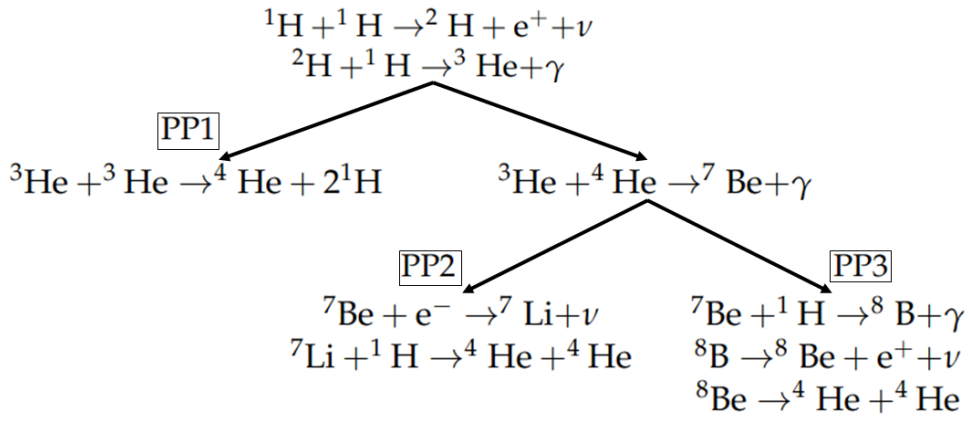

FIGURE 1.1: Scheme of the reaction that occurs in the PP-chain.

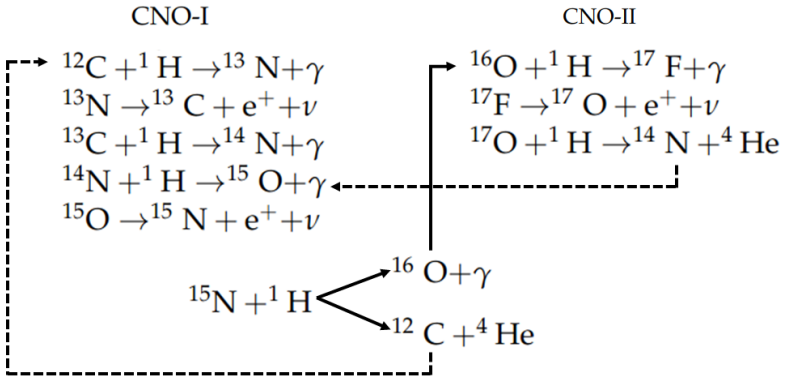

FIGURE 1.2: Scheme of the reaction that occurs in the CNO-cycle.

heavy elements remains constant during the hydrogen-burning phase. However, during the CNO cycle, the abundances of C, N, and O involved reach specific asymptotic values, which depend on the efficiency of each reaction in the chain.

The two reaction chains can take place simultaneously inside the star. However, depending on the temperature, the PP chain or the CNO cycle is favoured. For T in the range of $[0.6, 1.5] \cdot 10^7$ K the PP chain is dominant, for $T > 2 \cdot 10^7$ K the CNO cycle dominates. In terms of energy, the output from the two mechanisms are proportional to:

$$\epsilon_{pp} \propto \rho X_{^1H}^2 T^4, \tag{1.43}$$

$$\epsilon_{CNO} \propto \rho X_{^1H} X_{^{12}C} T^{18}, \tag{1.44}$$

where $X_{^1H}$ and $X_{^{12}C}$ are the mass fractions of hydrogen and carbon respectively in the burning region. When the CNO cycle is dominant, the energy output is too large to allow

radiation alone to transport the energy, forming a convective core.

1.5.2 Helium fusion

The helium burning phase is outside the MS which is the main phase I am focusing on in this study. Nevertheless, the low-mass stars I study in this work can reach helium fusion in the core, and here I briefly show the reactions that can occur. The helium in the core is burned by the triple α reaction (or 3α reaction). This happens in two steps.

$$\begin{aligned} {}^{4}\mathrm{He} + {}^{4}\mathrm{He} &\leftrightharpoons {}^{8}\mathrm{Be}, \\ {}^{8}\mathrm{Be} + {}^{4}\mathrm{He} &\rightarrow {}^{12}\mathrm{C} + \gamma. \end{aligned} \tag{1.45}$$

First, two nuclei of helium (or α particles) fuse forming a beryllium nucleus. Due to the temperature of the region, the beryllium particle decays very fast (10^{-16} s) back to helium. Despite this short lifespan, the collision time between particles is 10^5 times shorter, allowing the second step of the reaction to occur forming carbon nuclei by capturing the third α particle. As carbon accumulates in the core, it can react with helium forming oxygen. This element, in turn, reacts to form neon and subsequently higher elements.

$$\begin{aligned} {}^{12}\mathrm{C} + {}^{4}\mathrm{He} &\leftrightharpoons {}^{16}\mathrm{O} + \gamma, \\ {}^{16}\mathrm{O} + {}^{4}\mathrm{He} &\rightarrow {}^{20}\mathrm{Ne} + \gamma, \\ &\dots \end{aligned} \tag{1.46}$$

In stars, it is extremely rare for elements higher than neon to form by capturing helium nuclei. Typically, the core composition ends up being a ratio of 1:1 to 2:1 oxygen to carbon, depending on the rates of reactions in the core.

1.6 Equation of state

The equations (1.1) and (1.2) describe the internal structure of the star, although the variables P and ρ are not only related but also depend on the temperature. These three variables are related by the equation of state (EoS), formally described by

$$\rho \equiv \rho(P, T) \Leftrightarrow P \equiv P(\rho, T) \Leftrightarrow T \equiv T(P, \rho). \tag{1.47}$$

From these we can build up the whole thermodynamics inside the star from the different thermodynamic quantities such as the entropy S, the internal energy per unit mass U and the specific heat Q.

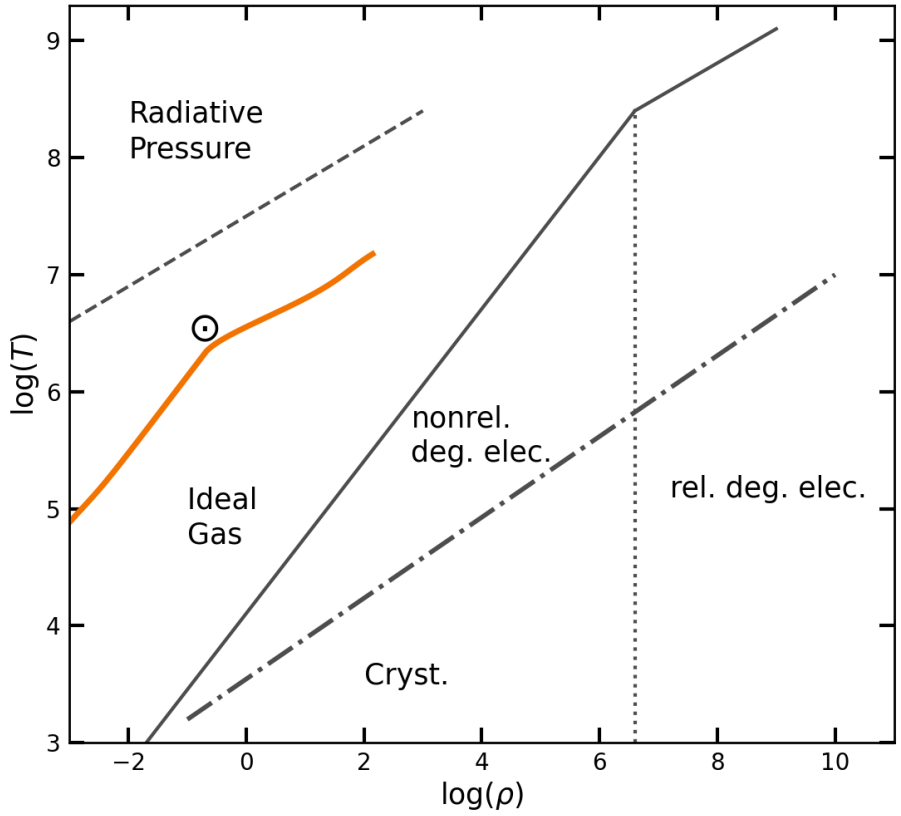

FIGURE 1.3: A sketch of the different regimes in the $\log(\rho) - \log(T)$ plane, where the EoS is dominated by the radiation pressure, the ideal gas regime, the degenerate electron gas in the non-relativistic and relativistic regime, and the crystalline regime. The orange line represents a stellar model of the Sun. The figure has been adapted from Kippenhahn & Weigert (1990).

One example of EoS is the ideal gas equation

$$P = \frac{R_g}{\mu}\rho T \tag{1.48}$$

where R_g is the gas constant and μ is the mean molecular weight. The equation (1.48) describes the behavior of the particles inside the star, allowing us to estimate all the thermodynamic variables. However, μ will be different if the gas particles are in a neutral or ionized state, allowing to describe it as

$$\mu = \mu(P, T) = \frac{\sum_i n_i A_i}{\sum_i n_i}, \tag{1.49}$$

where n_i is the number of particles per unit volume of the species i and A_i is the number of protons and neutrons of the species i. The species i include atomic particles in neutral and/or ionized states plus the free electrons of the ionized particle.

During most of the stellar evolution, the internal structure is described as an ideal gas. Figure 1.3 shows different regimes for the EoS and there we see in the orange solid line the

solar model where the ideal gas approximation works. Nevertheless, at different stages, it is possible that certain regions of the star follow different EoS, like the core of red giants (which is in a degenerate state). To model stars, it is necessary to use an EoS that has a parameter space that takes into account different regimes of matter. A number of EoS have been developed, such as the OPAL2005 EoS (Iglesias & Rogers, 1996) or the Saha-S EoS (Baturin et al., 2013).

1.7 Opacity

This section is based on the review of Alecian & Deal (2023).

The opacity is important for the internal structure of stars. It is essential to describe how the energy is transported inside the star, plus some physical mechanisms such as chemical transport processes (I look at these in detail in chapter 4). The photon, depending on its frequency ν, travels a mean free path l_ν without any interaction

$$l_\nu = \frac{1}{n\sigma_\nu}, \tag{1.50}$$

where n is the number of atoms per unit of volume and σ_ν is the cross-section for absorption of a photon with frequency ν. The opacity for a given frequency κ_ν is

$$\kappa_\nu = \frac{\sigma_\nu}{\mu}. \tag{1.51}$$

The calculation of κ_ν depends on various contributions such as

- **electron scattering (κ_s):** The photons interact with the free electrons in the star and change their trajectory without changing their frequency. This contribution is independent of the frequency and can be described by

$$\kappa_s \approx 0.2(1 + X), \tag{1.52}$$

  where X is the mass fraction of hydrogen.

- **free-free absorption (κ_{ff}):** The photon is absorbed by the particle system that is composed of a free electron and an ion. This increases the kinetic energy of the electron.

- **bound-free absorption (κ_{bf}):** The photon ionizes a neutral element as a result of its absorption.

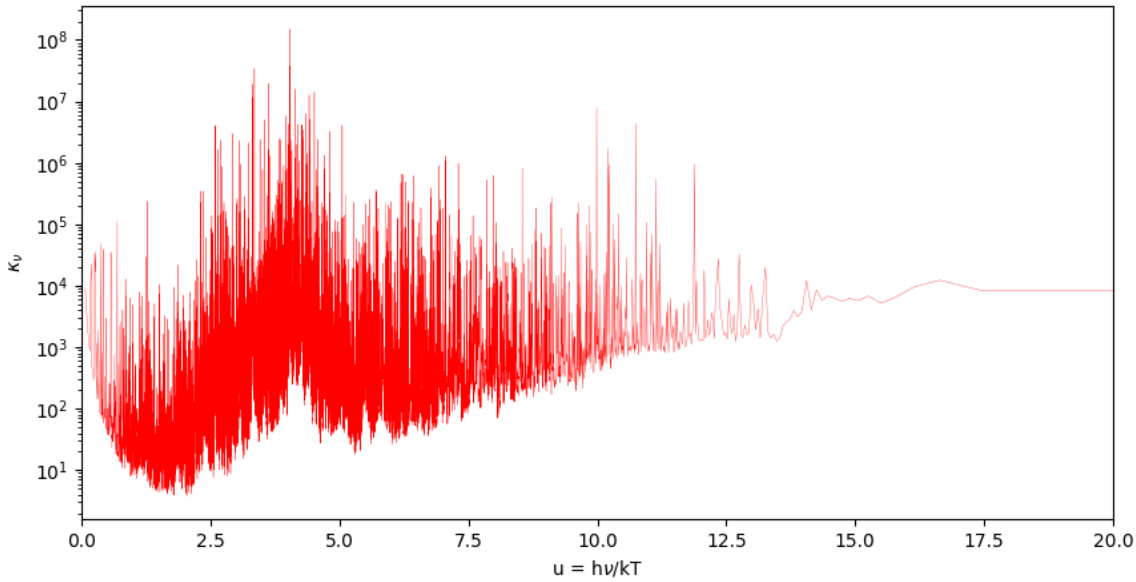

FIGURE 1.4: Example of monochromatic opacity (OP data) for calcium at a temperature of 10^5 K and an electron density of $10^{16.5}$cm^{-3}. The y-axis is the opacity in cm^{2}g^{-1}. Figure courtesy of Marin Vidal, master student under the supervision of O. Richard and M. Deal, private communication.

- **bound-bound absorption (κ_{bb}):** The photon is absorbed by a neutral particle, which raises it to a higher energy state.

However, the opacity depends on the temperature, density, and chemical composition; each element interacts differently with the photons, resulting in different individual opacities (their monochromatic opacities). Figure 1.4 shows the example of monochromatic opacity for calcium Ca.

Usually, it is only necessary to take into account the mean value of opacity at a given T, which is the Rosseland mean opacity (κ_R). Using the Planck function

$$B_\nu(T) = \frac{2h}{c}\frac{\nu^3}{\exp(u) - 1}, \tag{1.53}$$

we can determine the Rosseland mean opacity as

$$\frac{1}{\mu\kappa_R} = \frac{1}{\sigma_R} = \frac{\int_0^\infty \frac{1}{\sigma_\nu}\frac{\partial B_\nu}{\partial T}d\nu}{\int_0^\infty \frac{\partial B_\nu}{\partial T}d\nu} = \int_0^\infty \frac{F_u}{\sigma_u}du, \tag{1.54}$$

where h is the Planck constant, $u = \frac{h\nu}{k_B T}$ is the dimensionless energy, and k_B is the Boltzmann constant. σ_u is the cross-section for absorption of photons at dimensionless energy, and F_u is the normalized temperature derivative of the Planck function with respect to u (see Badnell et al. 2005). From this, we can see that the calculation of the Rosseland mean opacity must be performed at each point of the star, which has its own temperature

and density and also takes into account the contribution of opacity for all the elements and their abundances in that region. This is very demanding, requiring a detailed understanding of the interaction between the radiation and the atoms. Additionally, the calculation needs to be considered during the stellar evolution as the structure and chemical composition of the star changes over time.

In stellar models, the Rosseland mean opacity calculation from monochromatic opacity calculation can be done on-the-fly (like OP monochromatic: Seaton 2005), but it is currently very computationally expensive. To reduce the computation problem, various comprehensive pre-calculated tables have been published by different groups, covering different chemical mixtures and ranges of temperature and density. The Opacity Project (OP; Mendoza et al. 2007) and OPAL opacities (Iglesias & Rogers, 1996) take into account atomic absorption, which is important at higher temperatures. Molecular and dust absorption should be accounted for by specific low-temperature tables (like Ferguson et al. 2005). The combination of these tables allows a simple and fast calculation. However, it assumes a fixed chemical mixture throughout the evolution, which is not true due to nuclear reactions and chemical transport mechanisms. For best accuracy, the computation of the Rosseland mean opacity should be done at each mesh point and time step accounting for the detailed chemical abundances. Those approach has been implemented in several codes (Montpellier/Montreal code Turcotte et al. 1998, TGEC: Théado et al. 2009, Cesam2k20: Deal et al. 2018, MESA: Paxton et al. 2019).

1.8 Stellar evolution

In the previous sections, we described the basic equations that characterize the internal structure of stars. However, stars evolve over time, changing their chemical composition and losing continuously energy to space. The changes in the internal structure are slow (periods of millions here), so it is possible to define different stages of evolution with specific structural characteristics. We can divide stellar evolution into four main groups.

- **Very low-mass stars**, stars with masses $\lesssim 0.5\ M_\odot$, which are fully convective, and burn only hydrogen.

- **Low-mass stars**, stars with masses between 0.5 and 2.2 $M_\odot$, have a similar evolution to the Sun, they have a radiative zone, and can start the helium burning through the helium flashes.

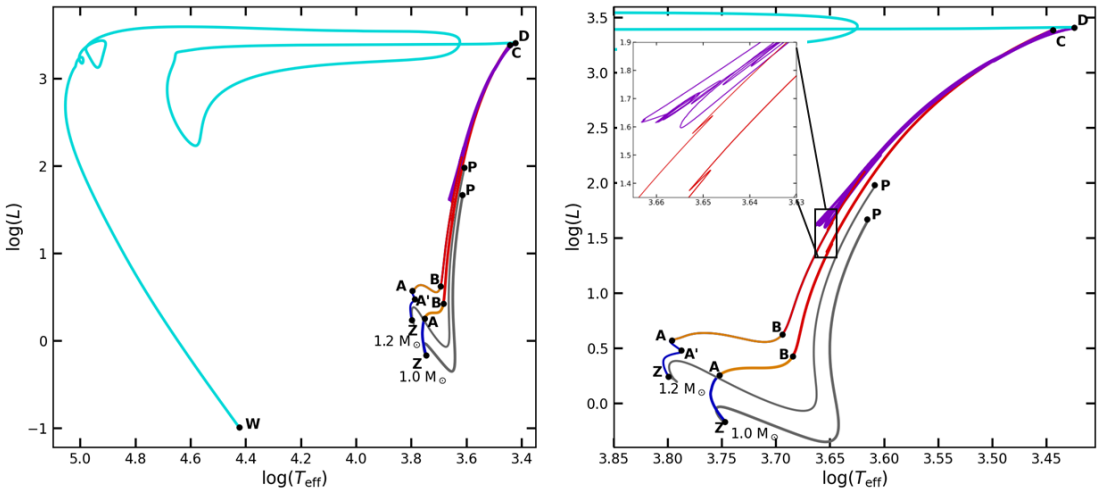

FIGURE 1.5: HR diagram of two evolutionary track of models of 1.0 $M_\odot$ and 1.2 $M_\odot$ stars. The colors represent the different stages of evolution where grey is the Pre-Main Sequence (PMS), blue is the Main Sequence (MS) stage, orange is the Sub-Giant (SG) stage, red is the Red Giant Branch (RGB), purple is the Horizontal Branch (HB) and Asymptotic Giant Branch (AGB), and cyan is the Planetary Nebula (PN) and White Dwarf (WD). The points represent the major evolutionary transitions between stages.

- **Intermediate mass stars**, they have masses between 2.2 and 10 $M_\odot$, and they start burning helium in a non-degenerative condition (no helium flash).

- **Massive stars**, they have masses $\gtrsim$ 10 $M_\odot$, and they go through the advance burning (can reach Fe element).

In this work, we study low-mass stars in MS (with masses between 0.5 and 1.8 $M_\odot$), which exhibit the same stage of evolution. Visually, the main difference is in L and $T_{\rm eff}$, which increase with the stellar mass.

So using the system of eq. 1.1, 1.2, 1.3, 1.4 and 1.42, we can model the evolution of stars. We can plot the full evolution of these stars in the Hertzsprung-Russell (HR, Hertzsprung 1911, Russell 1914) diagram, which shows the position of the star in the L and $T_{\rm eff}$ plane. Figure 1.5 shows the evolution of a 1.0 $M_\odot$ and a 1.2 $M_\odot$ stellar models in the HR diagram. Only part of the evolution of the 1.2 $M_\odot$ model is shown to highlight the main differences, because both examples go through the same phases. The evolutionary tracks in Fig. 1.5 are colored to represent the different stages of evolution. The points represent the major evolutionary transitions between stages and their order is P, Z, A, B, C, D, and W. In the following sections, we will outline the main characteristics of each stage.

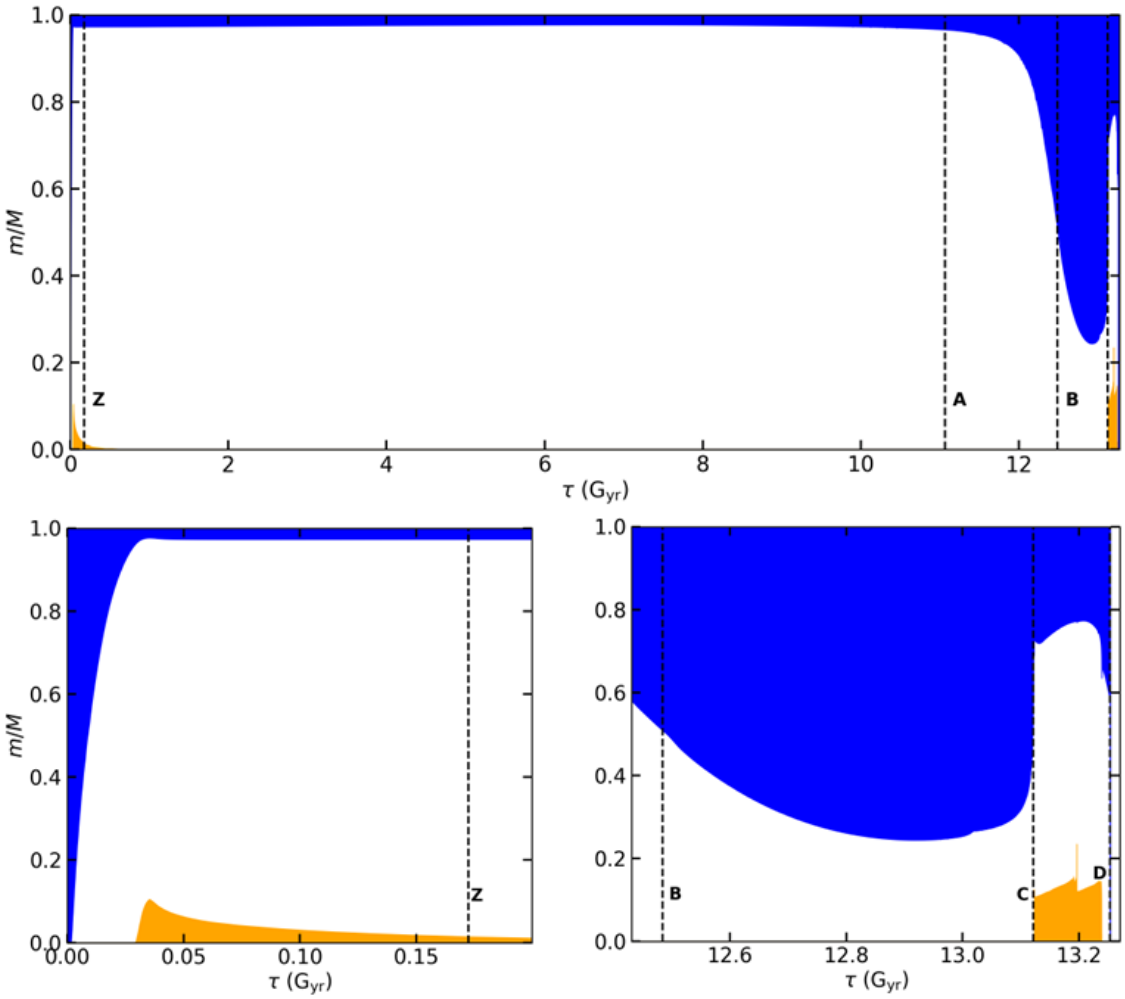

FIGURE 1.6: Kippenhahn diagram of 1.0 $M_\odot$ model, showing the evolution of convective (in blue for envelope, in orange for core) and radiative regions (in white) in the internal structure. The top panel is the full Kippenhahn diagram, the lower left panel is a zoom on the PMS stage, and the lower right panel is a zoom on the RGB and later stages of evolution.

1.8.1 Pre-main sequence

Stars are formed by the collapse of a giant molecular gas cloud, forming a protostar. The formation of the protostar is represented by point P in the HR diagram, from which it begins its evolution in the Pre-Main Sequence (PMS). During this phase, the protostar is constantly accreting material from its surroundings. It also has no nuclear reactions, and the luminosity it emits comes from the conversion of potential energy from its contraction. In the HR diagram of Fig. 1.5 we can divide this stage into two main PMS phases, the first where the evolution in the HR diagram is mainly a decrease of L with a very small variation of $T_{\rm eff}$, the second where $T_{\rm eff}$ increases with smaller variations of L. The first

phase is called the Hayashi track, this phase is characterized by the contraction of a fully convective protostar. The second phase is called the Henyey track, which begins when the internal temperature is high enough to form a radiative core. The evolution of the convective and radiative regions can be observed in the Kippenhahn diagram of Figs. 1.6 and 1.7. Both stars start fully convective and during the Henyey track the convective region recedes, becoming shallower for the more massive star as it reaches the end of the PMS phase, point Z. For more massive stars, this convective envelope can disappear almost completely.

The end of the PMS stage occurs when the hydrogen ignition occurs and it produces enough energy to stop the contraction, this is called the Zero Age Main Sequence (ZAMS, point Z). At the end of this phase, both stars have a convective core due to the burning of ^{3}He. In the stars, the ^{3}He abundance in the core is higher than the equilibrium abundances; when the star starts nuclear reactions, it efficiently burns the ^{3}He, producing an excess of energy that can only be transported by convection. However, when the ^{3}He reaches an equilibrium abundance, if it does not have a high enough temperature to induce the CNO cycle (case of the 1.0 $M_\odot$ model), the convective core disappears shortly after the start of the next phase, the MS.

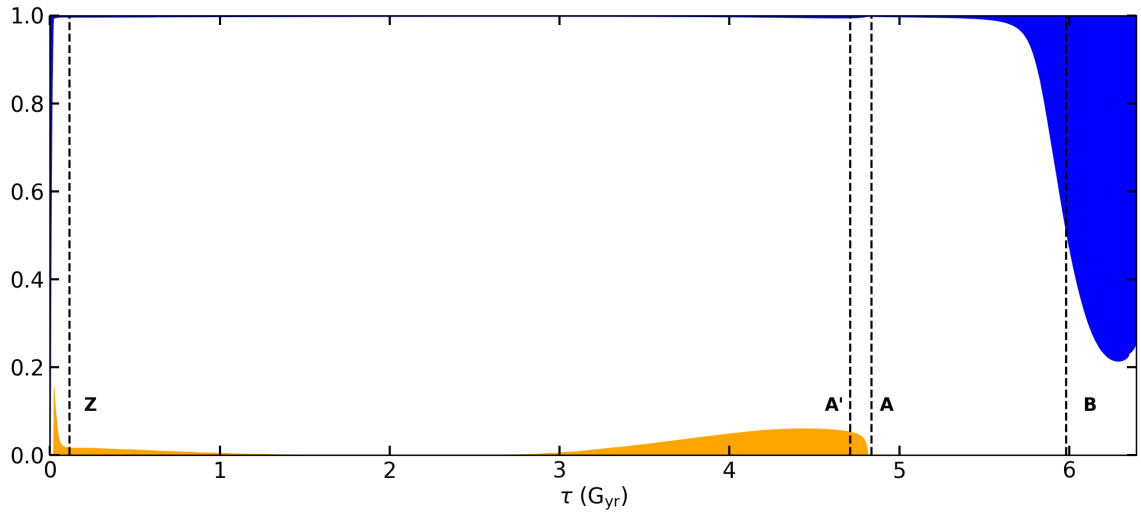

FIGURE 1.7: Kippenhahn diagram of 1.2 $M_\odot$ model, showing the evolution of convective and radiative regions. The color regions are the same as in Fig. 1.6

1.8.2 Main sequece

From the ZAMS to the end of the MS (point A) the star quietly burns hydrogen into helium without drastic changes in the internal structure. In the HR diagram, only small changes

in $T_{\rm eff}$ and L are expected. The convective envelope remains nearly the same depth. The convective core for the 1.0 $M_\odot$ star disappears after the ^{3}He abundance is at equilibrium, and since the main energy source is the PP chain, it does not provide enough energy to sustain a convective core. The 1.2 $M_\odot$ star barely sustains the convective core, as it can be seen in Fig. 1.7. This is a transition model where the CNO cycle starts to be the main chain of the nuclear reaction. The disappearance of the convective core coincides with the ^{3}He reaching equilibrium and increases again when the CNO cycle is at full efficiency. More massive stars have a permanent convective core during the MS.

The end of this stage occurs when the hydrogen in the core is completely converted into helium, it is called the Terminal Age Main Sequence (TAMS) at point A. This is the transition point to the SB stage. For stars with a radiative interior, the transition in the HR diagram between the MS and SG stages is subtle, as for the 1.0 $M_\odot$ model. In the case of the 1.2 $M_\odot$ model, and stars with a convective core, we find a hook in the HR diagram, the transition region between point A' and point A (Fig. 1.5). In this case, with the presence of a convective core, the hydrogen is depleted throughout the core at the same time and not only at the center first. Because of the rapid decrease in the rate of nuclear reactions, the star goes out of equilibrium. This leads to a rapid gravitational contraction as an attempt to sustain the energy production, leading to an increase in the effective temperature of the star until entering the SG phase.

The MS is the longest stage of stellar evolution. The low-mass stars spend several Gyr burning calmly the hydrogen in the core. For the ones in our example, the 1.0 $M_\odot$ star takes about $\sim$ 11 Gyr to burn completely the hydrogen, and for the 1.2 $M_\odot$ model, it is $\sim$ 4.6 Gyr. This is related to the central temperature, more massive stars can reach a higher temperature at the center, which allows higher rates of hydrogen burning.

1.8.3 Sub-giant and red giant branch

After low-mass stars have completely exhausted their hydrogen in the core, they cannot burn helium directly because the central temperature is not high enough to start the nuclear reaction. This leaves the star with an isothermal helium core and no nuclear reaction. To maintain hydrostatic equilibrium, the star begins to contract in the interior, causing the hydrogen to ignite in a shell outside the core, called the hydrogen burning shell. This shell increases the mass of the helium core but does not produce enough energy to stop the inner layers from contracting. As the inner layers contract, the outer layers expand. The star

increases its radius, decreasing its $T_{\rm eff}$ at a constant luminosity, and begins to expand its convective shell deep inside the star. Eventually, the central layers reach a density limit (or the mass limit for a non-degenerate isothermal core, the Schönberg-Chandrasekhar mass limit) that turns the quasi-ideal gas core into an electron-degenerate gas core. This marks the transition to the Red Giant Branch (RGB) phase (B point, see Fig. 1.5).

From point B, in the RGB phase, the inner layers of the star continue to contract while the outer layers expand, with a faster increase in their L and smaller changes in $T_{\rm eff}$. During this phase, the convective envelope reaches its maximum depth (the so-called first dredge-up, see Fig. 1.6 and 1.7), living a chemical discontinuity in the radiative region. As the star evolves in this phase, the hydrogen burning shell reaches the chemical discontinuity, leading to an abrupt decrease in luminosity, the so-called luminosity bump (we can see a zoom of this feature in the HR diagram in Fig. 1.5). After the luminosity bump, the star continues to rise in the RGB. The RGB ends (n.b. this and the following phases are not shown in Fig. 1.5 for 1.2 $M_\odot$ stellar model) when a region near the center reaches a high enough pressure and temperature to ignite helium nuclear reactions point C. Since the core is in a degenerate state, it starts a series of explosive events from the ignition of helium and their energy is used to lift the core degeneracy. This explosive phenomenon is called a helium flash. After the core is in an ideal gas state, the star quietly burns helium in the core. This leads to a smaller radius and luminosity when entering the Horizontal Branch (HB).

1.8.4 Horizontal branch and final stages of evolution

In the horizontal branch, the star uses helium to produce energy by converting it to carbon and oxygen in a convective core. During this phase, the production of carbon and oxygen causes a change in opacity that affects the convection in the central regions. This phase ends when the helium is exhausted and the core is composed of carbon and oxygen. The star enters the AGB phase, where the ignition of carbon and oxygen is not possible, and the core becomes an electron degenerate gas again. This causes the inner layers to contract and the outer layers to expand, increasing L. At this stage, the stars have a core of carbon and oxygen surrounded by a helium burning shell which in turn is surrounded by a hydrogen burning shell. The two burning shells are very close together and the interaction between the two creates a series of thermal instabilities, which are the thermal pulses. These pulses are a series of loops where there are increases and decreases in the

luminosity of the star in the HR diagram. The lower-mass star cannot ignite the carbon-oxygen core, and the series of interactions of the burning helium and hydrogen shells detach the outer layers. The outer layers escape the gravitational pull of the star, forming a planetary nebula (in the models this causes a rapid increase in $T_{\rm eff}$). The loss of the outer layers exposes the hotter and less luminous core of the star (point W), called the white dwarf, which is mainly composed of carbon and oxygen, with sometimes a thin envelope of helium and hydrogen.

Chapter 2

Asteroseismology

This chapter is based on Aerts et al. (2010), Chaplin & Miglio (2013), and Cunha (2018).

Asteroseismology is the study of the oscillations of stars. These are variations on the surface of the stars in L and T_{eff} that we can observe. Since they propagate inside the star, their properties depend on the internal structure. They provide a new insight into the interior of stars. There are two main types of excitation of oscillations:

- Self-excited oscillations;
- Stochastic oscillations.

The first is the conversion of thermal energy into mechanical energy. An example of this is the κ mechanism, which comes from the variation of opacity within the star that produces the oscillations. This happens in unstable oscillator stars such as Cepheids, δ Scuti, β Cephi, and others. The second are oscillations driven by the presence of a convective envelope. In the boundary between the convective and radiative zones, the upward and downward flux of convection can create random turbulent motions in the boundary that excite the oscillations. This type of oscillation was first observed in the Sun (Helioseismology) and then in other solar-type stars. The stars that exhibit this second type of oscillation are called solar-like oscillators, and these are the stars that are studied in this manuscript, in particular, the F-type stars are cool enough to have a fine convective envelope. In the next few sections, we look at the theory behind stellar oscillations.

2.1 The stellar pulsation equations

We first look to the general stellar structure equations. We have the system of equations that gives the mass conservation

$$\frac{\partial \rho}{\partial t} = -\boldsymbol{\nabla}(\rho \mathbf{v}), \tag{2.1}$$

the momentum conservation

$$\rho \frac{\partial \mathbf{v}}{\partial t} + \rho(\mathbf{v}\boldsymbol{\nabla})\mathbf{v} = -\boldsymbol{\nabla} P + \boldsymbol{\nabla}\phi, \tag{2.2}$$

and the Poisson's equation,

$$\boldsymbol{\nabla}^2 \phi = -4\pi G\rho, \tag{2.3}$$

where t is time, $\mathbf{v} = \frac{\partial \boldsymbol{\xi}}{\partial t}$ is the velocity vector, $\boldsymbol{\xi}$ is the displacement vector, $\boldsymbol{\phi}$ is the gravitational potential and $\boldsymbol{\nabla}$ is the operator containing the partial derivatives, in this case in spherical coordinates.

In this case, we only consider adiabatic oscillations. They are small enough not to make any energy exchange with the surroundings. The adiabatic exponent is then expressed as

$$\Gamma_1 = \frac{\rho}{P}\frac{\delta P}{\delta \rho}, \tag{2.4}$$

where δP and $\delta\rho$ are the Lagrangian perturbations in pressure and density.

With these four equations, we have the complete system of equations to derive the oscillations equations. We consider a first order perturbation as

$$\begin{aligned} \rho &= \rho_0 + \rho', \\ P &= P_0 + P', \\ \mathbf{v} &= \mathbf{v}', \\ \phi &= \phi_0 + \phi'. \end{aligned} \tag{2.5}$$

ρ_0, P_0 and ϕ_0 are the values at the equilibrium position (assuming $\mathbf{v}_0 = 0$ in the equilibrium state) and the ρ', P', $\mathbf{v}'$ and ϕ' are the first order perturbations. We now replace the perturbations in eq. 2.5 in the eq. 2.1 to 2.4 and neglecting all second and higher-order terms, we obtain the perturbation equations:

$$\frac{\partial \rho'}{\partial t} = -\boldsymbol{\nabla}\left(\rho_0 \frac{\partial \boldsymbol{\xi}}{\partial t}\right) \tag{2.6}$$

$$\rho_0 \frac{\partial^2 \boldsymbol{\xi}}{\partial^2 t} = -\boldsymbol{\nabla} P' + \rho_0 \boldsymbol{\nabla} \phi' + \rho' \boldsymbol{\nabla} \phi_0 \tag{2.7}$$

$$\boldsymbol{\nabla}^2 \phi' = -4\pi G \rho' \tag{2.8}$$

$$P' + \boldsymbol{\xi} \boldsymbol{\nabla} P_0 = \frac{\Gamma_{1,0} P_0}{\rho_0} (\rho' + \boldsymbol{\xi} \boldsymbol{\nabla} \rho_0) \tag{2.9}$$

2.2 General solution

All the variables P, ρ, ϕ and $\boldsymbol{\xi}$ can be described in spherical coordinates (r, θ, φ), so they have a dependence in r, θ, φ and in t. Using the separation of variables technique, the solution of the four equations can be obtained as

$$f'(r, \theta, \varphi, t) = \mathrm{R}\{f'(r) Y_\ell^m(\theta, \varphi) e^{-i\omega t}\} \tag{2.10}$$

$$\boldsymbol{\xi}(r, \theta, \varphi, t) = \mathrm{R}\left\{ \left[\xi_r(r) R_l^m(\theta, \varphi) \hat{a}_r + \xi_h(r) \left(\frac{\partial Y_\ell^m}{\partial \theta} \hat{a}_\theta + \frac{1}{\sin\theta} \frac{\partial Y_\ell^m}{\partial \varphi} \hat{a}_\varphi \right) \right] e^{-i\omega t} \right\} \tag{2.11}$$

where f' is the variable P, ρ and ϕ, ξ_r and ξ_h are the depth dependent amplitudes in the radial and horizontal components of the displacement, respectively. Y_ℓ^m are the spherical harmonics and ω is the angular oscillation frequency. We only consider the real components (R$\{\}$) to be consistent with a fully reflective boundary.

The spherical harmonics introduce the dependence on 2 quantum numbers, the angular (mode) degree ℓ, which is a positive integer and represents the number of surface nodes of the perturbation. The other number is the azimuthal order m, which takes on integer values between $-\ell$ and ℓ (inclusive), corresponding to the subset of surface nodes that cross the stellar equator. Figure 2.1 is a sketch of some spherical harmonics. Note that in order to detect the different set of m it is necessary to break the spherical symmetry (e.g. by considering rotation), which is not taken into account in this manuscript.

Taking the perturbation equations 2.6 to 2.9 and using the spherical harmonic property $\nabla^2 Y_\ell^m = -\frac{\ell(\ell+1)}{r} Y_\ell^m = -\kappa_h^2 Y_\ell^m$, where κ_h is the horizontal wave number, gives us the system of differential equations:

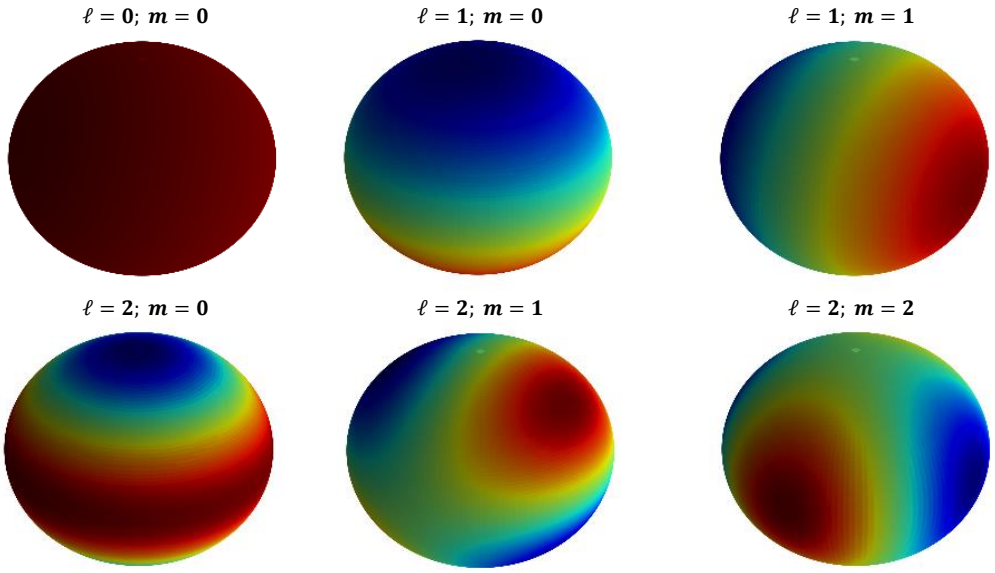

FIGURE 2.1: Sketch of some spherical harmonics.

$$\frac{c_0^2}{r}\frac{d}{dr}(r^2\xi_r) - g_0\xi_r - \left(\frac{S_\ell^2}{\omega^2} - 1\right)\frac{P'}{\rho_0} = \frac{S_\ell^2}{\omega^2}\phi', \tag{2.12}$$

$$\frac{dP'}{dr} + \frac{g_0}{c_0^2}P' - \rho_0(\omega^2 - N^2)\xi_r = -\rho_0\frac{d\phi'}{dr} \tag{2.13}$$

$$\frac{1}{r^2}\frac{d}{dr}\left(r^2\frac{d\phi'}{dr}\right) - \frac{\ell(\ell+1)}{r^2}\phi' = 4\pi G\left(\frac{P'}{c_0^2} + \frac{\rho_0 N^2}{g_0}\xi_r\right). \tag{2.14}$$

Here, two frequencies are defined: the Lamb frequency (S_ℓ) and the buoyancy frequency (N), which are given by

$$S_\ell^2 = \frac{\ell(\ell+1)c_0^2}{r^2},\ N^2 = g_0\left[\frac{1}{\Gamma_{1,0}}\frac{d\ln P}{dr} - \frac{d\ln\rho}{dr}\right]. \tag{2.15}$$

Where c_0 is the sound speed and g_0 is the gravity at equilibrium. Note that the buoyancy frequency is related to the structure of the star, where values of $N^2 > 0$ correspond to the stable regions of the star, the radiative zone, and $N^2 < 0$ correspond to the unstable regions, the convective zones. The S_ℓ^2 and N^2 are critical frequencies related to the acoustic and gravitational modes, which are solutions of the differential equations.

2.3 Oscillation modes

The system of equations (eq. 2.12 to 2.14) can be solved numerically. To do this, it is necessary to define the appropriate boundary condition. Boundary condition at the center $(r = 0)$ needs to impose no divergence in the solution. Surface boundary $(r = R)$ needs to take into consideration that the density should vanish outside the star and it depends on the stellar atmosphere. The solutions obtained are discrete values of the frequency ω. Their values are associated with a quantum number n (the radial order), which represents the number of nodes of the perturbation along the radial direction. The solution is characterized by three quantum numbers $\omega = \omega(n, \ell, m)$. Nevertheless, the solution have a degeneracy on the values of m, since we do not consider any mechanisms to break the spherical symmetry. In this case we have $\omega = \omega(n, \ell)$.

The discrete solutions can be divided into two types. The first are the gravity or g modes, generally characterized by low frequencies, which propagate in regions where $N^2 > 0$, i.e. radiative zones. These modes are excited by the upward motion (which may not be strictly vertical) of an element of a fluid in the stellar interior. This motion occurs at constant pressure, implying a perturbation of the density, which is pulled towards equilibrium by the gravitational force. In MS solar-like oscillators, the g-modes cannot be observed because they dissipate in the convective envelope. When they reach the surface, their amplitude is very small and it would require a lot of data (several decades) to detect them in the Sun. These modes have the peculiarity of being equally spaced in the period, by the period spacing

$$\Delta\Pi_{g,\ell} = \frac{2\pi}{\sqrt{\ell(\ell+1)}} \left(\int_{r1}^{r2} \frac{N}{r} \mathrm{dr} \right)^{-1} . \tag{2.16}$$

These modes are non-radial, i.e. $\ell > 0$, and are associated with negative values of n. There, the frequency increases with decreasing $|n|$ and increasing ℓ.

The second solutions are the acoustic modes (also called pressure modes or simply p-modes) and propagate in regions where their frequencies are greater than or equal to S_ℓ^2. They are excited by the stochastic motion of the fluid in the convective regions, which disturbs the local pressure and induces a pressure gradient that tries to restore the equilibrium state. Unlike the g-modes, it is possible to observe the p-modes in MS solar-like oscillators and they are equally spaced in frequency by the large frequency separation ($\Delta\nu$, which is presented in the next section). The p-modes propagate between the surface and a boundary region where S_ℓ^2 is equal to the mode frequencies, and they have frequencies

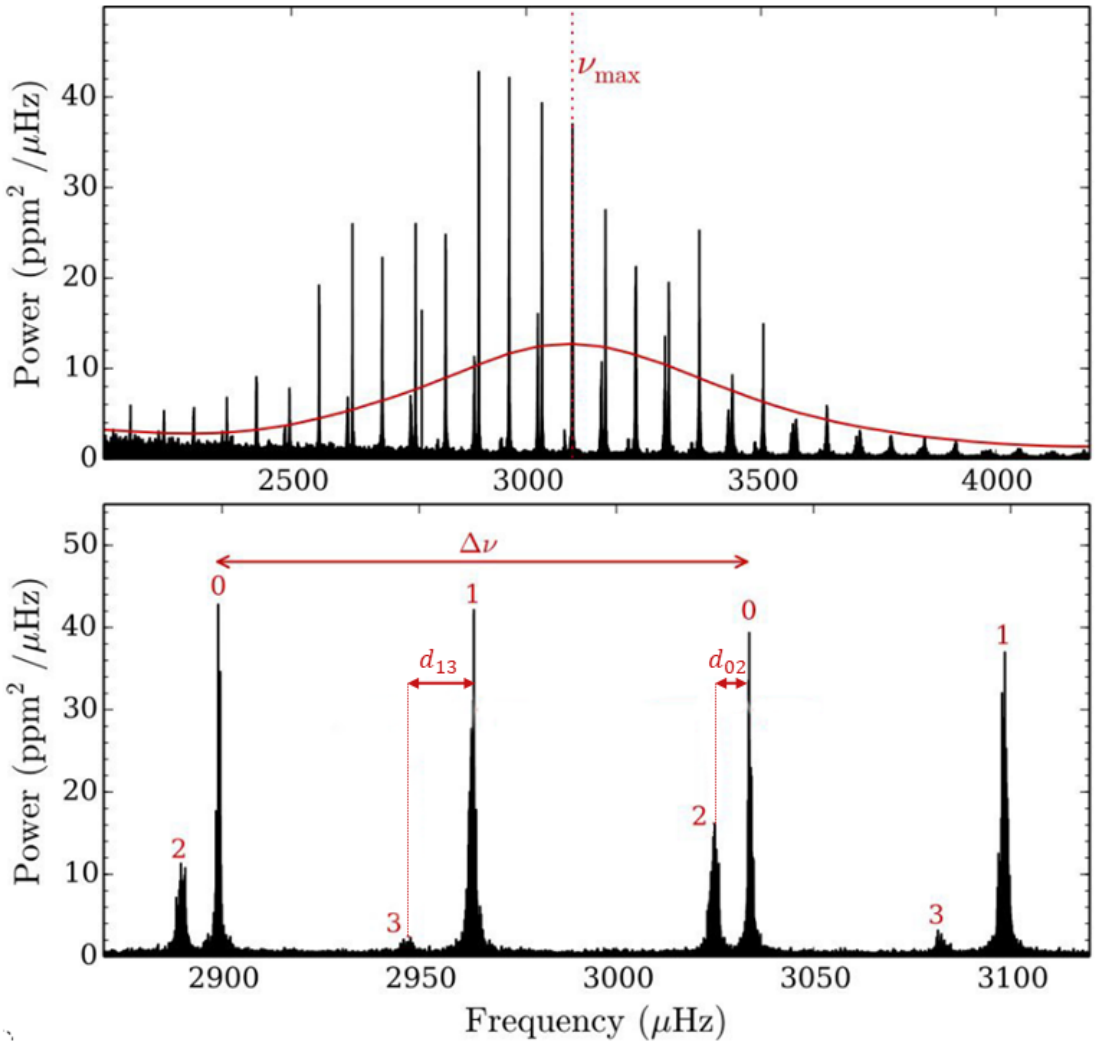

FIGURE 2.2: Power density spectrum of the Sun. The red line on the top panel shows a smoothing of the spectrum. The bottom panel shows a close-up of the large separations. Adapted from Cunha (2018).

greater than the g-modes. These modes are associated with positive values of n and their frequency increases with n and ℓ.

There is a third type of mode that appears in the late stage of evolution (SG or later). This type of mode appears due to the coupling of the g and p cavities. As the star evolves, the frequency of the p-mode decreases to values similar to those of the g-mode, creating a resonant mode called a mixed-mode. These modes are very short-lived during evolution and give a very sensitive constraint on age. However, in this work, I focus on MS stars, which do not show this type of mode.

2.4 Seismic observation and scaling relations

The observed seismic frequencies provide additional constraints on stellar models that help to improve stellar physics. With the seismic frequencies, which can be obtained from the seismic power density spectrum (example in Fig. 2.2), it is possible to better constrain the stellar interior of stars, giving more direct constraints on their mass, radius, and age. The dependence between M, R, and the seismic frequencies can be derived by a scaling relation with the seismic parameters obtained from each frequency and its spectrum. These are the frequency at maximum power $\nu_{\max}$ and the large frequency separation $\Delta\nu$. In the seismic spectrum, the amplitudes of the frequencies are modulated by a Gaussian function (called Gaussian envelope) with the maximum corresponding to $\nu_{\max}$ (see top panel of Fig. 2.2). This envelope can be approximated by an empirical relation defined with a standard deviation σ (Mosser et al., 2012).

$$\sigma = \frac{0.66\nu_{\max}^{0.88}}{2\sqrt{2\ln(2)}}. \tag{2.17}$$

$\nu_{\max}$ can be related to the stellar surface gravity g and the effective temperature $T_{\rm eff}$ of the star by the following scaling relation

$$\nu_{\max} \propto \frac{g}{\sqrt{T_{\rm eff}}} \propto \frac{M}{R^2\sqrt{T_{\rm eff}}}. \tag{2.18}$$

$\Delta\nu$ is defined as the separation between two modes of the same degree ℓ and successive radial order n (see bottom panel of Fig. 2.2). This quantity is related to the mean stellar density $\bar{\rho}$ by the following scaling relation

$$\Delta\nu = \nu_{n,\ell} - \nu_{n-1,\ell} \propto \sqrt{\bar{\rho}} \propto \sqrt{\frac{M}{R^3}}. \tag{2.19}$$

It is possible to combine the last two expressions to obtain the following two scaling relations

$$\frac{R}{R_\odot} \approx \left(\frac{\nu_{\max}}{\nu_{\max,\odot}}\right)\left(\frac{\Delta\nu}{\Delta\nu_\odot}\right)^{-2}\left(\frac{T_{\rm eff}}{T_{\rm eff,\odot}}\right)^{1/2}, \tag{2.20}$$

$$\frac{M}{M_\odot} \approx \left(\frac{\nu_{\max}}{\nu_{\max,\odot}}\right)^{3}\left(\frac{\Delta\nu}{\Delta\nu_\odot}\right)^{-4}\left(\frac{T_{\rm eff}}{T_{\rm eff,\odot}}\right)^{3/2}. \tag{2.21}$$

These empirical relations allow us to determine the radius and mass of stars by linking two observed seismic properties to the effective temperature. However, these scaling relations are only valid for the Sun and solar-type stars.

2.5 Small separation and frequency ratios

This section in based on the work of Roxburgh & Vorontsov (2003)

Other seismic constraints are the small frequency separations d_{02} and d_{13} (shown in the bottom panel of Fig. 2.2). These are the differences between two modes of different degrees and successive radial order.

$$\begin{aligned} d_{02}(n) &= \nu_{n,0} - \nu_{n-1,2}, \\ d_{13}(n) &= \nu_{n,1} - \nu_{n-1,3}. \end{aligned} \tag{2.22}$$

These parameters are more sensitive to the interior of the star but require to detection of modes with $\ell = 2$ and $\ell = 3$, which are not always observable (especially $\ell = 3$). It is possible to consider another small separations, the d_{01} and d_{10}, which are defined by the 5 point separations as

$$d_{01}(n) = \frac{1}{8}(\nu_{n-1,0} - 4\nu_{n-1,1} + 6\nu_{n,0} - 4\nu_{n,1} + \nu_{n+1,0}). \tag{2.23}$$

$$d_{10}(n) = -\frac{1}{8}(\nu_{n-1,1} - 4\nu_{n-1,0} + 6\nu_{n,1} - 4\nu_{n,0} + \nu_{n+1,1}). \tag{2.24}$$

With these small separations, it is possible to define the frequency ratios as

$$\begin{aligned} r_{01}(n) &= \frac{d_{01}(n)}{\Delta\nu_1(n)}, \\ r_{10}(n) &= \frac{d_{10}(n)}{\Delta\nu_0(n+1)}, \\ r_{02}(n) &= \frac{d_{02}(n)}{\Delta\nu_1(n)}, \\ r_{13}(n) &= \frac{d_{13}(n)}{\Delta\nu_0(n)}. \end{aligned} \tag{2.25}$$

$\Delta\nu_\ell(n)$ is the large frequency for the correspondent radial order and degree ℓ. This is a set of constraints that are sensitive only to the interior of the star and almost independent of the structure of the outer layers. This is useful because we are currently unable to model the stellar surface and its interaction with the frequencies correctly. The direct use of the individual frequencies requires empirical corrections to the surface effects (this is discussed in chapter 5.4.2). However, the use of ratios avoid this empirical correction but requires a sufficiently large set of individual frequencies to be used.

Chapter 3

Observational Constraints

Asteroseismology provides the strongest constraints on stellar models. It allows a more precise estimation of the stellar age because it is strongly related to the internal structure of the star. Missions like CoRoT/CNES (Baglin et al., 2006), *Kepler*/K2 (Borucki et al., 2010), and the Transiting Exoplanet Survey Satellite (TESS; Ricker 2016), provided high-quality data that filled the HR diagram with asteroseismic targets. However, the seismic data are still not available for every star. So it is necessary to use other constraints, the classical ones (e.g. $T_{\rm eff}$, [Fe/H], L). They can complement the seismic data and help to constrain the stellar properties. However, they do not usually bring as strong constraints as seismology on the interior of stars due to their degeneracy (because different stars can have the same observed properties). In this chapter, we detail these classical constraints and how they are obtained from the different observational methods.

3.1 Astrometry and photometry

Astrometry and photometry are two techniques for observing stars. Astrometry is the precise measurement of the positions and motions of celestial objects. It involves determining the positions and distances of stars and other celestial objects in the sky. It works by measuring the angle of displacement of the object in the sky from different observations. From this method, it is possible to obtain the stellar parallax, which is the apparent shift of the position of a star in the sky along two different lines of sight. Knowing the parallax (π), we can estimate the distance d of the star using

$$d(\mathrm{pc}) = \frac{1(\mathrm{AU})}{\pi}. \tag{3.1}$$

If we have one arcsecond in the parallax, we know by definition that the distance of the object is one parsec (pc = 3.26 light-years).

Photometry is the measurement of the brightness of celestial objects, across different wavelengths. It determines the flux of energy that the observer receive in a specific wavelength band from the star. From the direct photometric observation, we have the apparent magnitude (the brightness) of the observed object. The value of this parameter depends on the wavelength band at which the star is observed. The apparent magnitude m_{ξ} of the respective wavelength band (ξ), is related to the observed flux of the same band (F_{ξ}), by

$$m_{\xi} = -2.5 \log \left(\frac{F_{\xi}}{F_{\xi,0}} \right), \tag{3.2}$$

where $F_{\xi,0}$ is the zero-point reference flux for the respective band. The star Vega is an example of a reference star.

However, the apparent magnitude is not a strong constraint and its value depends not only on the star but also on how far the object is from the observer and on the interaction (extinction factor) of the light with the interstellar dust. Therefore, it is necessary to define an absolute magnitude (M), which is the magnitude the star would have if it was 10 pc away from the observer. So the absolute magnitude of a given band (M_{ξ}) is

$$M_{\xi} = m_{\xi} - 5 \log \left(\frac{d}{10\text{pc}} \right) - A_{\xi}, \tag{3.3}$$

where A_{ξ} is the extinction factor for a given band. It is also possible to define the magnitude for the full electromagnetic spectra, the bolometric magnitude M_{bol}. However, this parameter can not be estimated from direct observations. It is necessary to use a correction corresponding to a wavelength band, using the bolometric correction BC_{ξ}, defined as

$$BC_{\xi} = M_{\text{bol}} - M_{\xi}. \tag{3.4}$$

Knowing the bolometric magnitude of the star, and using the bolometric magnitude of the Sun $M_{\text{bol},\odot}$, we can determine the star's luminosity as

$$M_{\text{bol},\odot} - M_{\text{bol}} = -2.5 \log \left(\frac{L}{L_{\odot}} \right). \tag{3.5}$$

Examples of astrometric and photometric missions include the Two Micron All-Sky Survey (2MASS, Cutri et al. 2003), the Sloan Digital Sky Survey (SDSS, Szalay 1998), and Gaia (Gaia Collaboration et al., 2018). 2MASS and SDSS are two Earth-based missions.

2MASS, operating from 1997 to 2001, comprised two telescopes: one in the Northern Hemisphere (Arizona, USA) and one in the Southern Hemisphere (Chile), to observe the entire sky in near-infrared light. SDSS, based in New Mexico, USA, aims to create multi-color images covering more than one-third of the sky and has been operational since 2000. Gaia, a space mission launched by ESA in 2013, aims to map the position, distance, and motion of stars across the Milky Way, complemented by determining stellar brightness, temperature, and chemical composition. In the next chapters, the luminosity values used as constraints are computed from Gaia DR3 (Gaia Collaboration et al., 2021)

3.2 Spectroscopy

Spectroscopy is an observation method that measures the distribution in the energy of the different wavelengths in the light that comes from the star. From the distribution of this light (spectrum), it is possible to extract information on the chemical composition (the abundance of specific elements), and effective temperature of the star. The stellar radiation follows a blackbody emission, so the spectrum has a dependence on the temperature that follows the Planck law. The light of the star is a continuum spectrum, emitting in all wavelengths. However, when this spectrum is observed, it shows some discontinuity lines corresponding to the absorption by the chemical elements present in the stellar surface and atmosphere. Each chemical element has a very well define and unique absorption spectra. Knowing the strength of this line gives us the abundance of this element. The $T_{\rm eff}$ determination is done by fitting atmospheric models that best adjust the spectrum. The chemical abundances are usually measured by line withs. One of the chemical constraints determined from spectroscopy is the iron content ([Fe/H]).

With the determination of $T_{\rm eff}$ from spectroscopy and L from photometry, we have a direct location of the star in the HR diagram. Nonetheless, with these two constraints, we have a direct constraint on the radius of the stars. We can relate these three parameters with the Steffan-Boltzmann law considering the stars as a spherical blackbody with the following expression

$$L = 4\pi R^2 \sigma_{\rm SB} T_{\rm eff}^4. \tag{3.6}$$

where $\sigma_{\rm SB}$ is the Stefan-Boltzmann constant.

Examples of spectroscopic missions include the APO Galactic Evolution Experiment (APOGEE, Ahumada et al. 2020) and the Echelle SPectrograph for Rocky Exoplanet and Stable Spectroscopic Observations (ESPRESSO, Cupani et al. (2017)). Both missions are

ground-based. APOGEE has observed the sky since 2011, utilizing two main spectrographs: one in New Mexico, USA, and the other in the Atacama Desert, Chile. Its objective is to map the chemical compositions and radial velocities of stars across different regions of the Milky Way. The ESPRESSO spectrograph, based in Chile, aims to detect and characterize rocky exoplanets around nearby stars by measuring their radial velocities with high precision. It has been operational since 2017.

3.3 Direct observation of mass and radius

The direct measurement of the stellar mass, radius, and age is impossible in most of the cases. Usually, these parameters are determined by scaling relations or model fitting, using different seismic, photometric, and spectroscopic constraints. In the case of age determination, there are only indirect methods using empirical relations (e.g. Gyrochronology, Chemical Clocks) that are usually calibrated with stellar models.

For the stellar mass, it can only be directly determined when the stars are in binaries. Through the observation of the orbital motion of the stars around their center of mass, it is possible to determine the dynamical mass of the components of the system with very high precision. Nonetheless, having access to precise mass allows us to use them as laboratories to test the current stellar models. The radius in some cases can be determined using interferometric techniques providing a strong constraint in stellar models.

Chapter 4

Chemical Composition and Transport

In this manuscript, we have already seen the basic stellar structure equations that govern stars and the evolution of low-mass stars. However, taking into account a more complex set of input physics has an impact on the stellar structure and evolution. The consideration of rotation, mass loss, and chemical transport mechanisms is important, as they have a strong influence on the evolution, especially on the time that the star spends in the different phases. In this chapter, I describe the chemical transport mechanisms that change the overall chemical profile of the stars over time. In contrast, nuclear reactions mainly affect the chemical composition in the core of stars, except when the convective envelope penetrates deep inside the stars (e.g. dredge up).

The chemical composition is one of the key ingredients in stellar modeling. Changing it affects the amount of fuel the star has available for nuclear reactions. Also, different amounts of certain elements have different effects on opacity, leading to changes in the location of radiative and convective regions.

The abundance in stars can be defined in two main ways. We can define it in terms of mass fraction of the element i (X_i). We usually define the components as the fractional abundance of hydrogen (X), the fractional abundance of helium (Y), and the fractional abundance of heavy elements (Z), which is the abundance of all elements heavier than helium. As these are fractional abundances, we know that

$$X + Y + Z = 1. \tag{4.1}$$

In stellar interiors, Z can be considered as trace elements (except in the core when the star is burning helium or in later stages), since a large percentage of the abundance is hydrogen

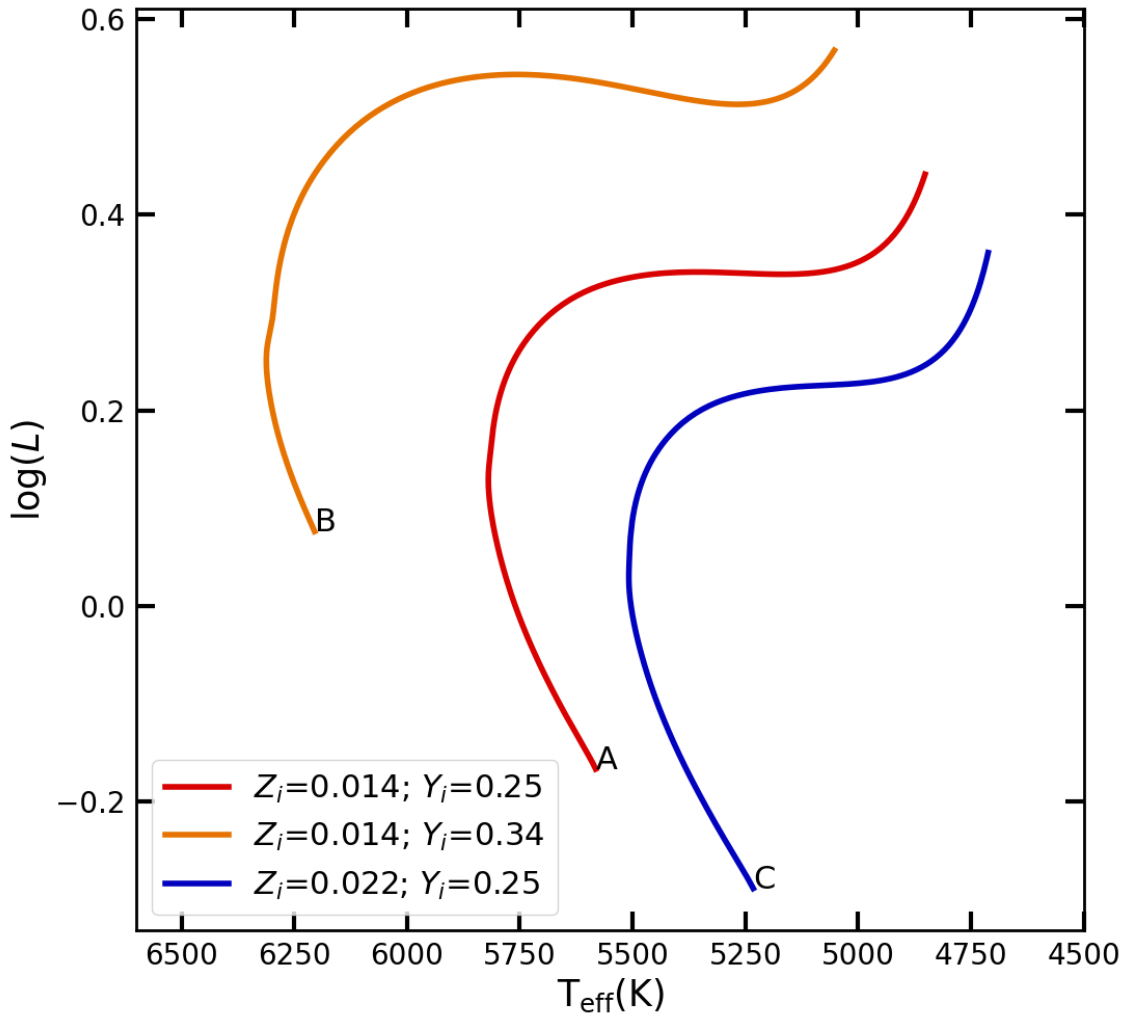

FIGURE 4.1: HR diagram of three evolutionary track of stellar models of 1.0 $M_\odot$ with different initial chemical composition of Y and Z.

and helium, where we find typical values ranging from: $X \sim [0.65; 0.75]$, $Y \sim [0.25; 0.34]$ and $Z \sim [0.0001; 0.05]$ (Kippenhahn & Weigert, 1990).

Changing the combination of these three parameters (accordingly with eq. 4.1) affects the stellar evolution. Figure 4.1 shows the evolutionary tracks of a 1.0 $M_\odot$ model with different sets of fractional abundances. In the HR diagram, we see that changing the initial fractional abundance of helium Y_i and heavy elements Z_i has an effect on L and $T_{\rm eff}$. Increasing Z_i (tracks A to C) decreases L and $T_{\rm eff}$, causing the star to evolve similarly to smaller mass stars. In the case where Y_i is larger (tracks A to B), this leads to an increase of L and $T_{\rm eff}$, and the star evolves as a higher mass star. This change in abundance has a direct effect on the opacities. Higher Z and/or lower Y leads to higher opacities, so lower L and $T_{\rm eff}$. The evolution time is also different. The time the star reaches the end of MS is $\sim$ 10 Gyr for track A, $\sim$ 4.5 Gyr for track B and $\sim$ 13.5 Gyr for track C.

If we want to characterize stars using only L and $T_{\rm eff}$, we find a degeneracy in the parameter space. The same mass can have different L and $T_{\rm eff}$ at the same point in its evolution, depending on the initial composition of the star. It is then necessary to consider the chemical composition as a constraint. However, X, Y, and Z are not direct observables. For a more observational description, we can express the relative abundance of an element i to an element j, using the Sun $\odot$ as a reference, as

$$[i/j] = \log\left(\frac{X_i}{X_j}\right) - \log\left(\frac{X_i}{X_j}\right)_\odot . \tag{4.2}$$

Usually, hydrogen is used as the reference element, and we can describe stellar metallicity as

$$[\mathrm{M/H}] = \log\left(\frac{Z}{X}\right) - \log\left(\frac{Z}{X}\right)_\odot . \tag{4.3}$$

However, the knowledge of the metallicity is difficult because we need to know the exact abundance of all elements heavier than helium, which is currently impossible. So the iron content

$$[\mathrm{Fe/H}] = \log\left(\frac{X_{\rm Fe}}{X}\right) - \log\left(\frac{X_{\rm Fe}}{X}\right)_\odot , \tag{4.4}$$

is used as a proxy for the metallicity. This gives us a good constraint on Z in the stellar models. Note, however, that $[\mathrm{M/H}] = [\mathrm{Fe/H}]$ only holds in certain cases.

Nevertheless, with $[\mathrm{Fe/H}]$ we only have a constraint for two variables in the compositions. So we need a second constraint, such as knowing the abundance of helium, but this is currently impossible to observe for low-mass stars. This is because the spectral lines of this element are only visible for stars with $T_{\rm eff} \geq 20000$ K. Nevertheless, there is an indirect method to obtain the abundance of helium by glitches (Verma et al., 2019). The glitch signature is an oscillation in the frequencies produced by discontinuities in the internal structure of stars, in this case, caused by the second ionization of helium. The amplitude of the signal is related to the abundance of helium in the region of the glitch. Using a high-quality seismic spectrum, it is possible to fit the oscillation signal and obtain the abundance of helium. In the following, constraints from glitches are not taken into account.

4.1 Chemical evolution

In this section, I follow the work presented in the papers Richer et al. (1998) and Alecian & Deal (2023), and in the book of Michaud et al. (2015)

Because surface abundances evolve over the lifetime of a star, knowing their current chemical composition is not enough to get the whole picture. From observations, we can only get the surface abundances or the abundance in the convective zone (as it can be considered fully mixed). The chemical profile changes with time due to nuclear reactions and/or chemical transport mechanisms. On one hand, the nuclear reactions, which I have already discussed in section 1.5 for low-mass stars, are localized only in the core. On the other hand, he chemical transport mechanism affects the whole distribution of elements inside of the star and is important in the radiative regions. In this work, I am interested in the effects of chemical transport mechanisms as they are the ones that change the chemical composition at the stellar surface.

There are several chemical transport mechanisms that can be microscopic (atomic diffusion) or macroscopic (rotation-induced mixing, thermohaline mixing, etc.). Atomic diffusion is a microscopic process driven by pressure, thermal, and chemical gradients inside the star. This process is often implemented in stellar models. However, used alone in the models of some stars, it can create unrealistic surface abundances. Although the inclusion of other mechanisms (e.g. rotation-induced mixing) is necessary, there is a vast number of them that are very expensive to compute, while others still need to be either identified or theoretically described. A more simplified way of considering the competing processes is to parameterize them, with a turbulent mixing coefficient. This formulation aims to parameterize all the diffusive processes that compete with atomic diffusion. In this work, I focus on including atomic diffusion and turbulent mixing in stellar models. We can describe the full chemical evolution of a specific element in a star in an approximate way as

$$\rho \frac{\partial X_i}{\partial t} = A_i m_p \left[\sum_j (r_{ji} - r_{ij}) \right] - \frac{1}{r^2} \frac{\partial}{\partial r} \left[r^2 \rho v_i \right] + \frac{1}{r^2} \frac{\partial}{\partial r} \left[r^2 \rho D_{\mathrm{T}} \frac{\partial X_i}{\partial r} \right]. \tag{4.5}$$

The first term on the right takes into account nuclear reactions, where r_{ij} is the rate of transformation of the element i into j, A_i is the atomic mass of the element i and m_p is the mass of a proton. The second term takes into account atomic diffusion, where v_i is the diffusion velocity of the element i. The last term corresponds to the turbulent mixing transport where D_{T} is the turbulent mixing coefficient.

4.2 Microscopic transport processes: Atomic diffusion

Microscopic processes act at small scale, affecting individual particles, without creating large motions of matter. One of them is atomic diffusion, it is the main mechanism known to redistribute the elements in stellar interiors and it slowly changes the surface abundances. The velocities of this process for trace elements i are described as

$$v_i = D_{i,p}\left[-\frac{\partial \ln X_i}{\partial r} + k_T\frac{\partial \ln T}{\partial r} + \frac{(Z_i+1)m_p g}{2k_B T} + \frac{A_i m_p}{k_B T}(g_{\mathrm{rad,i}} - g)\right]. \tag{4.6}$$

The first and second terms take into account the chemical and thermal gradients in the star, where k_T is the thermal diffusion coefficient. The third term is the effect of the electric field inside the star, where Z_i is the charge (or atomic number) of the element i. The last term is the pressure gradient. This is described by the two main sub-processes, the gravitational settling (g) component that the elements feel from the stellar gravity, and the radiative acceleration ($g_{\mathrm{rad,i}}$) that the element undergoes from the interaction with photons. The $D_{i,p}$ is the diffusion coefficient of the element i with respect to protons. The efficiency of atomic diffusion depends on the depth at which it acts and on the element being transported. The diffusion coefficient is proportional to the charge $\left(D_{i,p} \propto \frac{1}{Z_i}\right)$ and the ionization state of the element, creating a different chemical profile for each element.

Gravitational settling is the interaction of the elements with the local gravitational acceleration $\left(g = \frac{Gm}{r}\right)$, transporting the elements from the surface to the interior of the star, except for hydrogen which is moved to the surface of the star. It creates a stratification in the abundances in the radiative zone, while in the convective zone, the composition is uniform. During the MS, gravitational settling induces a decrease of the hydrogen abundance in the core, significantly impacting the duration of the MS phase. This process is particularly important to obtain accurate stellar ages.

4.2.1 Radiative accelerations

Radiative accelerations are the interactions of the elements with the radiation field in the star. These interactions result from the absorption of photons by the element, which pushes them towards the surface of the star. It can be described by

$$g_{\mathrm{rad,i}} = \frac{15}{16\pi^5 r^2}\frac{L}{c}\frac{\kappa_R}{X_i}\int_0^\infty \frac{\kappa_{\nu,i}}{\kappa_{\nu,\mathrm{all}}}P(u)\mathrm{d}u, \tag{4.7}$$

with

$$P(u) = u^4 \frac{e^u}{(e^u - 1)^2}. \tag{4.8}$$

To compute the radiative accelerations, it is necessary to have a complete knowledge of the opacities, taking into account the monochromatic opacity of each element $\kappa_{\nu,i}$ and the total monochromatic opacity $\kappa_{\nu,\mathrm{all}}$. This can be broken down into two main photon-element interactions. First, the bond-bond transition

$$g_{\mathrm{rad,i,line}} = \frac{1}{A_i m_p c N_i} \sum_l N_{i,k} \int_0^\infty \sigma_{i,l} F(\nu) d\nu, \tag{4.9}$$

where $N_{i,k}$ is the density number of the element i in the energy state k prior to the absorption of a photon from an energy transition l. $F(\nu)$ is the energy flux of photons, and $\sigma_{i,l}$ is the effective absorption cross section of the transition l at the respective frequencies ν. Secondly, the free-free and bond-free transition

$$g_{\mathrm{rad,i,cont}} = \frac{1}{A_i m_p c N_i} \sum_l N_{i-1,j} \int_{\frac{\chi_{i-1,j}}{h}}^\infty f_{i-1,j}(\nu) \sigma_{i-1,j} F_\nu d\nu, \tag{4.10}$$

where $f_{i-1,j}$ is the term that takes into account that part of the momentum is transferred to the element i, and the other part is transferred to the free electron. $\chi_{i-1,j}$ is the potential for ionisation of the element i from the energy level j. The total radiative accelerations can be described by

$$g_{\mathrm{rad,i}} = \frac{\sum_i N_i (g_{\mathrm{rad,i,line}} + g_{\mathrm{rad,i,cont}})}{\sum_i N_i}. \tag{4.11}$$

4.2.1.1 Computing radiative accelerations

The computation of radiative accelerations is not a direct calculation. Radiative accelerations need a deep understanding of the opacity inside the star, and to solve the integral in the full frequency spectra. There is different methods that simplifies the computation of this process. I describe two of the most efficient methods, one is the Interpolation Method, and the other is the semi-analytic or parametric Single-Valued Parameters (SVP) approximation.

Interpolation method

The Interpolation Method is one of the most accurate methods for computing radiative accelerations inside models. It was developed by Seaton (2005). This method considered

that the radiative accelerations of a element i as

$$g_{\mathrm{rad,i}} = \frac{1}{c}\frac{< A >}{A_i}\kappa_R \gamma_{\nu,i} F, \text{ with } \gamma_{\nu,i} = \int \frac{\sigma_{\nu,i}}{\sigma_{\nu,\mathrm{all}}} F_\nu \mathrm{d}\nu, \tag{4.12}$$

where $< A >$ is the mean atomic mass in the medium, and F is the total radiation flux. $\gamma_{\nu,i}$ is a function equivalent to the integral of eq. 4.7 and takes into account the detailed monochromatic cross-section (bound-bound, bound-free, and free-free transitions).

This method is based on the interpolation of $\gamma_{\nu,i}$ in a pre-computed grid obtained from OP data for a given element abundance, temperature, and free electrons density (N_e). This method, already implemented in several codes (e.g. TGEC: Théado et al. 2009, MESA: Hu et al. 2011), requires the use of the monochromatic opacity tables for the computation of the Rosseland mean opacity (eq. 1.54), which is still time-consuming.

Single-Valued Parameters

The Single-Valued Parameters (SVP) method approximates the eqs. (4.9) and (4.10). This method, developed by LeBlanc & Alecian (2004) and updated in Alecian & LeBlanc (2020), separates the dependence on atomic data and element abundances. It then parameterizes the atomic data into six parameters whose values are obtained from precalculated tables. This parameterization is made possible by the fact that some quantities are almost independent of the frequencies at the given stellar interior conditions.

In this method, the radiative accelerations equation for bond-bond transitions (eq. 4.9) is parameterized as

$$g_{\mathrm{rad,i,line}} \approx q\varphi_i^*(1+\xi_i^* C_i)\left(1+\frac{C_i}{b\psi_i^*}\right)^{\alpha_i}, \tag{4.13}$$

with

$$q = 5.575\cdot 10^{-5}\frac{N_e T_{\mathrm{eff}}^4}{T^{3/2}}\left(\frac{R}{r}\right)^2\frac{1}{A_i}, \text{ and } b = 9.83\cdot 10^{-23}\frac{N_e T^{-1/2}}{X_{\mathrm{H}}}. \tag{4.14}$$

X_{H} is the mass fraction of hydrogen, C_i is the concentration (in number) of the ion i relative to hydrogen. The parameter φ^* is related to the oscillator strength of the ion's transition, the parameter ψ^* is the ion linewidth, which primarily controls the saturation, and ξ^* is an additional parameter that also affects the saturation and appears when monochromatic opacities are considered. The α_i is calculated during the fitting of the parameterized g_{rad} to those calculated by opacity interpolation, and it is equal to -0.5 in the case of pure Lorentzian line profiles.

The other equation for free-free and free-bond transitions (eq. 4.10) is approximated by

$$g_{\mathrm{rad,i,cont}} \approx a_i \left[7.16 \cdot 10^{-26} \frac{N_e T_{\mathrm{eff}}^4}{T^{3/2}} \left(\frac{R}{r} \right)^2 \frac{1}{Ai^2} \Theta \right] \left(\frac{\chi}{1+\chi} \right)^{b_i}, \tag{4.15}$$

with

$$\Theta = \frac{N_{i-1,0} p_{i-1}}{N_{i-1} p_i g_0} \sum_k n_k g_k u_k^3 \left[\frac{u_k}{1 - e^{-u_k}} - e^{-u_k} \ln 1 - e^{-u_k} \right], \tag{4.16}$$

where χ is the abundance of the respective element with respect to the solar value, $N_{i-1,0}$ is the number density of the ground state of the ion $A^{+(i-1)}$, and N_{i-1} is the density of this ion, p_i is the partition function of A^i, n_k and g_k are the quantum number and the statistical energy weight of level k of $A^{+(i-1)}$, and u_k is evaluated at the ionization threshold frequency of level k, where $u = \frac{h\nu}{kT}$. The parameter a_i is introduced to correct for possible discrepancies in the hydrogen cross-section, and the parameter b_i is introduced to account for the possible saturation effect of bond-free transitions. The a_i and b_i are two parameters to be determined by fitting procedures such as α_i.

With this method, the dependence of the atomic data is parameterized in the six parameters φ, ψ, ξ, α_i, a_i, b_i. Alecian & LeBlanc (2020) provided in precomputed tables that are used to determine these six parameters during the radiative accelerations calculation, allowing this process to be computed in a very efficient manner. While faster than the method previously shown, it is less accurate, with maximum errors of 0.3 dex in $\log(g_{\mathrm{rad}})$. Also, this method is only valid for MS stars. The parameter tables are prepared only for stars with masses between 1.0 and 10.0 $M_\odot$. Radiative accelerations can only be calculated for twelve elements: C, N, O, Ne, Na, Mg, Al, Si, S, Ar, Ca, Fe. However, it is currently being updated as new detailed atomic data become publicly available. Théado et al. (2012), Deal et al. (2018) and Campilho et al. (2022) have compared the results obtained with the SVP method and results obtained with the interpolation method. They find that both methods give similar results, with errors most of the time much smaller errors than 0.3 dex.

4.2.2 Computation of atomic diffusion: Burgers formalism

Now I defined gravitational settling and radiative accelerations, it is necessary to determine the velocity distribution of the elements. Using eq. (8.2) is useful for treating the velocity for two or three elements, but it is not the most convenient and rigorous method. The most rigorous derivation of the diffusion velocity distribution is from the Boltzmann

equation, and various techniques have been proposed to solve this equation in an approximate way.

The Burgers formalism is one of these methods (Burgers, 1969), and it consists in solving the momentum transfer equation for each element i,

$$\frac{\partial P_i}{\partial r} + m_i N_i (g - g_{\mathrm{rad,i}}) + n_i Z_i (eE) = \sum_j K_{ij} \left[(w_i - w_j) + z_{ij} \frac{m_j r_i - m_i r_j}{m_i + m_j} \right], \tag{4.17}$$

the heat transfer for each element i,

$$\begin{aligned} \frac{5}{2} N_i k \frac{\partial T}{\partial r} = & -\frac{2}{5} K_{ii} z_i^{''} r_i - \frac{5}{2} \sum_{j \neq i} K_{ij} z_{ij} \frac{m_j}{m_i + m_j} (w_j - w_i) \\ & - \sum_{j \neq i} K_{ij} \frac{3m_i^2 + m_j^2 z_{ij}^{'} + 0.8 m_i m_j z_{ij}^{''}}{(m_i + m_j)^2} r_i \\ & + \sum_{j \neq i} K_{ij} \frac{m_i m_j}{(m_i + m_j)^2} (3 + z_{ij}^{'} - 0.8 z_{ij}^{''}) r_j, \end{aligned} \tag{4.18}$$

the mass conservation equation

$$\sum_i A_i m_i w_i = 0, \tag{4.19}$$

and the charge conservation equation

$$\sum_i Z_i m_i w_i = 0, \tag{4.20}$$

where m_i is the mass of element i, w_i is the net velocity relative to the center of mass. K_{ij} and z_{ij}, $z_{ij}^{'}$, $z_{ij}^{''}$, are respectively the coefficients related to the mutual resistances and the parameters related to the interactions between elements i and j. These equations are also solved for electrons.

Solving Burgers' equation directly or using a robust approximation (Thoul et al., 1994) gave us the diffusion velocity of all elements, which can be used in eq. (4.5).

4.3 Macroscopic transport processes: the example of convection

4.3.1 Convective mixing

Macroscopic processes create a motion of matter inside the star. The main example is convection (see sec. 1.4.2). For the transport of chemical elements, convection is modeled with a high diffusion coefficient that fully homogenizes the region. Also, the convective turnover timescale is much smaller compared to the typical time scales of microscopic transport processes. So the effect of atomic diffusion in this region is negligible.

Convection is an example of a macroscopic process but there are more, like rotation inducing-mixing, and semi-convections. Some of the effects of these processes on the chemical abundances can be parameterized with a turbulent diffusion coefficient (we explore this in the section below). However, due to our incomplete understanding or approximation to 1D modeling of convection, two main processes need to be considered, namely convective overshoot and penetration.

4.3.2 Convective overshoot and penetration

The blob of matter that is in motion in the convective region can reach the boundary between stable and unstable regions with a non-zero velocity. Due to the conservation of linear moment, the matter enters into the radiative region, bringing the matter from this region. We can define two different prescriptions, convective overshoot and penetration. The two promote an exchange of matter between the convective and radiative regions. With convective overshoot, the blob of matter goes beyond the convective region without impacting the thermal gradient, (in the overshoot region $\nabla = \nabla_{\rm rad}$). With convective penetration, the matter penetrates the stable region changing the thermal gradient to the adiabatic one ($\nabla = \nabla_{\rm ad}$, Zahn 1991) in the extended region. There is an alternative prescription for penetrative convection, where the thermal gradient has a smooth transition between the adiabatic and radiative gradient (see Christensen-Dalsgaard et al. 2011, Anders et al. 2022). The consideration of overshoot and penetration has a higher impact on the convective core, which brings new fuel from the stable region into the nuclear regions, extending the lifetime of the star. For the convective envelope, it is important to define correctly the boundary of the convective zone, as this has an impact on the transport of chemical elements and on the pulsations.

In stellar models, prescriptions can be used to extend the convective region. One is the step overshoot, which is a direct extension of the convective zone by a distance $l_{\rm OV}$, where

$$l_{\rm OV} = \alpha_{\rm OV} * H_P. \tag{4.21}$$

The $\alpha_{\rm OV}$ is the "overshoot" parameter and it has no relation with the $\alpha_{\rm MLT}$. The second is a treatment of overshoot as a diffusive process (Herwig, 2000) as

$$D(z) = D_0 \exp \frac{-2z}{f H_P}, \tag{4.22}$$

where z is the distance beyond the boundary of the convective region and f is the overshoot parameter. D_0 is the diffusive speed at the convective boundary determined from the MLT theory.

4.4 Turbulent mixing parameterization

It is possible to parameterize all the extra processes with a turbulent mixing coefficient. In this parameterization, it is assumed that all the chemical transport mechanisms in competition with atomic diffusion are diffusive processes (e.g. rotation-inducing mixing, thermohaline mixing). That way we can define a simple diffusion coefficient ($D_{\rm T}$) that will be parameterized. Optimally it would be preferable to consider the influence of each individual mechanism. Nevertheless, this prescription is easy to implement and calibrate in stellar models to consider the extra processes.

When considering turbulent mixing in stellar models, we can adopt different prescriptions. They will have different impacts on the diffusion profile of the star and influence differently the evolution of the chemical composition. We look to two prescriptions for the $D_{\rm T}$. The first one was described by Proffitt & Michaud (1991)

$$D_T = C \left(\frac{\rho_{\rm BC}}{\rho} \right)^n . \tag{4.23}$$

C and n are constants and $\rho_{\rm BC}$ is the density at the bottom of the convective envelope. In this prescription, the efficiency of turbulent mixing decreases with depth (as ρ increases). This way turbulent mixing partially mixes the radiative region close to the convective envelope. The two constants C and n depend on the parameterization considered. Usually, this prescription is used to reproduce the lithium abundance of the Sun. In the work of Eggenberger et al. (2022), they used $C = 1500$ and $n = 1.3$.

The second prescription was described by Richer et al. (2000) where

$$D_T = \omega D(\mathrm{He})_0 \left(\frac{\rho_0}{\rho} \right)^n . \tag{4.24}$$

ω and n are constants, ρ_0 and $D(\mathrm{He})_0$ are respectively the density and the diffusion coefficient of helium at a reference depth point 0. D(He) is computed following the analytical expression given by Richer et al. (2000),

$$D(\mathrm{He}) = \frac{3.3 \times 10^{-15} T^{2.5}}{4\rho \ln\left(1 + 1.125 \times 10^{-16} T^3 \rho^{-1}\right)}. \tag{4.25}$$

In this case, the turbulent mixing coefficient is anchored to a reference depth inside the star that can be defined as a specific temperature T_0 or envelope mass (ΔM_0), where the values of ρ_0 and $D(\mathrm{He})_0$ are computed. The reference temperature was used when turbulent mixing was calibrated to reproduce lithium surface abundances in Population II stars (e.g. Richard et al., 2002, 2005, Deal & Martins, 2021) and on the surface abundances of stars in clusters (e.g. Gruyters et al., 2013, 2016, Semenova et al., 2020, Dumont et al., 2021). In these cases, ω and n were set to 400 and 3, respectively, and the reference temperature was calibrated between $\log_{10}(T_0) = 5.7$ and 6.5, depending in the type of star. On the other hand, the reference mass was used to calibrate the turbulent mixing on the surface abundances of F- and A-type stars, setting ω and n to 10^4 and 4, respectively (Michaud et al., 2011a,b). They found a reference mass of $\Delta M_0 \sim [1-2]10^{-6}$ $M_\odot$ for these stars. A similar calibration was done by Verma & Silva Aguirre (2019) for three *Kepler* F-type stars. They calibrated the reference mass in order to reproduce the surface helium abundances that reproduce the glitch in the oscillation spectra caused by the second ionization zone of helium. They found a reference mass $\Delta M_0 = 5 \times 10^{-4}$ $M_\odot$, which is higher than the one derived for hotter and F-type stars.

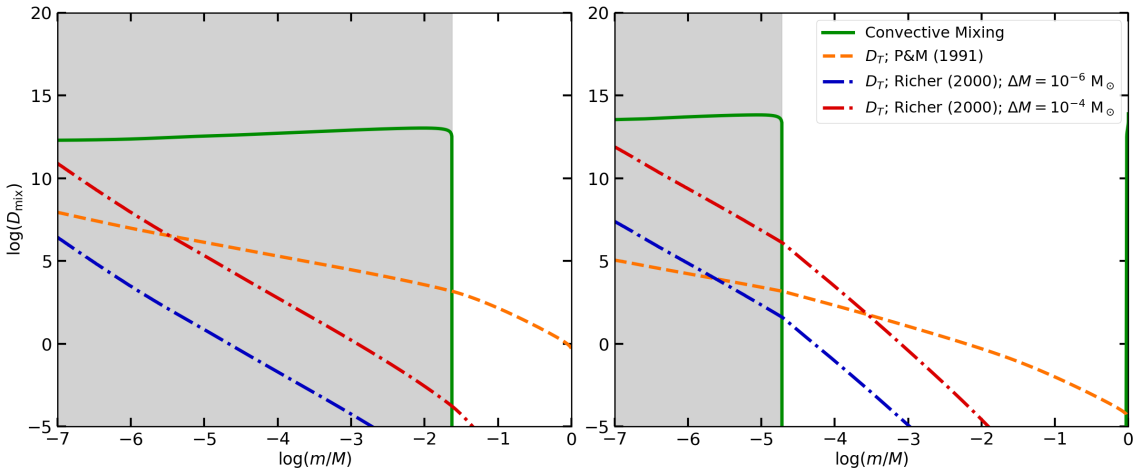

FIGURE 4.2: Stellar profiles showing the different mixing inside the stars in the middle of the MS for a 1.0 $M_\odot$ (left panel) and 1.4 $M_\odot$ (right panel) models. The green solid line represents the coefficient of convective mixing only, the orange dash line is the turbulent mixing coefficient from the prescription of Proffitt & Michaud (1991), the dotted dash lines are the turbulent mixing coefficient from the prescription of Richer et al. (2000). For the blue curve, $\Delta M = 10^{-6}$ $M_\odot$ and for the red curve $\Delta M = 10^{-4}$ $M_\odot$. The grey regions are the convective envelopes of the stars.

Figure 4.2 shows the different diffusive mixing coefficients. We see that each prescription gives different turbulent diffusion coefficient profiles, and that choice of the reference

depth affects the efficiency of the transport. The main difference between both prescriptions is the anchored point. For the Proffitt & Michaud (1991), it is the bottom of the convective zone, allowing the turbulent mixing coefficient to vary with the size of the convective zone during the evolution. For Richer et al. (2000), it is anchored to a reference depth (in this case envelope mass), which leads to a less dynamic turbulent mixing with stellar evolution but is more flexible to modify the efficiency of the transport.

Regardless of the differences, both prescriptions will partially homogenize the radiative zone. In this work, we explore the implications of using turbulent mixing coefficient in stellar models and how it affects the stellar characterization and chemical composition.

4.5 Modeling chemical composition in stars

When modeling stars, all processes must be considered simultaneously. In this work, I consider convection, convective overshoot (in the core), atomic diffusion, and turbulent mixing. Each of these processes has a different effect on the chemical evolution of stars. Figure 4.3 is a sketch of the different processes inside the star. It shows how the different processes compete in the star, and where they are expected to have an influence on the chemical evolution.

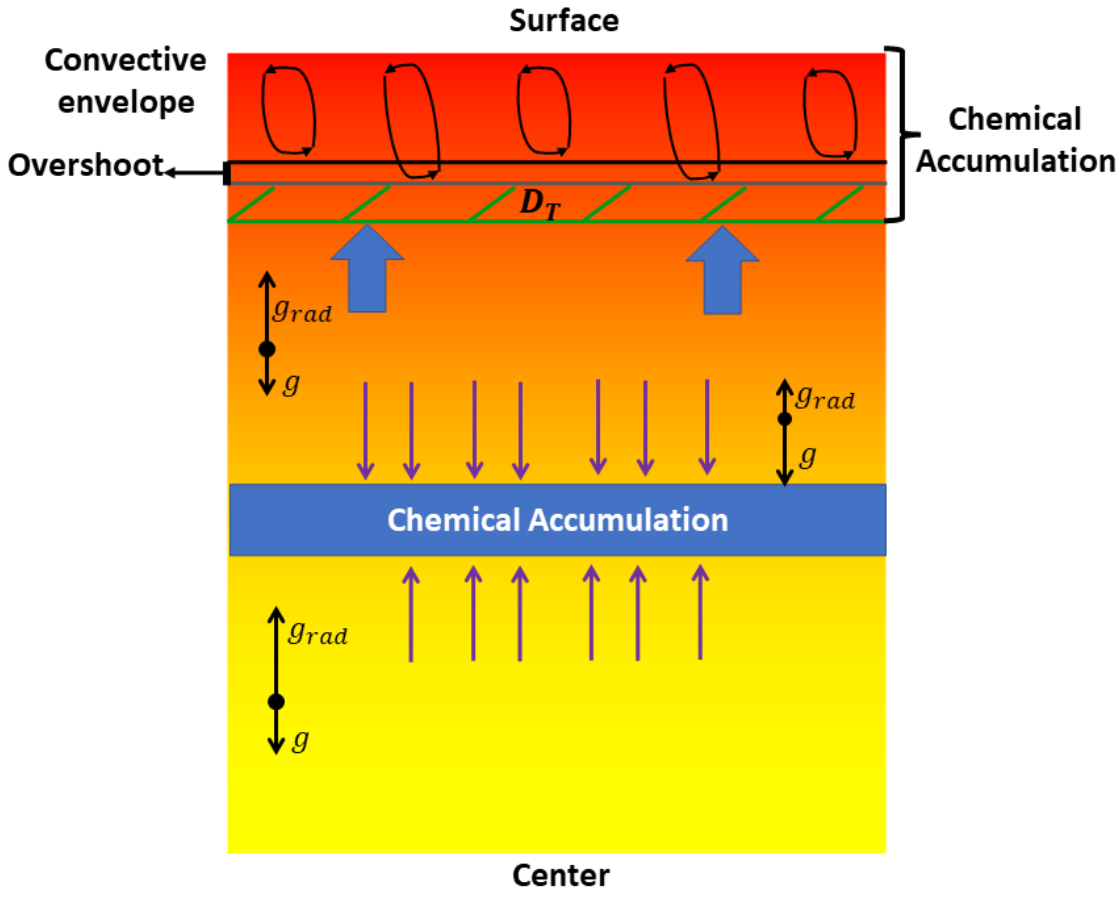

FIGURE 4.3: A sketch of the transport of chemical elements inside low-mass stars.

Part II

Stellar Evolution Code and Stellar Characterization

Chapter 5

How to Model a Star

To characterize stars with stellar models, there are two main procedures, one is on-the-fly modeling and the other is grid-based modeling. The first consists of an optimization process in which the models are generated in each iteration and compared with the observed constraints. This method can produce very accurate results and allows an easy change of the physical input considered (see for example Lebreton 2013, Chaplin & Miglio 2013, Lebreton & Goupil 2014), but it can be also extremely computationally expensive. On the other hand, the grid-based method uses a pre-calculated grid of models covering a range of parameters to search for the model that best fits the constraints. This can be expensive in terms of grid computation, but it is possible to reuse the grid on different stars (Silva Aguirre et al., 2015, 2017, Rendle et al., 2019, e.g.).

Characterizing a star with stellar models can be divided into three steps, regardless of whether we are using the on-the-fly or the grid-base modeling approach. The first step is to create the stellar models, the second step is to compute the stellar frequencies of the model (this step is optional since it is possible to characterize stars using only classical constraints, $T_{\rm eff}$, L, R and chemical composition), and the final step is to compare the model with the observations (inference). For on-the-fly modeling, these three steps are an interactive process; the run ends when the process converges to the stellar models that best fit the observational constraints. The case of grid-based modeling allows the addition of new stars with only one run of steps one and two, if the stellar parameters are within the computed grid.

In this chapter, I present the codes used to perform the various steps of stellar characterization: the stellar models, the seismic frequency calculations, and the optimization process. In this work, I have chosen to use the grid-based modeling, as I was looking

forward to test how the newly implemented physics impacts the characterizations of a sample of about 100 stars.

5.1 The MESA stellar evolution code

To create the stellar models, it is necessary to solve the stellar structure equations, taking into account all the necessary physics inputs, as well as the time evolution. For this task, I used the Modules for Experiments in Stellar Astrophysics (MESA, version r12778, Paxton et al. 2011, 2013, 2015, 2018, 2019). It is an open-source 1D stellar evolution code written in FORTRAN2003. It organizes in a modular structure with a large library of numerical and physical tools for simulating different stellar evolution scenarios. It provides a variety of EoS, opacities, nuclear reaction rates, elemental diffusion processes, atmospheric conditions, and more, which can be used in different evolutionary schemes. To solve the various systems of differential equations on the stellar structure, MESA uses the Runge-Kutta method, with second, third, or fourth order, and the two implicit extrapolation integrators, which can use a midpoint or Euler method. A Newton-Raphson solver can also be used to find nonlinear roots in multi-dimensional systems.

The large stellar microphysics and macrophysics library in MESA is divided into several modules. In the microphysics, MESA uses the Helmholtz free energy variables for the equation of state, with ρ and T as natural variables ($P(\rho, T)$). For opacities, the radiative opacity is combined with the electron conduction (in the presence of electron degeneracy) opacity at high temperatures. For low temperatures (e.g. Ferguson et al. 2005), the table includes the effect of molecules and grains. Nuclear reactions provide a range of rate options for elements up to nickel, including the weak reactions required for hydrogen burning, as well as neutron-proton conversion and electron and neutron capture. It can also account for the energy loss due to neutrino production in the nuclear reaction networks. MESA can also calculate particle diffusion by solving Burger's equation using Thoul et al. (1994) formalisms, and can also calculate material transport using a semi-implicit finite difference method. Radiative accelerations can also be considered using the Hu et al. (2011) calculation method, which requires monochromatic opacity data. This method is based on the OP data (Seaton, 2005). A more recent version of MESA (Jermyn et al., 2023) introduces a new method for computing radiative accelerations from monochromatic opacity described by Mombarg et al. (2022) that allows a more efficient method computation.

For macrophysics, MESA uses the Mixing Length Theory (MLT) of convection to compute the temperature gradient (∇) and the convective luminosity. The transport of chemical elements is treated with a diffusion coefficient in the convective regions. Overshoot and undershoot treatment at the boundaries of the convective regions can also be taken into account. For the stellar atmosphere, MESA provides several $T(\tau)$ relations (τ is the optical depth) that use the stellar mass, radius, and luminosity to estimate the surface pressure and temperature and their derivatives.

MESA is developed to work across multiple evolutionary regimes: From the PMS to the end of stellar evolution. It can evolve the very low to intermediate mass stars to the white dwarf stage. For massive stars, it can evolve until the supernova event. It can also evolve non-stellar objects from the formation and evolution of brown dwarfs and giant gas planets.

MESA is a flexible tool that enables the accomplishment of the objectives of this Ph.D. project. Although the two main prescriptions I study (turbulent mixing and SVP) are not implemented in this code, MESA provides a set of hooks* that allow an easy and fast implementation of the different physics that the user needs.

5.2 Input physics

In this study, my objective is to understand the impact of the implementation of the new transport processes (turbulent mixing and SVP) on stellar characterization. In this work, the following general input physics is used. I adopt the solar heavy element mixture given by Asplund et al. (2009), and the associated OPAL† opacity tables (Iglesias & Rogers, 1996). I use the OPAL2005 equation of state (Rogers & Nayfonov, 2002). I use the Krishna Swamy (1966) $T(\tau)$ relation for the atmospheric boundary condition. I follow the Cox & Giuli (1968) formalism for convection, using the mixing length parameter ($\alpha_{\rm MLT}$) obtained from a solar calibration (see next section). In the presence of a convective core, I take into account core overshoot following an exponential decay with a diffusion coefficient, as presented in Herwig (2000), setting the overshoot parameter to $f = 0.01$.

For turbulent mixing ‡, I implement both the formalisms developed by Proffitt & Michaud (1991) and Richer et al. (2000) in MESA using the hook *other_d_mix.f90*. For the

*external routines that can be modified without changing the source code.
†https://opalopacity.llnl.gov/
‡https://github.com/nmoedas/Turbulent_Mixing-MESA_Sript

SVP method* the implementation is not direct because MESA does not provide a hook for radiative accelerations. I had to make a direct change to the core routines of MESA (see chapter 10 for more details). This new version of MESA is not yet public.

5.2.1 Solar calibration

Before constructing the grids, it was necessary to perform a solar calibration. The Sun is the best benchmark star at our disposal. When computing stellar models for a given input physics, it is common practice to calibrate different parameters (initial chemical composition and mixing length parameter $\alpha_{\rm MLT}$) in order to obtain a model with the fundamental properties of the Sun at the age of the Sun (4.57 Gyr, Bahcall et al. 2005). Note that solar calibration is important to perform when the input physics are modified as they can affect the computation of opacity, convection, and transport elements among others. In this way the calibrations will be necessary to identify the initial chemical abundance, and the mixing parameters (e.g. $\alpha_{\rm MLT}$ parameter). Having the solar model calibrated can be used to test the optimization on the grid.

To perform the calibration, I use an "on-the-fly" modeling tool that I developed. With this tool, I compute several models, varying a set of free parameters between iterations and performing a χ^2 minimization to match as closely as possible the observed data of the current Sun, obtaining the calibration values for the free parameters ($Z_{\rm i}$, $Y_{\rm i}$ and $\alpha_{\rm MLT}$). For the main grids of my work that I computed (the ones presented in section 5.2.2), only two calibrations were necessary. I referred to them as Model 1 (used in grids A and B, see section 5.2.2) and Model 2 (used in grid C, see section 5.2.2). Model 2 has an extra parameter to constrain, the C constant from the Proffitt & Michaud (1991) turbulent mixing prescription (eq. 4.23). The extra parameter is added to reproduce the lithium surface abundance of the Sun, because without additional transport a solar model always has a too large abundance compared to observations.

For both calibrations, the $[{\rm Fe/H}]$, L, and $T_{\rm eff}$ of the current Sun are used as constraints. For Model 2 the lithium abundance is used as an additional constraint. For the calibration, I only took classical constraints into account. I used $L = 1{\rm L}_\odot$ and $T_{\rm eff} = 5777.0$ K with an error of $10^{-5}{\rm L}_\odot$ and 1 K, respectively, to match the position of the Sun in the HR diagram. I also set $[{\rm Fe/H}] = 0.0$ and Lithium $\epsilon_{\rm Li}$† $= 1.05$ (Asplund et al., 2009) with an error of 10^{-5}

*https://github.com/nmoedas/SVP_routine-MESA_implementation

†Lithium presence $\epsilon_{\rm Li} = \log(\frac{N_{\rm Li}}{N_{\rm H}}) + 12$

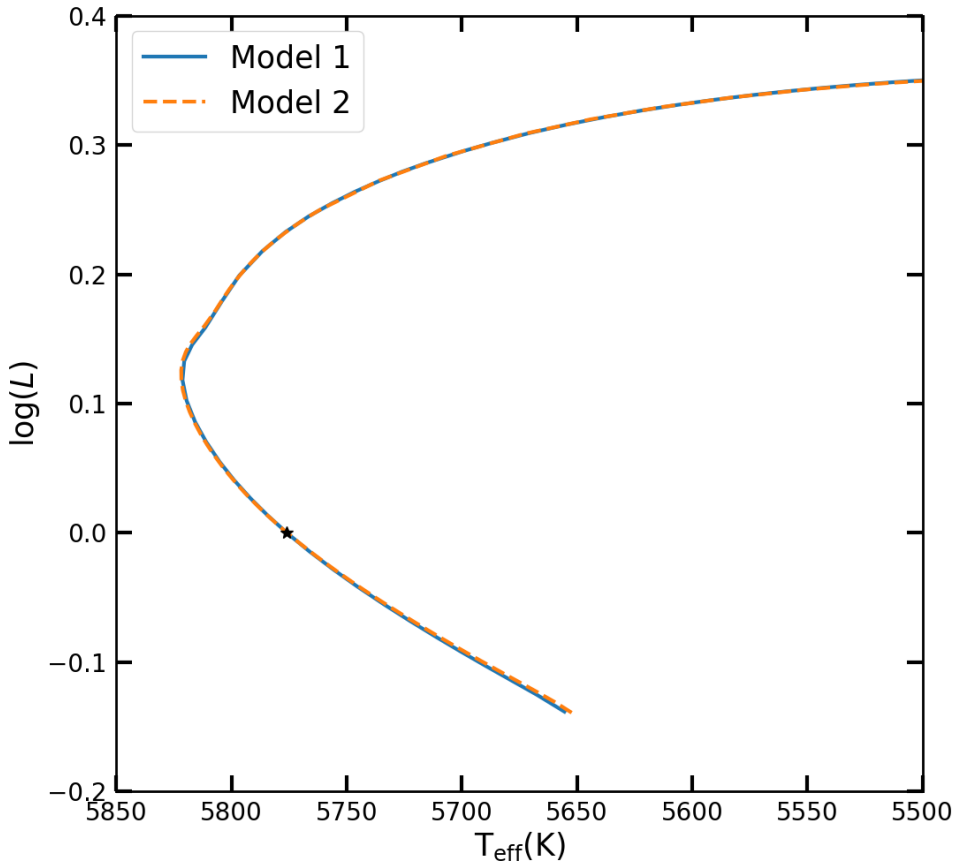

FIGURE 5.1: HR diagram of the calibrated models of the Sun. The evolutionary track of Model 1 is in blue and for Model 2 is in orange dash line. The black symbol represents $\odot$.

TABLE 5.1: The criteria used to change the initial parameters. var_{in} is the value of the constraint, and var_{out} is the value obtained from the model.

	$\text{var}_{\text{in}} < \text{var}_{\text{out}}$	$\text{var}_{\text{in}} > \text{var}_{\text{out}}$
L	Y_{i} decreases	Y_{i} increases
T_{eff}	α_{MLT} decreases	α_{MLT} increases
[Fe/H]	Z_{i} decreases	Z_{i} increases
Lithium	C increases	C decreases

and 0.10, respectively, to match the chemical composition of the Sun. To perform the solar calibration, I set the mass constant to $M = 1.0\ \text{M}_{\odot}$.

The tool I developed (written in Python), after setting the initial guess of the solar parameter, runs MESA, changing the parameters between runs depending on the quality of the fit. If [Fe/H] is too large compared to the observed value, it decreases Z; if L is larger, it decreases Y; if T_{eff} is larger, it decreases α_{MLT}; finally, if lithium is larger, it decreases C (this is summarized in the table 5.1). If they are smaller, the opposite happens. The variation of the free parameters at each step of the optimization process depends on

TABLE 5.2: The initial parameters of the solar calibrated models.

	X_i	Y_i	Z_i	$\alpha_{\rm MLT}$	C
Model 1	0.748095	0.266733	0.014828	1.710653	0
Model 2	0.722509	0.263174	0.014317	1.696688	1615.4863

TABLE 5.3: Parameters of the solar calibrated models compared to the Sun. Solar value for lithium is from Asplund et al. (2009) and for age from Bahcall et al. (2005).

	[Fe/H]	$\epsilon_{\rm Li}$	L ($L_\odot$)	R ($R_\odot$)	$T_{\rm eff}$ (K)	age (Gyr)
Model 1	-0.000010	2.1476	0.999989	0.99889	5776.045	4.5707
Model 2	0.000000	1.05236	1.000011	1.00010	5776.721	4.5700
Sun	0.0	1.05	1.0	1.0	5777	4.57

the difference between the observed and modeled values. This process continues until it converges to the constraints.

Part of the evolution of the calibrated solar models is shown in Fig. 5.1. The blue line corresponds to model 1 while the orange line is for model 2. The evolutionary tracks overlap for most of the evolution, and it can be seen that the tracks are very close to the position of the real Sun (marked with a black symbol). In tables 5.2 and 5.3 we can see the calibrated parameters for the solar models compared to those of the Sun. Both calibrations allow us to reproduce the observations of the Sun. But we see that changing the input physics has an effect in the initial parameters.

5.2.2 Grids of stellar models

During the development of this thesis, I computed several stellar models and grids that were used to test the implementation of turbulent mixing and the SVP method. The input physics is the same for all stellar models, the only modification is on the inclusion of atomic diffusion (gravitational settling and radiative accelerations), and turbulent mixing. Some of the test models and grids are presented and discussed in chapters (7 and 8). In the end, I computed three main grids, which are presented in tables 5.4 and 5.5.

The three grids cover the same parameter space in mass M initial metallicity $[{\rm M/H}]_{\rm i}$, and initial fractional abundance of helium Y_i (see table 5.4). The main difference is the chemical transport mechanisms taken into account. For all the grids, I saved structure models from the ZAMS to the bottom of the RGB. The first grid (Grid A) can be considered as "standard" as turbulent mixing is not included and only gravitational settling is taken into account and it is applied only for the lower-mass. This cut of atomic diffusion is done to avoid the large variations of surface abundances that occur for F-type stars. I defined

Table 5.4: Parameter space of the three main grids.

Grid	Mass		$[M/H]_i$		Y_i	
	Range	Step	Range	Step	Range	Step
A	[0.7;1.75]	0.05	[-0.4;0.5]	0.05	[0.24;0.34]	0.01
B						
C						

a criteria on the maximum variation of the iron surface abundance during the evolution Δ[Fe/H]. For a model $\Delta[Fe/H] > 0.2$ dex at some point during the evolution, then atomic diffusion is not taken into account (this is detailed in chapter 7). This criterion is better than cutting atomic diffusion of a given mass because of the effect of the initial chemical composition. It is of course not yet perfect because of the transition it induces in the grid.

The second grid of stellar models (Grid B) includes atomic diffusion without radiative accelerations. Turbulent mixing is included following Richer et al. (2000) prescription, but with specific calibration $D_{T,Fe}$ (Moedas et al., 2022, 2024) presented in more detail in in chapter 8. To describe it briefly, this turbulent mixing coefficient mimic the effect of radiative acceleration on iron surface abundances. It is not fixed and its efficiency increases with stellar mass.

The third grid of stellar models (Grid C) includes atomic diffusion with radiative accelerations using the SVP method. It also includes turbulent mixing in combination with two calibrations:

- for solar analogous, the Proffitt & Michaud (1991) prescription calibrated to reproduce the lithium abundance of the Sun;
- for hotter stars, the calibration of Verma & Silva Aguirre (2019) to reproduce the helium abundance of F-type stars.

The transition between both calibrations depends on the size of the convective envelope. If the convective envelope is more massive than the reference mass ($\Delta M = 10^{-5}$) I use the Verma & Silva Aguirre (2019) prescription, otherwise I use the Proffitt & Michaud (1991) prescription.

5.2.3 Grid parameter space: The helium problem

In the three grids, the helium parameter has been left free, but this can lead to some degeneracy during the optimization procedure because there is no direct observational

TABLE 5.5: Additional input physics of the three grids. $D_{T,\mathrm{Fe}}$ is the calibration of turbulent mixing presented in chapter 8, $D_{T,\mathrm{VSA19}}$ is the calibration done by Verma & Silva Aguirre (2019) (both used Richer et al. (2000) prescription), and $D_{T,\mathrm{PM91}}$ is the prescription of Proffitt & Michaud (1991).

Grid	Atomic Diffusion		Turbulent Mixing
	Gravitational Setteling	Radiative Accelerations	
A	$\Delta[\mathrm{Fe/H}]_{\mathrm{MAX}} < 0.2$	No	No
B	All models		$D_{\mathrm{T,Fe}}$
C		$M \geq 1.0\ \mathrm{M}_{\odot}$	$D_{T,\mathrm{PM91}}$ if $M_{CZ} \geq 10^{-5}\ \mathrm{M}_{\odot}$ $D_{T,\mathrm{VSA19}}$ if $M_{CZ} < 10^{-5}\ \mathrm{M}_{\odot}$

constraint on helium. Nevertheless, there is an indirect method to obtain the abundance of helium by glitches (Verma et al., 2019) (I referred to in 4). However, I do not perform glitch analysis in this work.

Because of the lack of constraints on the helium abundance (when not using glitch information), some of the solutions may be bimodal or uniform for this parameter. It is sometimes possible to find initial helium abundances lower than the primordial helium abundance $Y_0 = 0.2485$ (Cyburt et al., 2003). However, we only expect solutions larger or equal to Y_0 because of the chemical enrichment of the galaxy. As the Universe evolves, the abundance of helium increases as the star consumes hydrogen, enriching the environment with heavier elements.

To avoid the use of a free helium parameter it is possible to consider a relation to Z with a helium enrichment ratio

$$Y_{\mathrm{i}} = \frac{\Delta Y}{\Delta Z} Z_{\mathrm{i}} + Y_0, \tag{5.1}$$

where $\frac{\Delta Y}{\Delta Z}$ is the helium abundance ratio. This relation indicates that the variation in the abundance of helium is related to the variations in the metallicity of the environment. Although this allows to vary the helium and avoid the degeneracy created by a free parameter, there is still no consensus for the value of $\frac{\Delta Y}{\Delta Z}$. Different studies have reported different values for $\frac{\Delta Y}{\Delta Z}$. The work by Jimenez et al. (2003) and Casagrande et al. (2007) with nearby K dwarfs and a set of isochrones have reported values of $\frac{\Delta Y}{\Delta Z} \sim 2.1$. However the work of Balser (2006) reported 2 different values, $\frac{\Delta Y}{\Delta Z} \sim 1.6$ from the observations of metal-poor galaxies, from the Magellanic Cloud H II regions, and from the M17 abundances when temperature variations are taken into account. Using instead galaxy H II regions of S206 and M17, the estimation of $\frac{\Delta Y}{\Delta Z}$ is $\sim 1.41 \pm 0.62$, consistent with standard

chemical evolution models (Balser, 2006). Studying the chemical composition of the Sun, Serenelli & Basu (2010) show that different choices of solar composition lead to different values of $\frac{\Delta Y}{\Delta Z}$ within the range from 1.7 to 2.2. Looking at these different studies, we can consider that the value of $\frac{\Delta Y}{\Delta Z}$ is usually accepted to be between 1 and 3, for solar-type stars.

However, setting a fixed value of $\frac{\Delta Y}{\Delta Z}$ could introduce uncertainty into the models. Nsamba et al. (2021) showed that higher values of $\frac{\Delta Y}{\Delta Z}$ lead to smaller inferred masses and radii, and higher ages. We also compared what happens when using a free helium instead of a helium enrichment law finding that when $\frac{\Delta Y}{\Delta Z}$ is fixed, mass and radius tend to have lower values while age to higher values. But the size of the differences depends on the value of $\frac{\Delta Y}{\Delta Z}$. The higher this value, the higher the trends in the derived parameters.

There is no easy way to define the initial helium abundance in stellar models. In this work, free helium has been adopted to avoid the uncertainties of imposing a fixed $\frac{\Delta Y}{\Delta Z}$. The consideration of a free helium parameter in the grid allows us to continue the study of the helium enrichment law for future works.

5.3 Seismology in stellar models

The MESA code is a versatile tool that allows us to calculate a wide variety of stellar models. However, it does not provide us with the seismic data of the models. To exploit the full potential of the data, it is necessary to use a different tool to compute the seismic frequencies of each model. In this work, I adopted the GYRE stellar oscillation code (Townsend & Teitler, 2013) for this purpose. This is an open-source code written in FORTRAN 2008 that solves the stellar pulsation equations, eq. 2.12 to 2.14 and calculates the individual frequencies of the model star.

5.3.1 GYRE oscillation code

GYRE is prepared to handle both adiabatic and non-adiabatic problems by numerically solving the seismic differential equations using the Magnus Multiple Shooting numerical schemes. In this method, a grid of points between maximum and minimum frequencies (defined by the user) is created to reconstruct the eigenfunctions. It then uses the pulsation equations to construct a linear and homogeneous matrix that is used to determine the eigenfrequencies, which are the roots of the matrix determinant. With the eigenfrequencies, it integrates them to reconstruct the corresponding eigenfunctions.

In this work, I used GYRE to calculate the seismic frequencies of each stellar model from the stellar structure information. Nevertheless, the frequency interval must be defined. The range and location of the frequencies are different for each stellar model. To define the interval of frequencies to calculate the oscillations, I first identify the $\nu_{\rm max}$, which indicates the frequencies with maximum power. Knowing that the observed frequencies follow a Gaussian shape (Mosser et al., 2012) in their spectrum, I determine the deviation σ of the spectrum using eq. 2.17 assuming that the interval of expected detectable frequencies is $\nu_{\mathbf{max}} \pm 4\sigma$. With a 4σ interval we expect to compute more than the expected observed frequencies in real stars to avoid missing frequencies during optimizations. I only compute $\ell = 0$, $\ell = 1$, $\ell = 2$, and $\ell = 3$, since these are the only mode degrees expected to be observed ($\ell = 3$ only in the best cases).

5.4 Optimisation procedure

5.4.1 AIMS

For the optimization process, I use the Asteroseismic Inference on a Massive Scale (AIMS, Rendle et al. 2019) code. This is an open-source code written in Python. AIMS is an optimization tool that uses Bayesian statistics, Markov Chain Monte Carlo (MCMC), and interpolation to explore the parameter space of the grid and find the model that best fits the observational constraints.

Given the parameters of the observed star, AIMS searches for the best fitting model in parameter space (mass, metallicity, and other parameters varied in the stellar grid). It compares the parameters (A) of the different stellar models with the observed ones (O) using the Bayes theorem as

$$p(A|O) = p(O|A)p(A) \tag{5.2}$$

where $p(A)$ is the prior assumption. Assuming that the observable uncertainties follow a Gaussian distribution, the likelihoods of the models are

$$p(O|A) = \frac{1}{\sqrt{2\pi|C|}} \exp\left(-\frac{\chi^2}{2}\right), \tag{5.3}$$

where C is the covariance matrix of the observed parameters. In AIMS, the χ^2 can be determined in several ways during the optimization process. First, AIMS separates 2 main contributions: One that comes from the global constraints (X_i), which can be the classical constraints ($T_{\rm eff}$, [Fe/H], L, and others), and including the $\Delta\nu$ and $\nu_{\rm max}$ (are compared

using scaling relations),

$$\chi^2_{\rm global} = \sum_i^{N_{global}} \left(\frac{X_i^{\rm (obs)} - X_i^{\rm (mod)}}{\sigma(X_i)} \right) \tag{5.4}$$

where N_{global} is the number of global constraints considered in the optimizations. The other is the contribution of the individual seismic constraint (in the following I only consider the individual frequencies ν_i),

$$\chi^2_{\rm seis} = \sum_i^{N_{\rm seis}} \left(\frac{\nu_i^{\rm (obs)} - \nu_i^{\rm (mod)}}{\sigma(\nu_i)} \right), \tag{5.5}$$

where $N_{\rm seis}$ is the number of individual seismic constraints used. In both expressions, (obs) corresponds to the observed values and (mod) to the model values. To determine the total χ^2 AIMS considers different contributions for the individual frequencies. One is to consider that the individual seismic constraint contribution has an absolute (3:N) weight, where each individual seismic constraint has the same weight as each global constraint

$$\chi^2_{\rm total} = \chi^2_{\rm seis} + \chi^2_{\rm global}. \tag{5.6}$$

The other possibility is to consider the contribution of the individual seismic constraint with a relative (3:3) weight, where all seismic constraints have the same weight as all global constraints.

$$\chi^2_{\rm total} = \left(\frac{N_{\rm global}}{N_{\rm seis}} \right) \chi^2_{\rm seis} + \chi^2_{\rm global}. \tag{5.7}$$

Cunha et al. (2021) assessed the impact of using these two different ways to consider the weight in the frequencies. The weights 3:3 synthetically inflate the uncertainties of the individual frequencies, which allows the optimization procedure to explore more of the parameter space. However, this is not statistically correct as explained in Cunha et al. (2021). If we want the optimization to be statistically correct we should instead consider 3:N weights, which use the full potential of the seismic frequencies, leading to results with smaller uncertainties. On the other hand Cunha et al. (2021) also pointed out that the use of 3:N weights is more sensitive to incomplete or wrong modeling of stars and can lead to results that are incompatible with the global constraints. Which weight scheme to use is therefore still matter of debate.

Using this formulation AIMS provides the probability density function of each parameter. When comparing the results from different estimations we can use an absolute

difference,

$$\Delta X = X_i - X_r, \tag{5.8}$$

or a relative difference

$$\frac{\Delta X}{X_r}, \tag{5.9}$$

where X is the parameter value that is inferred, X_i is the value obtained using one of the grids, and X_r is value the obtained from the reference grid.

5.4.2 Surface corrections

Currently, there are large discrepancies between the simulated and observed seismic frequencies. This is due to our poor understanding of the temperature gradient in the superdiabatic layers in the model, and the use of an adiabatic approximation in the calculation of seismic frequencies. We also have a lack of description of the interaction between oscillations and convection at the surface. These are referred to as surface effects. This can be seen in the echelle diagram of the frequencies of the Sun, in Fig. 5.2. The model frequencies ($\nu_{\rm theo}$ in dark blue) differ from the observed ones ($\nu_{\rm obs}$ in red), and this difference is more pronounced for higher frequencies modes. As the mode has a higher frequency, its resonance cavity is closer to the surface, experiencing more surface effects.

The discrepancy of individual frequencies between models and observations poses a challenge in the optimization process, as it prevents a direct comparison without imposing large systematics in the inferred stellar properties. There are ways to avoid this problem. One is to use the frequency ratios (presented in section 2.5), which attenuates the surface effect in the modes. Another alternative is to use the empirical corrections. There are several prescriptions for surface correction in the literature (Kjeldsen et al. (2008), Sonoi et al. (2015), Ball & Gizon (2014)). In this work I have adopted the two terms surface corrections proposed by Ball & Gizon (2014). In their prescription they describe the seismic discrepancies $\delta\nu$ between models and observations as

$$\delta\nu = \left[a_{-1} \left(\frac{\nu}{\nu_{\rm ac}} \right)^{-1} + a_3 \left(\frac{\nu}{\nu_{\rm ac}} \right)^{3} \right] / I, \tag{5.10}$$

where a_{-1} and a_3 are the coefficients fitted to the stellar model, $\nu_{\rm ac}$ is the acoustic cutoff frequency, and I is the corresponding mode inertia. In this formulation, the first therm $\frac{\nu^{-1}}{I}$ takes into account the change in description in the convective zone near the surface, which affects the local pressure scale height. The second therm $\frac{\nu^3}{I}$ takes into account the

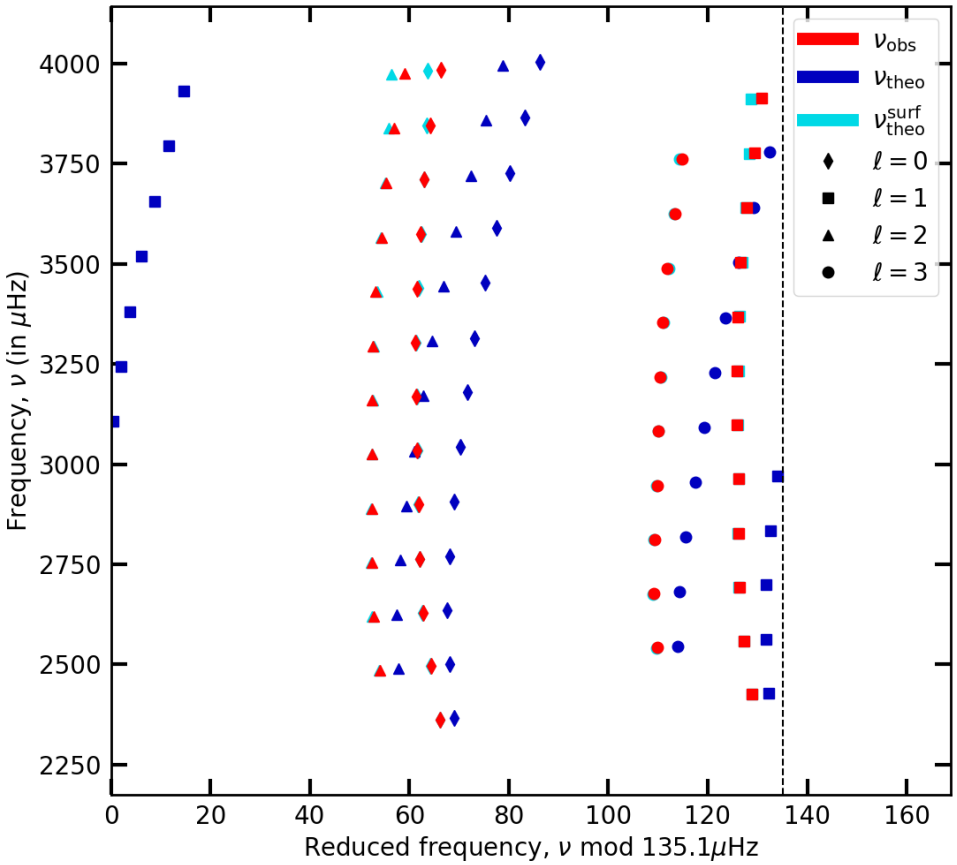

Figure 5.2: Echelle diagram of the individual frequencies of the Sun.

discrepancies caused by the magnetic field, which are concentrated in the filaments and have an effect on the local sound velocity. Figure 5.2 shows in cyan the corrected model frequencies of the Sun, where they overlap with the observed ones. We still do not have a perfect match, as we see at higher frequencies, but this still improves the comparison between models and observations and significantly reduces the discrepancy between the frequencies.

Chapter 6

Stellar Samples

In this work, I use a sample of asteroseismic stars observed by the *Kepler* telescope provided by two sources. The first source is the *Kepler* LEGACY sample from Lund et al. (2017, hereafter L17), and the second source is the work of Davies et al. (2016, hereafter D16), a study of 35 stars that are planet hosts. For all stars, I use as constraints their seismic data, individual frequencies $\nu_{n,\ell}$, $\nu_{\rm max}$, and classical constraints $T_{\rm eff}$, [Fe/H], and L. I also performed a dedicated study of the 94 Ceti system, which is presented in chapter 10.4.

6.1 *Kepler* Legacy sample

The *Kepler* Legacy sample is a catalog of 66 stars with the highest signal-to-noise ratio in the seismic frequencies observed by *Kepler*. All stars have at least 12 months of observations with a short-cadence of 58.89 s. The sample contains FGK-type stars in MS to early SG phases. The seismic data are provided by L17. L17 also provides the Sun as a star observed by Kepler, with the same quality of this sample. They used the light curves provided by the KASOC database* from which they extracted the power spectrum. Using a Bayesian Markov Chain Monte Carlo "peak-bagging" approach, they extracted parameters such as radial order, mode degree, frequency, amplitude, and line width for each individual star. For each individual mode, they provide the quality control parameter (the Bayes factor **K**) related to the probability of detecting a mode. The quality parameters are obtained by comparing the signal-to-noise ratio of the background noise (H_0)

*www.kasoc.phys.au.dk

with the signal of the mode (D). **K** can have the following values

$$\ln \mathbf{K} = \begin{cases} < 0 & \text{favours } H_0 \\ 0 \text{ to } 1 & \text{not worth more than a bare mention} \\ 1 \text{ to } 3 & \text{positive} \\ 3 \text{ to } 5 & \text{strong} \\ > 5 & \text{very strong} \end{cases} \tag{6.1}$$

In case of a true detection of a mode $\ln \mathbf{K}$ must be greater than one. For this sample, I only consider the detected modes that have $\ln \mathbf{K} \geq 3$. In this case, it is possible to have access to a sufficient number of modes for the optimization process. In some cases, there the quality is enough to have up to $\ell = 3$ modes.

For this sample, the spectroscopic parameters $T_{\rm eff}$ and [Fe/H] are taken from L17, except for 13 stars where I adopted the updated values provided in Morel et al. (2021). The observed $\nu_{\rm max}$ of the sample is provided in Silva Aguirre et al. (2017). Finally, I used the magnitudes and parallaxes from Gaia DR3 (Gaia Collaboration et al., 2021) to compute the L of the stars using the set of equations presented in chapter 3.1. It is important to note that some stars presented in L17 have [Fe/H] lower than the limits of my grid. Therefore, I selected only stars with [Fe/H] > -0.4 dex. Ignoring these stars, I end up selecting 62 of the 66 stars plus the Sun provided by L17.

6.2 Planet host sample

D16 provides the seismic data of 35 stars observed by *Kepler*. These stars are solar oscillators that are planet-host candidates or confirmed planet-host stars. Their light curves have enough signal-to-noise ratio to identify a clear presence of individual modes and their mode degree ℓ.

They used the same method as L17 for the mode identification, with the same quality parameter. However, in this case, I considered all modes with $\ln \mathbf{K} > 1$. In fact, selecting the same quality criterion as for L17 sample, I would end up with not enough number of modes (in some cases 3 individual modes) to perform a proper inference of the stellar properties.

In this case I used the $T_{\rm eff}$, [Fe/H] and $\nu_{\rm max}$ provided in D16. Similar to the previous sample, I computed L using the data provided by Gaia DR3, as I did with the

previous sample. For the selection, I used the same criteria so [Fe/H] as before but also excluding all stars showing mixed-modes, as my grids are not suitable to study these modes. In this sample, only two stars show mixed-mode detection (KIC7199397 and KIC8684730). D16 also provided three stars in common with L17 (KIC 3632418, KIC 9414417, and KIC 10963065), for which I decided to use the updated data provided by L17. Using these criteria, I selected 28 of the 35 stars from D16.

The overall sample consists of 91 stars: 62 from L17, 28 from D16, and the Sun. I use their seismic data $\nu_{n,\ell}$, $\nu_{\rm max}$, and their classic constrains $T_{\rm eff}$, [Fe/H], and L for the stellar characterization for the different tests I performed in this work. The distribution of the full sample is shown in the asteroseismic diagram of Fig. 6.1.

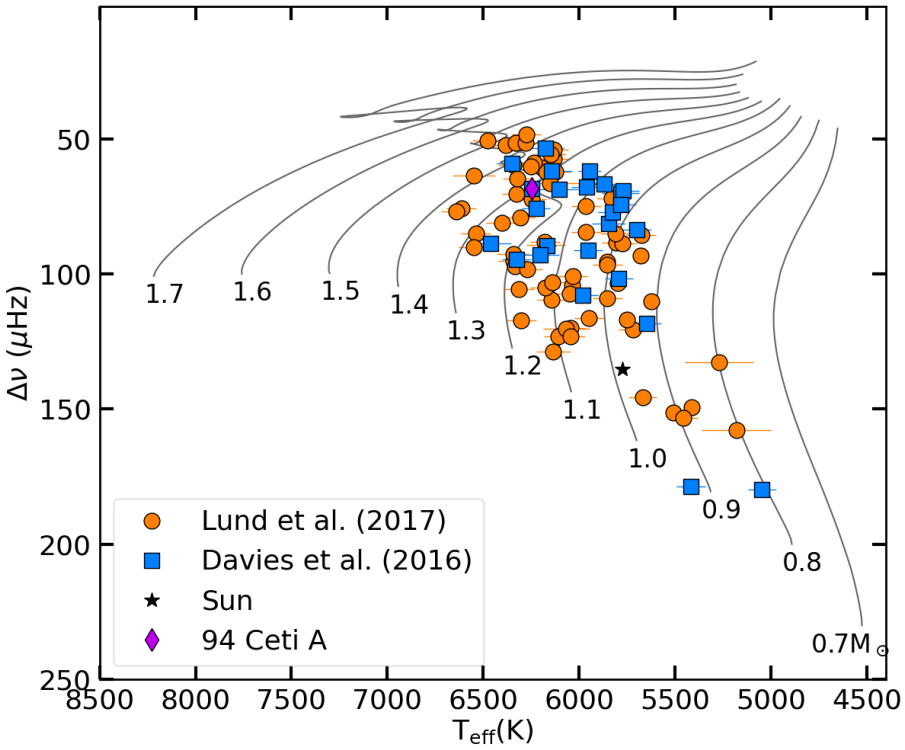

FIGURE 6.1: Asteroseismic diagram showing some computed evolutionary tracks with $[{\rm M/H}]_{\rm i} = 0.0$ and $Y_i = 0.26$ (that are not the Solar values) in solid black lines. The points show the distribution of the sample considered in this work, where the orange circles are taken from Lund et al. (2017), the blue squares are from Davies et al. (2016), the black symbol is the Sun, and the purple diamond 94 Ceti A.

Part III

Treatment of Atomic Diffusion

Chapter 7

Atomic Diffusion and Surface Abundances Variations

Chapters 7 and 8 present results published in Moedas et al. (2022) (the pdf in appendix A).

In chapter 4, we saw that there are different chemical transport mechanisms inside stars. In this chapter, I examine the effects of atomic diffusion in stellar models of FGK-type stars.

7.1 Test stellar models

In this chapter and in the next one, a large number of tests have been performed to identify the effects of atomic diffusion, leading to the implementation of turbulent mixing in stellar models. These tests have been carried out with individual models and small grids. The test grids were used to understand the surface abundance variations induced by atomic diffusion. They were also used to investigate the effect of turbulent mixing on stellar chemical evolution. The general input physics (EoS, opacity, nuclear rates, etc.) are the same as presented for grids A, B, and C in Chapter 5.2.2

Grid D includes atomic diffusion without radiative accelerations. The parameter space includes three values of initial metallicity and three helium enrichment ratios (including the solar calibrated values), and an equally spaced range of masses. Grid E includes radiative accelerations (using the Seaton 2005 method) and Rosseland mean opacity computed with OP monochromatic tables instead of the standard OPAL tables. This grid is restricted to the solar chemical composition and has a larger step in mass.

TABLE 7.1: Summary of the different stellar parameters and input physics used in each grid. In the 'Atomic Diffusion" column, g indicates that the models include atomic diffusion without radiative accelerations, and $g + g_{\rm rad}$ indicates that the models include atomic diffusion with radiative accelerations. In the following column, ΔM_0 is the value of reference mass used to compute turbulent mixing; 'None' means that we do not include turbulent mixing in the grid

Grid	Mass ($M_\odot$)		$[Fe/H]_i$		$\Delta Y/\Delta Z$		Atomic	ΔM_0 ($M_\odot$)	Opacity
	Range	Step	Range	Step	Range	Step	Diffusion		Table
D	[0.7;1.7]	0.02	-0.44; 0.06; 0.46	—	0.4;1.23;2.8	—	g	None	OPAL
E	[0.7;1.7]	0.1	0.06	—	1.23	—	$g + g_{\rm rad}$	None	OP mono
F1	[0.7;1.7]	0.1	-0.04; 0.06; 0.16	—	1.23	—	$g + g_{\rm rad}$	5×10^{-4}	OP mono
F2	1.2; 1.4	0.1	0.06	—	1.23	—	g	5×10^{-4}	OPAL
G1	[1.3;1.5]	0.025	[-0.1;0.2]	0.05	[0.2;4.0]	0.01 in Y	g	Parametrised	OPAL
G2	[1.3;1.5]	0.025	[-0.1;0.2]	0.05	[0.2;4.0]	0.01 in Y	No	None	OPAL
G3	[1.3;1.5]	0.025	[-0.1;0.2]	0.05	[0.2;4.0]	0.01 in Y	No	None	OPAL
G4	[1.3;1.5]	0.025	[-0.1;0.2]	0.05	[0.2;4.0]	0.01 in Y	g	None	OPAL

Grids F1 and F2 are similar to grid E with the additional inclusion of the effect of turbulent mixing following the calibration of Verma & Silva Aguirre (2019, hereafter VSA19). Grid F1 is computed with the solar metallicity ± 0.1 dex to allow the use of AIMS with this grid (AIMS requires at least 3 dimensions to run, e.g. mass, age and [Fe/H], see chapter 8). Grid F2 only includes two models for which radiative accelerations are neglected for the comparison with models from grid E and F1

Grids G1, G2, G3, and G4 are computed around the parameter space of the two test stars KIC 2837475 and KIC 11253226. These grids have been used to infer the fundamental properties of both stars. Grid F1 includes the turbulent mixing that I parameterized in chapter 8.2 and gravitational settling. Grids G2 and G3 include no transport other than convection. The difference between these two grids is in the solar-calibrated values. Grid G2 uses the same as grid D (calibration of model 1), while grid G3 includes the solar-calibrated value consistent with its input physics ($\alpha_{\rm MLT} = 1.5908152$, $X_0 = 0.72914669$, $Y_0 = 0.25765492$, and $Z_0 = 0.01319839$). Finally, Grid G4 is similar to Grid D, but with a different density in the parameter space.

Grid D is used as a reference when comparing grids E and F1. For grids F1, F2, G1, G2, G3, and G4 individual frequencies are computed. For these grids, the modes are saved between the ZAMS and RGB until the stars reach $\log(L) \geq 2.1$. The parameters of the grids are summarized in table 7.1.

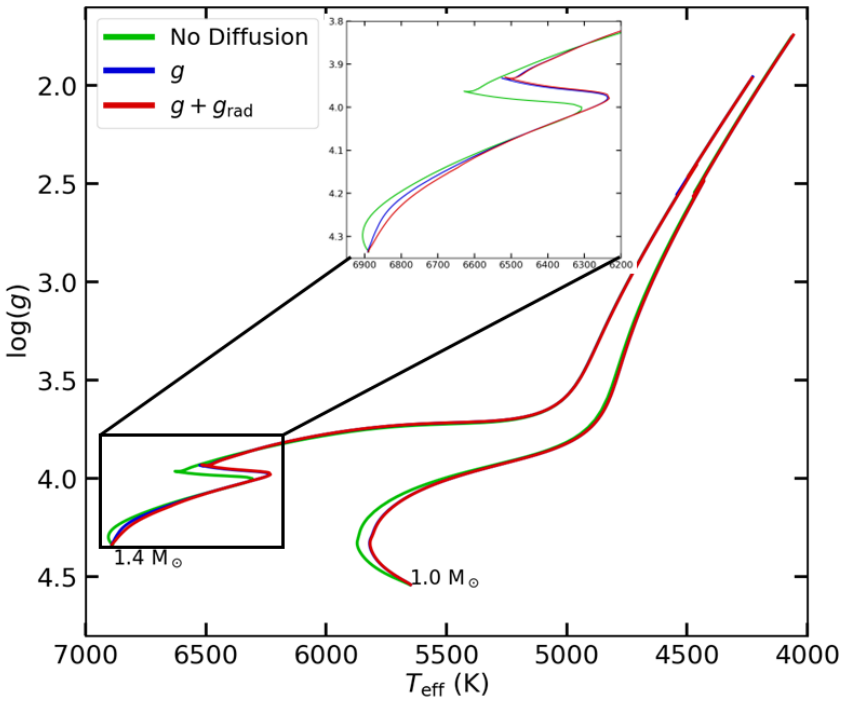

FIGURE 7.1: Kiel diagram of the evolutionary tracks with different treatment of atomic diffusion for stellar models of 1.0 and 1.4 $M_\odot$. The green line represents a model without atomic diffusion, the blue line represents a model that included only gravitational settling, and the red line represents a model that also included radiative accelerations. The blue and red lines mostly overlap in this figure.

7.2 Gravitational settling VS radiative accelerations

Here we look at the effects of gravitational settling and radiative accelerations when they are included in stellar models. Figure 7.1 shows the Kiel diagram ($\log(g)$ against $T_{\rm eff}$) of the evolutionary tracks of models with masses of 1.0 $M_\odot$ and 1.4 $M_\odot$ with an initial solar chemical composition. There we see the effect of adding atomic diffusion with and without radiative accelerations. The inclusion of atomic diffusion reduces the $T_{\rm eff}$. In the HR diagram, the effect of radiative accelerations is very small, especially for the 1.0 $M_\odot$ model for which there is no significant effect. The addition of atomic diffusion also has a strong effect on age. In fact, a 1.0 $M_\odot$ model without atomic diffusion reaches the TAMS at 10.38 Gyr, while adding atomic diffusion it reaches it at 9.72 Gyr, (i.e. difference of about 0.66 Gyr). For the 1.4 $M_\odot$ model, adding atomic diffusion changes the TAMS age from 3.01 Gyr to 2.96 Gyr. In brief, atomic diffusion accelerates stellar evolution in the MS because the hydrogen mass fraction is reduced by the settling of the heavy elements, depleting the core faster in fuel for the nuclear reactions. This is one of the reasons why

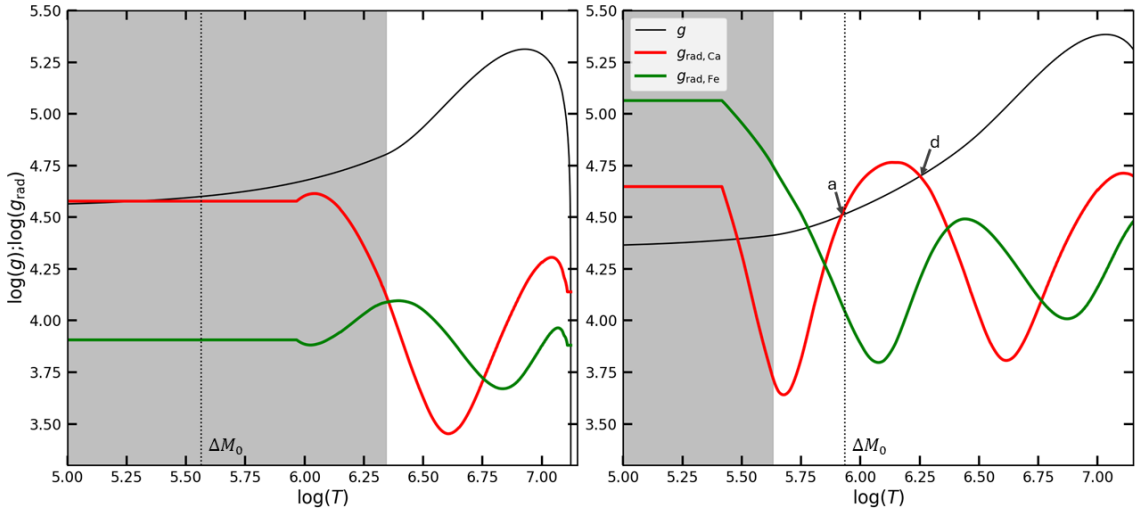

FIGURE 7.2: The profiles for gravity (black solid line) and radiative accelerations for Ca (red solid line) and Fe (green solid line) for a 1.0 (left panel) and 1.4 $M_\odot$ (right panel) model. The grey region is the convective envelope. The point 'a' is an accumulation point for calcium and point 'd' is a depletion point. The dashed line indicates the reference envelope mass used for the turbulent mixing from VSA19.

atomic diffusion must be taken into account to obtain the most accurate ages in stellar models.

7.2.1 Evolution of the chemical elements

The effect of atomic diffusion is different for each element and depends on its abundance, its ionisation state and on the photon flux. Figure 7.2 shows the gravity profiles (gravitational settling) and the radiative acceleration profiles for two elements (Ca and Fe) in 1.0 and 1.4 $M_\odot$ models (at the ZAMS). Outside the convective envelope represented by the grey area, gravitational settling dominates the radiative accelerations for the 1.0 $M_\odot$ model. In this case, elements in the radiative zone are transported to inner regions. For the 1.4 $M_\odot$ model, the radiative accelerations have a different behavior. In the case of calcium, there is a region where radiative accelerations are dominant, (between points a and d). In this region, the Ca is transported towards the surface, from point d (a depletion point) to point a (an accumulation point). In the case of iron, the radiative acceleration is higher than gravity closer to the convective envelope, inducing an accumulation in the surface convective zone.

In the convective regions (grey region of the figure 7.2), the transport of elements is independent of the behavior of gravity or radiative accelerations, since the convective mixing fully homogenizes the chemical composition. The accumulation and depletion

of an element in this zone depend on the radiative accelerations at the bottom of the convective envelope. For the 1.0 $M_\odot$ model, Ca and Fe are depleted. For the 1.4 $M_\odot$ model, Ca is depleted and Fe accumulates. Radiative accelerations profiles presented in Fig. 7.2 are constant in a large part of the convective zone. MESA apply this constant value in order to reduce the computational time, but it is not physical. However, it has no impact on the predicted abundance profiles since the convective regions are fully homogenized. Note that Campilho et al. (2022) tested these optimisation options for atomic diffusion in MESA and arrived to the same conclusion.

Although the evolution of the chemical profile affects the life of the star, we can only observe the surface and determine the abundance of the convective envelope. It is important to know how the surface chemical abundances change with time and these predicted profiles help us to understand where to expect accumulation and depletion zones in stars. However, they are not static and change as the star evolves (but during MS the changes are almost negligible).

7.2.1.1 Evolution of the fractional abundances

Let us see how the fractional abundances of X, Y, and Z change when atomic diffusion is taken into account. Figures (7.3) and (7.4) show the surface evolution for X, Y and Z for the 1.0 $M_\odot$ and 1.4 $M_\odot$ models, respectively. For the 1.0 $M_\odot$ model without atomic diffusion, the surface abundance of all elements at the surface are constant during all MS, as expected. However, after this phase, there is a decrease in X and an increase in Y. This is due to the fact that after the MS, the convective envelope expands into deep regions where the abundances are affected by nuclear reactions. The maximum variation point corresponds to the first dregs-up. After that, the surface abundances remain constant even with atomic diffusion (which is less efficient when stars have large convective envelopes). When atomic diffusion is included, there is a depletion of Y and Z and an increase of X at the surface. For this model, the inclusion of radiative accelerations has no effect on any of the abundances followed here.

For the 1.4 $M_\odot$ model, the case without atomic diffusion is the same as before. However, when atomic diffusion is taken into account, there is an extreme variation of all abundances. There is an almost complete depletion of Y and Z at the surface, creating an almost complete hydrogen surface, which is unrealistic. Adding radiative accelerations

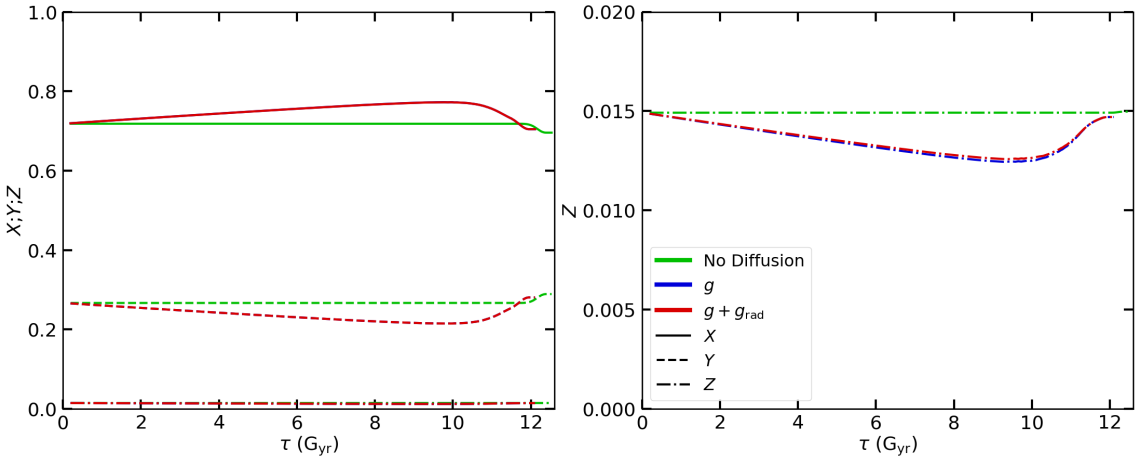

FIGURE 7.3: Surface evolution of the fractional abundances including or not atomic diffusion for a model with 1.0 $M_{\odot}$. The left panel presents all the fractional abundances, and the right panel presents a zoom only for Z.

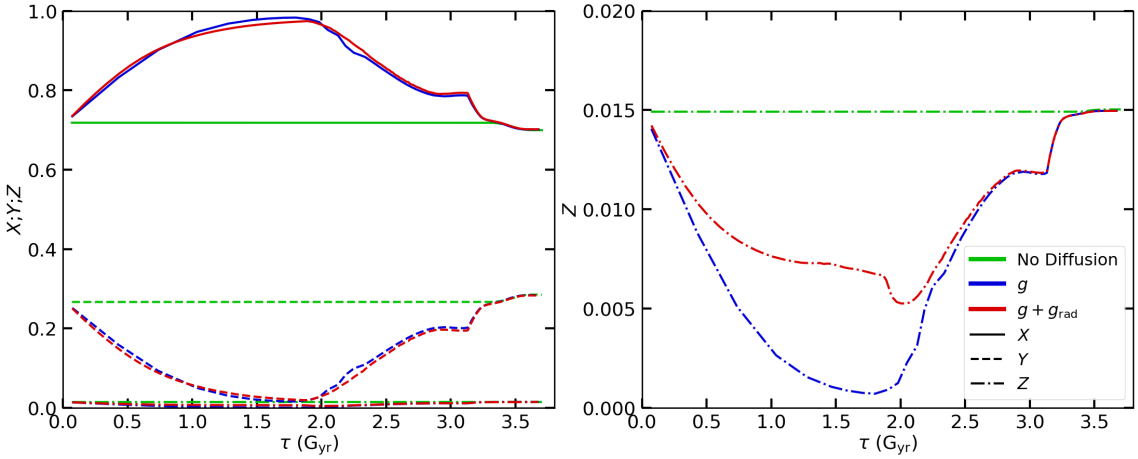

FIGURE 7.4: Same as Fig. 7.3, but for the case of a stellar model of 1.4 $M_{\odot}$.

in this case has a significant effect on Z at the surface, allowing the surface to be less depleted. However, there is no effect on X and Y, as expected, and it still leads to an almost complete depletion of helium at the surface, which is unrealistic. With these models, it is possible to identify problems with the inclusion of atomic diffusion for F-type stars, leading to unrealistic variations (over-depletion in these cases) that are not expected to be observed in non-chemical peculiar stars.

7.2.1.2 Variation of [Fe/H] with evolution

From observations, each element is observed individually and, usually, the [Fe/H] is the main constraint used for stellar characterization. It is important to understand how it evolves during the life of stars. This time, the evolution without atomic diffusion is not

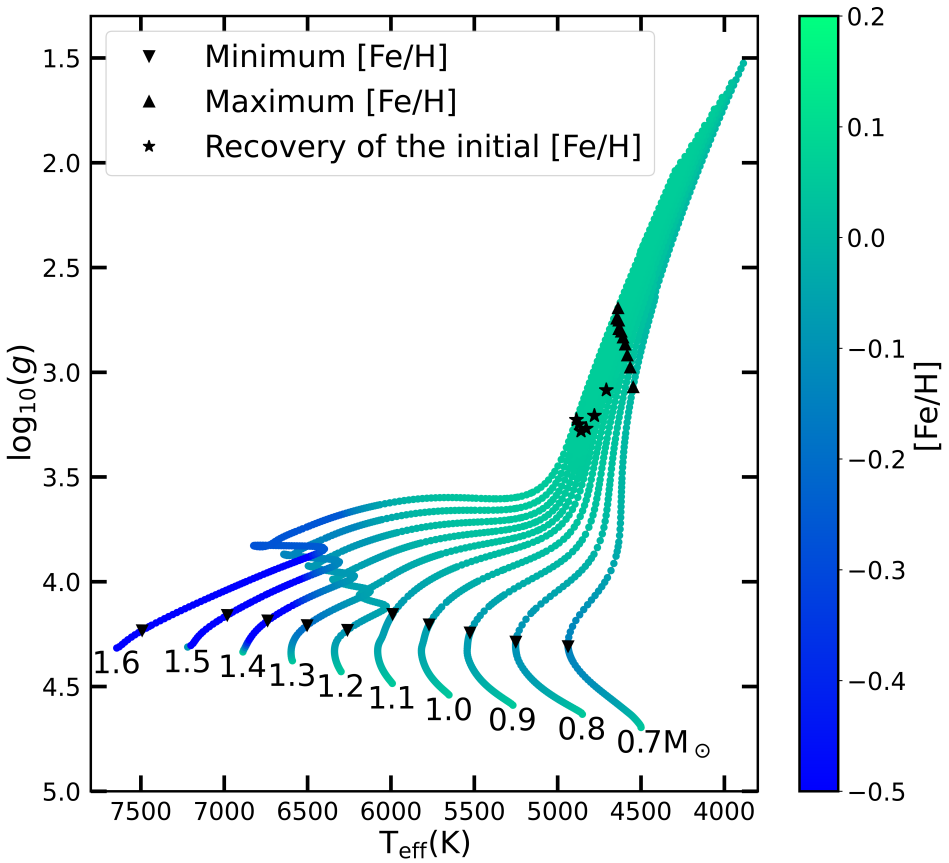

FIGURE 7.5: Kiel diagram of models from Grid A with [Fe/H]$_i$ = 0.06 and $\frac{\Delta Y}{\Delta Z}$ = 1.23. The color indicates the value of [Fe/H] at the stellar surface, the triangles down are the points where [Fe/H] reach a minimum, the triangles up are the points where [Fe/H] reaches a maximum, and the star symbols are the points where [Fe/H] reaches the initial value.

considered as it does not provide any new information. Let us first consider the evolution without radiative accelerations. Figure (7.5) shows the Kiel diagram of some models from grid A (color-coded for the value of [Fe/H] at the surface). The point where the maximum variation in the main sequence occurs is shown as a down triangle. The up triangle represents the point where the maximum surface abundance is reached during the first dredge-up, and the star symbol represents the point where the star regains its initial surface abundance. Figure (7.6) shows the surface evolution of [Fe/H] when atomic diffusion is taken into account with and without radiative accelerations.

Without radiative acceleration, the surface [Fe/H] decreases to a mass dependent minimum (large depletion, LD). The depletion is larger for the 1.4 $M_\odot$ model than for the 1.0 $M_\odot$ model, because atomic diffusion is much more efficient at higher masses. In the Kiel diagram we see that for stars without a convective core, the LD occurs near the end of the main sequence. For the more massive stars, this depletion occurs earlier, close to

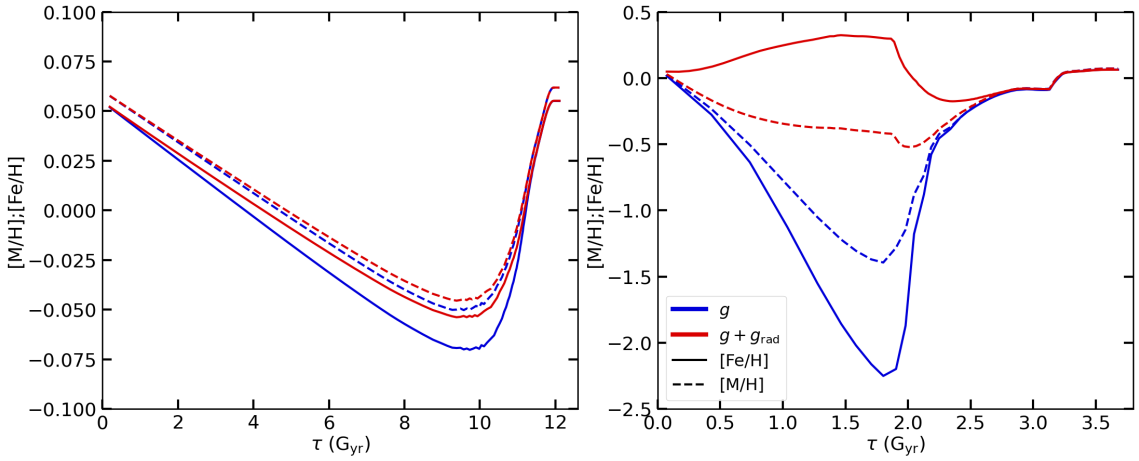

FIGURE 7.6: Surface evolution of the [Fe/H] and [M/H] considering or not radiative accelerations. The left panel presents the evolution for a 1.0 $M_\odot$, the right panel for a 1.4 $M_\odot$ model.

the beginning of the MS for the 1.6 $M_\odot$ model. For the F-type stars like the 1.4 $M_\odot$ model, the LD is much larger than expected for real stars. For more massive stars, the iron can be completely depleted at the surface at the ZAMS. The efficiency of atomic diffusion is related to the size of the convective zone. The convective envelope is smaller with the stellar mass, leading to a more efficient transport induced by atomic diffusion. In the absence of other competing processes, it leads to an over-depletion of heavy elements (and helium) at the surface.

Regardless of the mass, the surface [Fe/H] increases after the LD and reaches a maximum during the RGB phase, after the first dredge-up. The exact level of [Fe/H] at this maximum point depends on the stellar mass with values anyway close to the initial one. For the models shown in Fig. (7.5), only those with masses higher than 1.0 $M_\odot$ can reach or slightly exceed the initial composition. After this point, with atomic diffusion, the [Fe/H] decreases slowly at the surface, but the variations in these models are much smaller than the best observed uncertainties we have access to for this parameter (variations $\ll$ 0.01 dex).

When the radiative accelerations are included, the behavior is the same for the 1.0 $M_\odot$ model. The [Fe/H] decreases more slowly when this process is included in stellar models. In the case of 1.4 $M_\odot$, the evolution of this element is different. [Fe/H] increases at the surface during the MS. As the convective envelope expands, its abundance at the surface decreases. After the MS, the abundance of [Fe/H] is similar to the case with only gravitational settling and follows the same evolutionary behavior. This shows that for the lower mass stars, the effect of radiative accelerations is less significant than for higher masses.

For the 1.0 $M_\odot$ model, neglecting this process leads to a difference of $\sim$ 0.01 dex in [Fe/H]. For the model of 1.4 $M_\odot$, it can completely change the evolution of this element.

7.2.1.3 Evolution of [M/H] and [Fe/H]

[Fe/H] is usually used as a proxy for [M/H]. However, [M/H] can only be approximated by [Fe/H] in limited circumstances (e.g. the Sun), and it is only valid if the ratio of X(Fe) to Z remains the same, which is not always the case. Cases where surface [Fe/H] does not match [M/H] are alpha-enriched stars (Salaris & Weiss, 2001) or for F-type stars where atomic diffusion modifies the chemical mixture (Deal et al., 2018).

Looking back at Fig. 7.6, we can compare the evolution of [M/H] with [Fe/H]. Without radiative acceleration, the 1.0 $M_\odot$ model depletes [Fe/H] faster than [M/H]. For the 1.4 $M_\odot$ model, both parameters are depleted with a significant slowing of the depletion of [M/H]. For radiative acceleration, there is a significant difference in the evolution between [Fe/H] and [M/H] for the 1.4 $M_\odot$ model. In this case, [M/H] is depleted instead of enriched. This indicates that the approximation of [Fe/H] = [M/H] is not valid for these stars.

Therefore, when constraining stellar properties, [Fe/H] should not be approximated to [M/H]. Even if for the lower mass star the difference is smaller ($\sim$ 0.02 for the 1.0 $M_\odot$ model), it can introduce uncertainties close to the best abundance uncertainties. For the 1.4 $M_\odot$ model, it is important to note that even if the over-depletion of [Fe/H] is avoided, there is still a variation that is not expected for non-chemical peculiar stars.

7.2.1.4 Maximum chemical variation in MS

Often, when creating grids of stellar models, atomic diffusion is cut off at a certain point of the grid in order to avoid these unrealistic variations (e.g. Silva Aguirre et al. (2017), Nsamba et al. (2021)). This point is usually defined by the stellar mass: stars with masses lower than the defined one include atomic diffusion, and stars with higher masses do not include it. This method assumes that F-type and more massive stars keep their surface chemical composition constant (which may not be true). However, this cut in mass does not take into account the variation of the initial chemical composition, which has a strong influence on the evolution of the star. Chaboyer et al. (2001) show that inhibiting atomic diffusion at the surface layers (a depth of 0.005 $M_\odot$ to 0.01 $M_\odot$ from the surface) is sufficient to reproduce the abundances of globular clusters. However, they did not take into

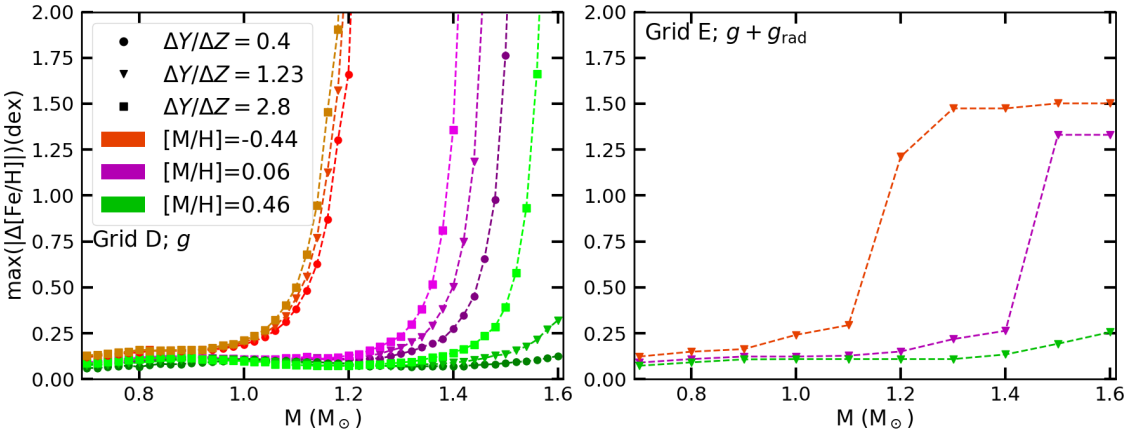

FIGURE 7.7: Maximum variation of [Fe/H] during the evolution (up to the tip of RGB) according to mass. The colors and symbols correspond to the values of $[Fe/H]_i$ and $\frac{\Delta Y}{\Delta Z}$. The maximum variation is determined for ages smaller than 13.5 Gyr for the models that evolve on longer timescales ($M \lesssim 0.95$ $M_\odot$). The left panel shows models that include atomic diffusion without radiative accelerations, and the right panel shows models that include radiative accelerations.

account the chemical composition of the stars, and this method is not so accurate for field stars, which presents asteroseismology and new high-resolution spectroscopy that were not available before.

Figure (7.7) shows the maximum variations of [Fe/H] at the stellar surface for the different models including atomic diffusion (models from grids D and E). If only gravitational settling is taken into account, the maximum depletion increases with the stellar mass. But it is also influenced by the initial chemical composition. The maximum depletion increases for lower metallicities and higher helium abundances, as expected, since the convective envelope size decreases in these cases. This suggests that when atomic diffusion is cut off grids of stellar models, a fixed mass cannot avoid the unrealistic variations for all models. Assuming a threshold of 1.2 $M_\odot$, metal-poor stars still reach large values of [Fe/H] variations. When radiative accelerations are taken into account, the behavior is the same for mass and initial chemical composition. The main difference is that the maximum variation reaches a plateau. Indeed, when the abundance of elements is large, there are not enough photons with the proper energy to share their momentum with the ions, which leads to the saturation of the effect of radiative accelerations (Michaud et al., 2015).

The maximum depletion caused by gravitational settling in Fig. (7.7) could be used to identify for which models atomic diffusion should be neglected (as I did in grid A). However, this procedure is incorrect. First, it is not physical, because chemical transport

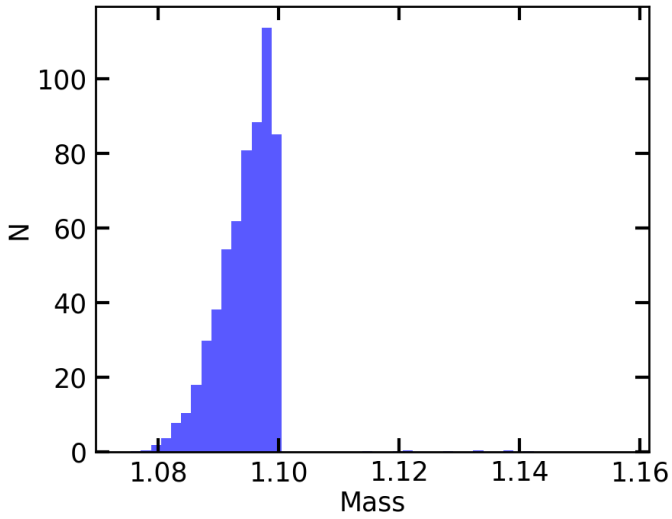

FIGURE 7.8: Probability density function of the mass for KIC 6521045.

mechanisms (atomic diffusion) should be included for all stellar models, and neglecting them introduces uncertainties. Second, it introduces uncertainties between stellar models with and without atomic diffusion. This problem has been identified when inferring the properties of some stars using Grid A. An example is KIC 6521045. Looking at the histogram showing the density probability function of the mass, we can identify a truncation problem in the middle of the parameter space of Grid A. This problem arises due to the discontinuity that the truncation of atomic diffusion creates in the parameter space. This discontinuity does not allow the parameter space to be well explored during the optimization process. In this case, the optimization will only find valid models with atomic diffusion, in which case it will impose a bias toward lower masses.

It is necessary to add atomic diffusion in all stellar models. However, atomic diffusion (even considering radiative accelerations) produces unrealistic variations for F-type and more massive stars. It is therefore necessary to add other mechanisms to counteract the effects of atomic diffusion. In this work, I consider a formulation that aims to replicate the effects of the competing diffusive mechanisms, the turbulent mixing formulation.

Chapter 8

Implementation and Test of Turbulent Mixing in Stellar Models

To avoid the unrealistic variations of the surface abundances caused by atomic diffusion, it is necessary to include other chemical transport mechanisms. I have investigated the possibility of introducing them through ad-hoc turbulent mixing prescriptions.

I have used both of the turbulent mixing recipes described in chapter 4.4 (eqs. 4.23 and 4.24). Here I investigate the effect of this turbulent mixing coefficient on the surface abundances of stellar models and the possibility of adding the effects of radiative accelerations in the calibration.

8.1 Effect of turbulent mixing on the chemical evolution of stars

The Verma & Silva Aguirre (2019, hereafter VSA19) calibration uses the Richer et al. (2000) turbulent mixing prescription (eq. 4.24). This calibration uses a reference mass ($\Delta M = 5 \times 10^{-4}\,M_\odot$) to reproduce the helium abundance of F-type stars. This prescription is very efficient in transporting chemical elements down to the reference depth, below which it decreases with ρ^{-4}. It only affects the chemical evolution of F-type or more massive stars. For less massive stars, the convective envelope reaches regions deeper than ΔM_0 (as seen in the left panel of Fig. 4.2), neutralizing the effects of other transport processes. In this section, I consider the effects of this prescription only for F-type stars, focusing on the case of a 1.2 and 1.4 $M_\odot$ models. The surface evolution of [Fe/H] and [M/H] of these two models is shown in Fig. 8.1.

I first consider the evolution of the iron surface abundance when radiative accelerations are taken into account. For the 1.2 $M_\odot$ model, turbulent mixing (models from grid F1, purple curves) attenuates the depletion of [Fe/H]. If the turbulent mixing is not included, the surface is 0.02 dex more depleted. Turbulent mixing effects are more significant for the more massive stars. In the case of the 1.4 $M_\odot$ model, the inclusion of turbulent mixing completely changes the behavior of the evolution of [Fe/H] at the surface: Instead of an enrichment, the model shows a steady depletion of this element (see in the right panel of Fig. 8.1). This is because the reference point of the turbulent mixing prescription reaches a region where the microscopic transport of iron is dominated by gravitational settling, leading to a depletion at the surface. Nevertheless, it prevents the unrealistic surface abundances.

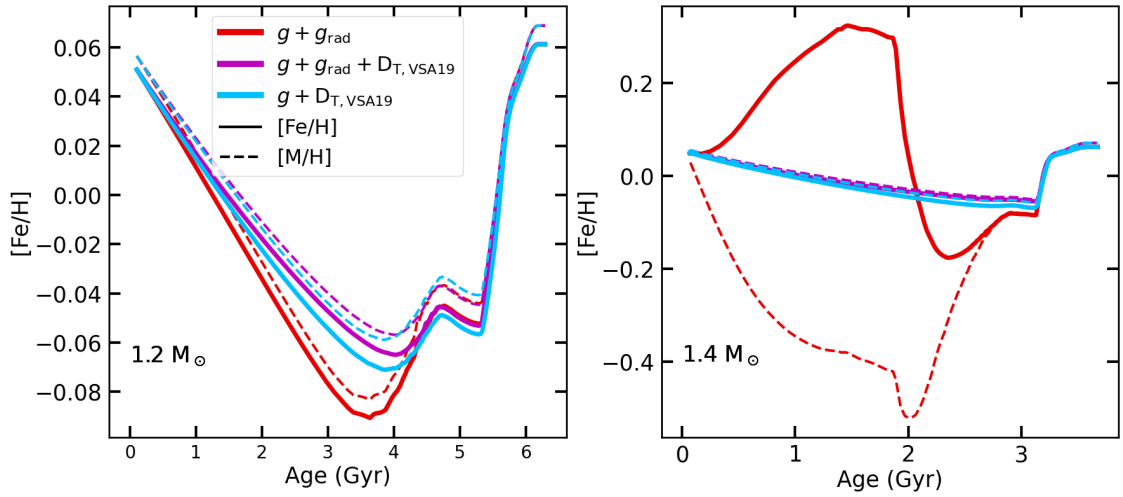

FIGURE 8.1: Variation of [Fe/H] (solid lines) and [M/H] (dashed lines) from the ZAMS to the tip of the RGB for $[Fe/H]_i = 0.06$. The purple and red lines represent models with and without turbulent mixing (both with radiative acceleration), and the cyan lines represent the model models including only turbulent mixing. The left panel presents the evolution for the 1.2 $M_\odot$ models and the right panel for the 1.4 $M_\odot$ models.

When radiative accelerations are neglected (models from grid F2, cyan curves), the depletion is larger than in the previous case. This indicates that even if the radiative accelerations are not dominant, they attenuate the effects of gravitational settling. For the 1.4 $M_\odot$ model, this can lead to a difference of up to 0.015 dex between models with and without radiative accelerations, and it can be larger for more massive stars. This suggests that radiative accelerations should not be neglected.

The case of the surface evolution of [M/H] is similar to that of [Fe/H]. For both models, the depletion of [M/H] is attenuated, and for the 1.4 $M_\odot$ model, turbulent mixing avoids the unrealistic surface abundances. Nevertheless, there is a difference of 0.01 dex

between [M/H] and [Fe/H], which is close to the uncertainties of the best observations for solar-like stars.

For the lighter elements like helium and hydrogen, as shown in Fig. 8.2 for the case of the 1.4 $M_\odot$ model, the inclusion of turbulent mixing prevents the unrealistic surface abundances caused by atomic diffusion. As we have seen, the inclusion of radiative accelerations has no effect on the evolution of these elements.

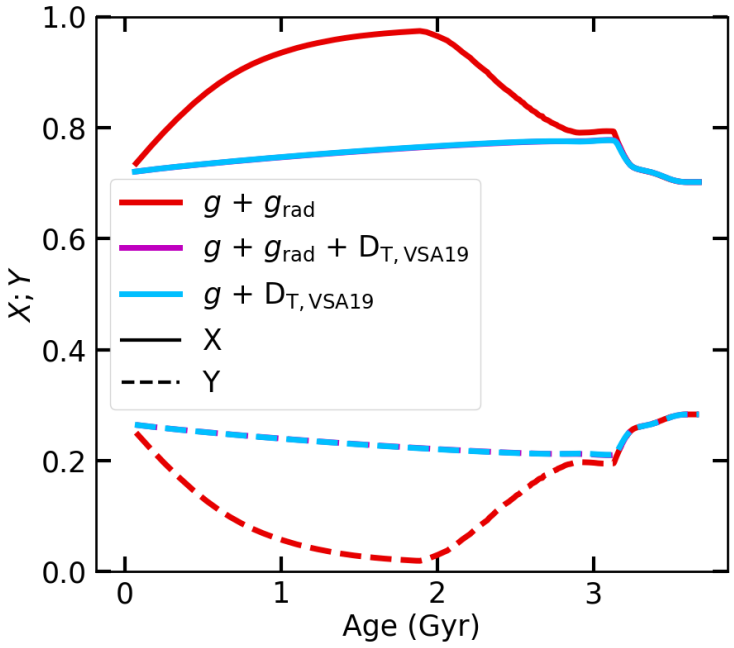

FIGURE 8.2: Surface evolution of the fractional abundances of hydrogen and helium for models with 1.4 $M_\odot$.

This shows the importance of turbulent mixing to avoid unrealistic surface abundances. Nevertheless, the inclusion of the radiative accelerations are important for an accurate modeling of the chemical evolution of the star. However, the inclusion of radiative accelerations does not allow the computation of a large number of stellar models to characterize stars accurately, as it is very computationally expensive. It is necessary to find more efficient ways to account for this process in stellar models. I studied two possible ways to include radiative accelerations:

- Calibrating the effect of radiative acceleration on iron in a turbulent mixing prescription.
- Implementing a parametric method for computing radiative accelerations, the Single-Valued Parameters method (see chapter 10).

8.2 Calibrating turbulent mixing to reproduce the effect of radiative accelerations on the surface abundances

The turbulent mixing prescriptions described in chapter 4.4 are parameterizations of the macroscopic transport processes in competition with atomic diffusion. It attenuates the variations of the surface abundances. Moreover, radiative accelerations push the elements towards the surface, slowing down the depletion at the surface. The final results on the surface abundances are similar to a turbulent diffusion coefficient, although the physical origin of the process is different. Furthermore, iron is the main element used as a constraint in stellar characterization. This is the reason why I focus on the evolution of this element. Nevertheless, it has to be noticed that calibrating the radiative accelerations effect on iron in a turbulent mixing diffusion coefficient affects all elements similarly, which is not accurate. Therefore this approach may only be valid for iron.

MESA provides a hook to implement this type of process without modifying the source code (using the *other_d_mix.f90* file). Since iron is depleted in all models including the VSA19 turbulent mixing considered in this study, it is possible to parameterize the effect of the radiative acceleration for this element by an increase in the efficiency of turbulent mixing (i.e. an increase in the mass of the reference point ΔM_0).

This turbulent mixing parameterization is equivalent to write the diffusion equation (eq. 4.5) as

$$\rho \frac{\partial X_i}{\partial t} = A_i m_p \left[\sum_j (r_{ji} - r_{ij}) \right] - \frac{1}{r^2} \frac{\partial}{\partial r} \left[r^2 \rho v'_i \right] + \frac{1}{r^2} \frac{\partial}{\partial r} \left[r^2 \rho D_{\mathrm{T,Fe}} \frac{\partial X_i}{\partial r} \right], \tag{8.1}$$

with

$$v'_i = D_{i,p} \left[-\frac{\partial \ln X_i}{\partial r} + k_T \frac{\partial \ln T}{\partial r} + \frac{(Z_i+1) m_p g}{2 k_B T} - \frac{A_i m_p}{k_B T} g \right]. \tag{8.2}$$

where $D_{\mathrm{T,Fe}}$ is the parameterized turbulent mixing coefficient to reproduce the effect of radiative acceleration on the evolution of the surface abundance of iron.

The efficiency of the turbulent mixing must be adjusted to account for the effects of radiation accelerations on iron. To do this, I vary ΔM_0. It is important to note that the effects of radiative accelerations depend in particular on the stellar mass. The more massive the star is, the more efficient the radiative accelerations would be. Thus ΔM_0 must depend on the properties of the star. Taking this into account, I parameterized the reference mass, as schematized in Fig. 8.3, and summarized by the following steps:

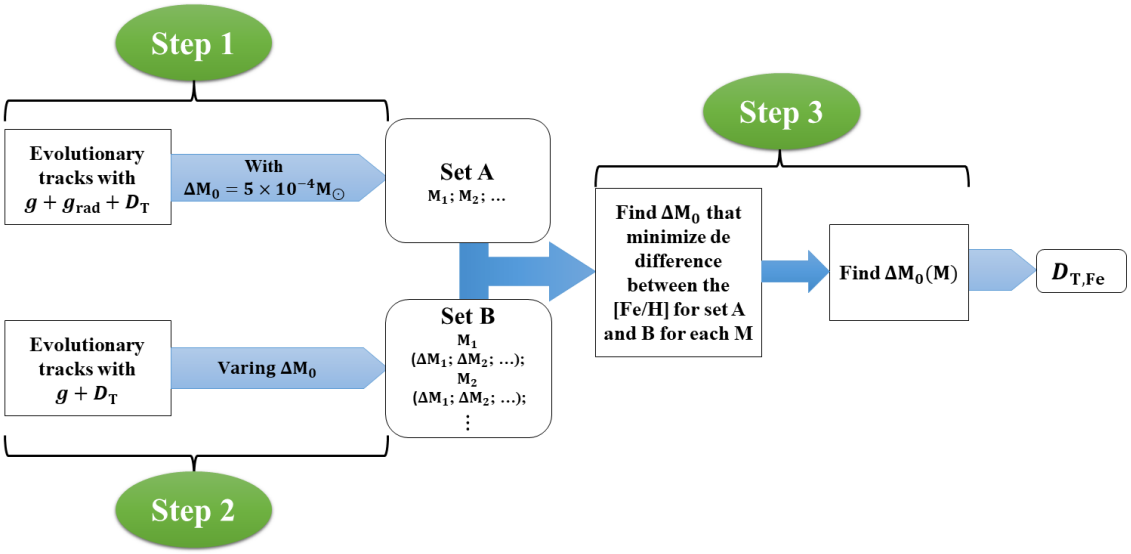

FIGURE 8.3: Parametrisation procedure of ΔM_0.

Step 1: To compute the reference stellar models, with different masses $\geq$ 1.2 $M_\odot$, including atomic diffusion with radiative accelerations, turbulent mixing with the ΔM_0 value of VSA19, and the initial solar chemical composition obtained from a solar calibration (Set A).

Step 2: For each reference model from Step 1, to compute a new set of models (set B) including atomic diffusion without radiative accelerations and different values of ΔM_0.

Step 3: To compare the surface [Fe/H] evolution of the reference models with those computed with different ΔM_0 values in step 2 for each mass of the grids. The best value is obtained by a minimization procedure. The relationship between ΔM_0 and the mass is then obtained by linear regression.

Following these steps, I calibrate the efficiency of turbulent mixing to reproduce the effects of radiative accelerations. The set of models I used as a reference were the models from Grid F1. With this calibration, I found that the ΔM_0 increases with the stellar mass of the model, as shown in Fig. 8.4. This indicates that to reproduce the effects of radiative accelerations, the efficiencies of turbulent mixing must increase. From this, I derived a linear expression that describes the variation of ΔM_0 with the stellar mass of the model as

$$\Delta M_0 \left(\frac{M^*}{M_\odot}\right) = 3.1 \times 10^{-4} \times \left(\frac{M^*}{M_\odot}\right) + 2.7 \times 10^{-4}. \tag{8.3}$$

It is important to note that this calibration depends on the input physics of the models. Moreover, this calibration only affects F-type or more massive stars, since the values of

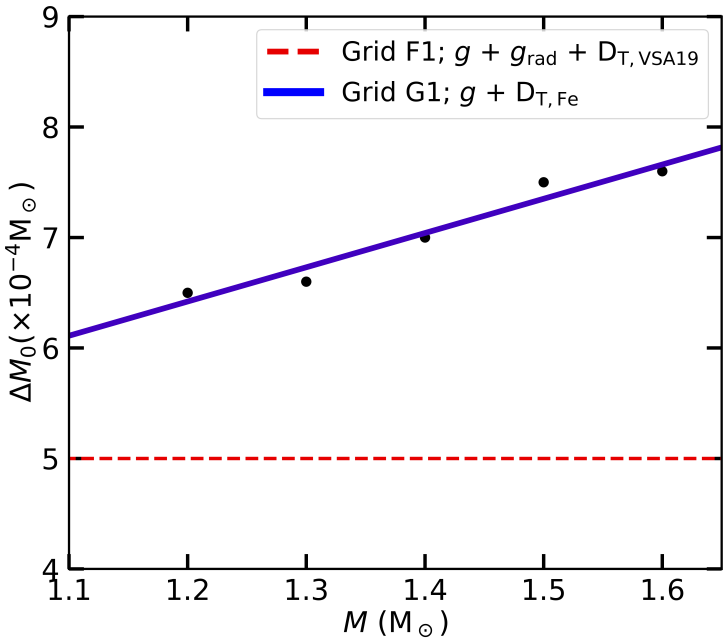

FIGURE 8.4: Values of the parameterize ΔM_0 as a function of the stellar mass here (black dots) and calibrated by VSA19 (red line). The blue line represents the linear fit presented in Eq. 8.3.

ΔM_0 are too small to have an impact on the evolution of stellar models with smaller mass (i.e. ΔM_0 is located inside the convective envelope for the latter).

8.2.1 Changing the initial metallicity

In the previous section, I kept fixed the initial composition during the calibration process. However, it is important to assess the impact of changing the initial chemical composition on ΔM_0.

Figure 8.5 shows the surface evolution of [Fe/H] for 1.2 and 1.4 $M_\odot$ models considering different initial chemical compositions. Here we can compare the models that include my calibrated turbulent mixing with VSA19 turbulent mixing including radiative accelerations. For both masses, increasing the initial metallicity does not affect the calibrated turbulent mixing. As the metallicity increases, the star behaves like a less massive star, and it does not seem to have a strong effect on the efficiency of the radiative accelerations (for the metallicities I tested).

For lower metallicity the effect is different. Decreasing metallicity increases the efficiency of radiative accelerations and the calibration does not hold anymore. This is expected since low metallicity stars behave like more massive ones. Nevertheless, the parametrization breaks only for the very low metallicities. The calibration is valid in the

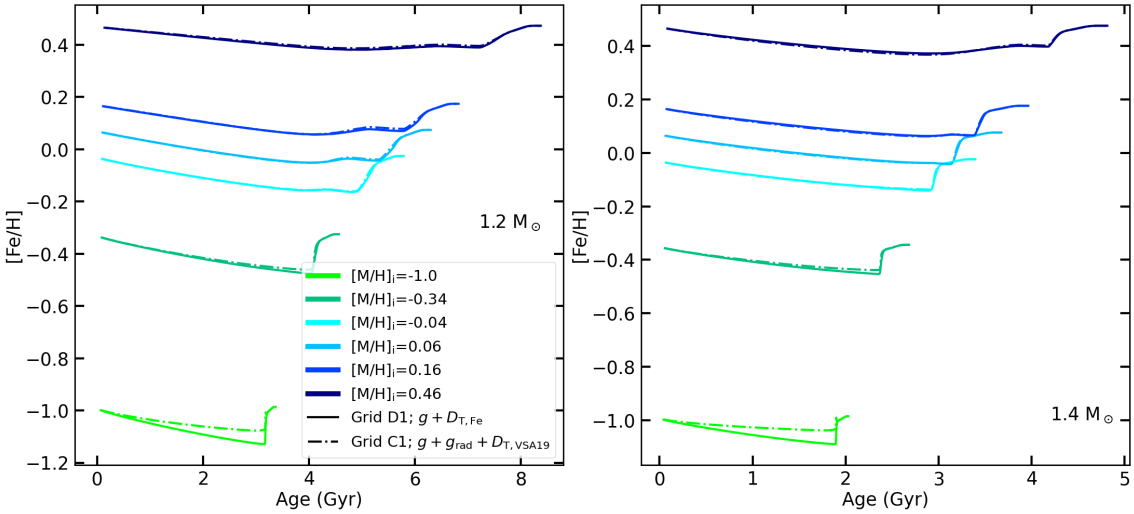

FIGURE 8.5: Evolution of [Fe/H] with time for 1.2 $M_\odot$ (left panel) and 1.4 $M_\odot$ (right panel) models at different initial chemical compositions. The solid lines represent models including atomic diffusion (without radiative accelerations) and the parameterization $D_{T,Fe}$ described in Sect. 8.2. The dot-dashed lines represent models including atomic diffusion with radiative accelerations and the $D_{T,VSA19}$ calibrated by VSA19.

regime around -0.5 to 0.5 dex in $[M/H]_i$ without the need for re-calibration (with maximum differences up to 0.04 dex).

8.2.2 Other elements

As I stated at the beginning of this section, the calibration includes the effects of radiative accelerations on iron, but may not be valid for the other elements, since the radiative accelerations are different for each element. In Figure (8.6) we see the surface abundance evolution of different elements (He, C, N, O, Mg, Al, Ca, and Fe) for the 1.4 $M_\odot$ model, comparing my calibrated turbulent mixing with radiative accelerations models. In the case of helium, we see that my calibrated turbulent mixing depletes less the surface. Turbulent mixing affects all the elements in the same way and helium (top left panel of Fig. 8.6) is less depleted even if radiative acceleration does not affect this element. Nevertheless, the difference between the two models is about 0.006 in mass fractions, which is comparable to the uncertainties of the surface helium abundances obtained by Verma et al. (2019).

In the case of carbon, nitrogen, magnesium, and aluminum (top middle, top right, middle, and middle right panels of Fig. 8.6, respectively), the calibrated turbulent mixing coefficient induces a very close evolution compared to the model that includes radiative

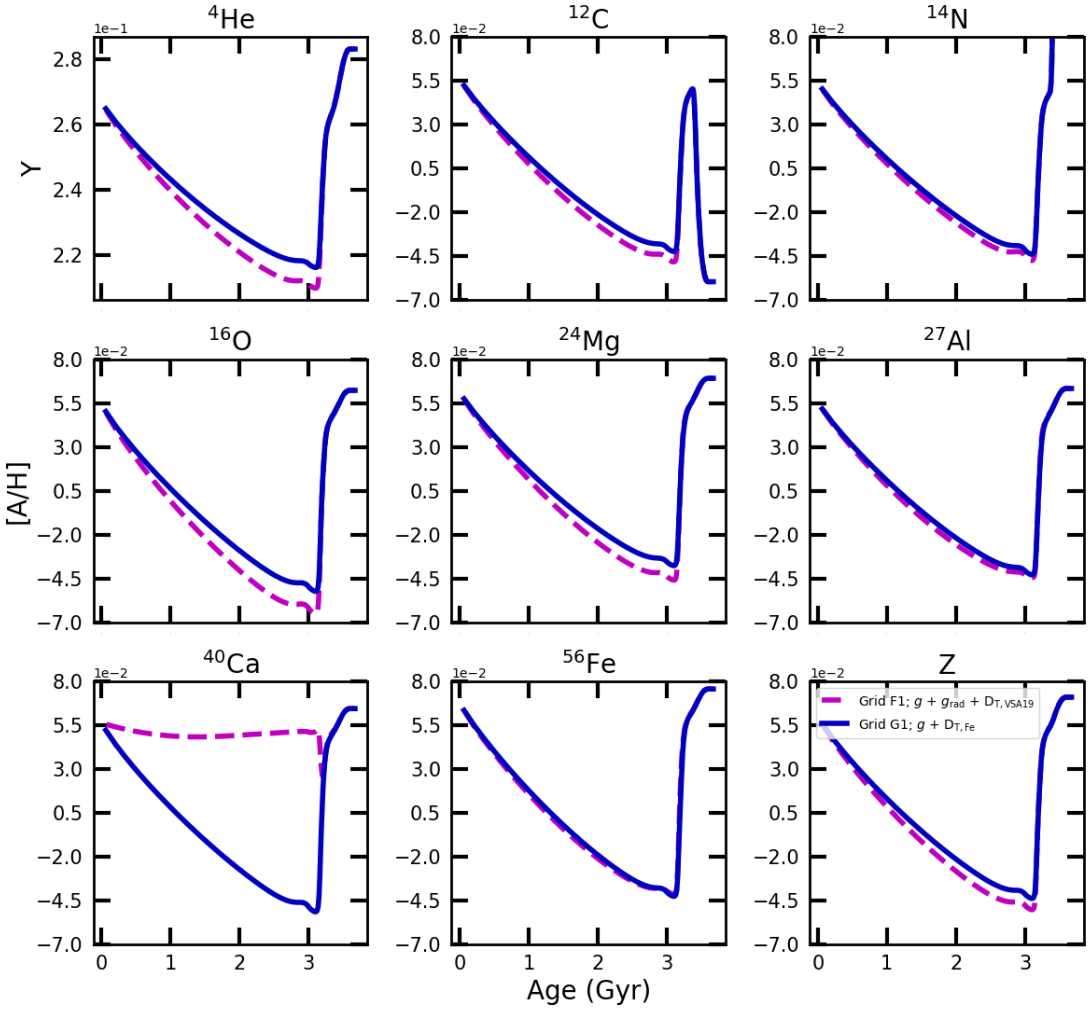

FIGURE 8.6: Evolution of the surface abundance of some chemical elements for a 1.4 $M_{\odot}$ model. The purple dashed lines represent a model including atomic diffusion with radiative accelerations and the turbulent mixing calibrated by VSA19, and the blue solid lines represent a model including atomic diffusion without radiative acceleration and the $D_{T,Fe}$ turbulent mixing parametrized in this work.

accelerations. The differences in surface abundances for these elements are, in fact, approximately 0.006 dex, 0.004 dex, 0.008 dex, and 0.004 dex for C, N, Mg, and Al, respectively. These differences indicate that both models are in agreement. For carbon, nitrogen, and magnesium, radiative accelerations are not efficient and there is almost no difference between the two models. For aluminum, the radiative acceleration efficiency is similar to iron (in this case).

For oxygen (middle left panel of Fig. 8.6), there is a significant difference of about 0.013 dex between both models. However, this difference is comparable to the uncertainties obtained from observations. Radiative acceleration for this element is less efficient than for iron.

Finally, in the case of calcium, the difference is not negligible. The inclusion of radiative accelerations lead to an almost constant surface abundance. This is not reproduced by the calibrated turbulent mixing, because in the model with radiative accelerations, the turbulent mixing reaches a region where the radiative accelerations are larger than gravity (see Fig. 7.2). For this reason, there is an accumulation or constant abundance of calcium at the surface. My turbulent mixing calibration cannot reproduce this behavior because the combination of gravitational settling and turbulent mixing coefficient can only lead to depletion.

8.2.3 Maximum variations of iron at the surface

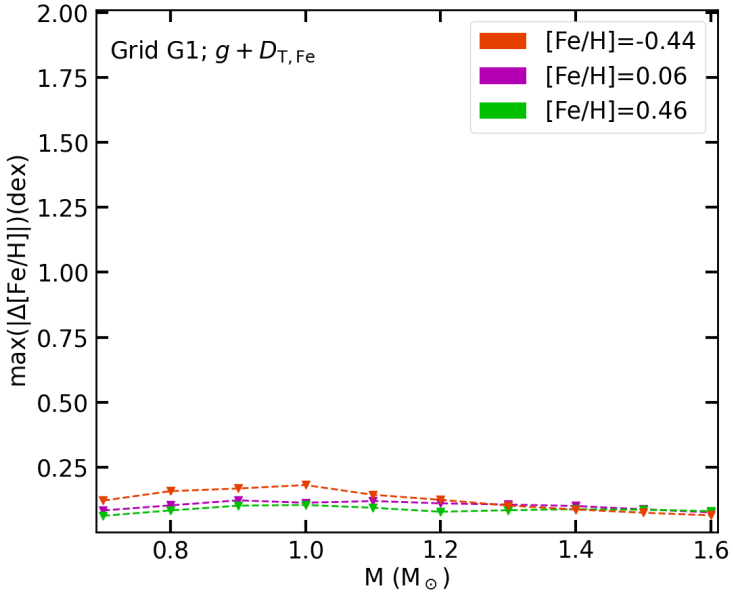

FIGURE 8.7: Same legend as Fig. (7.7) for the case of the calibrated turbulent mixing ($D_{T,Fe}$).

Looking at the maximum surface variations of the iron content in Fig. 8.7, we see that there are no unrealistic chemical variations as we previously saw in Fig. 7.7. This prescription allows us to include atomic diffusion in all stellar models, avoiding the unrealistic surface abundance variations that can be caused by gravitational settling and radiative accelerations in F-type stars.

Despite some limitations of the turbulent mixing calibrations, especially in the prediction of surface abundance for elements other than iron (e.g. Ca). This is a step toward an improvement of the accuracy of models, and the characterization of stars. In the following sections, I will carry out a seismic test with two *Kepler* stars. This will allow to impose a final validation in the inference of stellar properties using this calibration.

8.3 Impact on the inference of the stellar properties

8.3.1 Seismic validation

First, it is necessary to know if neglecting the radiative accelerations and using the calibrated turbulent mixing coefficient presented in chapter8.2 affects the seismic characterization of stars. To do this, I selected three stellar models along the evolutionary paths of grid G1 (which includes my turbulent mixing calibration) with 1.2, 1.4, and 1.6 $M_{\odot}$ in the MS stage. I inferred, with AIMS, their properties in grid F1 (which considered radiative acceleration) to quantify the validity of my parameterization. I used the effective temperature, [Fe/H], and individual seismic frequencies of the selected models as constraints.

TABLE 8.1: Global fundamental properties of the computed models and those obtained by the optimization.

	Mass ($M_{\odot}$)		Radius ($R_{\odot}$)		Age (Gyr)	
	Model	Inference	Model	Inference	Model	Inference
Model 1	1.20	1.20±0.01	1.240	1.240±0.004	2.1	2.1±0.2
Model 2	1.40	1.40±0.01	1.598	1.596±0.004	1.7	1.7±0.1
Model 3	1.60	1.60±0.01	1.870	1.870±0.004	1.2	1.2±0.1

Since we are using stellar models, we know the real values of their basic properties: mass, radius, and age. Table (8.1) shows the real properties of the models and those obtained from the inference. For the three models, the inferred, with AIMS, properties are consistent with the real values within the uncertainties. Now, for the seismic frequencies, the inference results are shown in the echelle diagram in Fig. 8.8. Note that since I am comparing models to models, the surface corrections are not necessary. The results show that there is an overlap in seismic frequencies between the models that include radiative accelerations and the models with calibrated turbulent mixing. This indicates that the effect on the seismic frequencies is negligible and that the use of the turbulent mixing calibration allows stellar properties to be inferred without bias.

8.3.2 Applications to Kepler stars

It is now important to assess the effects of turbulent mixing in the inference of the global properties of real stars. As a first test using AIMS, I inferred the properties of two stars from the Kepler Legacy sample (Lund et al., 2017), KIC 2837475 and KIC 112253226. These

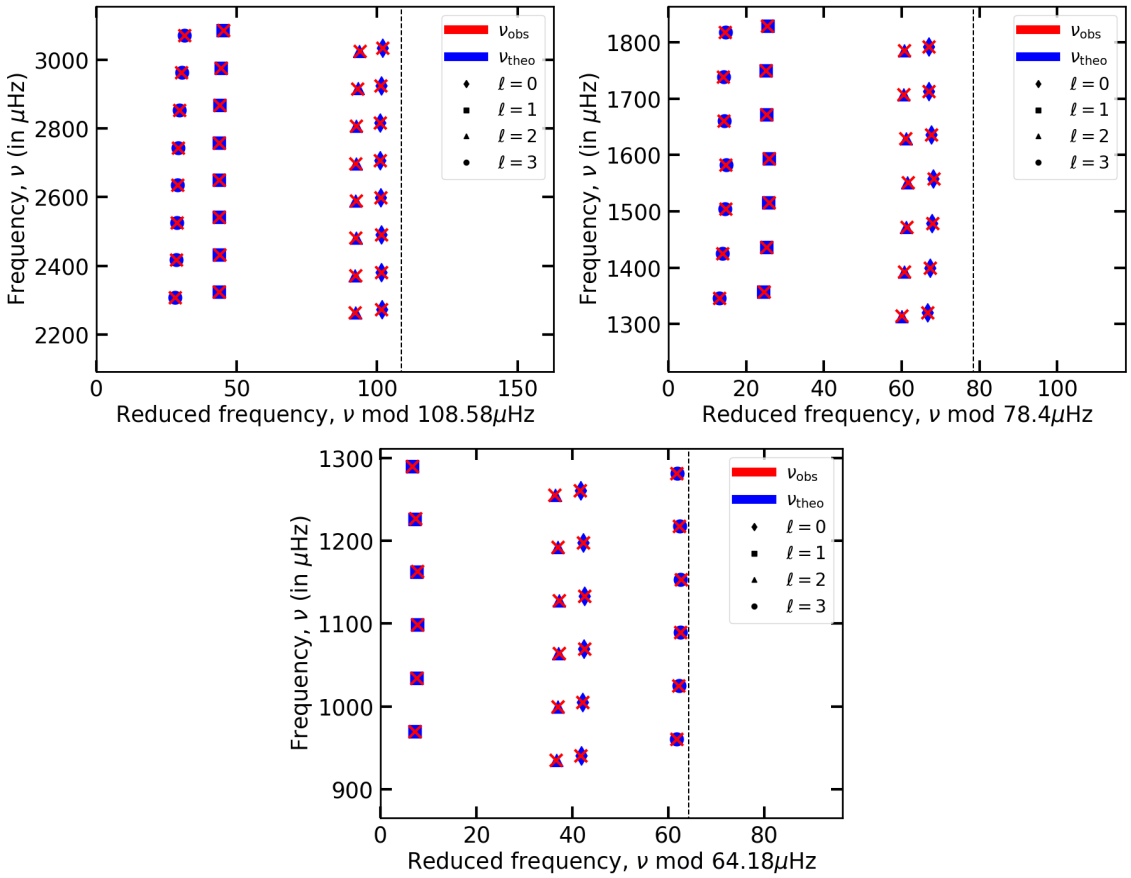

FIGURE 8.8: Echelle diagrams of the best optimization result. The top panels are for model with 1.2 $M_\odot$ (left panel), 1.4 $M_\odot$ (right panel). The bottom shows the results for the 1.6$M_\odot$. ν_{obs} are the frequencies used as constraints from the optimized model from Grid D1; ν_{theo} are the optimized frequencies from Grid C1.

are F-type stars and are two of the three stars studied in VSA19. They have similar chemical compositions, allowing smaller grids to be built for the optimization procedure. We infer the properties of these stars using grids G1, G2, G3, and G4 to disentangle the effects of atomic diffusion and turbulent mixing on the properties of the stars. The results are shown in the table (8.2).

Comparing the results from grids G1 and G2 shows the effect of considering the grid with turbulent mixing calibrations and a grid without transport (except convection) using the same solar calibrations. In this case, both mass and radius are consistent between the two inferences. The main difference is in the inference of the age, with a difference of 11% for KIC 2837475 and 12% for KIC 11253226.

The comparison of the results obtained with grids G1 and G3 shows the same effect (as the comparison of G1 and G2), but with both grids calibrated to the Sun according to

TABLE 8.2: Global fundamental properties obtained for the two studied stars.

KIC	Grid	Mass ($M_\odot$)	Radius ($R_\odot$)	Age (G_{yr})
2837475	G1	1.43±0.03	1.64±0.01	1.54±0.11
	G2	1.42±0.03	1.64±0.01	1.71±0.12
	G3	1.40±0.03	1.62±0.01	1.74±0.12
	G4	1.40±0.05	1.64±0.02	1.82±0.32
11253226	G1	1.41±0.02	1.61±0.01	1.53±0.11
	G2	1.41±0.03	1.61±0.01	1.71±0.11
	G3	1.39±0.03	1.61±0.01	1.76±0.11
	G4	1.41±0.04	1.61±0.02	1.60±0.21

their input physics. In this case, the age differs by about 13% and 15% for KIC 2837475 and KIC 11253226, respectively. In this case, there is a difference in radius of 2% for KIC 2837475 and a difference in mass of 1% for both stars. Nevertheless, both results are consistent within 1σ of the estimated errors. These two estimates show that neglecting chemical transport mechanisms leads to large errors in the ages.

The comparison of grids G1 and G4 shows an estimate of the effect of atomic diffusion alone near the core. In this case, the adjustment of the $[Fe/H]$ was done with the initial $[Fe/H]$ of the models, since the models show an unrealistic depletion of iron at the surface. In this case, the maximum difference in mass and radius is about 1% for both stars. For the age, however, there is a significant difference, similar to the values for grids G2 and G3 (about 10%).

This seems to indicate that most of the effect on the age is due to the consideration of atomic diffusion (mainly gravitational settling near the core). Turbulent mixing mainly affects the mass and radius determination by inducing a more realistic $[Fe/H]$ at the surface of the models. However, we cannot take this as a strong conclusion considering the large error in the age for the G4 grid.

The inclusion of a calibrated turbulent mixing allows the inclusion of atomic diffusion without unrealistic surface abundances. This improves the age determination and the predictions of stellar surface abundances in the models. Nevertheless, this is a first test, and in the next chapter, I extend it to a larger sample of FGK-type stars.

Chapter 9

Stellar Inference With Models Including Turbulent Mixing

The calibrations presented in the previous chapter manage to avoid the unrealistic chemical variations at the surface caused by gravitational settling, but it is important to understand its full impact on the stellar properties. In this chapter, I investigate how this prescription affects stellar characterizations, by performing a statistical analysis of the seismic sample of FGK-type stars presented in chapter 6. Here I compare the stellar properties obtained using the common way of modeling stars, (e.g. turning off atomic diffusion for F-type stars - Grid A), and the stellar properties obtained using models that include atomic diffusion and the calibrated turbulent mixing, presented in the previous chapter (Grid B). The work presented in this chapter is published in Moedas et al. (2024) (the pdf in appendix B).

9.1 Testing the inference constraints

Before testing the effects of using different input physics, we need to define which constraints we should use in the optimization process. I compare different sets of constraints:

Set 1: $T_{\rm eff}$, [Fe/H], and the individual seismic frequencies ($\nu_{n,\ell}$).

Set 2: $T_{\rm eff}$, [Fe/H], L, the individual seismic frequencies.

Set 3: $T_{\rm eff}$, [Fe/H], $\nu_{\rm max}$, the individual seismic frequencies.

Set 4: $T_{\rm eff}$, [Fe/H], and the ratios instead of the individual frequency.

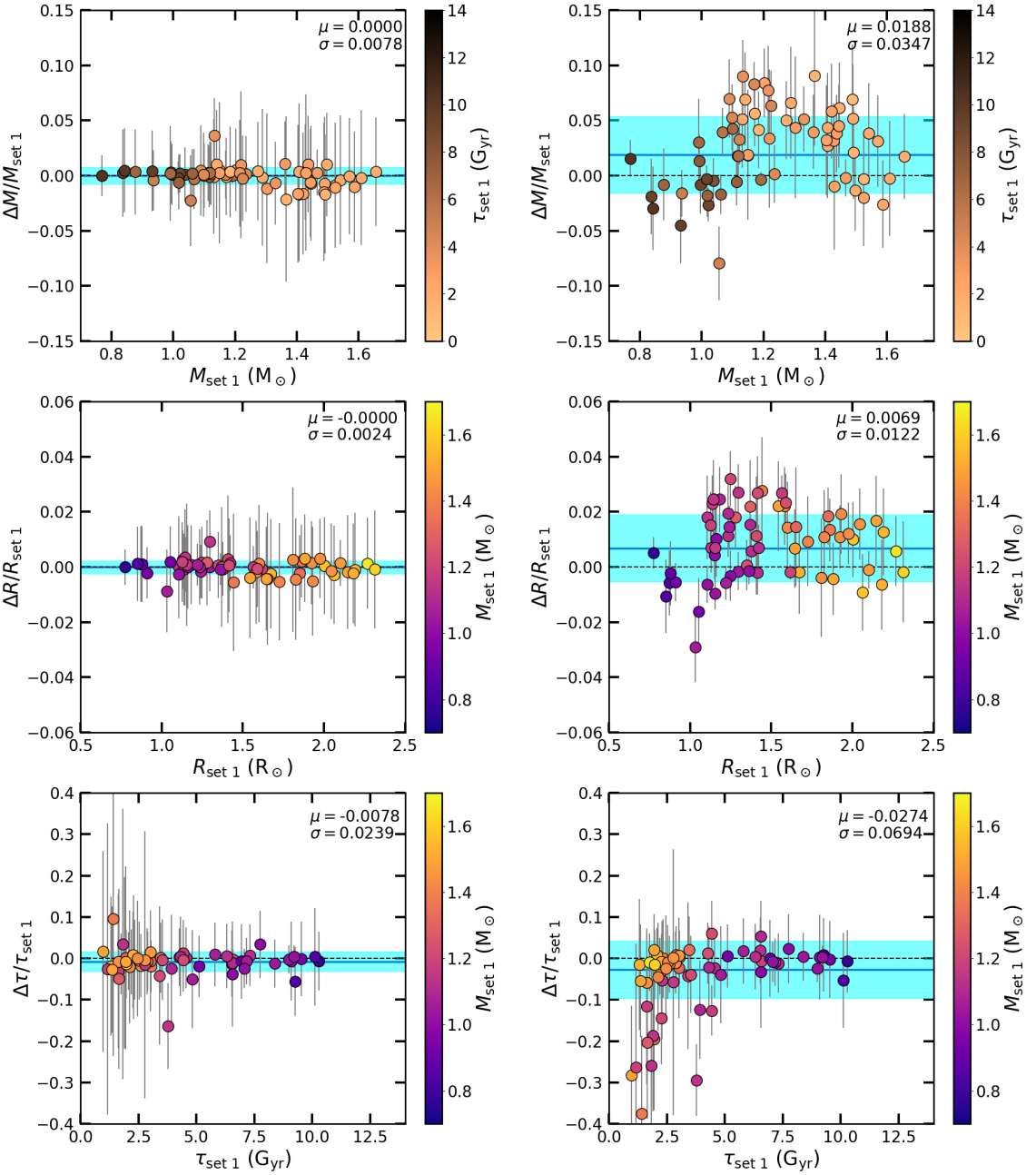

FIGURE 9.1: Comparison of inferred mass (top panels), radius (middle panels) and age (bottom panel), between Set 1 and Set 2 (left panels) and Set 1 and Set 3 (right panel).

For these tests, the results are similar, regardless of the grid, so I only show the results obtained with Grid B in the following. Moreover, these tests are only performed with the legacy sample L17.

The first set is less constrained, with only two global constraints, compared to three in sets 2 and 3. Adding luminosity (comparing sets 1 and 2 using the relative difference eq. 5.9) as a constraint has no statistical effect on the inference of mass, radius, and age (left panels of Fig. 9.1). This is due to the large uncertainties in the luminosity that we

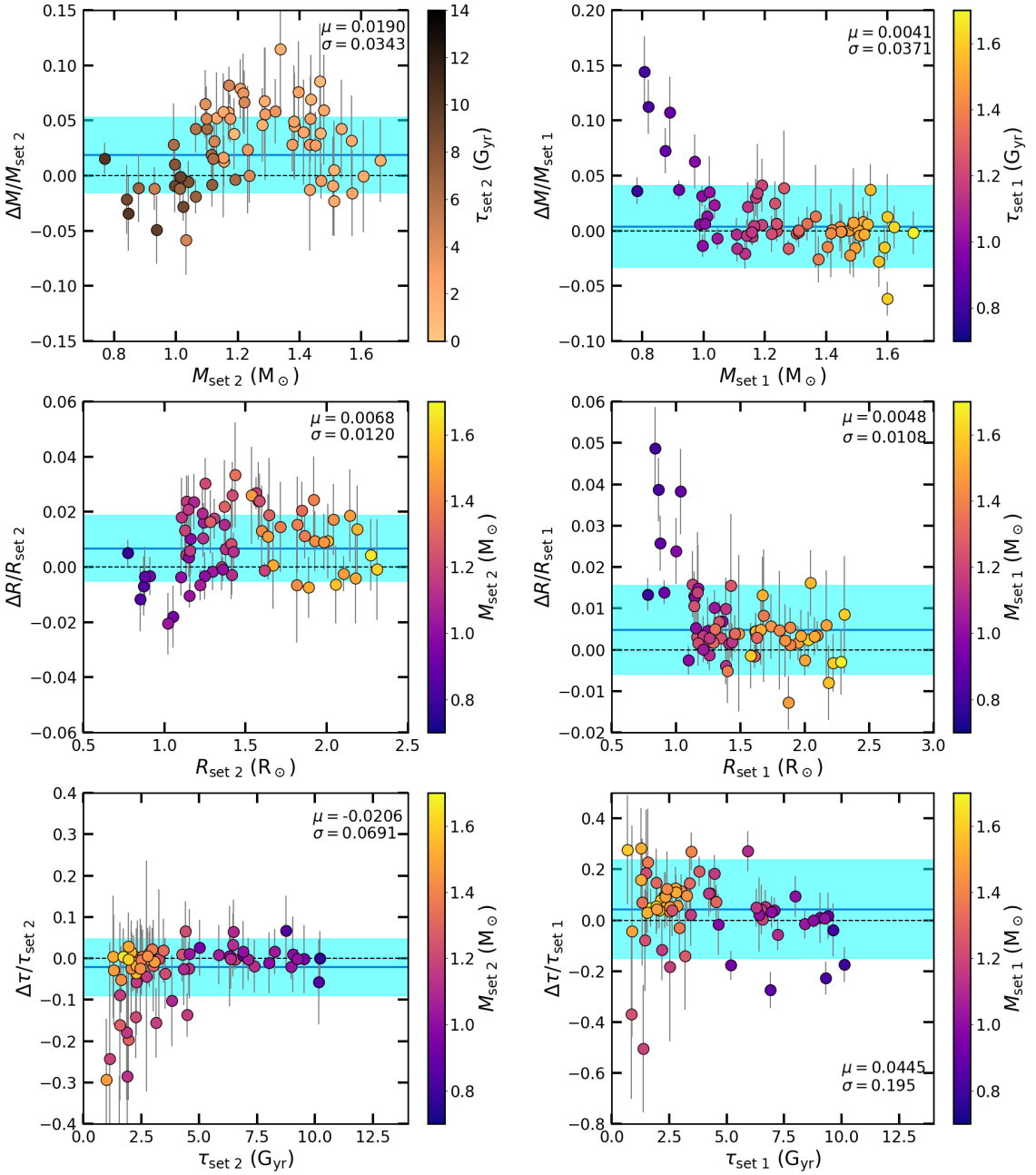

FIGURE 9.2: Comparison of inferred mass (top panels), radius (middle panels), and age (bottom panel), between Set 2 and Set 3 (left panels) and Set 1 and Set 4 (right panel).

have determined using eq. (3.5) and the Gaia data. Even though Gaia provided very high quality data with small uncertainties, the estimation method led to larger errors (due to the combination of errors using the propagation of uncertainties) that did not provide a strong constraint. So to have L as a constraint, it is necessary to have a better way to estimate this parameter with higher precision.

When adding $\nu_{\max}$ as a constraint (comparing sets 1 and 3), we see a significant impact on the inference of the fundamental properties, (right panel of Fig. 9.1). Adding $\nu_{\max}$ as

a constraint leads to higher masses and radii, and lower ages. This is expected since ν_{max} provides an additional constraint on the mass and radius of the stars. With higher masses, we expect lower ages as they evolve faster. Comparing sets 2 and 3 (left panels of Fig. 9.2), we see the same behavior as comparing sets 1 and 3, as expected, because the luminosity has not significant effect on the inference.

Considering the ratios instead of the individual frequencies (comparing sets 1 and 4) has a strong effect on the inference of the stellar properties, as we can see in the right panels of Fig. 9.2. Statistically, there is a significant effect on radius and age, with higher values being preferred when the ratios are used as constraints.

With these tests, I decided not to use the ratios because the optimization test often gave binomial distributions (or trimodal in some cases) regardless of whether we used ν_{max} or L as additional constraints. Without a constraint to avoid this degeneracy, I decided to use individual frequencies with surface corrections. The consideration of ν_{max} adds independent constraint for the sample and is expected to improve the estimation of the fundamental properties. This is the reason why I decided to adopt set 3 of constraints in the following sections.

9.2 Inference of stellar properties

9.2.1 The Sun

The Sun, due to its proximity which has allowed intensive studies, is the target for which we have the most precise observations. Therefore, the use of the degraded Sun from L17 as a benchmark star allows us to test the performance of the optimization procedure with the grids. Moreover, it can be used as a diagnostic for the grids, since if the solar properties are not retrieved, it indicates issues in the inferences of the stellar properties. The results for the Sun are shown in Table 9.1 and in Fig. 9.3 for both grids considering the relative (3:3) or absolute (3:N) weights for the constraints (see chapter 5.4.1 for more details about these weights).

The results are similar for both grids when we use the same weights in the optimization. This is expected because the input physics is the same for the low-mass models. In the models of Grid B, the effect of turbulent mixing is negligible, because the convective envelope already fully homogenizes the region where it should have an impact. For grid A, most of the models include atomic diffusion.

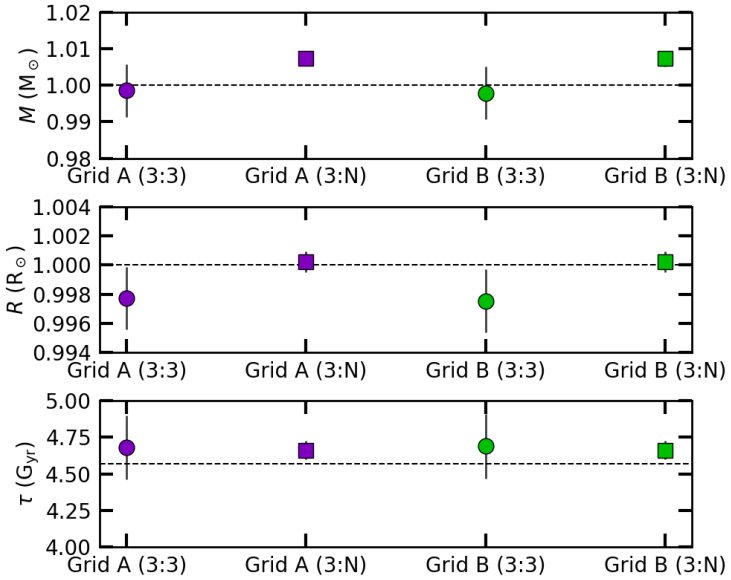

FIGURE 9.3: Optimisation results for the Sun, for mass (top panel), radius (middle panel) and age (bottom panel). The dashed line indicates the real value of the Sun.

TABLE 9.1: Solar properties from the optimization process. Age of the Sun used as reference 4.57 Gyr

		$M(\mathrm{M}_\odot)$	$R(\mathrm{R}_\odot)$	$\tau(\mathrm{G_{yr}})$	$\rho(\mathrm{g\,cm^{-3}})$
Grid A	3:3	0.999 ± 0.007	0.998 ± 0.002	4.68 ± 0.22	1.416 ± 0.001
	3:N	1.007 ± 0.002	1.000 ± 0.001	4.66 ± 0.06	1.418 ± 0.001
Grid B	3:3	0.998 ± 0.007	0.998 ± 0.002	4.69 ± 0.22	1.416 ± 0.001
	3:N	1.007 ± 0.002	1.000 ± 0.001	4.66 ± 0.06	1.418 ± 0.001

Comparing the same grid but different weights in the frequencies, we see with the 3:3 weights that the true properties of the Sun are within the 1σ uncertainties, except for the radius, which is within 2σ. In contrast, for the 3:N weights, only the radius has the true value within 1σ. For the age, it is within 2σ, and for the mass, it is within 4σ. The results are compatible with the current Sun and are in agreement with those obtained by Silva Aguirre et al. (2017).

9.2.2 Grid comparison

To understand the effects of turbulent mixing, I compare the derived properties of the sample presented in chapter 6 between grids A and B. Figures 9.4 show the results for the relative and absolute differences in mass, radius, and age, respectively. From a global perspective, we see that the change in the input physics does not induce a significant bias in the results. However, the mean dispersion for age can reach values of about 7%, and greater than 20% for individual stars. This indicates that changes in the input physics

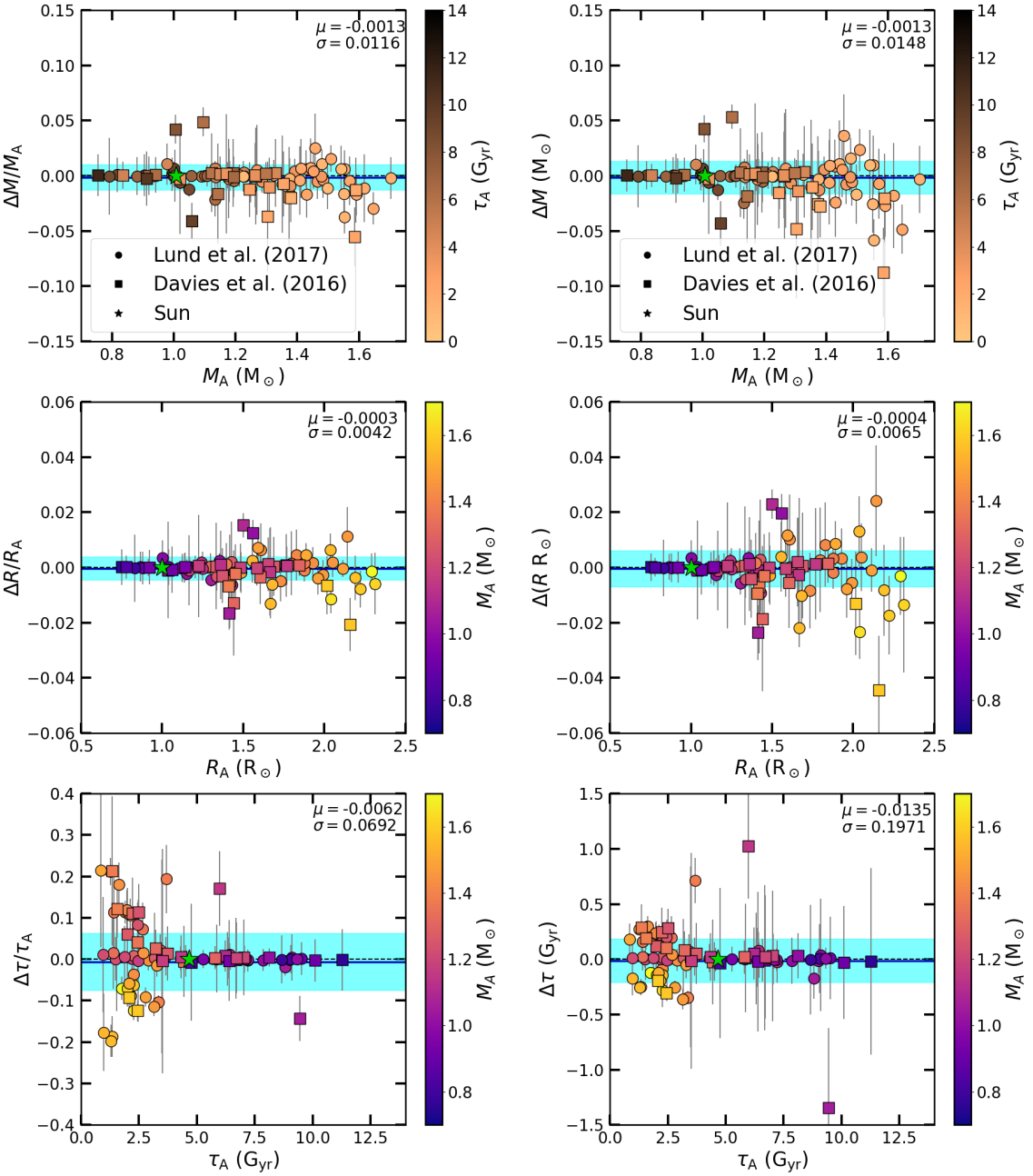

FIGURE 9.4: Relative difference (left panels) and absolute difference (right panels) for mass (top panels), radius (middle panels), and age (bottom panels) between grids A and B, for 3:N weights. The blue solid line indicates the bias, and the blue region is the 1σ standard deviation. Each point is color coded with the corresponding reference age (top panel) and mass (middle and bottom panels).

between grids (in particular the inclusion of turbulent mixing and atomic diffusion) have a strong influence on the age determination for individual stars.

We can see that for all parameters there is an increase in the dispersion of the relative difference (left panel of Fig. 9.4) with stellar mass. This indicates that the changes, we made to the grid, have indeed impacted the more massive stars. For the lower mass

stars, both grids include atomic diffusion and the turbulent mixing prescription has no significant effect since the turbulent mixing effect is within the convective envelope of these stars. For the more massive stars, the majority of Grid A models do not include atomic diffusion. Grid B models are expected to be affected by atomic diffusion in two ways. First, the models have a different surface composition at a given age, which affects the inferred stellar properties through the [Fe/H] constraint. Second, atomic diffusion changes the amount of time the star spends on the main sequence by depleting some of the hydrogen in the core. This can lead to a relative difference for individual stars of more than 5% in mass, 2% in radius, and 20% in age. However, this scatter may be just an artifact (especially for the young stars). To prove this, we can look at the absolute differences (right panels Fig. 9.4). We see that the dispersion in age increases with the stellar mass. For the higher masses, I found differences in age of 0.4 Gyr, which are much larger than those found for the lower masses. This leads to the conclusion that the dispersion in the relative difference needs to be taken with caution.

In Figure 9.4 we find three outliers (KIC 6521045, KIC 8349582, and KIC 10514430) in mass and age. The large difference found for these stars is caused by the way Grid A was computed, since these stars meet the boundary where atomic diffusion is turned off. As I showed in chapter (7.2.1.4), there is a discontinuity in the parameter space where models do and do not include atomic diffusion, leading to a larger scatter in the results. This shows that this usual way of building a grid (i.e., by cutting atomic diffusion at some point in the grid to avoid excessive variation of the surface abundances) can be a source of large uncertainties. The most physically consistent approach is to include atomic diffusion in all stellar models while allowing the other chemical transport mechanisms to compete. In this context, my calibrated turbulent mixing represents indeed a more reliable alternative, although far to be a complete description of the chemical transport mechanisms (as explained in the previous chapter).

9.3 Evaluation of seismic data and comparative analysis

In this section, I perform several tests to assess the robustness of the results. First, I test the effect of using different frequency weights. This was tested on synthetic stars in Cunha et al. (2021), while here I complement it with a test on a sample of observed stars. Second, I investigate how the quality of the seismic data affects the results since the sample was taken from two sources: D16 and L17. Finally, I compare my results with those obtained

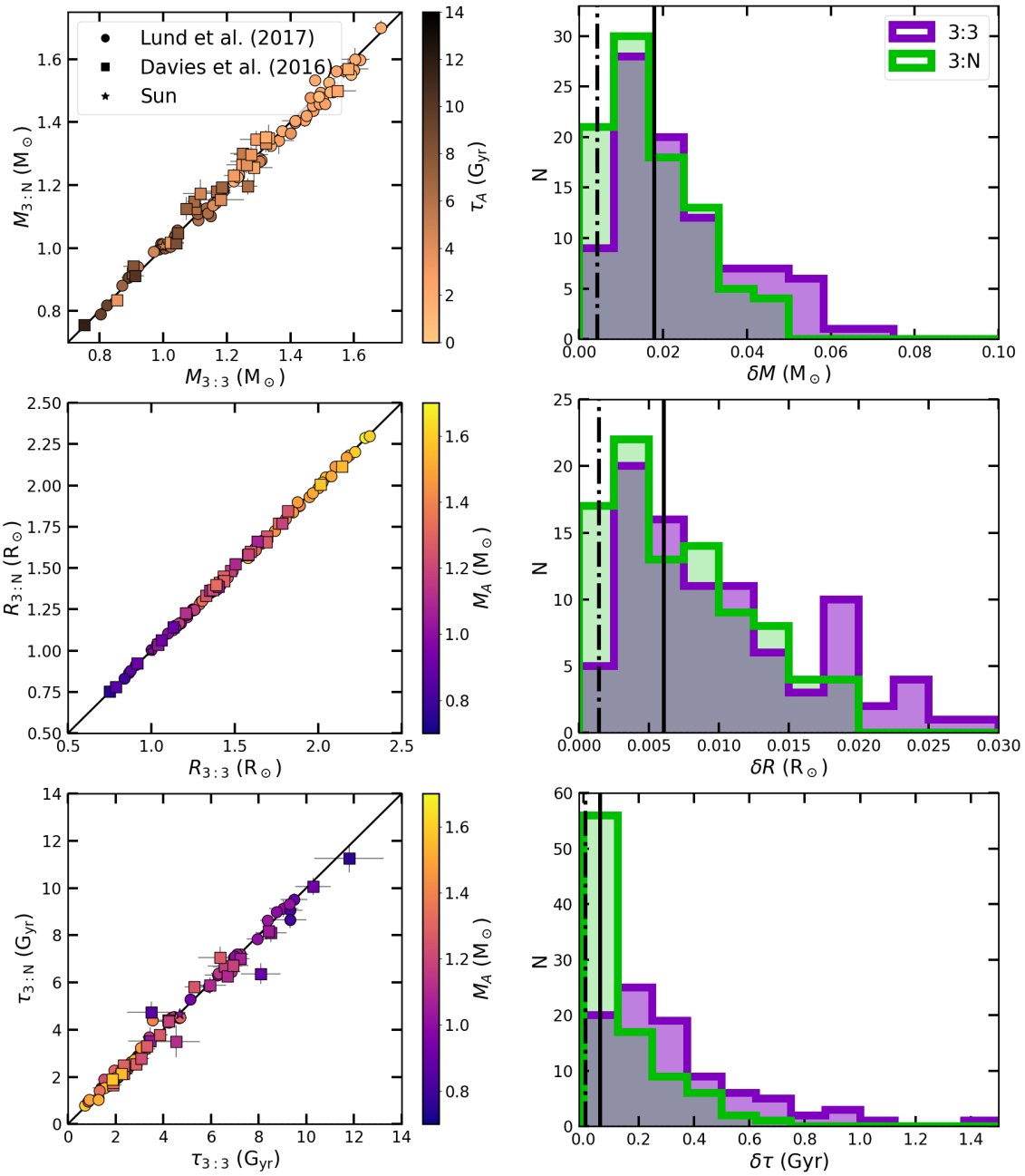

FIGURE 9.5: Left panels: Comparison of the properties inferred when using 3:N or 3:3 weights on the full sample, for mass (top panel), radius (middle panel), and age (bottom panel). Each point is color coded with the corresponding reference age (top panel) and mass (middle and bottom panels). Right panels: Histogram of uncertainties on the inferred parameters for the full sample and two different weights: mass (top panel), radius (middle panel), and age (bottom panel). The vertical dash-dotted line marks the value of the bias and the vertical solid line marks the value of the standard deviation.

for the same stars by different studies, Silva Aguirre et al. (2015) and Silva Aguirre et al. (2017). From here on, I only show the results obtained with Grid B, since the results for both grids are redundant and lead to the same conclusions (see section in the paper in appendix B).

9.3.1 Impact of the weight of the frequencies on the inferences

The use of different weights for the frequencies affects the optimization process. As explained in chapter 5.4.1, the 3:N weighting is statistically more correct, and does not allow the exploration of the full parameter space during optimization compared to the 3:3 weighting. It has to be noticed this is still an open debate in the community to decide which weight should be used during the inference of stellar properties (Cunha et al., 2021).

Figure 9.5 (left panels) shows the comparison between the use of the two weights. The change in weight has a greater effect on the mass and age determination (top and bottom panels). The parameter uncertainties for both cases are presented in the histograms of Fig. 9.5 (right panels) for all stars. I find that the two methods give different uncertainty distributions —in accordance with Cunha et al. (2021)— because the use of 3:3 weights is similar to artificially inflating the uncertainties of the frequencies. I also look at the statistics of the relative differences for the inferred mass, radius, and age between the two cases. There is no significant bias for any of the parameters: all biases are lower than 1%. There is a scatter in the results of 1.8%, 0.6%, and 6.1% for mass, radius, and age, respectively.

9.3.2 Comparison of uncertainties between L17 and D16

In this section, I investigate how the quality of the seismic data affects the results, in particular the relationship between the precision of the frequencies and the inferred fundamental properties of stars. Both L17 and D16 used the same method to identify the seismic modes and ensure their quality. The main difference is that L17 analyzed the stars with the highest signal-to-noise ratios observed by *Kepler*, and therefore the seismic data for this sample are expected to be of better quality.

The histogram of uncertainties for both sets of stars is shown in Fig. 9.6, for mass, radius, and age. The sample from D16 shows indeed a more scattered histogram than the one from L17 and tends to have higher uncertainties.

There are three stars in common between both samples (KIC3632418, KIC9414417, and KIC10963065), which can be used to quantify how the different frequency estimates affect the inference of the properties. Tables 9.2 and 9.3 show the results obtained using the seismic data provided by both references. I used the same $T_{\rm eff}$ and [Fe/H] as constraints, only changing $\nu_{\rm max}$ to be consistent with the individual frequency estimate in each paper. For the three stars in common, the D16 data tend to point toward smaller values of

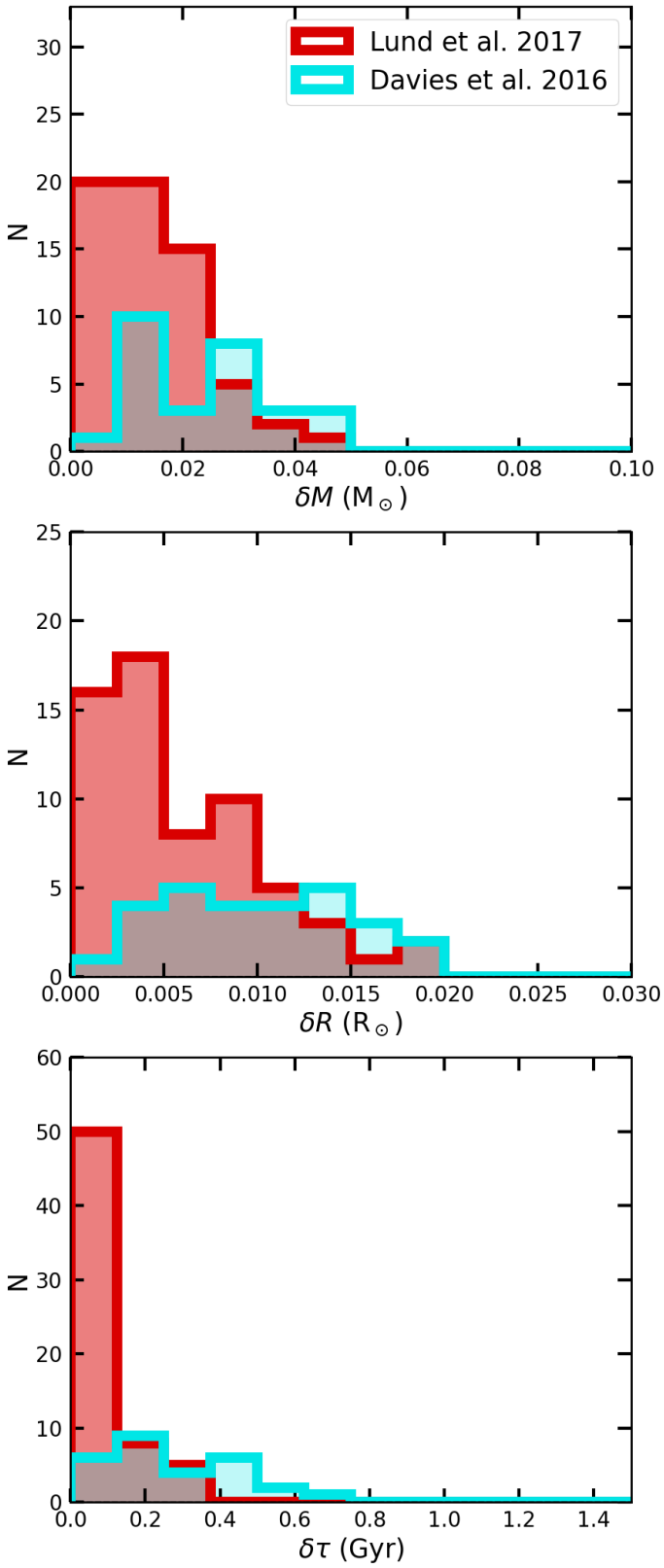

FIGURE 9.6: Histogram of uncertainties on the fundamental properties of stars from both samples using the 3:N weights: mass (top panel), radius (middle panel), and age (bottom panel).

TABLE 9.2: Inferred fundamental properties of the stars common to the D16 and L17 samples using the individual frequencies obtained in the respective works.

KIC		Mass ($M_\odot$)		Radius ($R_\odot$)		Age (G_{yr})	
		D16	L17	D16	L17	D16	L17
3632418	3:3	1.420±0.042	1.471±0.13	1.917±0.020	1.945±0.006	2.795±0.127	2.927±0.121
	3:N	1.405±0.024	1.437±0.017	1.911±0.011	1.931±0.008	2.719±0.051	2.888±0.051
9414417	3:3	1.434±0.052	1.502±0.019	1.935±0.025	1.967±0.009	2.483±0.125	2.571±0.103
	3:N	1.455±0.035	1.478±0.017	1.944±0.016	1.955±0.008	2.380±0.057	2.539±0.048
10963065	3:3	1.11±0.027	1.156±0.009	1.239±0.011	1.258±0.003	4.211±0.319	4.223±0.267
	3:N	1.08±0.013	1.135±0.005	1.237±0.005	1.249±0.002	4.121±0.095	4.307±0.089

TABLE 9.3: Inferred initial chemical composition of the stars common to the D16 and L17 samples using the individual frequencies obtained in the respective works.

KIC		$[M/H]_i$		Y_i	
		D16	L17	D16	L17
3632418	3:3	0.159±0.049	0.171±0.054	0.278±0.024	0.271±0.022
	N:3	0.221±0.230	0.228±0.026	0.290±0.013	0.289±0.014
9414417	3:3	0.151±0.052	0.152±0.068	0.275±0.070	0.276±0.024
	N:3	0.214±0.038	0.217±0.040	0.281±0.016	0.282±0.040
10963065	3:3	0.016±0.060	0.043±0.062	0.262±0.17	0.264±0.017
	N:3	-0.044±0.043	-0.054±0.044	0.258±0.11	0.259±0.011

mass, radius, and age compared to the L17 data. The uncertainties for all the properties are also larger. This suggests that small changes in the estimated individual abundance can have a significant impact on the results derived from them. A surprising result is that lower masses are associated with lower ages for these three stars from the D16 sample. A possible explanation for this correlation is the difference in the initial chemical compositions ($[M/H]_i$ and Y_i). In the case of D16, the best models have slightly lower $[M/H]_i$ and higher Y_i, which explain the lower ages.

The outputted uncertainties are expected to decrease as the quality improves. This hypothesis has been tested on synthetic stars in the work of Cunha et al. (2021), who found that the degraded data gave less accurate results, especially for ages.

9.3.3 Comparison with Silva Aguirre et al. (2015, 2017)

This work provides new parameters for the studied stars. Now, it is important to see how it compares with previous works. I compare the results obtained with Grid B, using the same relative weight (for consistency), with the results of Silva Aguirre et al. (2017), which analyzed the sample of L17, and with Silva Aguirre et al. (2015), which analyzed the sample of D16. It is important to note that in both works, the authors used different pipelines, and the grids were built with different codes and input physics. They also use different optimization codes in each pipeline and use a relative weight for each frequency.

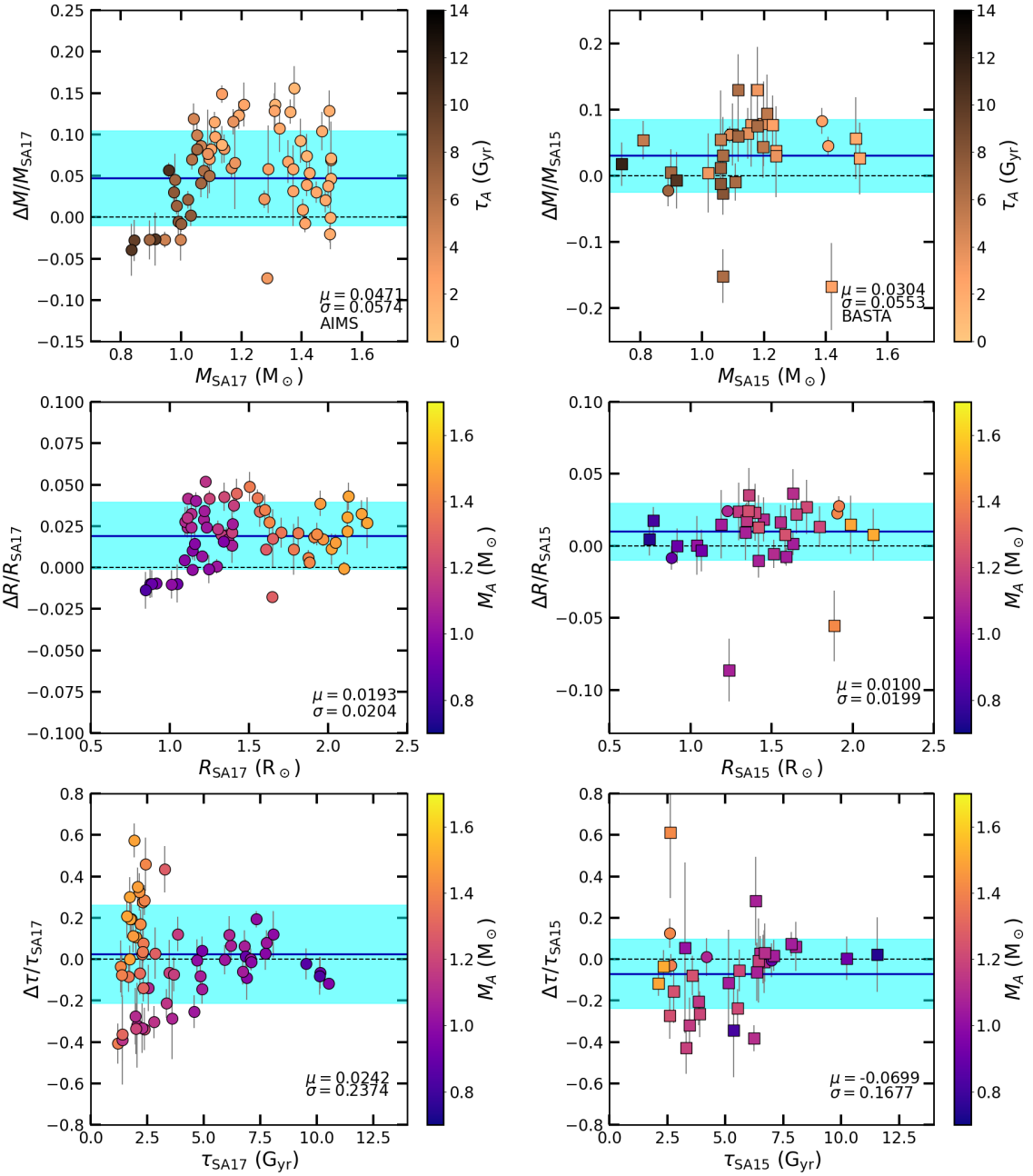

FIGURE 9.7: Left panels: Relative difference for mass (top panel), radius (middle panel), and age (bottom panel) between grid B and the results of Silva Aguirre et al. (2017) for the AIMS pipeline. The blue solid line indicates the bias, and the blue region is the 1σ deviation. Each point is color coded according to the corresponding reference age (top panel) and mass (middle and bottom panels). Right panels: Relative difference for mass (top panel), radius (middle panel), and age (bottom panel) between grid B and Silva Aguirre et al. (2015) results for the BASTA pipeline.

First, let us compare my results with those presented in Silva Aguirre et al. (2017). Here I present the comparison of only one of the seven pipelines used in their paper: AIMS (similar conclusions can be drawn for all the others). The selected pipeline uses the same evolutionary code (MESA) for the model computation and the same optimization

code (AIMS). However, the input physics of the models is different: their stellar models include the Grevesse & Noels (1993) solar mixture, an Eddington gray atmosphere, no atomic diffusion, and a fixed helium enrichment ratio ($\frac{\Delta Y}{\Delta Z} = 2.0$).

A comparison of my results with the AIMS pipeline of Silva Aguirre et al. (2017) is shown in the left panels Fig. 9.7. The results show a bias toward higher values for mass, radius, and age, with a spread of 6%, 2%, and 24%, respectively. However, the relative difference for an individual star can be up to 15% for mass, 5% for radius, and 60% for age.

I also compared the results of Silva Aguirre et al. (2017) with those of grid A. However, there was no significant difference, with a similar bias and scatter as compared to grid B. This suggests that the systematic effects arising from turbulent mixing are overshadowed by the other different ingredients (EOS, opacities, mixture, etc.).

We now compare our results for the stars of D16 with those presented by Silva Aguirre et al. (2015). As in the previous section, the results obtained from all pipelines in their work are similar and led to the same conclusions. Therefore, we present here only a comparison with the BASTA pipeline (right panels of Fig. 9.7).

Our results show a bias toward higher masses and radii, and a bias toward younger ages, with a dispersion of 6%, 2%, and 17% for mass, radius, and age, respectively. For some individual stars, the relative difference can be up to 20% for mass, 10% for radius, and 60% for age.

I also compared the result of grid A with Silva Aguirre et al. (2015). Nevertheless, a similar picture can be drawn as before. It shows again that the systematic uncertainties we observe are due to the different input physics ingredients used in the two papers and are not specifically related to the inclusion of turbulent mixing in Grid B.

Chapter 10

Single-Valued Parameters Method

In chapter 7-9 I show that the turbulent mixing coefficient allows us to include atomic diffusion in the stellar models of F-type and more massive stars, avoiding the unrealistic chemical variations. It can also be easily calibrated to produce the effects of radiative accelerations on the surface abundance of iron when it is depleted from the surface. However, this coefficient is a parameterization of different chemical transport mechanisms, such as rotation-induced mixing, thermohaline convection, and others. Each process has a different efficiency and importance depending on the type of stars and the evolutionary phase. Despite the successful application of a calibrated turbulent diffusion coefficient, proper modeling requires to disentangle the individual processes and their respective efficiency. Moreover, the calibration of turbulent mixing presented before acts on a global scale, affecting every element in the same way. The calibration presented in chapter 8.2 is only valid for predicting the surface abundance of iron. In fact, as we saw in chapter 8.2.2, the calibrated turbulent mixing coefficient ($D_{\mathrm{T,Fe}}$) was not able to reproduce the evolution of all elements, such as Ca, indicating the need to introduce radiative accelerations into the models. However, their full implementation in MESA is computationally expensive and not suitable for building large grids of stellar models.

In this chapter, I study the Single-Valued Parameters (SVP) method for calculating radiative accelerations. I implement it in MESA and compare it with other codes that already include this method such as Cesam2k20. Next, I analyze how this method compares to others, including those with a calibrated turbulent mixing coefficient, in characterizing observed stars. Finally, I assess its effectiveness in reproducing the surface chemical abundances of real stars.

10.1 Implementing SVP method in MESA

The SVP method was developed by G. Alecina and F. LeBlanc (LeBlanc & Alecian, 2004, Alecian & LeBlanc, 2020) and the routines to compute radiative accelerations are publicly available*. These routines require only a few input parameters to compute radiative accelerations, such as T, ρ, P, L, r, m, and X_i the mass faction of the elements being followed. The method is currently only applicable to MS stars (as the tables are only prepared for this stage). The implementation in MESA is not as simple as for turbulent mixing, since the code does not provide an external hook for the radiative accelerations. In this case, it is necessary to modify the MESA source code directly. To minimize code changes, I added a new hook into MESA to be used as an alternative to the default radiative accelerations. The implementation steps are presented in appendix C and a schematic is presented in Fig. C.1.

10.1.1 Influence of the SVP method on stellar models

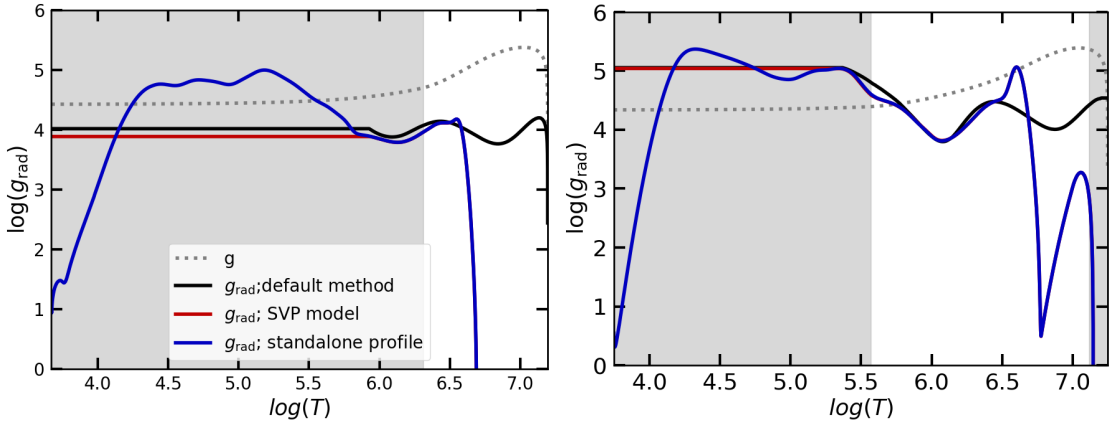

FIGURE 10.1: Radiative accelerations profiles in the left panel for the 1.0 $M_\odot$ model, and in the right panel for the 1.4 $M_\odot$ model. The gray region represents the convective envelope, the gray dashed line is the gravity, and the other lines are the radiative acceleration for iron. The black solid line is the "default model", and the red solid line is the "SVP model", the blue line is the "standalone profile".

The SVP method is provided with a standalone code that can compute the radiative accelerations of a given model and they provide several models from Cesam2k20 that can be used as examples to compute radiative accelerations. I compare the different radiative profiles for a solar and a 1.4 $M_\odot$ model computed with different methods:

- **Default model:** Computed with MESA using the Seaton (2005) interpolation method.

*https://gradsvp.obspm.fr/index.html

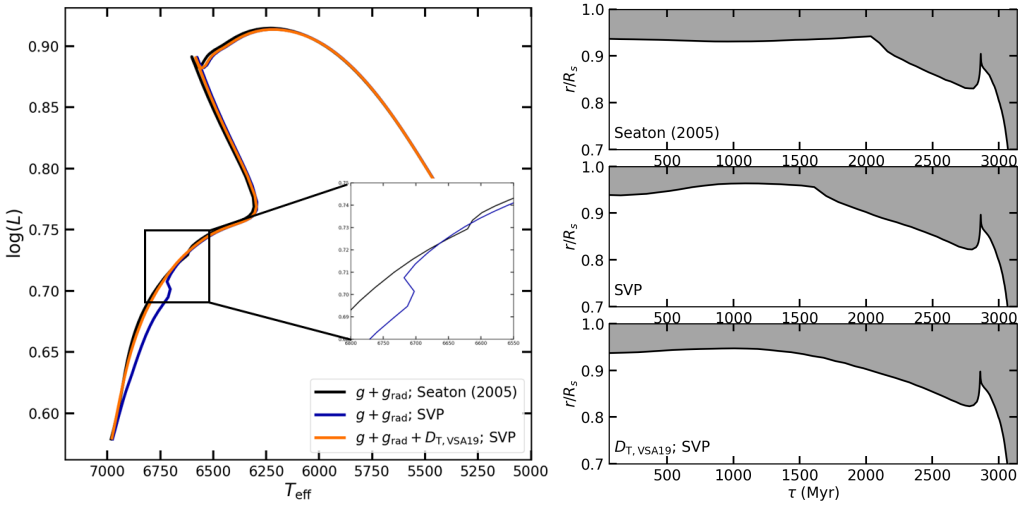

FIGURE 10.2: The left panel is the HR diagram of the evolution of different models of 1.4 $M_\odot$, the black line represents the evolution of a model including radiative accelerations computed with the "default" method, the blue line a model computed with the SVP method, and the orange line model computed with the SVP method and the turbulent mixing coefficient calibrated by VSA19. The right panels show the evolution of the convective envelope in the same models.

- **SVP model:** Computed with MESA using the implemented SVP method.
- **Standalone profile:** Cesam2k20 models using the SVP method provided by the standalone code.

The different radiative acceleration profiles for iron are shown in Fig. 10.1 for the 1.0 $M_\odot$ and 1.4 $M_\odot$ models. Inside the convective envelope, MESA sets the radiative accelerations uniform as we see for the "default model" and "SVP model". It has no impact because the chemical composition is fully homogenized in convective envelopes. The same profile is obtained with the "standalone" and "SVP" models, overlapping each other in the radiative region. Radiative accelerations in both cases are compatible, which indicates that SVP is correctly implemented in MESA. If we compare the radiative accelerations from the "default model" with the "SVP model" they present similar behaviors with a smaller difference, except at higher temperatures. The SVP method is not prepared for the very high-temperature regime ($\log(T) > 6.5$) at the central regions of the stars. For this case, SVP forces the radiative accelerations to zero at the central zone because this does not affect the global stellar evolution. This comparison shows that MESA is ready to calculate radiative accelerations with the SVP method.

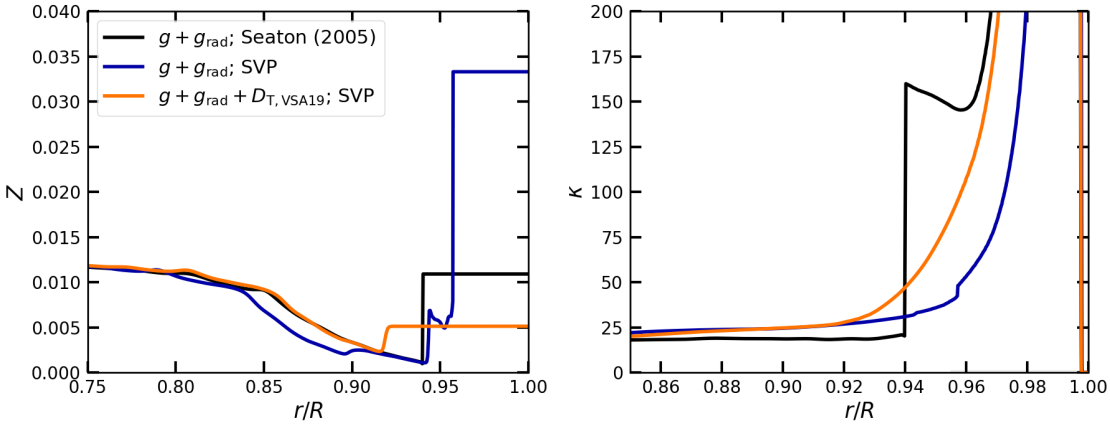

FIGURE 10.3: Internal profiles of the 1.4 $M_\odot$ model in the discontinuity point. The left panel is the heavy element profile and the right panel is the opacity profile. the color code is the same as in Fig. 10.2.

10.1.2 Numerical instabilities induced by radiative accelerations

When stellar models have small convective envelopes (F-type and higher stellar mass), the efficiency of atomic diffusion increases, and the heavy elements are transported faster in the outer layers. When turbulent mixing or undershooting are neglected, the inclusion of radiative accelerations can lead to numerical instabilities. These problems are amplified when the SVP approximation is used. Figure 10.2 shows the evolution of 1.4 $M_\odot$ models with radiative accelerations in the HR diagram (left panel) and the evolution of the size of the convective envelope (right panel). Models with radiative accelerations without turbulent mixing show an unexpected change in the evolution in the HR diagram, corresponding to an abrupt change in the size of the convective envelope (around 2 Gyr for the "default model" and 1.500 Gyr for the "SVP model").

These changes occur because of an increase of opacity induced by the accumulation of iron (and nickel for the default model) due to radiative accelerations. In Figure 10.3, the abundance profiles are shown at the discontinuity in the HR diagram. For the "SVP model", the perturbation occurs in the abundance profile, around 0.95 of the radius. For the "default model", there is an abrupt discontinuity in the opacity profile. As the convective envelope changes during the evolution, it encounters these perturbations, which create a change in $T_{\rm eff}$ and L, hence in the HR diagram.

These perturbations cause numerical problems that can lead to the code not to run or to a non-physical evolution. The instabilities increase at larger masses, as seen in Fig. 10.4 for a 1.6 $M_\odot$ model. The evolution of Z at the surface is very unstable when radiative accelerations are taken into account. This numerical instability is induced by the very

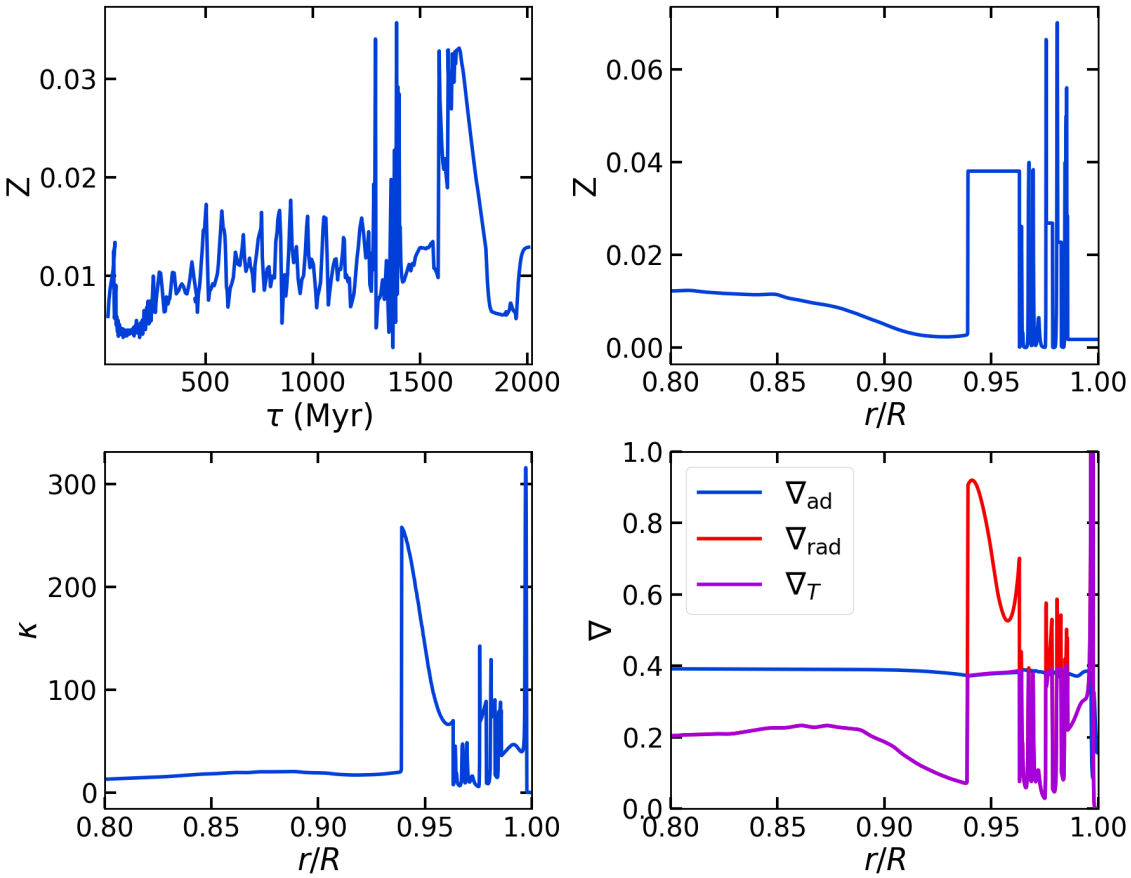

FIGURE 10.4: Evolution and profiles of a 1.6 $M_\odot$ model. The upper left panel shows the surface evolution of the heavier elements, the upper right panel the heavier element profile, the lower left panel the opacity profile, and the lower right panel the profile of the radiative (red), adiabatic (blue), and thermal (purple) gradients.

efficient transport of iron (and nickel) at the bottom of the convective envelope. Solving these instabilities would require setting a very small time step. This leads to an unstable evolution of the models up to a point when the models with higher masses cannot converge anymore. Models with higher masses cannot converge during the main sequence if radiative accelerations are taken into account, preventing the computation of a full evolution.

The only way of preventing these instabilities is to include extra mixing (as previously suggested by Théado et al. 2009, Deal et al. 2018, and references therein) which is nevertheless required to explain the surface abundances of these stars. As we can see in Figs. 10.2 and 10.3, adding the VSA19 calibration of the turbulent mixing prescription stabilizes the evolution. It also allows to extend the use of radiative accelerations to higher masses, avoiding the numerical problems.

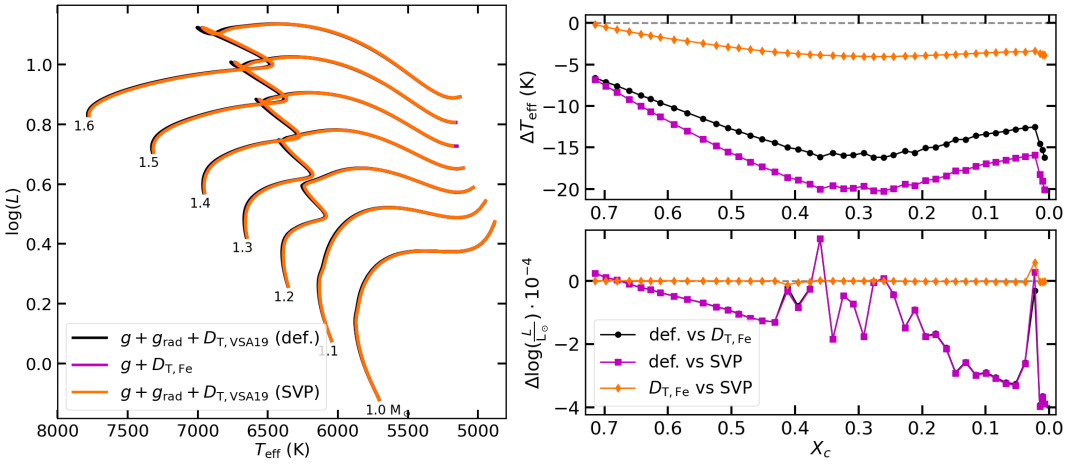

FIGURE 10.5: The left panel shows the HR diagram of different evolutionary tracks for the different radiative accelerations methods - the default method (black line), my calibrated turbulent mixing (purple line), and the SVP method (orange line). The right panel shows the difference for the 1.4 $M_\odot$ models for the different methods, for effective temperature (top panel) and luminosity (bottom panel) as a function of central hydrogen mass fraction. The black circles are the differences between the default method and the calibrated turbulent mixing, the purple squares are the differences between the default method and the SVP method, and the orange diamonds are the differences between our calibrated turbulent mixing coefficient ($D_{\mathrm{T,Fe}}$) and the SVP method.

10.1.3 Evolution of stellar models with the SVP method

Let us now compare the differences between calculating radiative accelerations using the default or SVP method, and how they perform against the turbulent mixing calibration presented in chapter 8.2, which accounts for the effect of radiative accelerations on the surface abundance of iron.

Figure 10.5 shows the evolution of models including different ways of accounting for radiative accelerations in an HR diagram (left panel). The right panel shows the difference between T_{eff} and $\log(L)$ for 1.4 $M_\odot$ model using the default method (as reference for black and purple circles) and the calibrated turbulent mixing as (reference for the orange circles). The three types of models almost overlap in the HR diagram, which indicates that the processes do not have a significant effect on this aspect of the stellar evolution. This is supported by the fact that the differences shown in the HR diagram are smaller than the uncertainties on T_{eff} and L expected from observations.

Despite showing negligible differences in the HR diagram, there are two main differences between the methods. The first one is the computational cost which can be very different from one method to another. The computational times for running a model from the ZAMS to the end of the SG stage are presented in table 10.1. The times given are an average of all stellar tracks for each treatment of the transport. The calculation is done

TABLE 10.1: The computation time of stellar models in MESA from ZAMS to the bottom of RGB, taking into account g gravitational settling, radiative accelerations ($g_{\rm rad}$), and turbulent mixing with our calibration ($D_{\rm T,Fe}$) or VSA19 calibration ($D_{\rm T,VSA19}$).

Model Physics	g	$g + g_{\rm rad} + D_{\rm T,VSA19}$	$g + D_{\rm T,Fe}$ (Moedas et al., 2022)	$g + g_{\rm rad} + D_{\rm T,VSA19}$ (SVP)	$g + g_{\rm rad} + D_{\rm T,VSA19}$ (Mombarg et al., 2022)
Time (min)	11	365	13	19	66

on the same computer with the same number of cores (in this case 5). As we can see, the default method available in MESA is very expensive, reaching almost 6 hours of computation. If we want to calculate the most accurate models with radiative accelerations, the default calculation is preferable. However, this is only feasible when computing a single or a small number of models. For large grids, such as Grids B and C, which have about 4356 evolutionary tracks, the computation time is predicted to be around 3 years. This computation time is not practical and does not take into account the grid diagnostic tests that need to be performed. Currently, an efficient computation of this process is preferable, even at the cost of a small loss of accuracy. In this case, using the SVP method and/or the calibrated turbulent mixing method, grids of the same size can be computed in about 2 months.

The second major difference between the methods is their effect on chemical evolution. Figure 10.6 shows the surface abundance evolution of several elements using the different treatments of the transport. For iron, all methods reproduce similar evolution. For the other elements, the SVP method predicts consistent evolution with the default method. In the case of calcium, my calibrated turbulent mixing cannot reproduce the effects of radiative acceleration, while the SVP method predicts a much closer evolution. This indicates that SVP allows for a better reproduction of the effects of radiative accelerations for each element in the stellar models compared to the calibration presented in chapter 8.2, with a more efficient computation than the default method available in MESA.

More recently, a new method for computing the Rosseland mean opacity and radiative accelerations from monochromatic opacity by Mombarg et al. (2022) has been implemented in a newer version of MESA (r23.05.1, Jermyn et al. 2023). This method, using the same specification, is about 6 times faster than the default method for calculating radiative accelerations. It decreases the estimated time for the grid calculation from 3 years to 6 months. In the following I used the SVP method I implemented to compute radiative accelerations, first to maintain consistency between versions of MESA through my work, and second due to the efficiency of the method. In addition, I want to test the performance

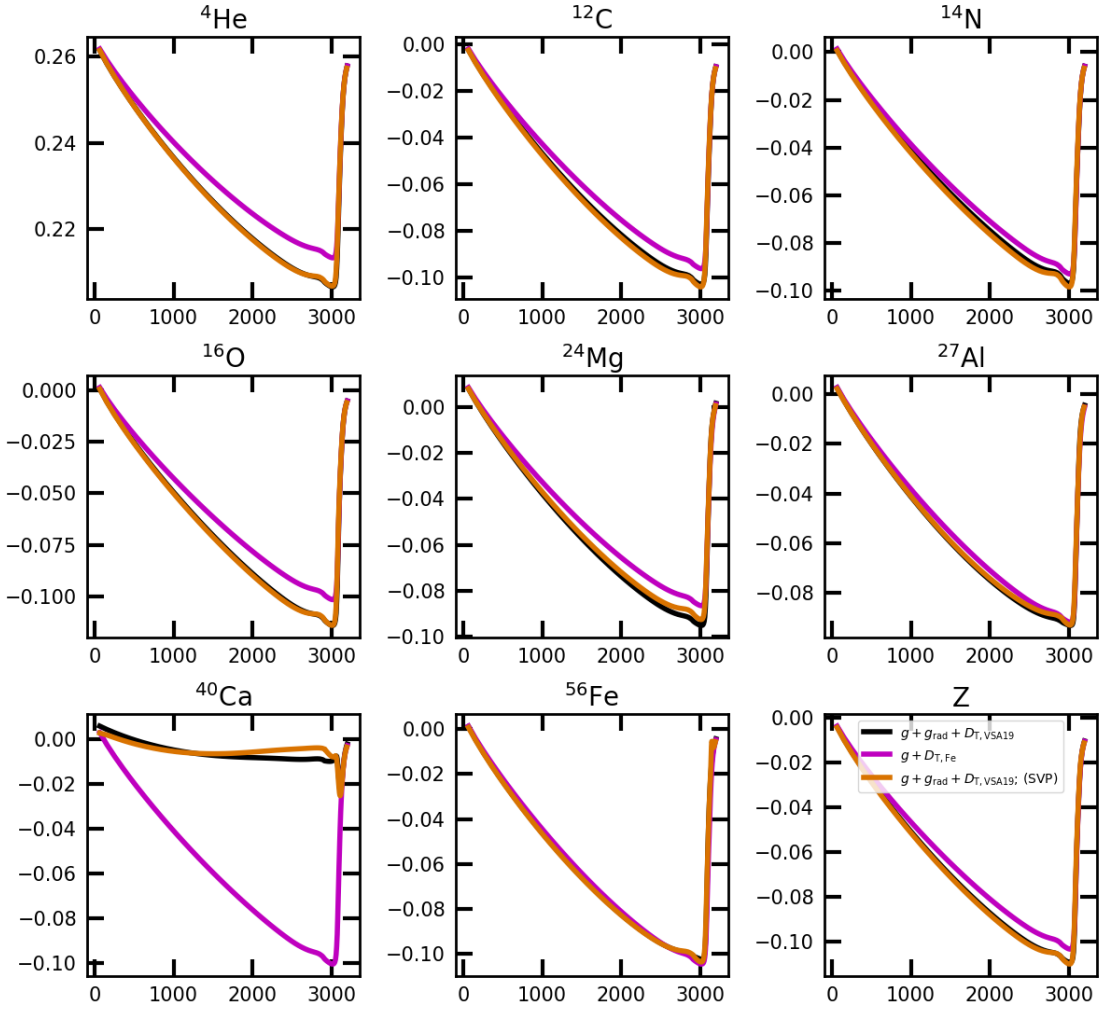

FIGURE 10.6: Same as Fig. 8.6, adding the radiative accelerations calculated with the SVP method (orange line).

of the SVP method for the characterization of stars, since it is a method that can be easily implemented in stellar evolution codes.

10.2 Sample characterization

In this section, I compare the inferred fundamental properties of the sample considered in this manuscript (L17, D16, and the Sun presented in chapter 6) using the different grids I developed. Here I introduce a new Grid C which includes the SVP method. I compare this new grid with the previously analyzed grids A and B. The properties of the grids are presented in detail in chapter 5.2.2.

10.2.1 Grid C vs Grid A

I first compare the results obtained with grids A and C, and the relative and absolute differences obtained for the stellar properties are shown in Fig. 10.7. The difference between the inferences shows a smaller bias, as we saw in chapter 9.2.2, but a higher dispersion of about 2.6%, 0.9%, and 7.2% for mass, radius, and age.

Looking at the higher masses, there is a larger scatter in the result, similar to the comparison of the results obtained with grids A and B. This confirms that neglecting atomic diffusion is the main source of systematics. Looking more closely at the lower mass stars ($< 1.2\,M_{\odot}$), there is a larger scatter compared to the more massive stars in the sample. This scatter is even larger if we look at the absolute differences (lower right panel of Fig. 10.8). This is due to the use of different prescriptions for turbulent mixing. For the more massive stars, the turbulent mixing prescription is the same in both grids, while for the low-mass stars is calibrated differently. In fact grid C in this regime includes the prescription from Proffitt & Michaud (1991) calibrated to reproduce the lithium abundance at the surface of the Sun. The scatter we see is because of not reproducing the surface abundance of lithium in the models. This can introduce relative uncertainties of up to 8%, 3%, and 10% for the determination of mass, radius, and age, respectively.

10.2.2 Grid C vs Grid B

The comparison of the estimated mass, radius, and age using grids B and C for the full sample is shown in Fig. 10.8 for absolute (3:N) weight in the frequencies. Overall, the results show very small biases (less than 1% for each parameter) and a scatter of 2%, 0.7%, and 5% for mass, radius, and age, respectively. This indicates that there is no significant effect of modeling the effect of radiative accelerations using a calibrated turbulent mixing coefficient or the SVP method for the inference of the fundamental properties of stars. I also find a large scatter for the lower mass stars for the same reasons as the previous section (different turbulent mixing prescription)

In summary, this indicates that my calibrated turbulent mixing reproduces well the global effects of radiative accelerations on the iron surface abundance in the stellar models.

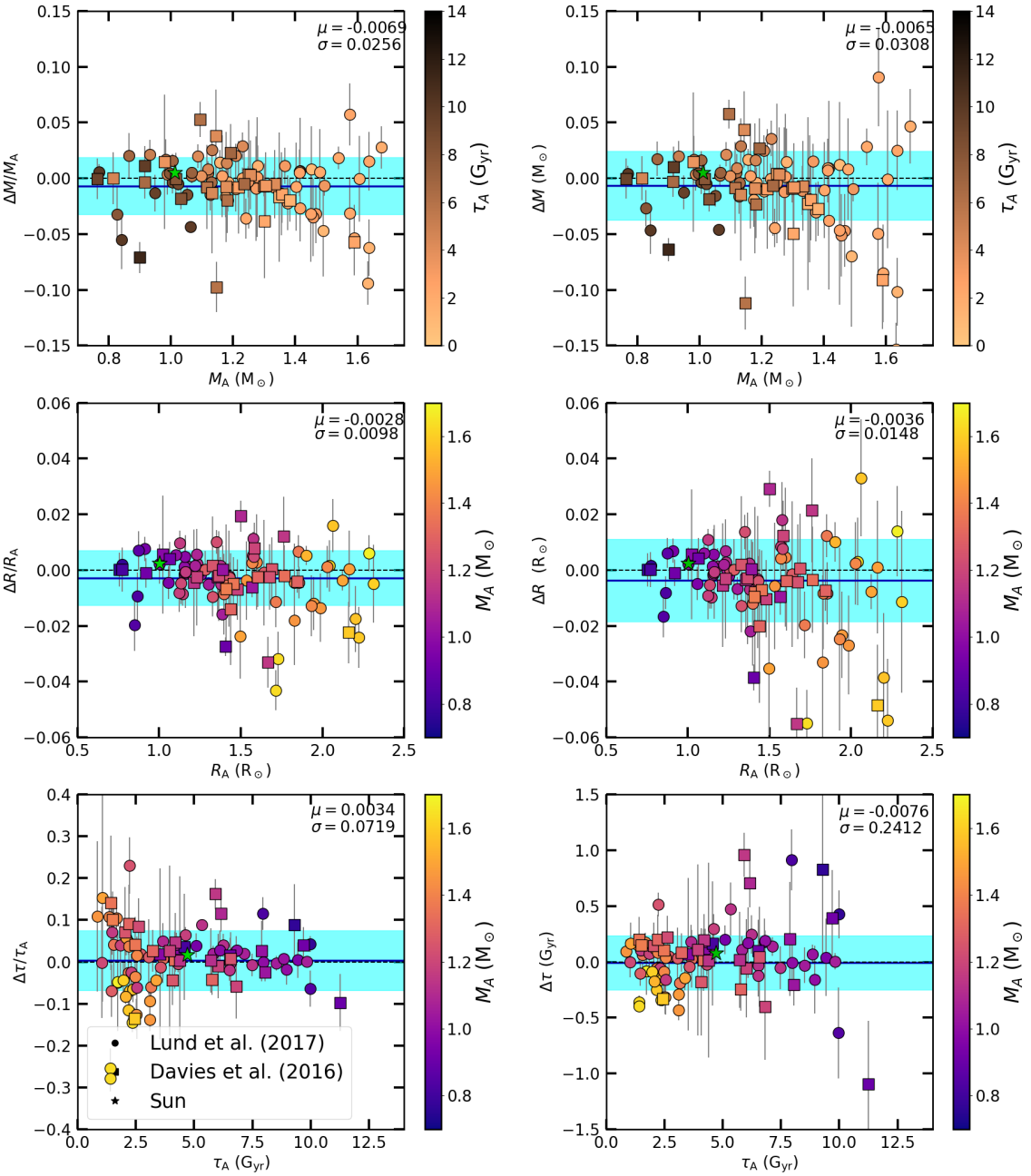

FIGURE 10.7: Relative difference (left panels) and absolute difference (right panels) for mass (top panels), radius (middle panels), and age (bottom panels) between grids A and C, for 3:N weights. The blue solid line indicates the bias, and the blue region is the standard deviation. Each point is color-coded with the corresponding reference age (top panel) and mass (middle and bottom panels).

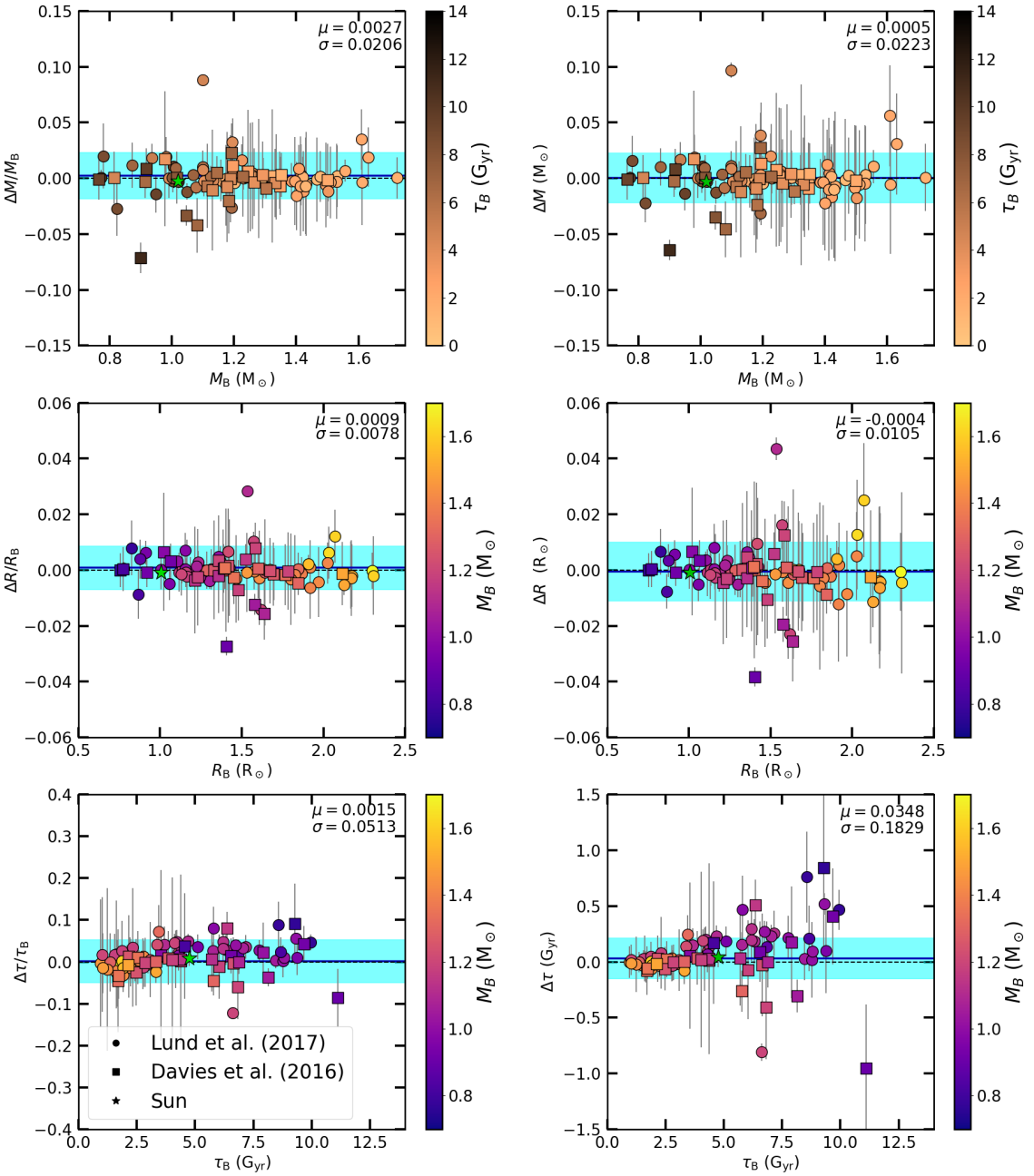

FIGURE 10.8: Relative difference (left panels) and absolute difference (right panels) for mass (top panels), radius (middle panels), and age (bottom panels) between grids B and C, for 3:N weights. The blue solid line indicates the bias, and the blue region is the standard deviation. Each point is color-coded with the corresponding reference age (top panel) and mass (middle and bottom panels).

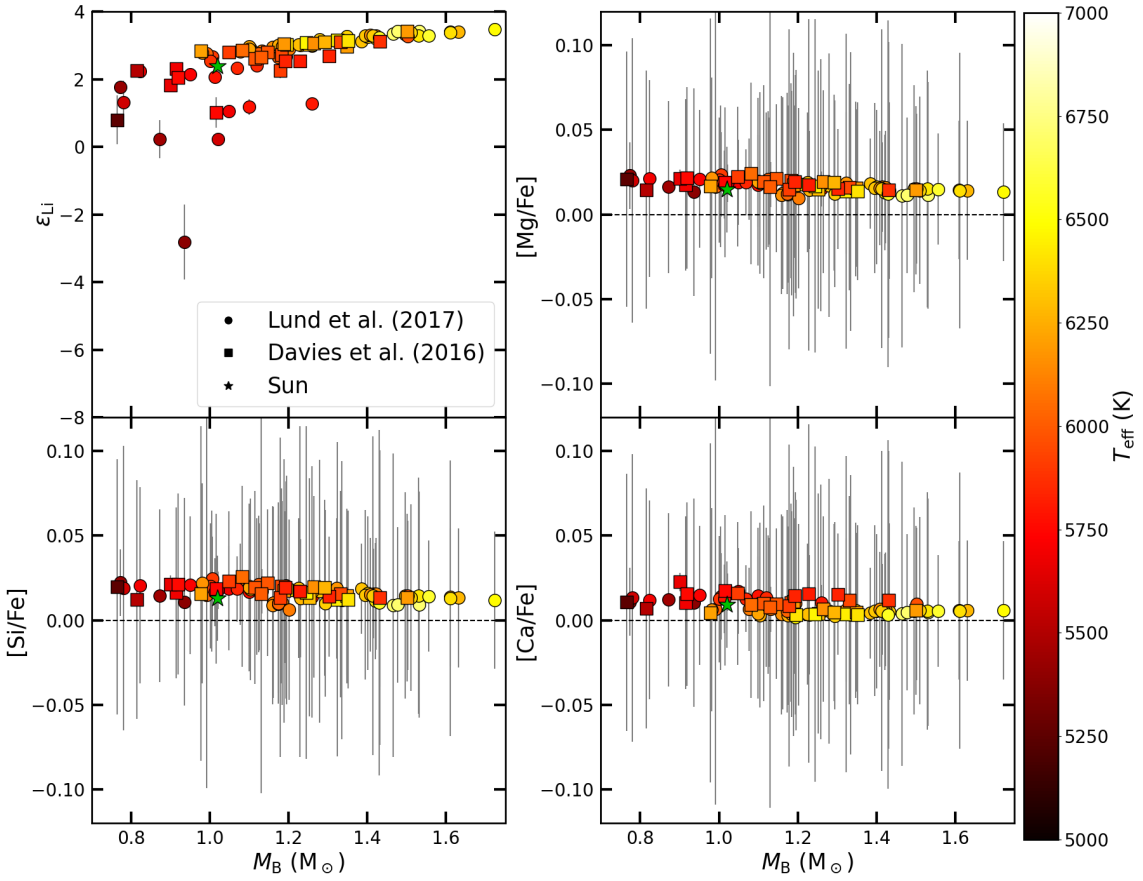

FIGURE 10.9: Surface abundances inferred for the sample of stars using Grid B. The upper left panel shows the predicted lithium surface abundance, the upper right shows the surface abundance of magnesium relative to iron, the lower left shows the surface abundance of silicon relative to iron, and the lower right shows the surface abundance of calcium relative to iron.

10.3 Stellar chemical composition

The main effect of using either the SVP method or a turbulent mixing calibration to model radiative accelerations is visible with the evolution of elements other than iron. The chemical abundances inferred from the different grids are hence not the same. Let's focus only on the surface abundances determined with grids B and C since these two grids are the ones including a more accurate modeling of the transport of chemical elements.

Figures 10.9 and 10.10 show the derived surface abundances of lithium, magnesium, silicon, and calcium with grids B and C, respectively. In the case of magnesium and silicon, both show the same behavior, with the surface abundance of this element being slightly higher than that of the iron one. In the case of lithium, there is a greater depletion for lower-mass stars for Grid C. It is expected that lower-mass MS stars have lower lithium values as the convective zone extends into deeper and hotter regions where this element is

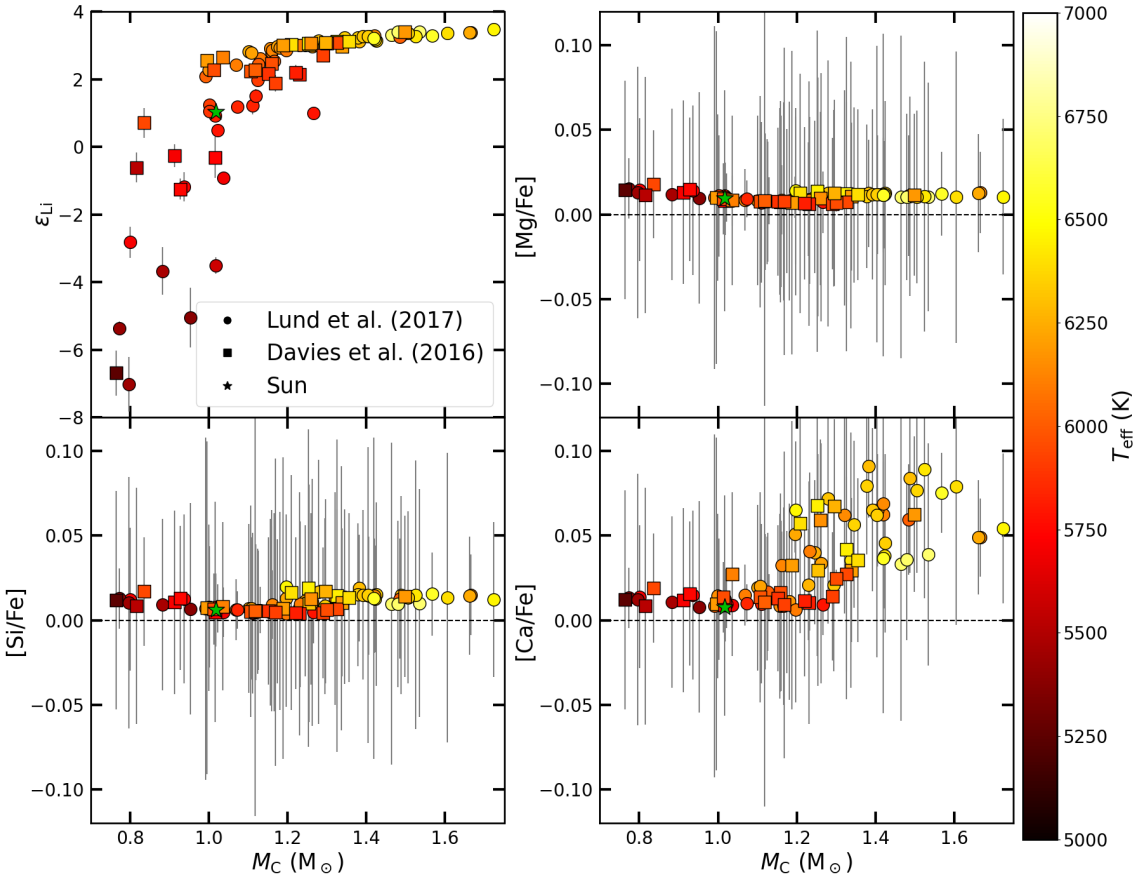

FIGURE 10.10: The same as Fig. 10.9 but for the abundances inferred with Grid C.

destroyed by proton capture. For Grid C, the introduction of a different turbulent mixing prescription and calibration (for the lower masses) extends the fully homogenized zone into deeper regions, allowing higher values of depletion. The case of calcium is different for the higher masses of the sample, due to the inclusion of turbulent mixing and the SVP method. For these stars, turbulent mixing reaches a region where there is an accumulation of this element when considering individual radiative accelerations. By including the SVP method, there is an increase in the surface abundance of this element with stellar mass in F-type stars, which does not occur when my calibrated turbulent mixing is used (because this way of modeling the surface abundances cannot produce accumulation, see chapter 8.2.2).

Morel et al. (2021) (hereafter M21) provides the surface abundances of carbon, magnesium, aluminum, sodium, silicon, calcium, and lithium for 13 stars, 12 of which are part of our sample. This allows me to compare these observed abundances with the inferred ones from the grids.

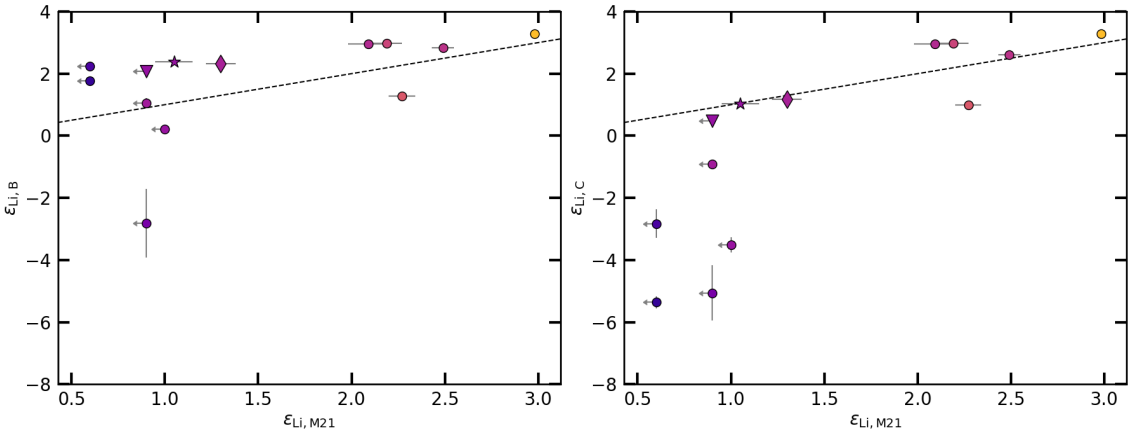

FIGURE 10.11: Estimated lithium abundances versus observed abundances from M21. The left panel shows the inferred abundances using Grid B and the right panel shows the inferred abundances using Grid C. The diamond and down triangle symbols refer to the 16 Cyg A and B stars (KIC 12069424 and KIC 12069449), respectively, and the star represents the Sun. The arrows pointing to the left indicate upper limits. The dashed line indicates where the observed value is equal to the estimated value.

10.3.1 Lithium

Lithium is an important element for calibrating the extra mixing below the convective envelope because it is easily destroyed at low temperatures, providing strong constraints on the efficiency of the transport. For a standard solar model without extra mixing, the estimated abundance of lithium is much higher than the one determined from observations. The lithium abundances estimated using my turbulent mixing model are shown in the left panel of Fig. 10.11. Most of the low-mass stars have higher lithium abundances than observed, indicating that the mixing in these models is not efficient enough to transport lithium into deeper layers where it is destroyed. The models with my calibrated turbulent mixing coefficient ($D_{\mathrm{T,Fe}}$) cannot reproduce the observed abundances of lithium.

As expected, when turbulent mixing is calibrated to reproduce the lithium abundance of the Sun (grid C, right panel of Fig. 10.11), the abundances of solar analogs are in better agreement with the determination of M21. This is confirmed with 16 Cyg A and B (KIC 12069424 and KIC 12069449), two solar-type stars that are usually used to check the quality of the solar-analogues models. For 16 Cyg A, the inferred value is within 2σ of the observed one, while for 16 Cyg B is in agreement with the observation within 1σ. It is important to keep in mind that the calibration of turbulent mixing for grid C was done with one star (the Sun) which is not sufficient since the mixing efficiency may be different for each star. Moreover, additional events may affect the abundance of lithium such as

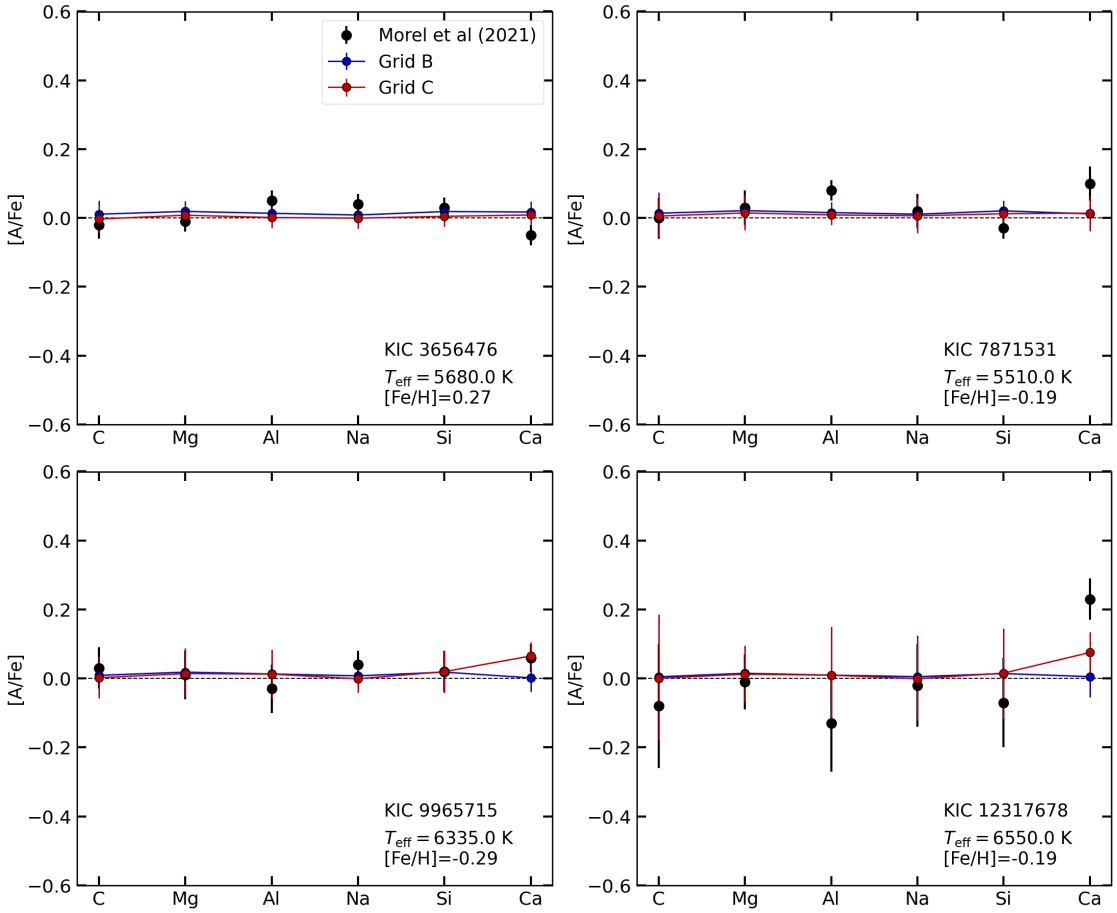

FIGURE 10.12: Comparison of the estimated and observed abundances of four stars from the M21 sample.

the accretion of planetary matter during its evolution (e.g. Deal et al. 2015 and references therein)

For the higher mass stars, there is no difference in the predictions because the radiative acceleration does not affect this element. Also, the difference in turbulent mixing efficiencies between the two grids is not large enough to produce a significant difference in the lithium surface abundances.

10.3.2 Inference of the stellar abundances

For the other elements, Fig. 10.12 shows the observed and predicted abundances (with grids B and C) for carbon, magnesium, aluminum, sodium, silicon, and calcium for four stars. These four stars summarize the different results we can obtain. For the G-type stars (the upper panels), the predicted surface abundance of KIC 3656476 (left panel) is consistent with the observations for all elements. For KIC 7871531 (right panel) all predicted

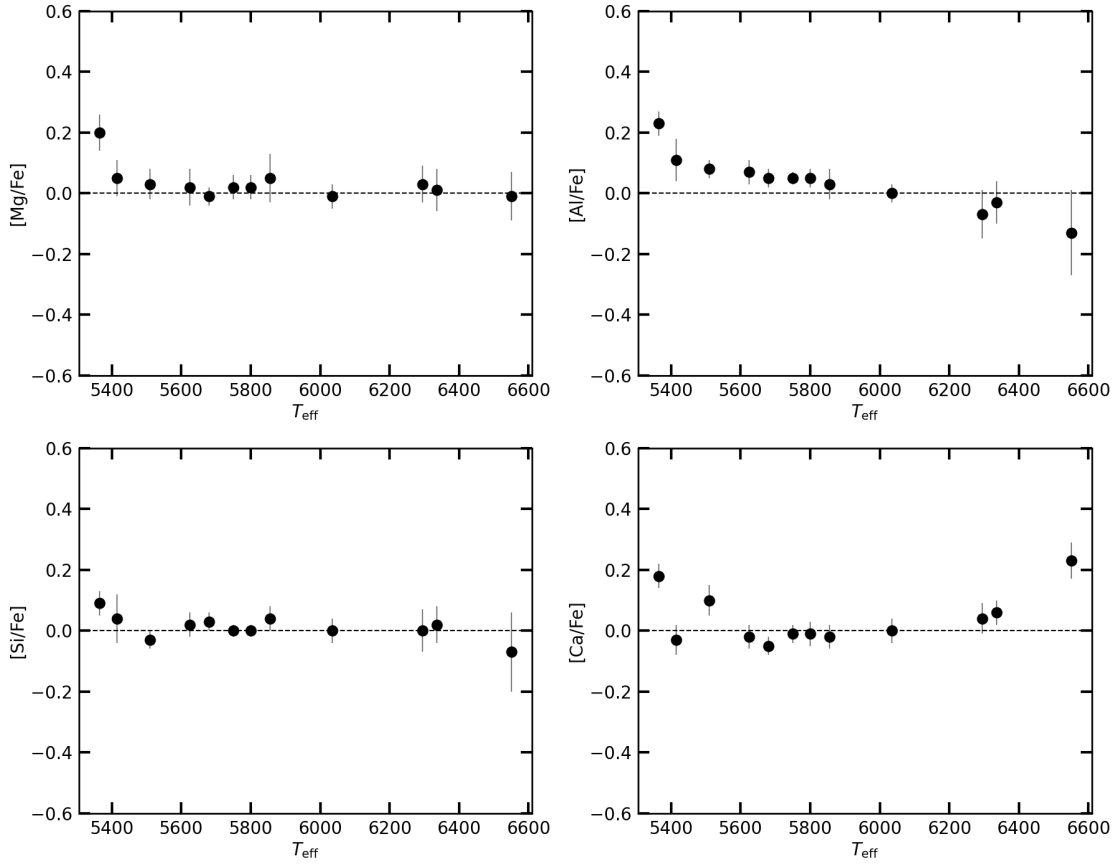

FIGURE 10.13: The M21 abundance of magnesium (top left panel), aluminum (top right panel), silicon (bottom left panel), and calcium (bottom right panel) as a function of effective temperature.

abundances are in agreement with the observation except for Al and Ca. This could indicate a slight α enrichment for this star, although there is no enrichment in Mg and Si (also α elements). If this is an α-enriched star, my models are expected to not be able to reproduce these abundances as I do not change the element mixture (I only consider the solar one). For these two stars, there is no difference between the predictions obtained with grid B and C, as expected for G-type stars.

For the two F-type stars (lower panels), both grids yield similar abundances, except for calcium, which is higher when the SVP method is taken into account (Grid C). Regarding the comparison with observations, for KIC 12317678 (right panel), the predicted surface abundances are in agreement with the observed ones, except for calcium. This star shows a high calcium abundance, and SVP models can predict abundances closer than turbulent mixing models. However, it is not sufficient to explain the observed surface abundance for this star. This indicates that either the efficiency of the extra mixing is too low (for calcium) in grid C or the star is enhanced in calcium compared to the Sun.

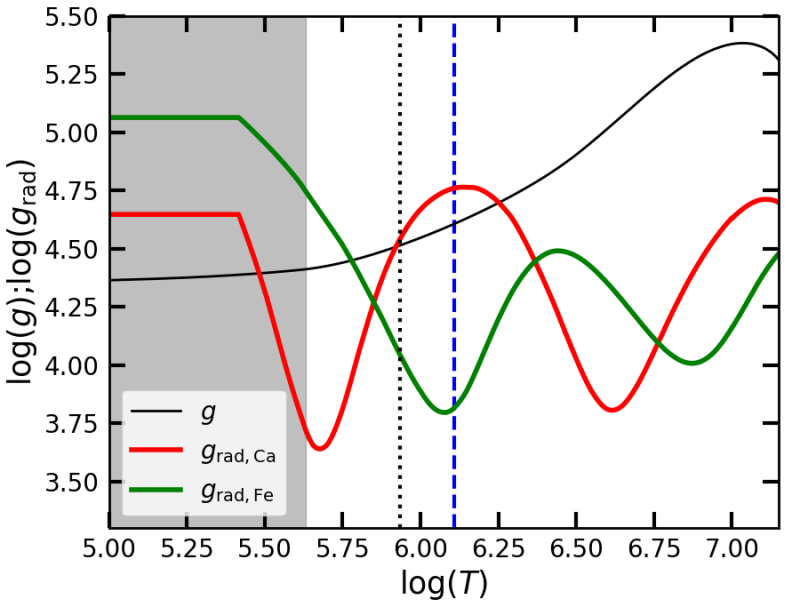

FIGURE 10.14: The profile for gravity (black solid line) and radiative accelerations for Ca (red solid line) and Fe (green solid line) for a 1.4 $M_\odot$ model. The gray region is the convective envelope. The dashed line indicates the reference envelope mass used for the turbulent mixing calibration from VSA19 and the dashed blue line is the reference envelope mass ($\Delta M_0 = 2.4 \cdot 10^{-3}$ $M_\odot$) for the maximum accumulation of Ca at the surface of the model.

It is important to note that for most of the elements, increasing the efficiency of the extra mixing decreases the impact of atomic diffusion. However, calcium is an exception in this case. Figure 10.14 shows the radiative profiles of iron and calcium. In the case of calcium, enhancing the efficiency of turbulent mixing (by increasing the ΔM_0), the mixing reaches a point where the radiative accelerations are higher than gravity. The maximum effects of radiative accelerations are observed around a reference mass envelope of $\Delta M_0 = 2.4 \cdot 10^{-3}$ $M_\odot$ (blue dash line of the plot).

For the L17 and D16 samples, the calcium abundances predicted from Grid C for F-type stars increase with the effective temperature, as we see in the lower right panel of Fig. 10.10. In the lower right panel of Fig. 10.13, the calcium abundance is plotted against the effective temperature for the M21 sample. From this, it seems that the prediction of the models is in agreement with observations, supporting the conclusion that radiative accelerations have a strong impact on calcium for F-type stars. For Mg, Al, and Si, the abundance with the temperature is constant for F-type stars as expected (see Fig. 10.13). There are also two low-temperature stars with higher calcium abundances, which are probably α-enhanced stars, as they also show higher abundances of Mg, Al, and Si. However, since this is a small sample, there are no statistical arguments to support it.

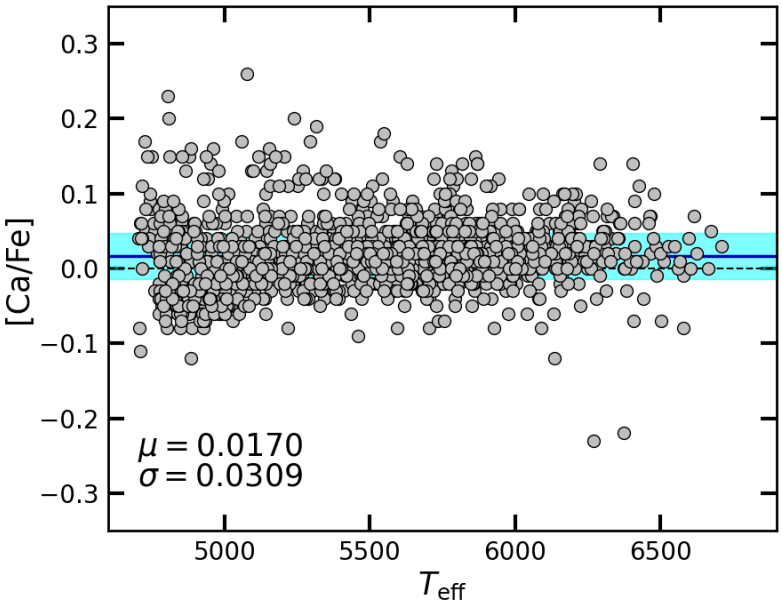

FIGURE 10.15: The abundance of calcium relative to iron as a function of effective temperature for the Brewer et al. (2016) sample.

I extend the analysis to a larger sample using the surface abundances determined by Brewer et al. (2016), for more than 1600 FGK stars. Figure 10.15 shows the calcium abundances of the Brewer et al. (2016) sample. Although we see that there is a tendency for calcium to be 0.02 dex higher than iron for the full sample, there is no tendency for the abundance of calcium to increase with effective temperature. This suggests that the transport processes competing with atomic diffusion are probably less efficient than what I included in Grid C (turbulent mixing coefficient calibrated by VSA19 on helium abundances obtained from the analysis of seismic glitch signature). Another possibility is that KIC 12317678 is a chemically peculiar star for which the competing transport processes are more efficient, leading to a strong impact of radiative accelerations on Calcium.

10.4 The 94 Ceti system

We have shown that an accurate modeling of the transport of chemicals is necessary to model F-type stars. As a test of the tools I developed, I presented here an analysis of a system of planets host stars, the 94 Ceti system.

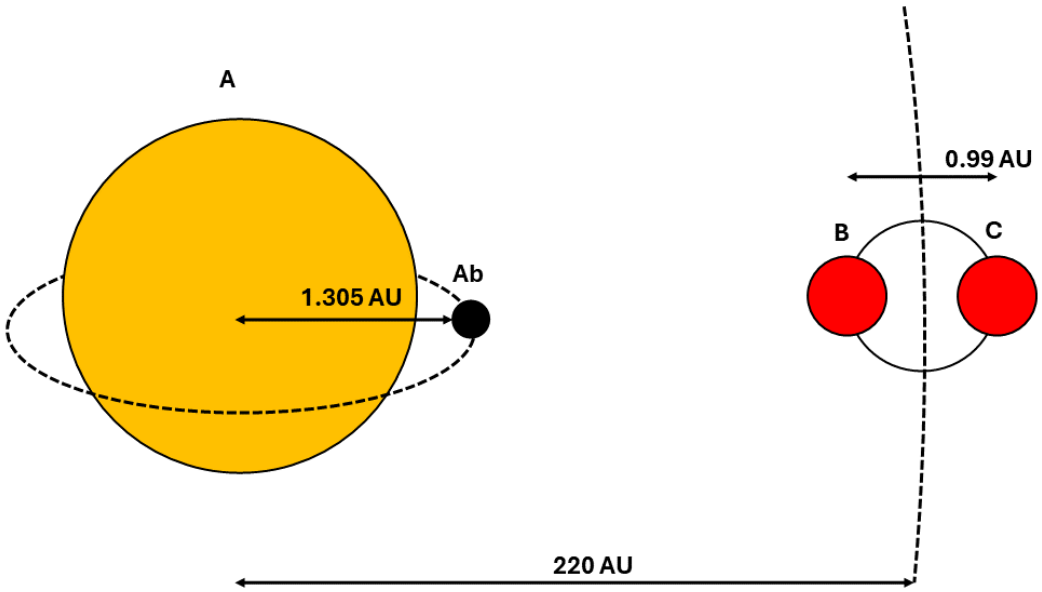

FIGURE 10.16: Sketch of the 94 Ceti System

10.4.1 System data

94 Ceti is a multi-binary stellar system at a distance of ∼22.9 PC from the Sun ($\pi = 43.70 \pm 0.13$ mas from Gaia Collaboration et al. 2021). Its main component is a naked-eye F-type star (94 Ceti A) with a magnitude G=4.922 $\pm$ 0.003 orbited by two M dwarfs (94 Ceti B and C) located at 220 $\pm$ 5 AU (Roberts et al., 2011), which in turn orbit each other at 0.99 $\pm$ 0.02 AU (Röll et al., 2010, 2012). The main component hosts a Jupiter-like planet orbiting at 1.42 $\pm$ 0.01 AU with a mass of $M_p \sin i = 1.68 M_J$ (Mayor et al., 2004). More recent estimates put the exoplanet closer to the host star at 1.305 $\pm$ 0.016 AU and estimate a less massive planet $M_p \sin i = 1.37 M_J$ (Wittenmyer et al., 2009). Two dust disks are detected, one around the main stellar component and one around the two M dwarf pairs (Wittenmyer et al., 2009). Figure 10.16 shows a sketch of the system, and the orbital parameters of the stellar components are summarized in table 10.2.

The properties of this system have been estimated in several works. Mayor et al. (2004) studied the main component and obtained a mass of 1.34 $M_\odot$ and an age of 2.4 Gyr. The mass was determined by interpolation of a grid of Geneva stellar evolution models, and the age was estimated from activity indicators. Röll et al. (2010, 2012) discovered the M dwarf couple using interferometry, and estimated the mass of each M dwarf component to be 0.55 $M_\odot$ and 0.34 $M_\odot$. The most recent studies of this system were performed by Deal et al. (2017), who used the system to study the effect of atomic diffusion resulting also in a new determination of the parameters of the F-type component. Using asteroseismic data from HARPS, they found that the main component has a mass of 1.44 $M_\odot$ and an age of 2.38 Gyr, i.e. they presented a more massive star than found in previous studies and an age compatible with that obtained from activity indicators.

This system is an excellent laboratory for understanding planet formation around F-type and multi-binary systems. Here I revisit this system using the new light curves obtained by TESS and I re-derive the fundamental properties of the F-type stars using the new models developed during this thesis. I also use the available orbital information to derive the properties of the entire system.

10.4.2 Observational data

New observations of this system have been made and provided additional constraints. Sousa et al. (2021) used high quality spectroscopic data from FEROS, HARPS, and UVES spectrographs, and the Gaia DR3 to provide new updated classic constrains for the SWEET-Cat catalogue. One of the stars is the main component of the 94 Ceti system, providing a new effective temperature $T_{\rm eff} = 6249 \pm 27$ K and iron content $[{\rm Fe/H}] = 0.27 \pm 0.02$ dex. From an interferometry analysis performed by van Belle & von Braun (2009), a precise radius $R = 1.898 \pm 0.070$ $R_\odot$ has been measured for 94 Ceti A. This star was observed by TESS in 2 sectors (sector 4 in 2018 and sector 31 in 2020), both with a cadence of 120 s. These observations provided new light curves that can be used to determine the seismic data for the main component of the system. The light curve of the stars was processed by Rafael Garcia (CEA, France, collaborator) allowing the extraction of a set of individual frequencies for the stars with a large frequency separation $\Delta\nu = 68.3 \pm 1$ μHz. Table 10.3 contains the frequencies that were measured with confidence.

TABLE 10.2: Orbital parameters of the M-dwarfs.

	Orbit A-BC	Orbit B-C
Semi-major axis (a, AU)	220±5	0.99±0.02
Period (P, yr)	2029±41	1.04±0.01
Eccentricity (e)	0.26±0.01	0.36±0.01
Inclination (i, ^{o})	104±2	108.5±0.7
periapsis (ω, ^{o})	342±7	334.9±2.3
Ascencion (Ω, ^{o})	97±2	190.9±1.0

TABLE 10.3: Individual Seismic Frequencies of 94 Ceti A obtained from TESS light curve.

n	$\ell = 0$	$\ell = 1$
16	—	1202.31±1.26
17	1237.65±1.20	—
18	1307.69±1.13	1339.08±0.71
23	—	1684.05±1.14

TABLE 10.4: Inference results for 94 Ceti A, for the different tests and different considerations of the frequencies weight (3:3) and (3:N).

		Mass ($M_\odot$)	Age (Gyr)
Grid B	3:3	1.494±0.061	2.337±0.100
	N:3	1.496±0.060	2.341±0.101
Grid C	3:3	1.496±0.064	2.295±0.101
	N:3	1.496±0.063	2.296±0.102

10.4.3 Parameters determination

10.4.3.1 94 Ceti A

With the updated constraints on the F-type star, I can infer its fundamental properties using the grids developed during this Ph.D. The inferred masses and ages are shown in table 10.4. Figure 10.17 shows the inferred parameters compared to previous estimations. My results point towards a slightly more massive star, with a relative difference of 11.6% and 3.9% compared respectively to Mayor et al. (2004) and Deal et al. (2017). Compared to Deal et al. (2017), my results are compatible with the error bars, which is not the case with Mayor et al. (2004). This is expected because Deal et al. (2017) also uses seismic constraints, which is not the case for Mayor et al. (2004) where only spectroscopic and photometric constraints were used. For the age determination, my result points toward a slightly younger star than previous determinations, with a relative difference of 4.4% and 3.6% compared to Mayor et al. (2004) and Deal et al. (2017), respectively. In both cases, my results are compatible with the uncertainties. In the case of Mayor et al. (2004), the age estimation was performed using the activity indicator, which is a good alternative for age estimation when seismic data are not available. As 94 Ceti is a multi-binary system we can assume that all components have the same age.

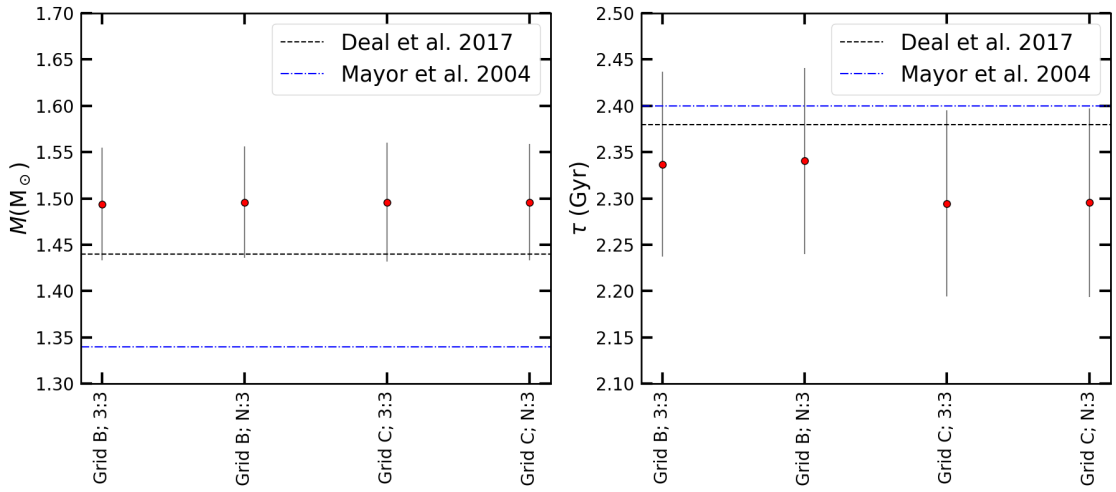

FIGURE 10.17: New estimated masses (left panel) and ages (right panel) compared to previous estimates. The black dashed line is the estimate from Deal et al. (2017) and the blue dotted dashed line is the estimate from Mayor et al. (2004).

10.4.3.2 M dwarfs 94 Ceti B and C

Determining the properties of the M dwarfs requires a different approach. The grids I developed are not set up for M dwarfs because they do not cover their region of parameter space ($M \lesssim 0.6$ M$_\odot$), and the input physics I used is not set up to model these very low-mass stars. The determination of the properties of the main component allows us to estimate the properties of the system. Knowing the mass of 94 Ceti A allows us to redetermine the mass of the planet using the radial velocity technique, and the combined mass of the M-dwarf couple using Kepler's laws. Due to the binary nature of the system, we can use Kepler's third law to determine the mass from the semi-major axis and orbital period of the M dwarfs. In this case, since the two M dwarfs are orbiting each other, we can consider them as a single body and use their orbital parameters relative to 94 Ceti A. Using Kepler's third law

$$\frac{a^3}{P} = \frac{G(M+m)}{4\pi^2}, \tag{10.1}$$

where a is the semimajor axis, P is the orbital period, M and m are the masses of the more and less massive components of the system, respectively, it is possible to determine the combined mass of the two M dwarfs.

Using the orbital parameters given in table 10.2, I estimated the combined mass of the M dwarfs to be close to the solar values (see table 10.5). To disentangle the masses of both M dwarfs it is necessary to have prior information about the ratio of the masses of the two M dwarfs. From the mass estimates of Röll et al. (2010, 2012) I determined that the

TABLE 10.5: Estimated mass for the M dwarfs.

		M_{BC} ($M_\odot$)	M_B ($M_\odot$)	M_C ($M_\odot$)
Grid B	3:N	1.093±0.214	0.675±0.132	0.418±0.082
Grid C	3:N	1.093±0.215	0.675±0.133	0.418±0.082

more massive M dwarf is about 61.8% of the combined mass. This gives a rough estimate for the pair, which is also shown in the table 10.5. With this estimate, the more massive component has the mass of a K-type star.

10.4.3.3 Exoplanet 94 Ceti Ab

The properties of the exoplanet are strongly correlated with those of the star. To obtain an estimate of the mass, the radial velocity signal is used, and for a given radius the flux ratio is obtained from the transit signal. For this system, there is only detection of radial velocities and no detection of transit. In this case the total observation time is much smaller than the orbital period of the planet (1.47 yr), which does not allow the detection of a transit signal.

In this case, only the minimum mass ($M_p \sin i$) can be re-estimated using the new mass of 94 Ceti A. The estimates using the radial velocity were done by Olivier Demangeon (IA, Portugal, collaborator) using the radial velocities from Wittenmyer et al. (2009). The updated value for the mass is given in table 10.6. Compared to previous estimates, this result makes the planet 13.7% less massive than Mayor et al. (2004) and 5.8% more massive than Wittenmyer et al. (2009).

TABLE 10.6: Estimated mass of the exoplanet.

		$M_p \sin i$ (M_J)
Grid B	3:N	1.45±0.11
Grid C	3:N	1.46±0.11

Unfortunately, estimating the mass of the planet requires the knowledge of the inclination orbit, which is not known. Nevertheless, we can still determine the probability of this object to be a planet. An object is defined as a planet if $\lesssim 13\ M_J$, and as a brown dwarf if the mass is higher. The inclination would need to be smaller than 6.4 degrees for the object to be a brown dwarf, so we can conclude that it is a planet with 92.9% confidence. Deal et al. (2017) estimated (using rotational splitting in the frequencies) that the star is observed equator-on. If we assume that the planet orbits in the equator plane of the star

so $\sin i \approx 1$. The mass of the object is then close to the minimal mass estimation and 94 Ceti Ab can be identified with confidence as a planet.

The results benefit from additional data, to improve the determination of the individual frequencies. Currently, there are no plans to re-observe the system with TESS (the sector plane does not overlap with the system). Nevertheless, I plan in the future, to use the observed data used by Deal et al. (2017) and collaborators, to see if it is possible to improve the frequency measurements.

Conclusion

In this thesis, I examined the chemical transport mechanisms in F-type stars. What are the implications of ignoring these mechanisms, and how can we account for them without creating unrealistic chemical compositions? Various studies (Valle et al., 2014, 2015, Nsamba et al., 2018, Cunha et al., 2021) have shown that neglecting atomic diffusion, particularly gravitational settling, can lead to uncertainties in solar-type stars that are larger than those imposed by future missions (PLATO impose 10%, 2%, and 10% for mass, radius, and age, Rauer et al. (2024)). Recently Rehm et al. (2024) studied the inclusion of radiative accelerations in stellar models of B-type stars. With the inclusion of the process, they were able to produce a full spectrum of seismic modes, without artificial simulation. The consideration of atomic diffusion is essential in stellar models. However, the main problem is that atomic diffusion in F-type and more massive stars creates unrealistic chemical variations. Additionally, the primary methods for calculating radiative accelerations are unreliable for computing a large number of stellar models due to their computational inefficiency. There are two main results derived from this work. First, turbulent mixing is essential to be included in stellar models, as it simulates the effects of the processes in competition with atomic diffusion. Second, there are alternative methods to reproduce the effects of radiative accelerations without introducing major uncertainties in stellar models. I tested two methods: the first was to parameterize the effects of radiative accelerations within a turbulent mixing prescription, and the second was to introduce an approximate way to compute radiative accelerations using the SVP method.

Part of this work involved exploring the effects of atomic diffusion in stellar models and how to avoid over-variations of the surface abundances for F-type stars. Using the Verma & Silva Aguirre (2019) turbulent mixing parameterization as a starting point helped to prevent these chemical variations, allowing for more accurate prediction of the chemical evolution in the models. The next step was to introduce the effect of radiative acceleration, which was achieved by parameterizing turbulent mixing to account for this

process. I showed that the efficiency of this parameterization (in F-type stars) must increase with stellar mass (eq. 8.3). The downside was that turbulent mixing acts globally, affecting all elements in the same way. Since this parameterization was based on radiative acceleration on iron, all elements are influenced similarly to this element. For some elements, this does not lead to significant uncertainties because radiative accelerations either affect them similarly to iron or do not significantly influence them. However, for other elements that are accumulated at the surface (e.g. calcium), the evolutionary behavior is not accurately reproduced. Nonetheless, the turbulent mixing parameterization I proposed allows for a better prediction of the evolution of the surface abundances of iron, which is the main observational chemical constraint used to characterize stars. This method is a step towards improving the inference of fundamental properties. I compared these new models to the standard ones. Where atomic diffusion is cut off for higher mass stars. The new approach reduces the uncertainties by up to 5%, 2%, and 20% for mass, radius, and age, respectively.

To achieve a better chemical description in the models, radiative accelerations should be taken into account. The next step was to implement a more efficient computation of radiative accelerations in MESA. In this work, I implemented the SVP method developed and provided by Alecian & LeBlanc (2020). I compared the inference of fundamental properties obtained with models including the SVP method and the standard models. The results are similar to those obtained with turbulent mixing, suggesting that neglecting atomic diffusion can lead to comparable uncertainties. When I compared the results with the models including the calibration of turbulent mixing presented in Chapter 8.2 ($D_{\mathrm{T,Fe}}$), the differences were smaller than 5% for higher mass stars, indicating that F-type stars are equivalent in terms of inferring fundamental properties. In contrast, there is a significant difference for lower mass stars, where a larger dispersion results in uncertainties up to 8%, 3%, and 10% in mass, radius, and age, respectively. This dispersion is not due to the consideration of radiative accelerations but rather to a different approach in turbulent mixing. In the case of the SVP method, turbulent mixing was calibrated to reproduce the lithium abundance at the surface of the Sun. This suggests that neglecting the reproduction of this element can lead to non-negligible uncertainties in the inference of stellar parameters.

The two methods of accounting for radiative accelerations show significant differences in the evolution of the surface abundance. Specifically, in the case of lithium, models using the SVP method show a better agreement with observations. However, this improvement

was not due to radiative accelerations (since this process does not affect lithium). It is rather the consideration of a different turbulent mixing calibration that enabled this improvement in the prediction of the surface abundances of lithium. For other elements, both methods do not show major discrepancies, except for calcium. In the case of calcium, with the SVP method, the combination with turbulent mixing resulted in an accumulation or constant abundance of the element at the stellar surface, whereas with my turbulent mixing calibration, it produced a depletion. Compared to the observations of Morel et al. (2021), the models using the SVP method showed better agreement. Specifically, for KIC 12317678, this method yields a calcium abundance closer to the observed value. This suggests that the SVP method provides a more realistic prediction of the evolution of the surface abundance compared to those using my turbulent mixing calibration. However, Morel et al. (2021) studied a small sample with a low number of F-type stars, which limits the ability to draw statistical conclusions. Upon examining the variation of calcium abundance with effective temperature in a larger sample (Brewer et al., 2016), I found no evidence that calcium accumulates in F-type stars. This suggested that the turbulent mixing used in stellar models may need to be less efficient. Nevertheless, this did not invalidate the case of KIC 12317678. This particular star exhibits notably higher calcium abundance, and the combination of these chemical processes improves the chemical characterization of this star.

The new TESS data have provided new asteroseismic data for thousands of stars. In this work, I study the 94 Ceti system, a multi-binary system of one F-type star and two M dwarfs that host an exoplanet. In collaboration with Rafael Garcia, we derived individual frequencies from the TESS light curves, which allowed us to update the characterization of the system. I derived a slightly higher mass and a lower age compared to previous estimates. This allows us to estimate the mass of the M dwarf using the Kepler laws and to determine a new minimum mass for the exoplanet using radial velocities. Asteroseismology allows us to fully characterize stellar systems, and future missions (e.g., PLATO) will provide us with new seismic data that will allow us to characterize new stellar systems.

In summary, it is crucial to incorporate chemical transport mechanisms into stellar models to reduce uncertainties in stellar characterization. This includes considering both atomic diffusion and turbulent mixing, which is essential to reproduce the effects of various processes in competition with atomic diffusion. To better model stars, radiative accelerations need to be considered, either using my calibrated turbulent mixing or the SVP method. Both approaches should improve the inference of fundamental properties. The

primary distinction lies in the chemical evolution predicted by each method. This work is a step forward to better stellar characterization. The next step is to model every transport process individually (rotational inducing mixing, thermohaline convection, etc.) for the most accurate modeling and characterization of stars in the context of future missions (e.g. PLATO, Ariel, etc.).

Future Work

The focus of this work has been to reproduce a more realistic chemical evolution in the stellar models. A natural next step of this work is to investigate the impact of the combination of atomic diffusion and turbulent mixing across the HR diagram. In this project, I focused on the MS stars and the uncertainties they impose on the inference of their properties. However, it is important to see how this affects the later stages of evolution, especially the SG and RGB stages. Understand if the uncertainties propagate from the MS through the evolution, or if they are suppressed by the expansion of the convective envelope.

In this work, I used a constant core overshoot and $\alpha_{\rm MLT}$, which impose systematics in the inferred properties. A constant overshoot can cause a convective core to appear at lower masses, or artificially extend the convective core after the ZAMS, while it should disappear almost immediately for lower-mass stars. It can also lead to small convective cores for more massive stars that should have larger cores. A constant $\alpha_{\rm MLT}$ mainly affects the smaller masses. It affects the efficiency of convection and has a strong influence on the radius of the models and consequently on their seismic data determination. Including $\alpha_{\rm MLT}$ as a free parameter would allow us to reduce the uncertainties in the determination of the fundamental properties.

A natural continuation of the work is to disentangle the different chemical transport mechanisms included in the turbulent mixing prescription and add them to the stellar models. I am particularly interested in studying the rotation-induced mixing. Rotation has an important impact on stellar structure and evolution and I currently do not include it in my models. It is important to understand how the angular momentum is transported inside the stars, the gradients they create, and how they couple with the transport of chemical elements inside the stars.

The tools I am developing are already a step toward improving stellar models and should allow us to better characterize the stars we observe. So I am interested in using

them to characterize a larger sample of stars, especially those that have exoplanets orbiting them. I will also use them to continue the study of the 94 Ceti system, to understand more about the system and how the chemical transport mechanisms I am using affect the chemical composition of the star.

Bibliography

Aerts, C., Christensen-Dalsgaard, J., & Kurtz, D. W. 2010, Asteroseismology

Ahumada, R., Prieto, C. A., Almeida, A., et al. 2020, ApJS, 249, 3

Alecian, G. & Deal, M. 2023, Galaxies, 11, 62

Alecian, G. & LeBlanc, F. 2020, MNRAS, 498, 3420

Anders, E. H., Jermyn, A. S., Lecoanet, D., & Brown, B. P. 2022, ApJ, 926, 169

Asplund, M., Grevesse, N., Sauval, A. J., & Scott, P. 2009, ARA&A, 47, 481

Badnell, N. R., Bautista, M. A., Butler, K., et al. 2005, MNRAS, 360, 458

Baglin, A., Auvergne, M., Barge, P., et al. 2006, in ESA Special Publication, Vol. 1306, The CoRoT Mission Pre-Launch Status - Stellar Seismology and Planet Finding, ed. M. Fridlund, A. Baglin, J. Lochard, & L. Conroy, 33

Bahcall, J. N., Basu, S., Pinsonneault, M., & Serenelli, A. M. 2005, ApJ, 618, 1049

Ball, W. H. & Gizon, L. 2014, A&A, 568, A123

Balser, D. S. 2006, AJ, 132, 2326

Baturin, V. A., Ayukov, S. V., Gryaznov, V. K., et al. 2013, in Astronomical Society of the Pacific Conference Series, Vol. 479, Progress in Physics of the Sun and Stars: A New Era in Helio- and Asteroseismology, ed. H. Shibahashi & A. E. Lynas-Gray, 11

Borucki, W. J., Koch, D., & et al. 2010, Science, 327, 977

Bressan, A., Marigo, P., Girardi, L., et al. 2012, MNRAS, 427, 127

Brewer, J. M., Fischer, D. A., Valenti, J. A., & Piskunov, N. 2016, ApJS, 225, 32

Burgers, J. M. 1969, Flow Equations for Composite Gases

Campilho, B., Deal, M., & Bossini, D. 2022, arXiv e-prints, arXiv:2201.03439

Casagrande, L., Flynn, C., Portinari, L., Girardi, L., & Jimenez, R. 2007, MNRAS, 382, 1516

Chaboyer, B., Fenton, W. H., Nelan, J. E., Patnaude, D. J., & Simon, F. E. 2001, ApJ, 562, 521

Chaplin, W. J., Kjeldsen, H., Christensen-Dalsgaard, J., et al. 2011, Science, 332, 213

Chaplin, W. J. & Miglio, A. 2013, ARA&A, 51, 353

Christensen-Dalsgaard, J., Monteiro, M. J. P. F. G., Rempel, M., & Thompson, M. J. 2011, MNRAS, 414, 1158

Cox, J. P. & Giuli, R. T. 1968, Principles of stellar structure

Cunha, M. S. 2018, in Astrophysics and Space Science Proceedings, Vol. 49, Asteroseismology and

Exoplanets: Listening to the Stars and Searching for New Worlds, ed. T. L. Campante, N. C. Santos, & M. J. P. F. G. Monteiro, 27

Cunha, M. S., Roxburgh, I. W., Aguirre Børsen-Koch, V., et al. 2021, MNRAS, 508, 5864

Cupani, G., D'Odorico, V., Cristiani, S., et al. 2017, in Astronomical Society of the Pacific Conference Series, Vol. 512, Astronomical Data Analysis Software and Systems XXV, ed. N. P. F. Lorente, K. Shortridge, & R. Wayth, 209

Cutri, R. M., Skrutskie, M. F., van Dyk, S., et al. 2003, VizieR Online Data Catalog, II/246

Cyburt, R. H., Fields, B. D., & Olive, K. A. 2003, Physics Letters B, 567, 227

Davies, G. R., Silva Aguirre, V., Bedding, T. R., et al. 2016, MNRAS, 456, 2183

Deal, M., Alecian, G., Lebreton, Y., et al. 2018, A&A, 618, A10

Deal, M., Escobar, M. E., Vauclair, S., et al. 2017, A&A, 601, A127

Deal, M., Goupil, M. J., Marques, J. P., Reese, D. R., & Lebreton, Y. 2020, A&A, 633, A23

Deal, M. & Martins, C. J. A. P. 2021, A&A, 653, A48

Deal, M., Richard, O., & Vauclair, S. 2015, A&A, 584, A105

Dumont, T., Charbonnel, C., Palacios, A., & Borisov, S. 2021, A&A, 654, A46

Dumont, T., Palacios, A., Charbonnel, C., et al. 2020, arXiv e-prints, arXiv:2012.03647

Eggenberger, P., Buldgen, G., Salmon, S. J. A. J., et al. 2022, Nature Astronomy, 6, 788

Eggenberger, P., Meynet, G., Maeder, A., et al. 2010, A&A, 519, A116

Ferguson, J. W., Alexander, D. R., Allard, F., et al. 2005, ApJ, 623, 585

Gaia Collaboration, Brown, A. G. A., Vallenari, A., et al. 2018, A&A, 616, A1

Gaia Collaboration, Brown, A. G. A., Vallenari, A., et al. 2021, A&A, 649, A1

Grevesse, N. & Noels, A. 1993, Physica Scripta Volume T, 47, 133

Gruyters, P., Korn, A. J., Richard, O., et al. 2013, A&A, 555, A31

Gruyters, P., Lind, K., Richard, O., et al. 2016, A&A, 589, A61

Gruyters, P., Nordlander, T., & Korn, A. J. 2014, A&A, 567, A72

Hertzsprung, E. 1911, Publikationen des Astrophysikalischen Observatoriums zu Potsdam, 63

Herwig, F. 2000, A&A, 360, 952

Hidalgo, S. L., Pietrinferni, A., Cassisi, S., et al. 2018, ApJ, 856, 125

Hu, H., Tout, C. A., Glebbeek, E., & Dupret, M. A. 2011, MNRAS, 418, 195

Iglesias, C. A. & Rogers, F. J. 1996, ApJ, 464, 943

Jermyn, A. S., Bauer, E. B., Schwab, J., et al. 2023, ApJS, 265, 15

Jimenez, R., Flynn, C., MacDonald, J., & Gibson, B. K. 2003, Science, 299, 1552

Kippenhahn, R. & Weigert, A. 1990, Stellar Structure and Evolution

Kjeldsen, H., Bedding, T. R., & Christensen-Dalsgaard, J. 2008, ApJ, 683, L175

Krishna Swamy, K. S. 1966, ApJ, 145, 174

LeBlanc, F. & Alecian, G. 2004, MNRAS, 352, 1329

Lebreton, Y. 2013, in EAS Publications Series, Vol. 63, EAS Publications Series, ed. G. Alecian, Y. Lebreton, O. Richard, & G. Vauclair, 123–133

Lebreton, Y. & Goupil, M. J. 2014, A&A, 569, A21

Ledoux, P. 1947, ApJ, 105, 305

Lund, M. N., Silva Aguirre, V., Davies, G. R., et al. 2017, ApJ, 835, 172

Mayor, M., Udry, S., Naef, D., et al. 2004, A&A, 415, 391

Mendoza, C., Seaton, M. J., Buerger, P., et al. 2007, MNRAS, 378, 1031

Michaud, G., Alecian, G., & Richer, J. 2015, Atomic Diffusion in Stars

Michaud, G., Richer, J., & Richard, O. 2011a, A&A, 529, A60

Michaud, G., Richer, J., & Vick, M. 2011b, A&A, 534, A18

Moedas, N., Bossini, D., Deal, M., & Cunha, M. 2024, arXiv e-prints, arXiv:2401.14924

Moedas, N., Deal, M., Bossini, D., & Campilho, B. 2022, A&A, 666, A43

Mombarg, J. S. G., Dotter, A., Rieutord, M., et al. 2022, ApJ, 925, 154

Morel, T., Creevey, O. L., Montalbán, J., Miglio, A., & Willett, E. 2021, A&A, 646, A78

Mosser, B., Elsworth, Y., Hekker, S., et al. 2012, A&A, 537, A30

Nsamba, B., Campante, T. L., Monteiro, M. J. P. F. G., et al. 2018, MNRAS, 477, 5052

Nsamba, B., Moedas, N., Campante, T. L., et al. 2021, MNRAS, 500, 54

Pasetto, S., Chiosi, C., Cropper, M., & Grebel, E. K. 2015, in IAU General Assembly, Vol. 29, 2245637

Paxton, B., Bildsten, L., Dotter, A., & et al. 2011, ApJS, 192, 3

Paxton, B., Cantiello, M., Arras, P., et al. 2013, ApJS, 208, 4

Paxton, B., Marchant, P., Schwab, J., et al. 2015, ApJS, 220, 15

Paxton, B., Schwab, J., Bauer, E. B., et al. 2018, ApJS, 234, 34

Paxton, B., Smolec, R., Schwab, J., et al. 2019, ApJS, 243, 10

Pietrinferni, A., Hidalgo, S., Cassisi, S., et al. 2021, ApJ, 908, 102

Proffitt, C. R. & Michaud, G. 1991, ApJ, 371, 584

Rauer, H., Aerts, C., Cabrera, J., et al. 2024, arXiv e-prints, arXiv:2406.05447

Rauer, H., Catala, C., Aerts, C., et al. 2014, Experimental Astronomy, 38, 249

Rehm, R., Mombarg, J. S. G., Aerts, C., et al. 2024, arXiv e-prints, arXiv:2405.08864

Rendle, B. M., Buldgen, G., Miglio, A., et al. 2019, MNRAS, 484, 771

Richard, O., Michaud, G., & Richer, J. 2002, ApJ, 580, 1100

Richard, O., Michaud, G., & Richer, J. 2005, ApJ, 619, 538

Richer, J., Michaud, G., Rogers, F., et al. 1998, ApJ, 492, 833

Richer, J., Michaud, G., & Turcotte, S. 2000, ApJ, 529, 338

Ricker, G. R. 2016, in AGU Fall Meeting Abstracts, P13C–01

Roberts, Lewis C., J., Turner, N. H., ten Brummelaar, T. A., Mason, B. D., & Hartkopf, W. I. 2011, AJ, 142, 175

Rogers, F. J. & Nayfonov, A. 2002, ApJ, 576, 1064

Röll, T., Neuhäuser, R., Seifahrt, A., & Mugrauer, M. 2012, A&A, 542, A92

Röll, T., Seifahrt, A., Neuhäuser, R., Köhler, R., & Bean, J. 2010, in EAS Publications Series, Vol. 45, EAS Publications Series, 429–432

Roxburgh, I. W. & Vorontsov, S. V. 2003, A&A, 411, 215
Russell, H. N. 1914, Popular Astronomy, 22, 331
Salaris, M. & Cassisi, S. 2015, A&A, 577, A60
Salaris, M. & Weiss, A. 2001, A&A, 376, 955
Schwarzschild, M. 1958, Structure and evolution of the stars.
Seaton, M. J. 2005, MNRAS, 362, L1
Semenova, E., Bergemann, M., Deal, M., et al. 2020, A&A, 643, A164
Serenelli, A. M. & Basu, S. 2010, ApJ, 719, 865
Silva Aguirre, V., Davies, G. R., Basu, S., et al. 2015, MNRAS, 452, 2127
Silva Aguirre, V., Lund, M. N., Antia, H. M., et al. 2017, ApJ, 835, 173
Sonoi, T., Samadi, R., Belkacem, K., et al. 2015, A&A, 583, A112
Sousa, S. G., Adibekyan, V., Delgado-Mena, E., et al. 2021, A&A, 656, A53
Szalay, A. 1998, in Astrophysics and Algorithms, 8
Théado, S., Alecian, G., LeBlanc, F., & Vauclair, S. 2012, A&A, 546, A100
Théado, S., Vauclair, S., Alecian, G., & LeBlanc, F. 2009, ApJ, 704, 1262
Thoul, A. A., Bahcall, J. N., & Loeb, A. 1994, ApJ, 421, 828
Townsend, R. H. D. & Teitler, S. A. 2013, MNRAS, 435, 3406
Turcotte, S., Richer, J., Michaud, G., Iglesias, C. A., & Rogers, F. J. 1998, ApJ, 504, 539
Valle, G., Dell'Omodarme, M., Prada Moroni, P. G., & Degl'Innocenti, S. 2014, A&A, 561, A125
Valle, G., Dell'Omodarme, M., Prada Moroni, P. G., & Degl'Innocenti, S. 2015, A&A, 575, A12
van Belle, G. T. & von Braun, K. 2009, ApJ, 694, 1085
Verma, K., Raodeo, K., Basu, S., et al. 2019, MNRAS, 483, 4678
Verma, K. & Silva Aguirre, V. 2019, MNRAS, 489, 1850
Vick, M., Michaud, G., Richer, J., & Richard, O. 2010, A&A, 521, A62
Weiss, A. & Schlattl, H. 2008, Ap&SS, 316, 99
Wittenmyer, R. A., Endl, M., Cochran, W. D., Levison, H. F., & Henry, G. W. 2009, ApJS, 182, 97
Zahn, J. P. 1991, A&A, 252, 179

Appendix A

Paper Moedas et al. (2022) A&A

A&A 666, A43 (2022)
https://doi.org/10.1051/0004-6361/202243210

Astronomy & Astrophysics

Atomic diffusion and turbulent mixing in solar-like stars: Impact on the fundamental properties of FG-type stars

Nuno Moedas[1,2], Morgan Deal[1], Diego Bossini[1], and Bernardo Campilho[1,2]

[1] Instituto de Astrofísica e Ciências do Espaço, Universidade do Porto, CAUP, Rua das Estrelas, 4150-762 Porto, Portugal
e-mail: nmoedas@astro.up.pt
[2] Departamento de Física e Astronomia, Faculdade de Ciências da Universidade do Porto, Rua do Campo Alegre, s/n, 4169-007 Porto, Portugal

Received 27 January 2022 / Accepted 9 June 2022

ABSTRACT

Context. Chemical composition is an important factor that affects stellar evolution. The element abundance on the stellar surface evolves along the lifetime of the star because of transport processes, including atomic diffusion. However, models of stars with masses higher than about 1.2 $M_{\odot}$ predict unrealistic variations at the stellar surface. This indicates the need for competing transport processes that are mostly computationally expensive for large grids of stellar models.
Aims. The purpose of this study is to implement turbulent mixing in stellar models and assess the possibility of reproducing the effect of radiative accelerations with turbulent mixing for elements like iron in order to make the computation of large grids possible.
Methods. We computed stellar models with the Module for Experiments in Stellar Astrophysics code and assessed the effects of atomic diffusion (with radiative acceleration) in the presence of turbulent mixing. Starting from a turbulent mixing prescription already calibrated on helium surface abundances of F-type stars as a reference, we parametrised the effect of radiative accelerations on iron with a turbulent diffusion coefficient. Finally, we tested this parametrisation by modelling two F-type stars of the *Kepler* Legacy sample.
Results. We found that, for iron, a parametrisation of turbulent mixing that simulates the effect of radiative acceleration is possible. This leads to an increase in the efficiency of the turbulent mixing to counteract the effect of gravitational settling. This approximation does not affect significantly the surface abundances of the other elements we studied, except for oxygen and calcium. We demonstrate that this parametrisation has a negligible impact on the accuracy of the seismic properties inferred with these models. Moreover, turbulent mixing makes the computation of realistic F-type star models including the effect atomic diffusion possible. This leads to differences of about 10% in the inferred ages compared to results obtained with models that neglect these processes.
Conclusions. The inclusion of turbulent mixing and atomic diffusion with radiative accelerations allows a more realistic characterisation of F-type stars. The parametrisation of the effect of radiative acceleration on iron opens the possibility to compute larger grids of stellar models in a reasonable amount of time, which is currently difficult when the different chemical transport mechanisms, especially radiative accelerations, are considered, although this parametrisation cannot simulate the evolution of abundances of all elements (e.g. calcium).

Key words. diffusion – turbulence – stars: abundances – stars: evolution – asteroseismology

1. Introduction

The precise and accurate determination of stellar fundamental properties (such as age, mass, and radius) through stellar modelling is needed in many astrophysics applications, from the characterisation of exoplanetary systems to the reconstruction of the evolution and chemical history of the Milky Way. For example, stellar models have been largely used to interpret the data obtained with the missions *Kepler*/K2 (Borucki et al. 2010) and the Transiting Exoplanet Survey Satellite (TESS; Ricker 2016) and to put constraints on the targeted stars. These instruments provided and still provide high-quality asteroseismic data with exquisite precision that will be further enriched by future space missions such as PLAnetary Transits and Oscillations of stars (PLATO/ESA; Rauer et al. 2014). However, the current stellar models are still suffering from large uncertainties (especially on the age), which will be critical for the interpretation of these new high-quality data (e.g. PLATO requires 10% accuracy on the age of a star similar to the Sun). For this reason, it is crucial to improve the ways we model stars.

One of the main ingredients responsible for the uncertainties on stellar ages is the transport of chemical elements. This transport is driven by processes (microscopic and macroscopic) in competition that lead to a redistribution of chemical elements with important effects on the internal structure, the evolution, and the surface abundances of stars. One of these processes is atomic diffusion. This process is mainly driven by pressure, temperature, and chemical gradients (Thoul et al. 1994; Baturin et al. 2006) and affects the distribution of chemical elements at the surface and inside stars.

Atomic diffusion mainly consists in the competition between two sub-processes. One is the gravitational settling that makes the chemical elements move towards the interior, except for hydrogen which is moved to the surface of the star. The other is the radiative acceleration that pushes some elements, mainly the heavy ones, towards the surface of stars due to a transfer of momentum between photons and ions. Its efficiency depends on the mass and metallicity of the stars, as shown in Deal et al. (2018), among others, increasing with mass and decreasing with metallicity. Although, gravitational settling alone had proven to be successful in predicting the surface abundances of low-mass stars (Chaboyer et al. 2001; Salaris & Weiss 2001), radiative accelerations need to be included in stellar models with a small surface convective zone (e.g. in solar-metallicity stars with

an effective temperature higher than ~6000 K, Michaud et al. 2015). However, for stars more massive than the Sun, the predicted surface abundance variations are often larger than those observed in clusters (e.g. Gruyters et al. 2014, 2016; Semenova et al. 2020), which indicates the need to include other competing transport mechanisms. It is then crucial to identify and model the transport processes in competition with atomic diffusion (e.g. Eggenberger et al. 2010; Vick et al. 2010; Deal et al. 2020; Dumont et al. 2020). Nevertheless, the identification and accurate modelling of all processes competing with atomic diffusion is still ongoing and will require a considerable amount of effort. These processes are either diffusive or advective. Assuming that the processes are fully diffusive, an alternative solution is to parametrise the efficiency of a turbulent mixing induced by the competing transport processes, using the surface abundances of stars in clusters as constraints (Gruyters et al. 2013, 2016; Semenova et al. 2020). Recently, Verma & Silva Aguirre (2019, hereafter VSA19) calibrated a prescription of turbulent mixing using the helium surface abundances of three F-type stars of the *Kepler* Legacy sample. These abundances were derived from an asteroseismic analysis of the glitch induced by the helium second ionisation region.

The accurate inference of the fundamental stellar properties of stars observed by large surveys requires large grids of stellar models with an accurate transport of chemicals. However, including these processes (e.g. atomic diffusion with radiative accelerations) in large grids of stellar models is still computationally expensive. Solutions to this issue need to be found for future large surveys (e.g. PLATO). The first goal of this paper is to characterise the effects of atomic diffusion (with radiative accelerations) for solar-like oscillating stars and to quantify the variation in [Fe/H] from the main sequence (MS) to the red giant branch (RGB) bump. In addition, and because [Fe/H] (iron abundance) is the main chemical constraint used for the inference of stellar fundamental properties, we also address the difference with [M/H] (overall metallicity) throughout the evolution. Focusing on F-type stars, which are the most impacted by atomic diffusion, the second goal is to quantify the impact of turbulent mixing (taking as a reference the calibration of VSA19) on the surface abundances. Then we propose a parametrisation for the effect of radiative acceleration on the iron surface abundance with an enhanced turbulent diffusion coefficient in order to make the computation of models faster without losing the contribution of radiative acceleration. Finally, we validate these models with the inferences of the properties of two F-type *Kepler* Legacy stars.

This article is structured as follows. In Sect. 2 we present the input physics of the models. In Sect. 3 we address the effects of atomic diffusion and discuss its impact on the surface abundance variations solar-like MS stars. In Sect. 4 we quantify the effect of turbulent mixing and parametrise the effect of radiative acceleration of iron. Finally, we test the impact of these models on the stellar property inferences of two *Kepler* Legacy stars in Sect. 5, and we conclude in Sect. 6.

2. Stellar models

2.1. Input physics

The stellar models are computed with the Modules for Experiments in Stellar Astrophysics (MESA r12778) stellar evolution code (Paxton et al. 2011, 2013, 2015, 2018, 2019). The input physics summarised below are the same for all the models, except for the transport of chemical elements and the opacity tables. We adopt the solar heavy elements mixture given by Asplund et al. (2009). We use OP[1] monochromatic opacity tables (Seaton 2005) when radiative accelerations are taken into account and OPAL[2] opacity tables (Iglesias & Rogers 1996) in the other cases. We use the OPAL2005 equation of state (Rogers & Nayfonov 2002). For nuclear reactions, we use the NACRE reaction rates (Angulo 1999) except for ^{14}N(p,γ)^{15}O (Imbriani et al. 2005) and ^{12}C(α,γ)^{16}O (Kunz et al. 2002). For the boundary condition at the stellar surface we use Krishna-Swamy atmosphere (Krishna Swamy 1966). For convection we follow the prescription of Cox & Giuli (1968). In the presence of a convective core we implemented core overshoot following an exponential decay with a diffusion coefficient, as presented in Herwig (2000),

$$D_{\rm ov} = D_0 \exp\left(-\frac{z}{f H_{\rm p}}\right), \tag{1}$$

where D_0 is the diffusion coefficient at the border of the convective unstable region, z is the distance from the boundary of the convective region, $H_{\rm p}$ is the pressure scale height, and f is the overshoot parameter set to $f = 0.01$. Different solar calibrations are performed depending on the input physics of the models. The different $\alpha_{\rm MLT}$ values and initial chemical compositions are given in Sect. 2.4.

2.2. Atomic diffusion

Atomic diffusion occurs during the whole evolution of stars, and mainly acts in radiative zones (since convective motions almost instantaneously homogenise the chemical composition). Its impact at the surface depends on the extension of the convective envelope since its efficiency decreases with depth. Hence, a more efficient transport is present when the surface convective zone is small. This particularly affects the MS stars, where the extension of the envelope mainly depends on the stellar mass (higher mass, smaller convective envelope). On the other hand, during the sub-giant (SG) phase and the beginning of the RGB, the envelope starts to increase, reaches its greatest depth (known as the first dredge-up), and almost restores the surface metallicity to its initial value.

The chemical evolution of an element i in the stellar interior is described by the following equation:

$$\rho \frac{\partial X_i}{\partial t} = A_i m_{\rm p} \left[\sum_j (r_{ji} - r_{ij})\right] + \frac{1}{r^2}\frac{\partial}{\partial r}\left[r^2 \rho D_{\rm T} \frac{\partial X_i}{\partial r}\right] - \frac{1}{r^2}\frac{\partial}{\partial r}\left[r^2 \rho v_i\right]. \tag{2}$$

The first term takes into consideration the nuclear reactions, where r_{ij} is the reaction rate of the reaction that transforms element i into j. The second term takes into consideration all macroscopic diffusive processes that act inside the star, which are in competition with atomic diffusion with $D_{\rm T}$ the turbulent diffusion coefficient, r the radial coordinate, and ρ the local density.

The last term corresponds to the effects of atomic diffusion, where v_i is the diffusion velocity of element i that, in the case of a trace element, can be expressed as

$$v_i = D_{i,{\rm p}}\left[-\frac{\partial \ln X_i}{\partial r} + k_T \frac{\partial \ln T}{\partial r} + \frac{(Z_i+1) m_{\rm p} g}{2 k_{\rm B} T} + \frac{A_i m_{\rm p}}{k_{\rm B} T}(g_{{\rm rad},i} - g)\right], \tag{3}$$

[1] http://cdsweb.u-strasbg.fr/topbase/TheOP.html
[2] https://opalopacity.llnl.gov/

where A_i is the atomic mass of element i, m_p is the proton mass, T is the temperature, $D_{i,p}$ is the diffusion coefficient of element i relative to protons, k_T is the thermal diffusivity, k_B is the Boltzmann constant, and Z_i is the atomic charge of the element i. The first and second terms represent the effect of the chemical and temperature gradients, respectively. The third term represents the effect of the electric field. The last and dominant term represents the effect of the pressure gradient and is decomposed into two main processes, the radiative accelerations ($g_{rad,i}$) and gravitational settling (g).

Atomic diffusion in MESA is computed following the Thoul et al. (1994) method with diffusion coefficients computed from Paquette et al. (1986) (see Paxton et al. 2011 for more details). Paxton et al. (2015) improved the treatment of atomic diffusion by including the effects of radiative acceleration following the work of Hu et al. (2011). Radiative accelerations are computed using a modified version of the OP package (OPCD, Seaton 2005). We followed the recommendations of Campilho et al. (2022) to set up all the options provided by MESA to control the modelling of atomic diffusion.

We computed models including atomic diffusion with and without radiative acceleration. When including radiative acceleration, the Rosseland mean opacity is computed using the OP monochromatic opacity tables in Seaton (2005) instead of the OPAL tables at a fixed heavy elements mixture. This ensures that the opacity profile, hence the internal structure, is consistent with the internal redistribution of heavy elements induced by radiative accelerations during the whole evolution.

2.3. Turbulent mixing

The origins of many processes in competition with atomic diffusion are still unknown. The main candidates are either diffusive (e.g. rotation-induced mixing; Palacios et al. 2003; Talon 2008; Dumont et al. 2020) or advective (e.g. mass loss; Vick et al. 2010), or both. In this work we consider that the competing transport processes are diffusive and all their contributions can be approximated by a turbulent diffusion coefficient. This coefficient (D_T) was implemented in MESA following the prescription described in Richer et al. (2000)

$$D_T = \omega D(\mathrm{He})_0 \left(\frac{\rho_0}{\rho}\right)^n , \tag{4}$$

where ω and n are constants, ρ_0 and $D(\mathrm{He})_0$ are respectively the density and the diffusion coefficient of helium at a reference depth, and $D(\mathrm{He})$ was computed following the analytical expression given by Richer et al. (2000):

$$D(\mathrm{He}) = \frac{3.3 \times 10^{-15}\, T^{2.5}}{4\rho \ln\left(1 + 1.125 \times 10^{-16}\, T^3/\rho\right)}. \tag{5}$$

Previous studies used either a fixed envelope mass (ΔM_0) or a fixed temperature (T_0) for the reference depth. The temperature was used as reference point when turbulent mixing was calibrated on lithium surface abundances in Population II stars (e.g. Richard et al. 2002, 2005; Deal & Martins 2021) and on the surface abundances of stars in clusters (e.g. Gruyters et al. 2013, 2016; Semenova et al. 2020; Dumont et al. 2021). In all of these cases ω and n were set to 400 and 3, respectively. In these studies the reference temperature was calibrated between $\log_{10}(T_0) = 5.7$ and 6.5, the value being dependent on the type of stars (i.e. lower temperatures of Population II stars than solar-like stars). On the other hand, the mass was used as a reference point to calibrate the turbulent mixing on the surface abundances of F- and A-type stars, where ω and n were set to 10^4 and 4, respectively (Michaud et al. 2011a,b). The reference point in mass was found to be $\Delta M_0 \sim [1-2] \times 10^{-6}\, M_\odot$ for these stars. VSA19 performed a similar calibration on three *Kepler* stars. The calibration was made in order to obtain surface helium abundances that fit the observed glitch in the oscillation spectra that was caused by the second ionisation zone of helium. They found a reference mass $\Delta M_0 = 5 \times 10^{-4}\, M_\odot$, which is higher than for A- and F-type stars. In this work we use ΔM_0 as reference instead of T_0 because, as Richer et al. (2000) noted, the surface abundances of elements other than lithium mainly depend on the envelope mass mixed by turbulent mixing. Using T_0 could lead to different envelope masses throughout the evolution. Since the focus of this paper is solar-like oscillating MS stars, we decided to use the value calibrated by VSA19 as a reference.

2.4. Grids of stellar models

We computed different grids of stellar models to quantify the effect of atomic diffusion and turbulent mixing on solar-like MS stars:

- Grid A includes atomic diffusion without radiative accelerations. For this grid we computed models with a range of masses equally spaced, three initial metallicities, and three helium enrichment ratios, including the solar calibration ($[\mathrm{M/H}]_i = 0.06$ dex and the helium-to-heavy element enrichment ratio $\Delta Y/\Delta Z = 1.23$). The solar-calibrated values are $\alpha_{MLT} = 1.7106532$, $X_0 = 0.71843711$, $Y_0 = 0.26673452$, and $Z_0 = 0.01482837$.
- Grid B has the same input physics as grid A except for the inclusion of radiative accelerations and the Rosseland mean opacity computed with OP monochromatic tables instead of standard OPAL tables. The grid is restricted to the solar chemical composition. We used the same solar-calibrated input parameter as Grid A. We tested that is has a negligible impact on the models.
- Grids C1 and C2 are similar to Grid B with the additional inclusion of the effect of turbulent mixing following the calibration of VSA19. Grid C1 is computed with solar metallicity ± 0.1 dex to allow a comparison with an optimisation method (see Sect. 5.1). Grid C2 does not have radiative acceleration and only includes a few models for comparison with the models of Grids B and C1. Because the turbulent mixing parametrisation has no impact on solar models (i.e. the reference depth of Eq. (4) is inside the surface convective zone of the Sun), we used the same solar-calibrated input parameters as Grid A.
- Grids D1, D2, D3, and D4 are computed around the parameter space of KIC 2837475 and KIC 11253226. All grids are used to infer the fundamental properties of both stars. Grid D1 includes the turbulent mixing parametrised in Sect. 4.2 and gravitational settling. Grid D2 and D3 include no transport except convection. The difference between these two grids is in the solar-calibrated values. Grid D2 uses the same as Grid A, while grid D3 includes the solar-calibrated value consistent with its input physics ($\alpha_{MLT} = 1.5908152$, $X_0 = 0.72914669$, $Y_0 = 0.25765492$, and $Z_0 = 0.01319839$). Finally, D4 includes atomic diffusion without radiative accelerations, without turbulent mixing, and with solar-calibrated values similar to Grid A.

Grid A is used as a reference when compared to grids B and C1. For grids C1, C2, D1, D2, D3, and D4 individual frequencies are computed using the GYRE oscillation code (Townsend & Teitler 2013). The parameters of the grids are summarised in Table 1.

Table 1. Summary of the different stellar parameters and input physics used in each grid.

Grid	Mass ($M_\odot$)		[Fe/H]$_i$		$\Delta Y/\Delta Z$		Atomic	ΔM_0 ($M_\odot$)	Opacity
	Range	Step	Range	Step	Range	Step	diffusion		table
A	[0.7; 1.7]	0.02	−0.44; 0.06; 0.46	–	0.4; 1.23; 2.8	–	g	None	OPAL
B	[0.7; 1.7]	0.1	0.06	–	1.23	–	$g + g_{\rm rad}$	None	OP mono
C1	[0.7; 1.7]	0.1	−0.04; 0.06; 0.16	–	1.23	–	$g + g_{\rm rad}$	5×10^{-4}	OP mono
C2	[1.2; 1.4]	0.1	0.06	–	1.23	–	g	5×10^{-4}	OPAL
D1	[1.3; 1.5]	0.025	[−0.1; 0.2]	0.05	[0.2; 4.0]	0.01 in Y	g	Parametrised	OPAL
D2	[1.3; 1.5]	0.025	[−0.1; 0.2]	0.05	[0.2; 4.0]	0.01 in Y	No	None	OPAL
D3	[1.3; 1.5]	0.025	[−0.1; 0.2]	0.05	[0.2; 4.0]	0.01 in Y	No	None	OPAL
D4	[1.3; 1.5]	0.025	[−0.1; 0.2]	0.05	[0.2; 4.0]	0.01 in Y	g	None	OPAL

Notes. In the 'Atomic Diffusion' column, g indicates that the models include atomic diffusion without radiative accelerations and $g + g_{\rm rad}$ indicates that the models include atomic diffusion with radiative accelerations. In the following column ΔM_0 is the value of reference mass used to compute turbulent mixing; 'None' means that we do not include turbulent mixing in the grid.

3. Atomic diffusion and surface abundances

In this section, we focus on the evolution of the surface chemical composition, quantifying the differences between the predicted [Fe/H] and [M/H] when atomic diffusion is included in stellar models. We also compare the surface abundance evolution induced by atomic diffusion including or not radiative accelerations.

3.1. Surface abundances

The chemical composition of a star can be defined by

$$X + Y + Z = 1, \tag{6}$$

where X is the mass fraction of hydrogen, Y is the mass fraction of helium (^{3}He + ^{4}He), and Z is the mass fraction of all the elements heavier than helium. However, these quantities are not directly observed in stars, but the surface abundances of individual element relative to other elements are. By definition, the element surface abundance of an element A relative to an element B is

$$[A/B] = \log_{10}(N_A/N_B) - \log_{10}(N_A/N_B)_\odot, \tag{7}$$

where N_A and N_B are the surface number fraction of the elements A and B, respectively. The term indexed with $\odot$ refers to the photospheric solar values. Following this definition, the iron abundance can be obtained with the expression

$$[{\rm Fe/H}] = \log_{10}(N_{\rm Fe}/N_{\rm H}) - \log_{10}(N_{\rm Fe}/N_{\rm H})_\odot. \tag{8}$$

The expression can be converted into mass fraction with the expression

$$\log_{10}(X_{\rm Fe}/X_{\rm H})_\odot = \log_{10}(N_{\rm Fe}/N_{\rm H})_\odot + \log_{10}(A_{\rm Fe}), \tag{9}$$

where $X_{\rm H}$ and $X_{\rm Fe}$ are the surface hydrogen and iron mass fractions, $N_{\rm H}$ and $N_{\rm Fe}$ are the number of atoms of hydrogen and iron at the solar surface, and $A_{\rm Fe}$ is the atomic mass of iron. Most of the time, instead of using Eq. (8), the surface iron abundance [Fe/H] is approximated by the metallicity [M/H] with the expression

$$[{\rm Fe/H}] \sim [{\rm M/H}] = \log_{10}(Z/X) - \log_{10}(Z/X)_\odot. \tag{10}$$

To understand the possible uncertainties caused by this approximation for stars others than the current Sun, we compare the surface iron abundances obtained from Eq. (8) with the metallicity obtained from Eq. (10). For both equations, we use the solar values of Asplund et al. (2009), $\log_{10}(N_{\rm Fe}/N_{\rm H})_\odot = -4.50$ and $\log_{10}(Z/X)_\odot = -1.7423$.

3.2. Variation in [Fe/H] with evolution

Figure 1 shows the evolution of [Fe/H] estimated using Eq. (8) (solid lines) and the metallicity estimated with Eq. (10) (dashed lines) for three different masses, with and without radiative acceleration. In this section we first focus on the global behaviour of the iron surface abundance throughout the evolution.

Models including atomic diffusion without radiative accelerations (grid A). During the evolution of models without radiative acceleration, the surface [Fe/H] (blue solid curves) decreases until it reaches a minimum (largest depletion, LD). This minimum depends on the mass. On one hand, the LD is larger for a 0.7 $M_\odot$ model than for a 1.0 $M_\odot$ model because the duration of the MS is longer for lower masses, so atomic diffusion has more time to act. On the other hand, the LD is larger for a 1.4 $M_\odot$ model than for a 1.0 $M_\odot$ model because atomic diffusion is much more efficient for higher masses. This is partly due to the smaller size of the surface convective zone. Figure 2 shows the Kiel diagram ($\log(g)$ against $T_{\rm eff}$) for some models of grid A (colour-coded for the value of [Fe/H]). The LD of each track is represented by the down triangles. We can see in this figure that for models without convective cores, this point occurs at the end of the MS, while for models with convective cores, it occurs in the MS.

After the LD the surface [Fe/H] increases to its maximum due to the first dredge-up (i.e. the penetration of the surface convective layers during the sub-giant branch and low RGB). This point in the diagram is represented by the up triangle in Fig. 2. The level of [Fe/H] reached depends on the stellar mass, with values close to the initial one. For the models presented in Fig. 2, only those with masses higher than 1.0 $M_\odot$ can reach or slightly surpass the initial composition. Figure 1 shows, for the 1.4 $M_\odot$ models, that the iron abundance reaches a local maximum at the end of the MS, then decreases until the end of the MS hook, before increasing again. This phenomenon is due to the presence of a convective core in the MS. During the transition from MS to the SG phase, the stellar structure adjusts rapidly to the cessation of nuclear reactions in the core, which induces a brief pause in the deepening of the surface convective envelope (around 3 Gyr in the bottom panel of Fig. 1).

After the maximum value of [Fe/H] is reached on the RGB phase, atomic diffusion slightly decreases it (up to about 10^{-5} dex). However, the depletion is much slower due to the large extent of the convective envelope. These effects are

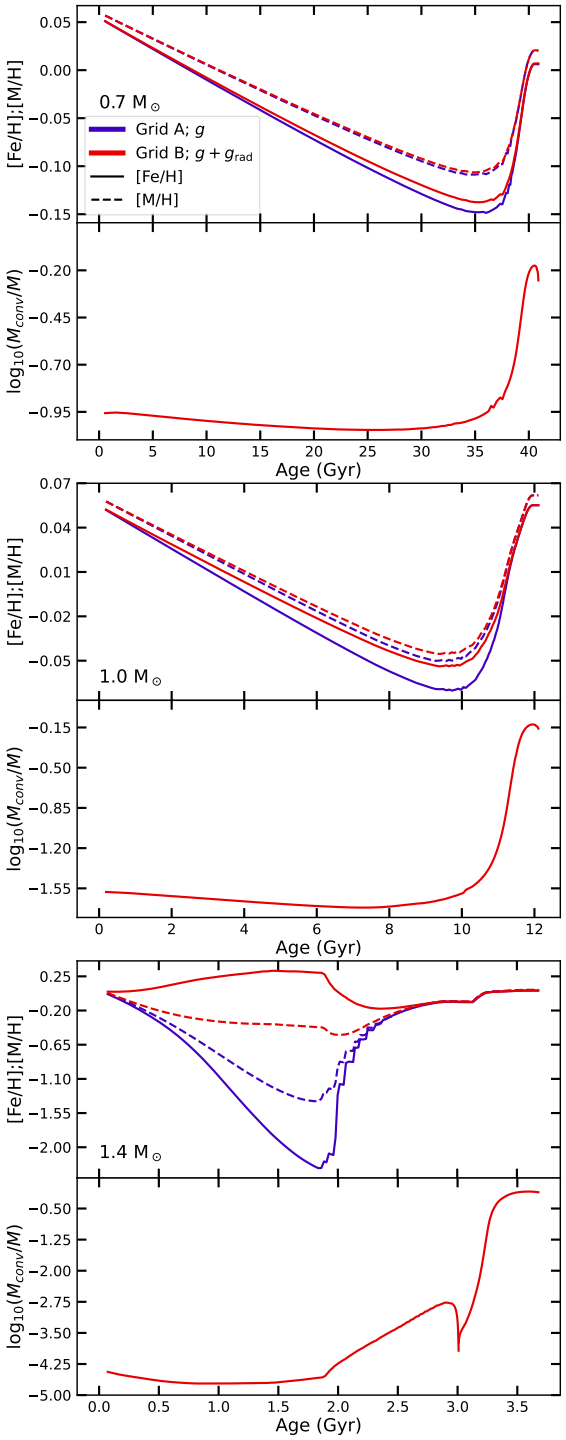

Fig. 1. Variation in [Fe/H] (solid lines, top of all subplots) and [M/H] (dashed lines, top of all subplots), and evolution of the convective envelope mass divided by the total mass of the model (bottom of all subplots) from the ZAMS to the tip of the RGB for $[Fe/H]_i = 0.06$. The red and blue lines represent models with and without radiative acceleration. *Top panels*: are for 0.7 $M_\odot$ models, *middle panels*: for 1.0 $M_\odot$ models, and *bottom panels*: for 1.4 $M_\odot$ models.

insignificant compared to the observed uncertainties on [Fe/H]. A zoom-in of Fig. 2 around the F-type stars is also presented in the top panels of Fig. A.1.

Models including atomic diffusion with radiative accelerations (grid B). With radiative accelerations (red curves), the

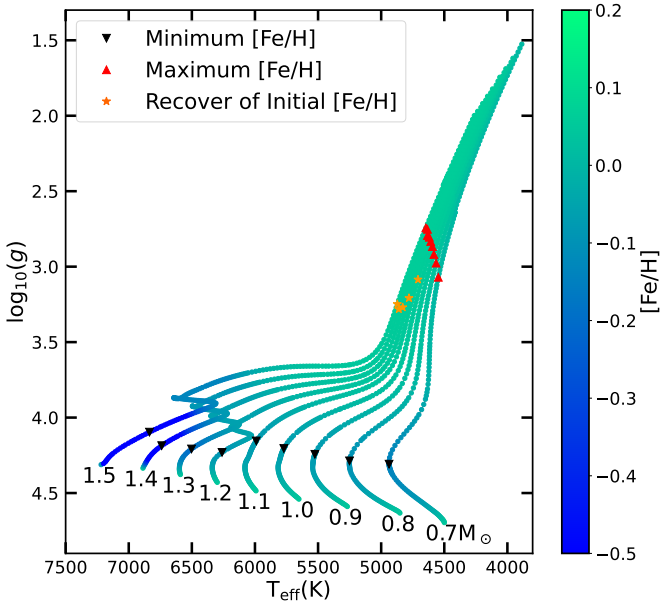

Fig. 2. Kiel diagram of models from Grid A with $[Fe/H]_i = 0.06$ and $\frac{\Delta Y}{\Delta Z} = 1.23$. The colour indicates the value of [Fe/H] at the stellar surface, the triangles down are the points where [Fe/H] reach a minimum, the triangles up are the points where [Fe/H] reaches a maximum, and the star symbols are the points where [Fe/H] reaches the initial value.

behaviour is similar for the 0.7 and 1.0 $M_\odot$ models. The iron surface abundance decreases with time, albeit at a lower rate, although for models with 1.4 $M_\odot$ we can see a substantial difference in the evolution of [Fe/H]. We see that the [Fe/H] increases at the surface during the MS evolution leading to higher abundances than the initial values, which avoids the large depletion of iron seen for models without radiative acceleration. After the MS the values of [Fe/H] becomes similar to the models that do not include radiative accelerations and follow the same evolution. This shows that by including radiative accelerations the chemical evolution after the MS induces a negligible difference in the surface abundances for stars with masses lower than 1.4 $M_\odot$ at solar metallicity. All the results presented in this section are consistent with previous studies (e.g. Deal et al. 2018, and references therein). The middle panels of Fig. A.1 show this evolution of the surface [Fe/H] and [M/H] for F-type stars.

3.3. [Fe/H] vs. [M/H]

Independently of the transport included in stellar models, it is important to compare the correct chemical indicators between data and models. For example, even if [M/H] can be approximated by [Fe/H] in a specific case (i.e. the Sun), this approximation is only valid if the ratio of X(Fe) to Z remains the same. However, it has already been shown that this is not always the case, for example for alpha-enriched stars (Salaris & Weiss 2001) or for F-type stars in which atomic diffusion modifies the chemical mixture (Deal et al. 2018). This is especially crucial when only [Fe/H] is used as a chemical constraint to infer the stellar properties of stars.

For the 0.7 and 1.0 $M_\odot$ models with and without radiative accelerations (grids B and A, respectively), Fig. 1 shows that both the surface [Fe/H], estimated with the iron abundance (Eq. (8)), and the actual metallicity, estimated using Z/X ([M/H], Eq. (10)) have a similar evolution, with the first having a faster decrease rate than the second. For the 1.4 $M_\odot$ model

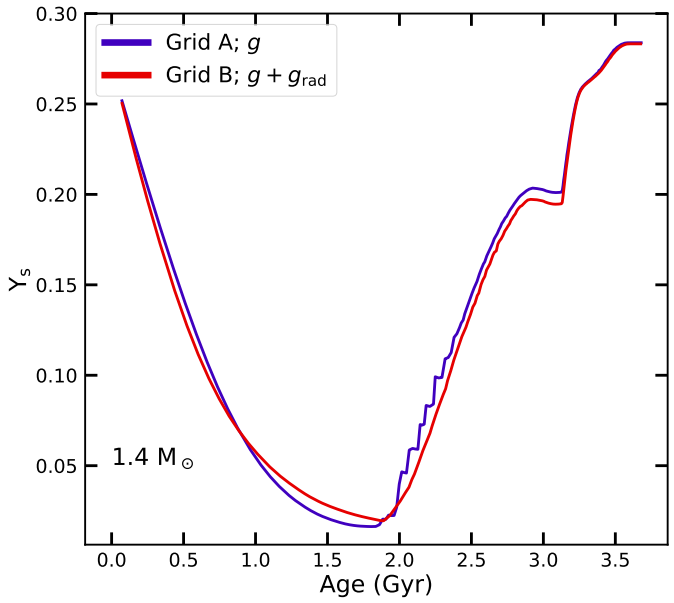

Fig. 3. Evolution of the surface mass fraction of helium with (red curves) and without (blue curves) radiative accelerations for a 1.4 $M_\odot$ stellar model with $[M/H]_i = 0.06$ and $\Delta Y/\Delta Z = 1.23$.

with radiative accelerations, we see instead that [Fe/H] increases while [M/H] decreases. This is in agreement with the results of Deal et al. (2018). This occurs because the transport of chemical elements induced by atomic diffusion is different for each element. While iron is accumulated at the surface, most of the metals are depleted from the surface. Without radiative accelerations we expect iron to be depleted more quickly than the other metals.

Therefore, with radiative accelerations, approximating [Fe/H] using Z/X induces an overestimation of the actual [Fe/H] for the low masses and an underestimation for the case of 1.4 $M_\odot$ and higher masses. For models that do not include radiative accelerations the difference can be up to ∼0.04 dex for a 0.7 $M_\odot$ model, ∼0.02 dex for a 1.0 $M_\odot$ model, and ∼0.8 dex for a 1.4 $M_\odot$ model, at solar metallicity. For models including radiative accelerations, this difference can be up to ∼0.03, ∼0.01, and ∼0.8 dex for the 0.7, 1.0, and 1.4 $M_\odot$ models, respectively. The effect is larger for the 1.4 $M_\odot$ model since the diffusion timescale is smaller compared to the lower masses, and the differences between Z and iron are then more significant. This shows how crucial the definition of metallicity in stellar models may be, and how the way it is compared to abundances obtained from observations can lead to uncertainties, especially for the more massive stars in which competing transport to atomic diffusion is not always efficient (e.g. AmFm stars; Richer et al. 2000).

3.4. Variation in helium surface abundances

Atomic diffusion acts with different efficiency for each element. Not all the elements are in fact supported by radiative acceleration. This is the case of helium. As shown in Fig. 3 for a 1.4 $M_\odot$ model, the helium surface abundance goes down to 0.01 in mass fraction, while it is not expected to go below about 0.18 for solar-like oscillating MS stars (Verma et al. 2019). This strengthens the need for the implementation of competing transport processes in stellar models.

4. Turbulent mixing in stellar models

As seen in the previous section, atomic diffusion changes the surface chemical composition and radiative accelerations need to be included for the more massive models. However, the variations shown in Fig. 1 for the 1.4 $M_\odot$ models are unrealistic compared to the variations observed for stars in clusters (e.g. Gruyters et al. 2014, 2016; Semenova et al. 2020). To account for the missing transport processes in stellar models, turbulent mixing was proposed as a solution (e.g. Richer et al. 2000; Michaud et al. 2011b). In this section we use the expression proposed by Richer et al. (2000) for turbulent mixing, taking as a reference the calibration performed by VSA19 and we quantify the impact of this calibration on the surface abundances of solar-like oscillating MS stars. Then we carry out a parametrisation of the turbulent mixing that takes into account the effects of radiative accelerations with the objective to make the computation of stellar models faster. From here we focus on stars with convective cores for which atomic diffusion leads to unexpected surface abundance variations. This corresponds to stars with mass higher than ∼1.2 $M_\odot$ at solar metallicity. This mass is different for every initial chemical composition.

4.1. Evolution of the surface abundances

We first investigate the surface abundance evolution of iron with models that include the effect of turbulent mixing, following the calibration in VSA19, and atomic diffusion with radiative accelerations. The evolution of the surface [Fe/H] for two different masses (1.2, 1.4 $M_\odot$) is shown in Fig. 4. We start by focusing on the models including radiative accelerations and turbulent mixing (grid C1, purple curves). The inclusion of turbulent mixing attenuates the depletion of [Fe/H] for the stellar model with 1.2 $M_\odot$. In this case the LD is about 0.02 dex smaller than the model without turbulent mixing (grid B, red curves). The inclusion of turbulent mixing has a more significant effect in the stellar model with 1.4 $M_\odot$. The surface enrichment predicted by the model that includes atomic diffusion with radiative accelerations is now prevented. Instead, the turbulent mixing model exhibits a steady depletion of iron during evolution because the envelope mass homogenised by turbulent mixing reaches depths where the effects of gravitational settling are dominant compared to radiative acceleration.

For the models including turbulent mixing and atomic diffusion without radiative accelerations (grid C2, cyan curves) the depletion is larger than in the previous case (grid C1). Even if radiative accelerations are not dominant compared to the gravity below the reference point ($\Delta M_0 = 5 \times 10^{-4}$ $M_\odot$, above this point the turbulent mixing homogenises the chemical composition), a difference between grid C1 and C2 models is still present (up to 0.015 dex for the 1.4 $M_\odot$ models). This indicates that radiative accelerations should still not be neglected in this case.

The difference between [M/H] and [Fe/H] is about 0.01 dex for the 1.2 and 1.4 $M_\odot$ models including turbulent mixing of grid C2. This is smaller than for the models presented in Sect. 3.3, but still close to the order of magnitude of the uncertainties of surface abundances sometimes found in the literature.

Lighter elements like helium are not affected by radiative accelerations. Models including these processes or not will predict the same depletion of helium at the surface. This can be seen in Fig. 5, where the helium surface abundance is shown for the 1.4 $M_\odot$ models presented in Fig. 4. As expected for this element, models with turbulent mixing predict the same surface abundance variation with and without radiative acceleration. We

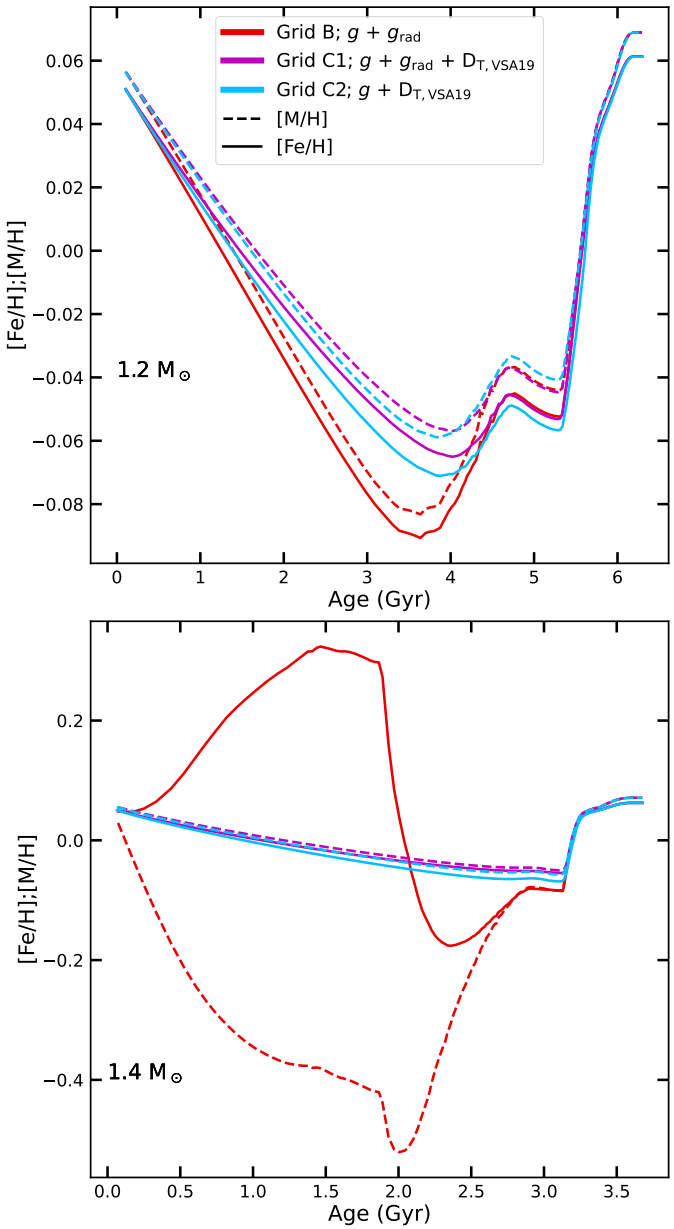

Fig. 4. Variation in [Fe/H] (solid lines) and [M/H] (dashed lines) from the ZAMS to the tip of the RGB for $[Fe/H]_i = 0.06$. The purple and red lines represent models with and without turbulent mixing (both with radiative acceleration), and the cyan lines represent the model with only turbulent mixing. *Top panel*: is for the 1.2 $M_\odot$ models and *bottom panel*: is for the 1.4 $M_\odot$ models.

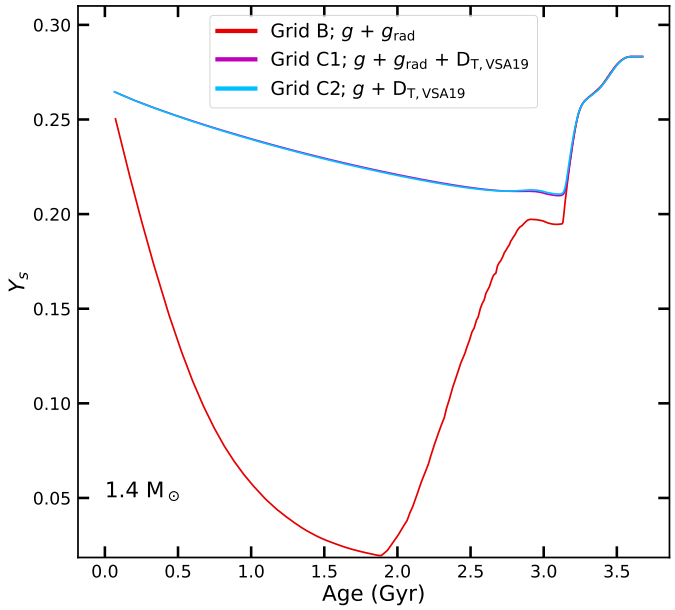

Fig. 5. Same as Fig. 4, but for the evolution of helium surface abundances of the 1.4 $M_\odot$ model.

can also see that at the beginning of the evolution (at the zero age main sequence, ZAMS) there is a different abundance at the stellar surface. This is due to an extra depletion of helium occurring during the PMS because of the more efficient atomic diffusion in models without turbulent mixing.

4.2. Parametrising radiative acceleration on iron with a turbulent diffusion coefficient

As seen in the previous section, neglecting radiative accelerations when the turbulent mixing calibrated by VSA19 is taken into account leads to differences of up to 0.015 dex in [Fe/H]. This difference could even be larger for more massive stars or stars undergoing less efficient competing macroscopic transport. With the objective of computing large grids of stellar models for the fundamental stellar property inferences of large-scale surveys, the effect of radiative accelerations should be included somehow for accurate stellar properties. Since iron is depleted in all models including the VSA19 turbulent mixing considered in this study, it is possible to parametrise the effect of the radiative acceleration for this element by an increase in the efficiency of turbulent mixing (i.e. an increase in the mass of the reference point ΔM_0). This ensures that the computed models will have an iron surface abundance evolution that is close to the accurate value. Moreover, the implementation of turbulent mixing significantly reduces the variation in the metal mixture in the whole model, thus allowing the use of the classical opacity table. Simultaneously, it reduces the computationally demanding calculation of radiative accelerations and allows larger grids to be built in shorter times. Nevertheless, this parametrisation of the effect of radiative accelerations on iron should only be used in specific applications such as the stellar properties inference, which only uses [Fe/H] as a constraint for the chemical composition. An alternative and optimal solution would be to use the single valued parameter (SVP) approximation (Alecian & LeBlanc 2020) in order to compute radiative accelerations more efficiently. However, this method has not been implemented yet in MESA.

The parametrisation we propose is equivalent to rewriting the diffusion equation as

$$\rho\frac{\partial X_i}{\partial t} = A_i m_p\left[\sum_j (r_{ji} - r_{ij})\right] + \frac{1}{r^2}\frac{\partial}{\partial r}\left[r^2\rho D_{\mathrm{T,Fe}}\frac{\partial X_i}{\partial r}\right] - \frac{1}{r^2}\frac{\partial}{\partial r}\left[r^2\rho v_i'\right], \quad (11)$$

with

$$v_i' = D_{i,p}\left[-\frac{\partial \ln X_i}{\partial r} + k_\mathrm{T}\frac{\partial \ln T}{\partial r} + \frac{(Z_i+1)m_\mathrm{p}g}{2k_\mathrm{B}T} - \frac{A_i m_\mathrm{p} g}{k_\mathrm{B}T}\right]. \quad (12)$$

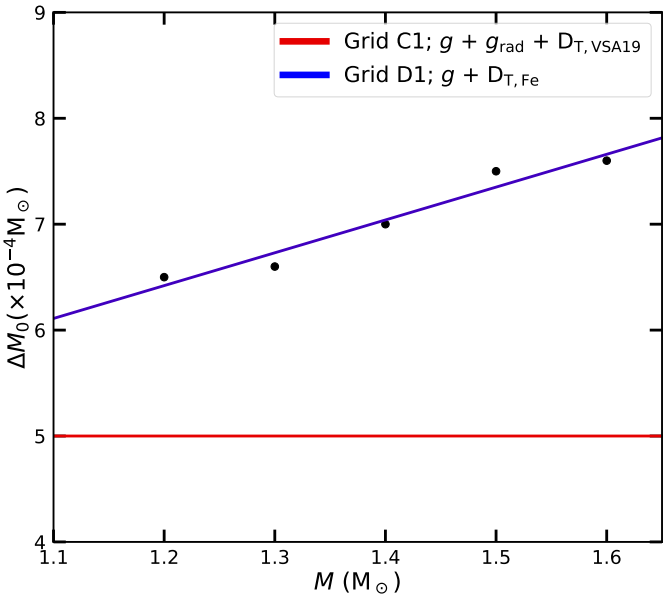

Fig. 6. Values of the ΔM_0 as a function of the stellar mass parametrised in Sect. 4.2 (black dots) and calibrated by VSA19 (red line). The blue line represents the linear fit presented in Eq. (13).

where $D_{T,Fe}$ is parametrised using Eq. (4) to make the surface abundance variation in iron match that of models including radiative accelerations.

We quantify ΔM_0 as a function of the stellar mass following the procedure described in Appendix B. Figure 6 shows the increase in ΔM_0 needed to obtain a [Fe/H] evolution similar to models including turbulent mixing ($D_{T,VSA19}$) and radiative accelerations (grid C1). The increase in ΔM_0 with mass is explained by the fact that for more massive stars radiative accelerations are more efficient at pushing iron to the surface. For the input physics (see Sect. 2.4), the initial chemical composition (solar calibrated), and the reference calibration value $D_{T,VSA19}$ used to compute the approximation and the models we derive a simple linear expression that describes the variation in ΔM_0 with the mass:

$$\Delta M_0 \left(\frac{M^*}{M_\odot}\right) = 3.1 \times 10^{-4} \times \left(\frac{M^*}{M_\odot}\right) + 2.7 \times 10^{-4}. \quad (13)$$

This expression should be calibrated every time the input physics of the model changes.

4.2.1. Changing initial metallicity

As previously stated, the efficiency of atomic diffusion depends on the initial chemical composition, and so the parametrisation presented in Eq. (13) may not be valid for every composition. In order to test its validity domain, we compute, using the turbulent diffusion coefficient parametrised in the previous section ($D_{T,Fe}$), models with 1.2 and 1.4 $M_\odot$ and with $[Fe/H]_i = -1.0, -0.34, -0.04, 0.06, 0.16$, and 0.46 dex. Figure 7 shows the evolution of the surface [Fe/H] for the different initial values. Firstly, we see that the $D_{T,Fe}$ models give very satisfactory iron abundance predictions for $[Fe/H]_i$ between −0.4 and 0.4 dex. For lower initial metallicity, the $D_{T,Fe}$ models deviate from models including radiative accelerations by up to 0.04 dex. This is most likely due to the decrease in the convective envelope with $[Fe/H]_i$, which allows radiative accelerations to affect the surface abundances more strongly.

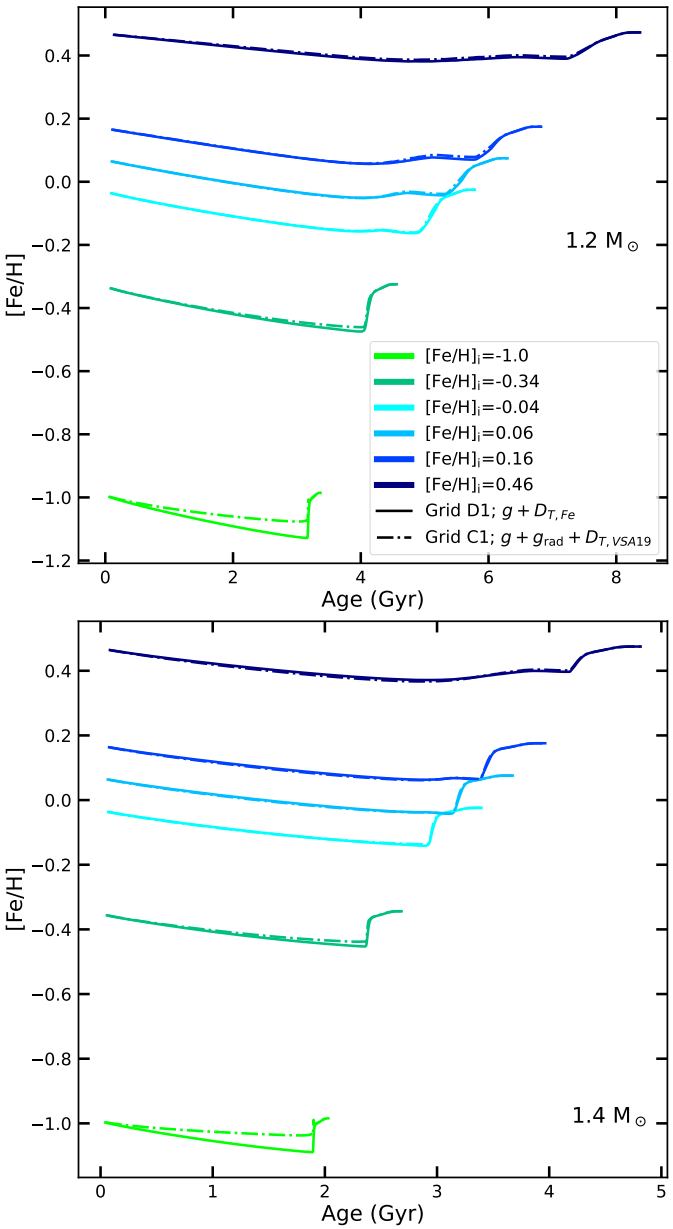

Fig. 7. Evolution of [Fe/H] with time for 1.2 $M_\odot$ (*top panel*) and 1.4 $M_\odot$ (*bottom panel*) at different initial chemical compositions. The solid lines represent models including atomic diffusion (without radiative accelerations) and the parametrisation of $D_{T,Fe}$ presented in Sect. 4.2, and the dot-dashed lines represent models including atomic diffusion with radiative accelerations and the $D_{T,VSA19}$ calibrated by VSA19.

4.3. Effects for other elements

Each element is affected differently by radiative accelerations, and the parametrisation presented in Sect. 4.2 may not be adapted for other elements than iron. Figure 8 shows the evolution of the surface abundances of He, C, N, O, Mg, Al, Ca, and Fe for two 1.4 $M_\odot$ models: one including turbulent mixing ($D_{T,VSA19}$) and atomic diffusion with radiative accelerations (grid C1) and the second including the parametrisation presented in this study ($D_{T,Fe}$).

For helium (top left panel of Fig. 8), the parametrised $D_{T,Fe}$ retains more helium at the surface. However, the difference is smaller than 0.025 dex (0.006 in mass fraction), which is of the

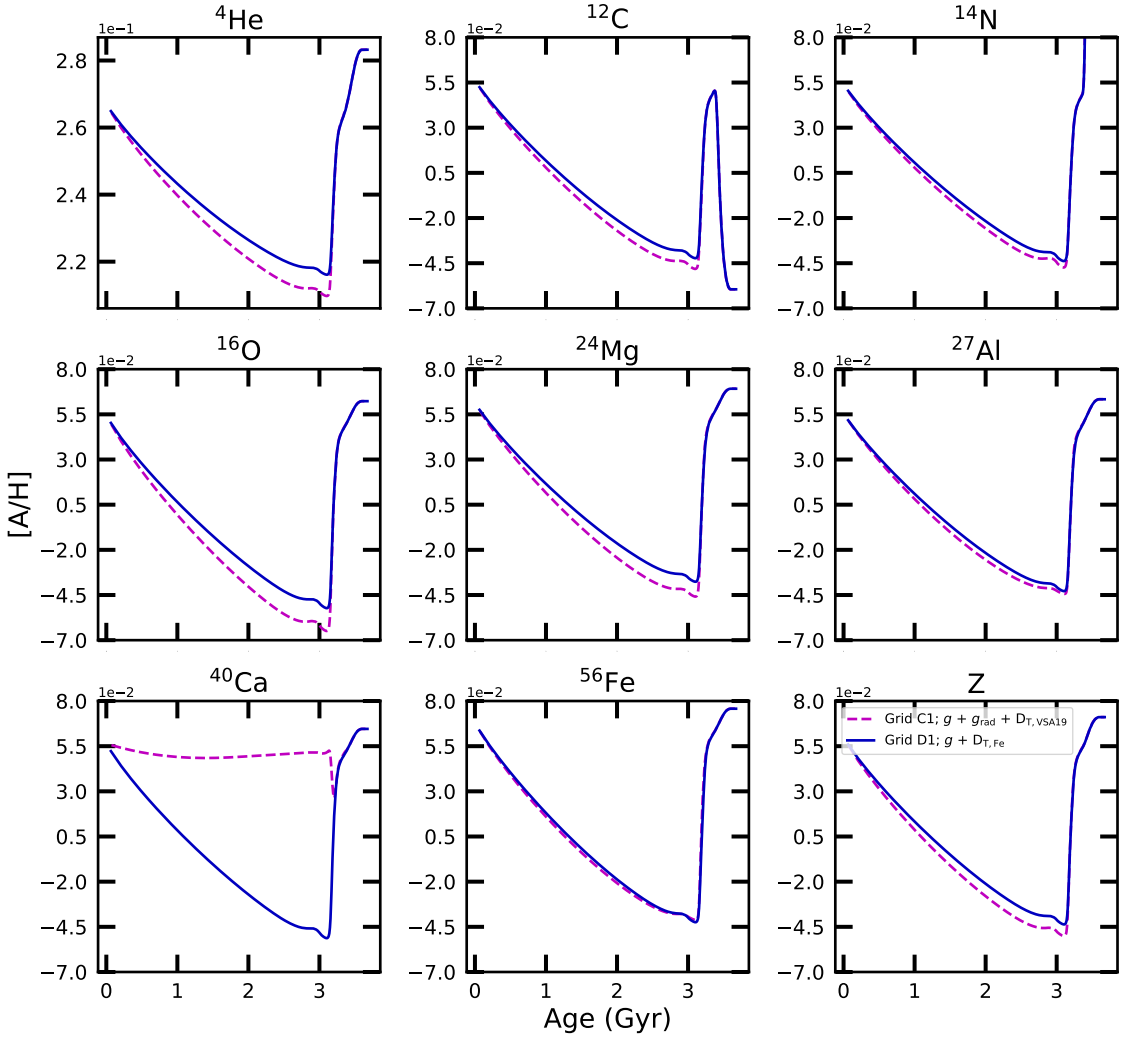

Fig. 8. Evolution of the surface abundance of some chemical elements for a 1.4 $M_{\odot}$ model. The purple dashed lines represent a model including atomic diffusion with radiative accelerations and the turbulent mixing calibrated by VSA19, and the blue solid lines represent a model including atomic diffusion without radiative acceleration and the $D_{\rm T,Fe}$ turbulent mixing parametrised in Sect. 4.2.

order of magnitude of the uncertainty of the helium surface abundances obtained by Verma et al. (2019).

Elements like carbon, nitrogen, magnesium, and aluminium (top middle, top right, middle, and middle right panel of Fig. 8, respectively) show good agreement with very small differences (about 0.006 dex, 0.004 dex, 0.008 dex, and 0.004 dex, respectively). This agreement is due to the fact that these elements are either not supported by radiative accelerations (C, N, Mg) or are supported with a similar efficiency to iron (Al) in this specific case.

For oxygen (middle left panel of Fig. 8), the $D_{\rm T,Fe}$ parametrisation starts to show a significant difference of about 0.013 dex, which is comparable to observed uncertainties. It indicates that radiative acceleration has a smaller impact on this element compared to the others.

Finally, for calcium (bottom left panel of Fig. 8), we see that our parametrisation cannot reproduce the radiative acceleration in this element. In the model with radiative acceleration and $D_{\rm T,VSA19}$ turbulent mixing (Grid C1), calcium is almost at equilibrium during the evolution (gravitational settling and radiative acceleration cancelling each other out). Radiative acceleration on calcium is greater than on iron in this case. This behaviour cannot be reproduced by turbulent mixing calibrated on an element that is not in this situation (iron in this case), and is the reason why the parametrisation we propose cannot be valid for all elements.

4.4. Maximum variation in the iron surface abundance in solar-like stars

Figure 9 shows the maximum variation in [Fe/H] for stellar models including atomic diffusion without (top panel, Grid A) and with (middle panel, Grid B) radiative accelerations, and $D_{\rm T,Fe}$ models (bottom panel, Grid D1). For models including atomic diffusion without radiative accelerations (grid A) we verify that the maximum variation (in this case the largest depletion) increases with mass as the efficiency of gravitational settling increases. We also see that at higher masses the maximum variation reaches very high and unrealistic values (up to 2 dex) compared with variations observed in clusters (e.g. Gruyters et al. 2014, 2016; Semenova et al. 2020). The maximum variation also depends on the chemical composition. We see that by decreasing the initial metallicity, the variations in [Fe/H] reach unrealistic values at lower masses. Moreover, the higher $\Delta Y/\Delta Z$ is, the sooner the depletion appears (in terms of mass). A higher initial metallicity leads to a higher opacity, hence a higher convective

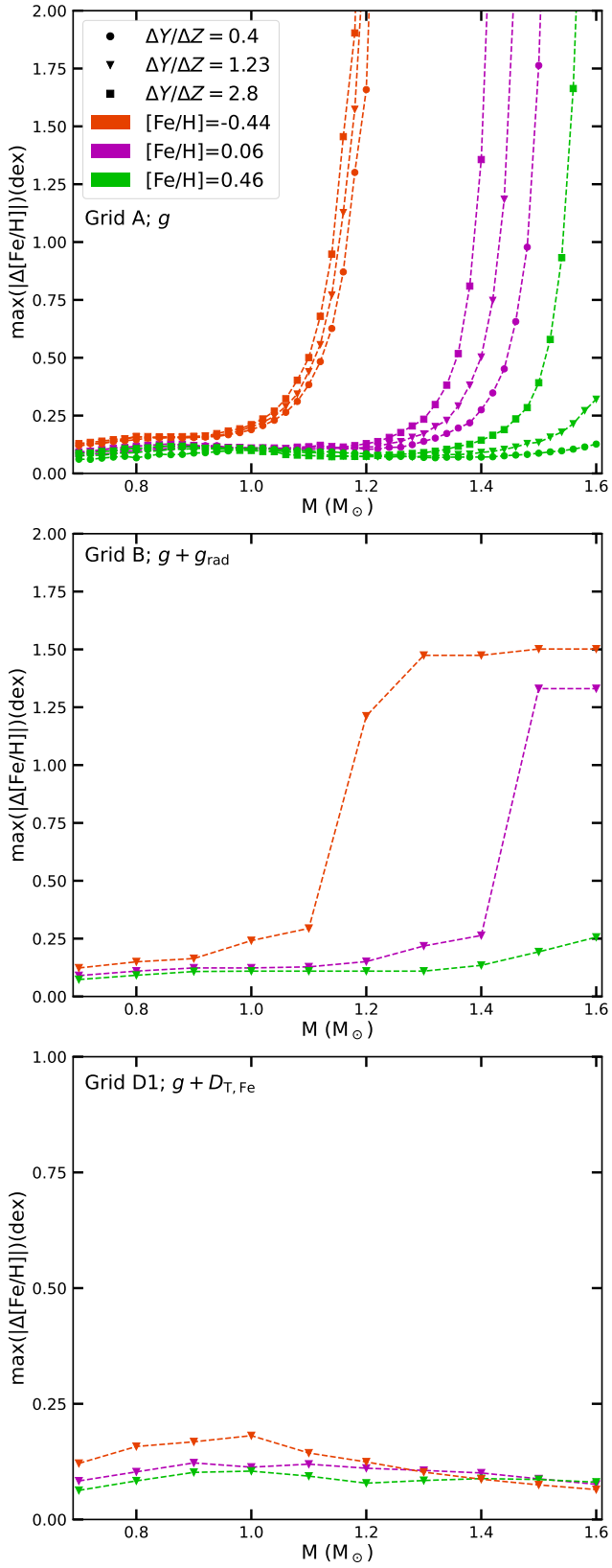

Fig. 9. Maximum variation in [Fe/H] during the evolution (up to the tip of RGB) according to mass. The colours and symbols correspond to the values of $[Fe/H]_i$ and $\Delta Y/\Delta Z$. The maximum variation was determined for ages less that 13.5 Gyr for the models that evolve on longer timescales ($M \lesssim 0.95$). *Top panel*: includes atomic diffusion without radiative accelerations, the *middle panel* shows models that include radiative acceleration, and the *bottom panel* shows $D_{T,Fe}$ models.

region and a less efficient effect of atomic diffusion. A higher $\Delta Y/\Delta Z$ decreases the opacity, which leads to a shallower convective zone and a more efficient effect of atomic diffusion.

For models including atomic diffusion without radiative accelerations (grid B), the maximum variation in [Fe/H] corresponds to a depletion or an accumulation at the surface depending on the stellar mass. As seen in the previous plot (top panel of Fig. 9), the maximum variation increases as the stellar mass increases, although for the higher stellar masses it reaches values of maximum variation that are not expected for chemically non-peculiar stars, but only for chemically peculiar stars such as Fm stars (e.g. Richer et al. 2000). The fact that the maximum variation reaches a plateau is due to the saturating effect of radiative accelerations (Michaud et al. 2015). Changing the initial metallicity has a similar effect for models without radiative acceleration. By decreasing the initial metallicity, the variation reaches large values at smaller masses.

For the $D_{T,Fe}$ models (grid D1), we see that the maximum variation in iron is smaller than 0.2 dex during the whole evolution from the MS to RGB. As expected, this shows that turbulent mixing avoids the unrealistic chemical abundance variations induced by atomic diffusion.

5. Impact on the stellar properties inference

In this section we test the models including the parametrisation of turbulent mixing $D_{T,Fe}$ using classical and seismic constraints. For the optimisation of the stellar fundamental properties, we use the code Asteroseismic Inference on a Massive Scale (AIMS; Rendle et al. 2019).

5.1. Seismic validation of the models

To test the seismic validity of the parametrisation, we select three models along the tracks with masses equal to 1.2, 1.4, and 1.6 $M_\odot$ and $[Fe/H]_i = 0.06$ dex computed including atomic diffusion without radiative accelerations and the turbulent mixing calibrated in Sect. 4.2 ($D_{T,Fe}$), as targets (from Grid D1). Then we derive their global fundamental properties (mass, radius and age) using the AIMS optimisation code and the grid C1 (see Sect. 2.4), in order to quantify the validity of the parametrisation. We use the effective temperature, [Fe/H], and the individual frequencies as constraints. We give the two classical constraints the same weight as all the individual frequencies. Because the targets are models, the surface correction terms are not applied. The results are shown in Table 2 where we see that the properties of the three target models are well retrieved within 1σ. Figure 10 shows that the echelle diagrams of the best fitting models of the grid are overlapping one of the three targets. This indicates that the parametrised models give similar results in terms of seismic frequencies to the models including radiative accelerations and can be used to infer the stellar properties.

5.2. Application on Kepler stars

We applied the $D_{T,Fe}$ models for the inference of the global properties of two stars from the Kepler Legacy sample, KIC 2837475 and KIC 112253226. These are two of the three stars used in VSA19. We selected these two stars because they have similar chemical compositions, which allowed us to build a smaller grid for the optimisation procedure. All the seismic and classical constraints are taken from Lund et al. (2017). We also considered the two surface correction terms of Ball & Gizon (2014). Table 3

Table 2. Global fundamental properties of the computed models and those obtained by the optimisation.

	Mass ($M_\odot$)		Radius ($R_\odot$)		Age (Gyr)	
	Model	Inference	Model	Inference	Model	Inference
Model 1	1.2	1.20 ± 0.01	1.240	1.240 ± 0.004	2.1	2.1 ± 0.2
Model 2	1.4	1.40 ± 0.01	1.598	1.596 ± 0.004	1.7	1.7 ± 0.1
Model 3	1.6	1.60 ± 0.01	1.870	1.868 ± 0.004	1.2	1.2 ± 0.1

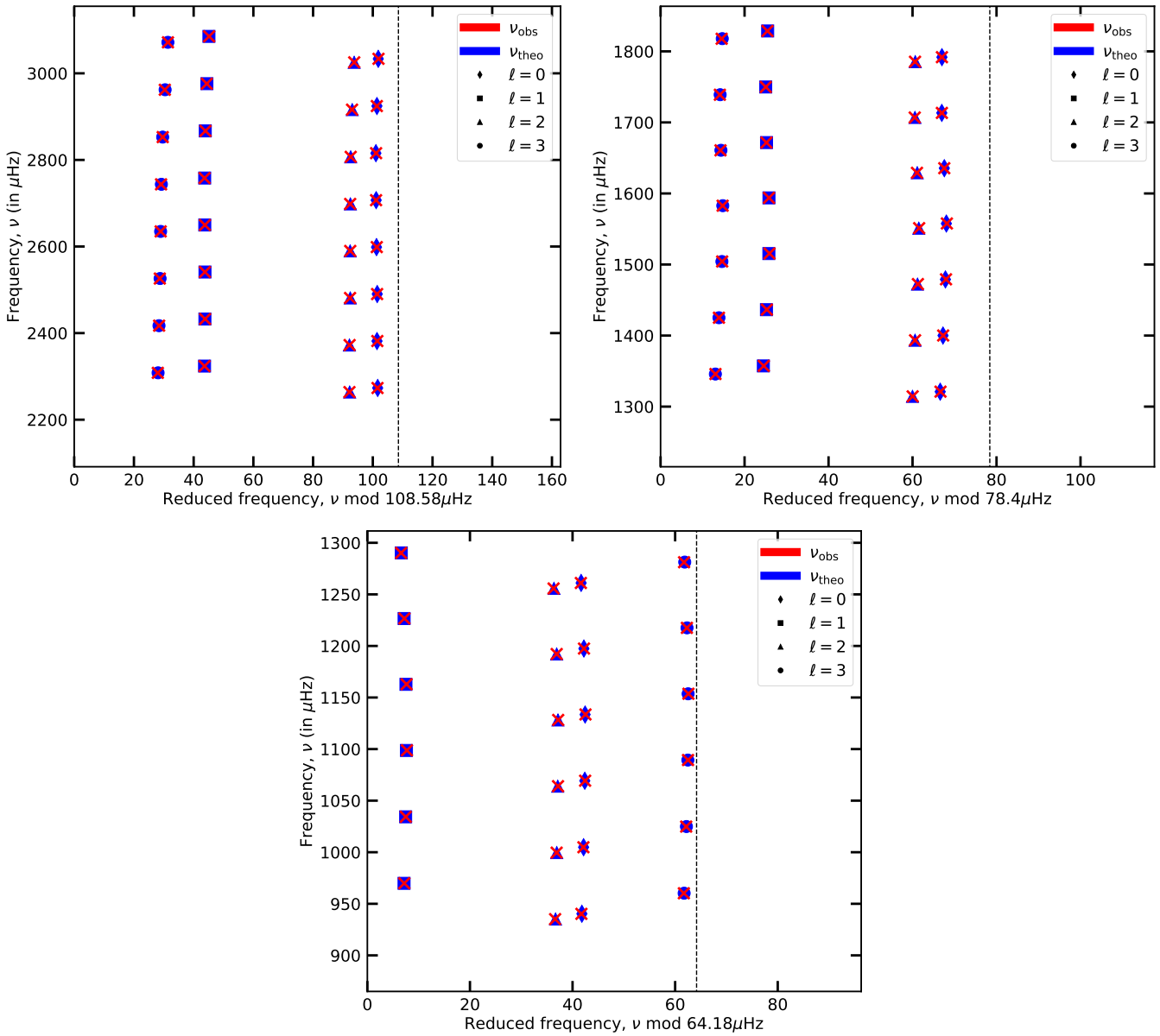

Fig. 10. Echelle diagram of the best optimisation result. *Top panel*: is for a star with 1.2 $M_\odot$, the *middle* is for 1.4 $M_\odot$, and the *bottom* is for 1.6 $M_\odot$. $\nu_{\rm obs}$ are the frequencies used as constraints from the optimised model from Grid D1; $\nu_{\rm theo}$ are the optimised frequencies from Grid C1.

presents the results of the inferred global properties using different grids of stellar models.

We used grids D1, D2, D3, and D4 in order to disentangle the impact of atomic diffusion and the turbulent mixing on the inferred fundamental properties. The comparison of the results obtained with grids D1 and D2 shows the impact of both processes compared to a grid without transport (except convection) using the same solar calibration as grid D1. In this case the masses and radii are similar with both grids and for the two stars. The main impact of including transport in the models is on the age (about 11% and 12% for KIC 2837475 and KIC 11253226, respectively).

The comparison of the results obtained with grids D1 and D3 shows the same impact but with both grids being calibrated to the Sun according to their input physics. The age differences are slightly larger, about 13% and 15% for KIC 2837475 and

Table 3. Global fundamental properties obtained for the two studied stars.

KIC	Grid	Mass ($M_\odot$)	Radius ($R_\odot$)	Age (Gyr)
2837475	D1	1.43 ± 0.03	1.64 ± 0.01	1.54 ± 0.11
2837475	D2	1.42 ± 0.03	1.64 ± 0.01	1.71 ± 0.12
2837475	D3	1.40 ± 0.03	1.62 ± 0.01	1.74 ± 0.12
2837475	D4	1.40 ± 0.05	1.64 ± 0.02	1.82 ± 0.32
11253226	D1	1.41 ± 0.02	1.61 ± 0.01	1.53 ± 0.11
11253226	D2	1.41 ± 0.03	1.61 ± 0.01	1.71 ± 0.11
11253226	D3	1.39 ± 0.03	1.61 ± 0.01	1.76 ± 0.11
11253226	D4	1.41 ± 0.04	1.61 ± 0.02	1.60 ± 0.21

KIC 11253226, respectively. For the radius the difference is 2% for KIC 2837475, and for the mass the differences are about 1% for both stars. Nevertheless, masses and radii are all within 1σ.

The comparison of grids D1 and D4 shows an estimation of the impact of atomic diffusion alone close to the core. To do this we fitted the observed [Fe/H] with the initial [Fe/H] of the models in order not to include the effect of the unrealistic depletion of iron at the surface when no competing transport processes are taken into account. Again, both grids are calibrated to the Sun according to their input physics. The differences in mass and radius are around 1% at maximum. The main effect is on age with similar values to the comparisons with grids D2 and D3. This seems to indicate that most of the effect on age is due to atomic diffusion (mainly gravitational settling close to the core), while turbulent mixing mainly affects the mass and radius determination by inducing a realistic [Fe/H] at the surface of the models. However, we cannot take this as a strong conclusion considering the large error in age for the grid D4.

6. Conclusions

In this work, we used the MESA stellar evolutionary code to compute all the stellar models. We first quantified the effect of atomic diffusion, with and without radiative accelerations, on the evolution of the surface abundance of iron. We confirmed that our models are consistent with previous studies. We also showed that [M/H] and [Fe/H] can be different (~0.02 dex depending on the mass and the transport processes of chemical elements included in the models, i.e. comparable with the error on iron abundance). The observed [Fe/H] being the main constraint on the chemical abundance of stars, comparing it with model predictions of [M/H] may then lead to large uncertainties, especially for the determination of stellar fundamental properties.

We also quantified the effects of turbulent mixing in stellar models. We first considered the calibration done by VSA19. As expected, turbulent mixing is efficient at preventing strong variations in the surface abundances induced by atomic diffusion. Nevertheless, it does not suppress the effect of atomic diffusion. In the context of accurate stellar fundamental property inferences (of mass, radius, and age) of large samples of stars, there is a need for large grids of stellar models including these processes. Because the computation of large grids including atomic diffusion with radiative acceleration is computationally expensive, we propose a parametrisation of the turbulent mixing to include the competing effect of radiative acceleration. We focused the parametrisation on iron alone because this is currently the only element used as a chemical constraint. To achieve this, we parametrised an increase in the efficiency of turbulent mixing to match the competition of the radiative acceleration. For the other elements the parametrisation performs rather well, except for oxygen and calcium. For helium the difference induced by the parametrisation is of the same order of magnitude as the uncertainties on the helium surface abundances obtained from *Kepler* stars (Verma et al. 2019). However, this parametrisation should be used for studies relying only on iron abundances. For a better chemical characterisation, a full treatment of radiative acceleration should still be preferred.

We finally compared models including the full treatment of atomic diffusion and turbulent mixing with the $D_{\mathrm{T,Fe}}$ models. We found no relevant differences in the seismic properties. We also performed the characterisation of two F-type stars of the *Kepler* Legacy sample (KIC 2837475 and KIC 11253226) with four different grids (D1, D2, D3, and D4). We identified that the main effect is on age reaching differences of about 11−15% between the $D_{\mathrm{T,Fe}}$ models and models without transport except for convection. We also identified that atomic diffusion is the main contributor to this difference in age. However, we cannot draw a strong conclusion considering the possible cancellation effect of atomic diffusion and turbulent mixing.

The proposed parametrisation makes the computation of large grids of stellar models as fast as those including atomic diffusion without radiative acceleration. Nonetheless, the parametrisation should be performed any time the input physics is different. For example, input physics predicting hotter models would require a more efficient turbulent mixing to account for the more efficient radiative accelerations.

The parametrisation was designed especially for the purposes of fundamental property inference, and for stellar evolution codes including time-consuming atomic diffusion (with radiative acceleration) computation. The implementation of such parametrisation is straightforward and can be applied using the 'hook' functionality of MESA. The natural next step is the implementation of the single valued parameter approximation in MESA in order to compute models with radiative accelerations in a more efficient way, which requires a deeper modification of the code. This work is only a first step towards the computation of large grids of stellar models including the best compromise between accuracy and computational cost.

Acknowledgements. This work was supported by FCT/MCTES through the research grants UIDB/04434/2020, UIDP/04434/2020 and PTDC/FIS-AST/30389/2017, and by FEDER – Fundo Europeu de Desenvolvimento Regional through COMPETE2020 – Programa Operacional Competitividade e Internacionalização (grant: POCI-01-0145-FEDER-030389). N.M. acknowledges support from the Fundação para a Ciência e a Tecnologia (FCT) through the Fellowship UI/BD/152075/2021 and POCH/FSE (EC). D.B. and M.D. are supported by national funds through FCT in the form of a work contract. We thank the anonymous referee for the valuable comments which helped to improve the paper. We also thank Elisa Delgado-Mena for fruitful discussion.

References

Alecian, G., & LeBlanc, F. 2020, MNRAS, 498, 3420
Angulo, C. 1999, AIP Conf. Ser., 495, 365
Asplund, M., Grevesse, N., Sauval, A. J., & Scott, P. 2009, ARA&A, 47, 481
Ball, W. H., & Gizon, L. 2014, A&A, 568, A123
Baturin, V. A., Gorshkov, A. B., & Ayukov, S. V. 2006, Astron. Rep., 50, 1001
Borucki, W. J., Koch, D., Basri, G., et al. 2010, Science, 327, 977
Campilho, B., Deal, M., & Bossini, D. 2022, A&A, 659, A162
Chaboyer, B., Fenton, W. H., Nelan, J. E., Patnaude, D. J., & Simon, F. E. 2001, ApJ, 562, 521
Cox, J. P., & Giuli, R. T. 1968, Principles of Stellar Structure (New York: Gordon and Breach)
Deal, M., & Martins, C. J. A. P. 2021, A&A, 653, A48
Deal, M., Alecian, G., Lebreton, Y., et al. 2018, A&A, 618, A10
Deal, M., Goupil, M. J., Marques, J. P., Reese, D. R., & Lebreton, Y. 2020, A&A, 633, A23

Dumont, T., Palacios, A., Charbonnel, C., et al. 2020, A&A, 646, A48
Dumont, T., Charbonnel, C., Palacios, A., & Borisov, S. 2021, A&A, 654, A46
Eggenberger, P., Meynet, G., Maeder, A., et al. 2010, A&A, 519, A116
Gruyters, P., Korn, A. J., Richard, O., et al. 2013, A&A, 555, A31
Gruyters, P., Nordlander, T., & Korn, A. J. 2014, A&A, 567, A72
Gruyters, P., Lind, K., Richard, O., et al. 2016, A&A, 589, A61
Herwig, F. 2000, A&A, 360, 952
Hu, H., Tout, C. A., Glebbeek, E., & Dupret, M. A. 2011, MNRAS, 418, 195
Iglesias, C. A., & Rogers, F. J. 1996, ApJ, 464, 943
Imbriani, G., Costantini, H., Formicola, A., et al. 2005, Eur. Phys. J. A, 25, 455
Krishna Swamy, K. S. 1966, ApJ, 145, 174
Kunz, R., Fey, M., Jaeger, M., et al. 2002, ApJ, 567, 643
Lund, M. N., Silva Aguirre, V., Davies, G. R., et al. 2017, ApJ, 835, 172
Michaud, G., Richer, J., & Richard, O. 2011a, A&A, 529, A60
Michaud, G., Richer, J., & Vick, M. 2011b, A&A, 534, A18
Michaud, G., Alecian, G., & Richer, J. 2015, Atomic Diffusion in Stars (Switzerland: Springer International Publishing)
Palacios, A., Talon, S., Charbonnel, C., & Forestini, M. 2003, A&A, 399, 603
Paquette, C., Pelletier, C., Fontaine, G., & Michaud, G. 1986, ApJS, 61, 177
Paxton, B., Bildsten, L., Dotter, A., et al. 2011, ApJS, 192, 3
Paxton, B., Cantiello, M., Arras, P., et al. 2013, ApJS, 208, 4
Paxton, B., Marchant, P., Schwab, J., et al. 2015, ApJS, 220, 15
Paxton, B., Schwab, J., Bauer, E. B., et al. 2018, ApJS, 234, 34
Paxton, B., Smolec, R., Schwab, J., et al. 2019, ApJS, 243, 10
Rauer, H., Catala, C., Aerts, C., et al. 2014, Exp. Astron., 38, 249
Rendle, B. M., Buldgen, G., Miglio, A., et al. 2019, MNRAS, 484, 771
Richard, O., Michaud, G., & Richer, J. 2002, ApJ, 580, 1100
Richard, O., Michaud, G., & Richer, J. 2005, ApJ, 619, 538
Richer, J., Michaud, G., & Turcotte, S. 2000, ApJ, 529, 338
Ricker, G. R. 2016, AGU Fall Meeting Abstracts, P13C-01
Rogers, F. J., & Nayfonov, A. 2002, ApJ, 576, 1064
Salaris, M., & Weiss, A. 2001, A&A, 376, 955
Seaton, M. J. 2005, MNRAS, 362, L1
Semenova, E., Bergemann, M., Deal, M., et al. 2020, A&A, 643, A164
Talon, S. 2008, Mem. Soc. Astron. It., 79, 569
Thoul, A. A., Bahcall, J. N., & Loeb, A. 1994, ApJ, 421, 828
Townsend, R. H. D., & Teitler, S. A. 2013, MNRAS, 435, 3406
Verma, K., & Silva Aguirre, V. 2019, MNRAS, 489, 1850
Verma, K., Raodeo, K., Basu, S., et al. 2019, MNRAS, 483, 4678
Vick, M., Michaud, G., Richer, J., & Richard, O. 2010, A&A, 521, A62

Appendix A: Evolution of the iron surface abundance for different transport processes of chemicals

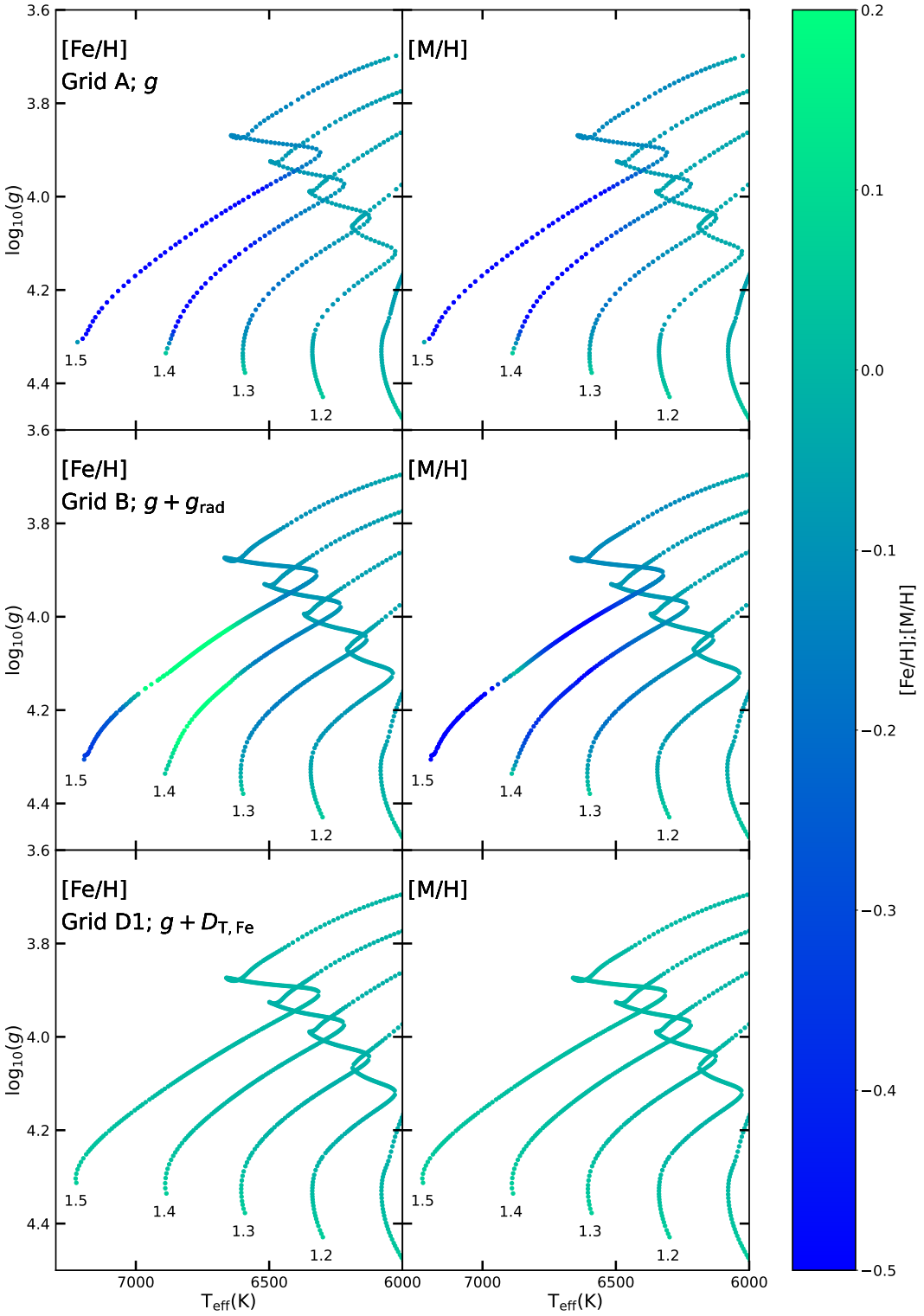

Fig. A.1. Kiel diagram of stars with $[Fe/H]_i$ and $\frac{\Delta Y}{\Delta Z} = 1.23$ (see description in Appendix A). The sub-panels are labelled as follows: g for models that include atomic diffusion without radiative accelerations; $g + g_{rad}$ for models that include atomic diffusion with radiative accelerations; $g + D_{T,Fe}$ for models that include atomic diffusion without radiative accelerations and the turbulent diffusion coefficient parametrised in Section 4.2 (see Table 1 for more details about the input physics).

In this appendix we present Fig. A.1, which shows a Kiel diagram similar to Fig. 2 for some evolutionary tracks focused on the MS of stars with masses higher than 1.2 $M_\odot$. The top panels show models from Grid A, the middle panels from Grid B, and the bottom panels from Grid D1. For the left panels, the colour represents the surface [Fe/H], while it represents the [M/H] for the right panels.

For the [Fe/H], in the case with only gravitational settling (top panel) we see the depletion of the surface abundances due to atomic diffusion, which is stronger for the higher mass stars. When the radiative acceleration is included (middle panel) we see that an accumulation effect can occur for stars with 1.4 $M_\odot$ or higher, instead of the depletion effect for the smaller ones. For models with turbulent mixing (bottom panels), the variations caused by atomic diffusion are smaller and almost unnoticeable in this diagram. For the case of [M/H] (right panels), the results are similar to those for [Fe/H], except for the case with radiative accelerations where we see depletion instead of enrichment in the surface abundances.

Appendix B: Calibrating the turbulent mixing

The parametrised turbulent mixing proposed in this study depends on the stellar physics used in the models. Therefore, it is necessary to calibrate the reference mass any time the physics is changed. We provide here the general steps used to recalibrate our parametrisation for any physics considered:

Step 1: Compute the reference stellar models, with different masses $\geq 1.2\,M_\odot$, including atomic diffusion with radiative accelerations, turbulent mixing with the ΔM_0 value of choice, and the solar initial chemical composition obtained from a solar calibration (set A).

Step 2: For each reference model from Step 1, compute a new set of models (set B) including atomic diffusion without radiative acceleration, and different values of ΔM_0.

Step 3: Compare the surface [Fe/H] evolution of the reference models with those computed with different ΔM_0 values in Step 2 for every mass of the grids. The best value is obtained by a minimisation procedure. The relation between ΔM_0 and the mass is then obtained with linear regression.

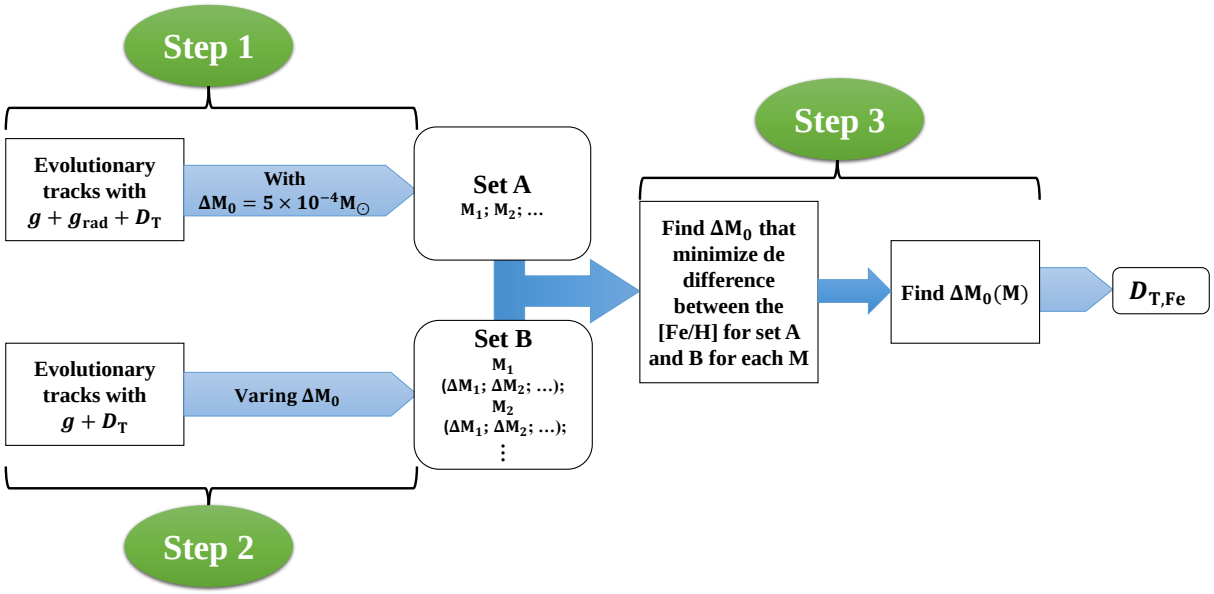

Fig. B.1. Parametrisation procedure of ΔM_0.

Appendix B

Paper Moedas et al. (2024) A&A

A&A, 684, A113 (2024)
https://doi.org/10.1051/0004-6361/202348506

Astronomy & Astrophysics

Characterisation of FG-type stars with improved transport of chemical elements

Nuno Moedas[1,2], Diego Bossini[1,3,4], Morgan Deal[5], and Margarida S. Cunha[1]

[1] Instituto de Astrofísica e Ciências do Espaço, Universidade do Porto, CAUP, Rua das Estrelas, 4150-762 Porto, Portugal
e-mail: nmoedas@astro.up.pt
[2] Departamento de Física e Astronomia, Faculdade de Ciências da Universidade do Porto, Rua do Campo Alegre s/n, 4169-007 Porto, Portugal
[3] Dipartimento di Fisica e Astronomia Galileo Galilei, Università di Padova, Vicolo dell'Osservatorio 3, 35122 Padova, Italy
[4] Osservatorio Astronomico di Padova – INAF, Vicolo dell'Osservatorio 5, 35122 Padova, Italy
[5] LUPM, Université de Montpellier, CNRS, Place Eugène Bataillon, 34095 Montpellier, France

Received 6 November 2023 / Accepted 22 January 2024

ABSTRACT

Context. The modelling of chemical transport mechanisms is crucial for accurate stellar characterisations. Atomic diffusion is one of these processes and is commonly included in stellar models. However, it is usually neglected for F-type or more massive stars because it produces surface abundance variations that are unrealistic. Additional mechanisms to counteract atomic diffusion must therefore be considered. It has been demonstrated that turbulent mixing can prevent excessive variation in surface abundances, and can also be calibrated to mimic the effects of radiative accelerations on iron.
Aims. We aim to evaluate the effect of calibrated turbulent mixing on the characterisation of a sample of F-type stars, and how the estimates compare with those obtained when chemical transport mechanisms are neglected.
Methods. We selected stars from two samples: one from the *Kepler* LEGACY sample and the other from a sample of *Kepler* planet-hosting stars. We inferred their stellar properties using two grids. The first grid considers atomic diffusion only in models that do not show excessive variation in chemical abundances at the stellar surface. The second grid includes atomic diffusion in all the stellar models and calibrated turbulent mixing to avoid unrealistic surface abundances.
Results. Comparing the derived results from the two grids, we find that the results for the more massive stars in our sample show greater dispersion in the inferred values of mass, radius, and age due to the absence of atomic diffusion in one of the grids. This can lead to relative uncertainties for individual stars of up to 5% on masses, 2% on radii, and 20% on ages.
Conclusions. This work shows that a proper modelling of the microscopic transport processes is crucial for the accurate estimation of their fundamental properties – not only for G-type stars but also for F-type stars.

Key words. asteroseismology – diffusion – turbulence – stars: abundances – stars: evolution

1. Introduction

The accurate and precise characterisation of stars is fundamental to our understanding of the evolution of the Universe. Advances have been made thanks to the high-quality data provided by missions such as CoRoT/CNES (Baglin et al. 2006), *Kepler*/K2 (Borucki et al. 2010), and the Transiting Exoplanet Survey Satellite (TESS; Ricker 2016). These missions have provided new constraints with asteroseismology that are linked to the stellar interior and evolution, and missions launched in the near future, such as PLAnetary Transits and Oscillations of stars (PLATO/ESA; Rauer et al. 2014), will provide additional high-precision data.

However, it is currently difficult to achieve the accuracy requirements imposed by the PLATO mission in terms of masses, radii, and particularly ages (an accuracy of 10% is required on the ages of stars similar to the Sun; Rauer et al. 2014). This is due to our lack of knowledge and approximations made in calculations of the physical processes taking place inside stellar models. One source of uncertainty is linked to the modelling of chemical transport mechanisms acting inside stars. These processes can be either microscopic or macroscopic and can compete with each other, leading to redistribution of the chemical elements inside a star, which affects its internal structure, evolution, and abundance profiles. Atomic diffusion is one of these processes. This microscopic transport process is driven mainly by pressure, temperature, and chemical gradients, redistributing the elements throughout the stellar interior (Michaud et al. 2015). Valle et al. (2014, 2015) tested the impact of diffusion on stellar properties and found that neglecting it can lead to uncertainties of 4.5%, 2.2%, and 20% on mass, radius, and age. In a model-based controlled study performed in the context of PLATO, Cunha et al. (2021) found that atomic diffusion can impact the accuracy of the inferred age by approximately 10% for a 1.0 $M_{\odot}$ star close to the end of the main sequence. Furthermore, using real data from *Kepler*, Nsamba et al. (2018) found a systematic difference of 16% in the ages inferred from grids with and without diffusion on a sample of stars with masses of less than $M = 1.2\ M_{\odot}$. These results highlight the need to enhance our understanding and modelling of atomic diffusion and other chemical transport mechanisms.

Atomic diffusion can be decomposed into two main competing subprocesses. One is gravitational settling, which brings the elements from the stellar surface into the deep interior; except for hydrogen, which is transported from the interior to the surface. The other is the radiative acceleration that pushes some

elements – mainly the heavy ones – towards the surface of stars due to a transfer of momentum between photons and ions. Several studies have shown that the efficiency of the processes depends on the stellar fundamental properties, which translate into an increase in the efficiency with mass and a decrease with metallicity (see e.g. Deal et al. 2018; Moedas et al. 2022, and references therein). Although the works of Chaboyer et al. (2001) and Salaris & Weiss (2001) prove that gravitational settling is sufficient to predict the surface abundances of low-mass stars, the effects of radiative accelerations become important for stars with a small surface convective zone (e.g. for solar-metallicity stars with an effective temperature of higher than ~6000 K; Michaud et al. 2015). Nevertheless, for stars more massive than the Sun, atomic diffusion alone causes variations on the surface abundances that are larger than those observed in clusters (e.g. Gruyters et al. 2014, 2016; Semenova et al. 2020). This indicates a need for additional chemical-transport mechanisms, including radiative accelerations. However, radiative acceleration is highly computationally demanding and is therefore often neglected in stellar models (Weiss & Schlattl 2008; Bressan et al. 2012; Hidalgo et al. 2018; Pietrinferni et al. 2021).

Some works (e.g. Eggenberger et al. 2010; Vick et al. 2010; Deal et al. 2020; Dumont et al. 2021, and references therein) demonstrated the necessity to include other chemical-transport processes in competition with atomic diffusion. Nevertheless, identification and accurate modelling of the different processes are still ongoing. The processes that can be considered are either diffusive or advective. If we assume that all of them are fully diffusive, we can parameterise their effects by considering a turbulent mixing coefficient, which can be constrained using the surface abundances of stars in cluster (Gruyters et al. 2013, 2016; Semenova et al. 2020). This was performed in F-type stars by Verma & Silva Aguirre (2019), where the authors used the glitch induced by the helium second ionisation region to calibrate the turbulent mixing coefficient that best reproduces the helium surface abundances. Eggenberger et al. (2022) also showed that the effect of the rotation-induced mixing in the Sun could be parameterised with a simple turbulent diffusion coefficient expression. More recently, Moedas et al. (2022) found that it is possible to add the effects of radiative accelerations on iron into the turbulent mixing calibration. This latter study showed that this calibration depends on the stellar mass (as the mass increases, the value of turbulent mixing is increased to mimic the effect of radiative accelerations). Such parameterisation of the transport should improve determinations of stellar mass, radius, and especially age. Moreover, it allows the inclusion of atomic diffusion without generating the unrealistic surface-abundance variations (for nonchemically peculiar stars) this latter would induce if incorporated alone. However, Moedas et al. (2022) also showed that, as expected, the turbulent mixing calibration is not able to reproduce the evolution of all chemical elements. Nevertheless, it reproduces the abundance of iron, which is the main element used as an observational constraint in stellar models, allowing a global characterisation of stars. We note that the calibration is only valid for a given physics and it should be redone when this latter is changed or when the initial chemical composition is different, especially for different alpha-enhancement.

In this work, we use the calibration presented in Moedas et al. (2022) to characterise a sample of FG seismic stars selected from the *Kepler* LEGACY sample (Lund et al. 2017) and the planet-host stars studied by Davies et al. (2016). We use these stars to see how the calibrated turbulent mixing performs in stellar characterisation and to see how the results compare to the determinations obtained with standard models for F-type stars (i.e. without atomic diffusion).

This article is structured as follows. In Sect. 2 we present the input physics of the grids of stellar models. In Sect. 3 we present the stellar sample we use. In Sect. 4 we explain the optimisation process considered. The main results of the stellar characterisation are presented in Sect. 5. We discuss the results of using different seismic frequency weights and data quality, and a comparison with the results of previous works in Sect. 6. We conclude in Sect. 7.

2. Stellar models

2.1. Stellar physics

In order to assess the impact of turbulent mixing on the stellar properties, we built two grids of stellar models. The models are computed with the Modules for Experiments in Stellar Astrophysics (MESA) r12778 evolutionary code (Paxton et al. 2011, 2013, 2015, 2018, 2019) and the input physics is the same as grid D1 of Moedas et al. (2022). We adopted the solar heavy elements mixture given by Asplund et al. (2009), and the OPAL[1] opacity tables (Iglesias & Rogers 1996) for the higher-temperature regime, and the tables provided by Ferguson et al. (2005) for lower temperatures. All tables are computed for a given mixture of metals. We use the OPAL2005 equation of state (Rogers & Nayfonov 2002). We used the Krishna Swamy (1966) atmosphere for the boundary condition at the stellar surface. We follow the Cox & Giuli (1968) for convection, imposing the mixing length parameter $\alpha_{\rm MLT} = 1.711$, in agreement with the solar calibration we performed 'on the fly' for both grids. In the presence of a convective core, we implemented core overshoot following an exponential decay with a diffusion coefficient, as presented in Herwig (2000):

$$D_{\rm ov} = D_0 \exp\left(-\frac{2z}{fH_{\rm p}}\right), \tag{1}$$

where D_0 is the diffusion coefficient at the border of the convectively unstable region, z is the distance from the boundary of the convective region, $H_{\rm p}$ is the pressure scale height, and f is the overshoot parameter set to $f = 0.01$.

We include turbulent mixing in one of the grids using the prescription of Richer et al. (2000),

$$D_{\rm T} = \omega D({\rm He})_0 \left(\frac{\rho_0}{\rho}\right)^n, \tag{2}$$

where ω and n are constants, ρ and D(He) are the local density and diffusion coefficient of helium, and the index 0 indicates that the value is taken at a reference depth. The D(He) was computed following the analytical expression given by Richer et al. (2000):

$$D({\rm He}) = \frac{3.3 \times 10^{-15} T^{2.5}}{4\rho \ln\left(1 + 1.125 \times 10^{-16} T^3/\rho\right)}, \tag{3}$$

where T is the local temperature. In this work, we set ω and n to 10^4 and 4, respectively (Michaud et al. 2011a,b). We considered the turbulent mixing parameterisation performed by Moedas et al. (2022), where they added the effects of radiative acceleration on iron. These authors used a reference envelope mass (ΔM_0, as the reference depth) to indicate the depth that turbulent mixing reaches inside the star. Moedas et al. (2022) suggest that this parameter varies with the mass of the star as

[1] https://opalopacity.llnl.gov/

Table 1. Parameter space and transport processes of the grids of stellar models.

Grid	Mass ($M_\odot$)		$[M/H]_i$		Y_i		Atomic diffusion	Turbulent mixing
	Range	Step	Range	Step	Range	Step		
A	[0.7;1.75]	0.05	[−0.4;0.5]	0.05	[0.24;0.34]	0.01	Δ[Fe/H]$_{MAX}$ < 0.2	No
B							All models	$D_{T,Fe}$

Notes. The atomic diffusion in the stellar models does not consider radiative accelerations.

$$\Delta M_0 \left(\frac{M^*}{M_\odot}\right) = 3.1 \times 10^{-4} \times \left(\frac{M^*}{M_\odot}\right) + 2.7 \times 10^{-4}. \quad (4)$$

Higher values of ΔM_0 result in more efficient mixing due to turbulent mixing, which in turn accounts for the radiative acceleration process. For more information, see the work of Moedas et al. (2022; and references therein).

2.2. Parameter space

Both grids cover the same parameter space, with masses ranging between 0.7 and 1.75 $M_\odot$ in steps of 0.05 $M_\odot$, initial metallicities $[M/H]_i$[2] from −0.4 to 0.5 dex in steps of 0.05 dex, and an initial helium mass fraction Y_i of between 0.24 and 0.34 in steps of 0.01. The two grids differ in terms of the chemical transport mechanisms incorporated. In grid A, turbulent mixing is not included and only atomic diffusion without radiative acceleration is taken into account, and only in models where maximum variation of the iron content at the surface during all the evolution is Δ[Fe/H][3]> 0.2 dex. This is to avoid unrealistic, excessive variations caused by atomic diffusion (see Moedas et al. 2022 for more details). Also, by considering Δ[Fe/H], we take into account the effects of changing the initial chemical composition on the efficiency of atomic diffusion (the size of the convective envelope changes with the chemical composition). It is therefore expected that the majority of models of low-mass stars will include atomic diffusion in this grid. All stellar models with mass lower than 1.0 $M_\odot$ are not affected by this criterion and include atomic diffusion. Stars with masses higher than 1.4 $M_\odot$ are all affected and atomic diffusion is not included. For all stellar masses in between, the initial chemical composition is the deciding factor as to whether the model is affected or not, with fewer models including atomic diffusion as stellar mass increases. For example, for models with a mass of 1.3 $M_\odot$, only models with $[M/H]_i = 0.5$ and $Y_i = 0.24$ include atomic diffusion, and for models with a mass of 1.0 $M_\odot$, only models with $[M/H]_i = -0.4$ and $Y_i = 0.34$ do not include atomic diffusion.

In grid B, we include turbulent mixing using the calibration performed in Moedas et al. (2022), where the efficiency of the turbulent mixing increases with stellar mass following Eq. (4). The inclusion of this mechanism allows us to avoid the effects of excessive variation in chemical abundances and to include atomic diffusion in all the stellar models of the grid.

For both grids, we saved the models from the zero-age main sequence (ZAMS) to the bottom of the red-giant branch (RGB) stage. We also computed the individual frequencies for each stellar model using the GYRE oscillation code (Townsend & Teitler 2013). The main properties of the grids are summarised in Table 1.

[2] $[M/H] = \log(Z/X) - \log(Z/X)_\odot$.
[3] $[Fe/H] = \log(X(Fe)/X) - \log(X(Fe)/X)_\odot$.

3. Stellar sample

The sample is selected from two different sources. The first source is the *Kepler* LEGACY sample from Lund et al. (2017, hereafter L17), which is a sample of 66 stars with the highest signal-to-noise ratio in the seismic frequencies observed by *Kepler*. The second source is the work of Davies et al. (2016, hereafter D16), a study of 35 stars (32 of them different from L17) that are planet hosts. For both samples, we only selected stars with [Fe/H] > −0.4 to stay within the parameter space of the grids. The smallest value of [Fe/H] is −0.37 dex; we note that the value of [Fe/H] is usually smaller than [M/H] in the stellar models, reaching a difference of up to 0.04 dex, as reported in Moedas et al. (2022), allowing the stars selected to be well within the grid parameter space. We excluded two stars from D16 that present mix-modes in the detection (KIC7199397 and KIC8684730). Finally, we included the degraded Sun as presented in L17 as a control star. Thus, we obtained a sample of 91 stars (62 from L17, 28 from D16, and the Sun). The distribution of the full sample is presented in the asteroseismic diagram of Fig. 1.

For all the stars, we use the effective temperature ($T_{\rm eff}$), iron content ([Fe/H]), frequency of maximum power ($\nu_{\rm max}$), and individual seismic frequencies (ν_i) as constraints. We use the constraints given in the respective papers, except for 13 stars of L17, for which we use the $T_{\rm eff}$ and [Fe/H] values updated in Morel et al. (2021).

Although the method used to characterise the L17 and D16 samples is the same, the quality of the seismic data for the L17 sample is better because the stars were observed for at least 12 months longer by the *Kepler* mission. This allows us to see how the data quality will impact the uncertainties in the fundamental stellar property inferences. This aspect is discussed in Sect. 6.2.

4. Optimisation process

The fundamental properties of the sample defined in the previous section are inferred using both grids in combination with the asteroseismic inference on a massive scale (AIMS, Rendle et al. 2019) code. AIMS is an optimisation tool that uses Bayesian statistics and Markov chain Monte Carlo (MCMC) to explore the grid parameter space and find the model that best fits the observational constraints. In the present work, we use the two-term surface corrections proposed by Ball & Gizon (2014) in order to compensate for the difference between theoretical and observed frequencies, which is due to the incomplete modelling of the surface layers of stars. We also explored the different ways of considering the χ^2 in the optimisation. AIMS distinguishes the contribution of the global constraints X_i (in our case $T_{\rm eff}$, [Fe/H],

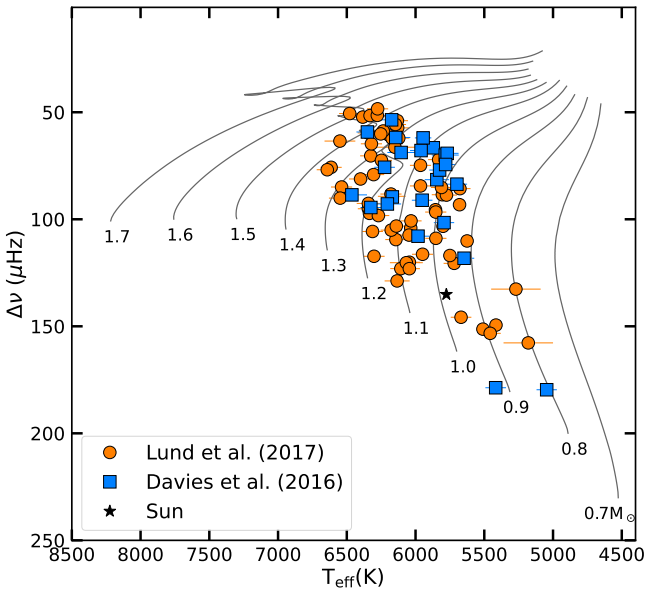

Fig. 1. Asteroseismic diagram showing some computed evolutionary tracks with $[M/H]_i = 0.0$ and $Y_i = 0.26$ (that are not the Solar values) in solid black lines. The points show the distribution of the sample considered in this work, where the orange circles are taken from L17, the blue squares are from D16, and the black star is the Sun.

and ν_{max}),

$$\chi^2_{global} = \sum_i^3 \left(\frac{X_i^{(obs)} - X_i^{(mod)}}{\sigma(X_i)} \right) \quad (5)$$

and the constraints from individual frequencies ν_i,

$$\chi^2_{freq} = \sum_i^N \left(\frac{\nu_i^{(obs)} - \nu_i^{(mod)}}{\sigma(\nu_i)} \right), \quad (6)$$

where (obs) corresponds to the observed values and (mod) corresponds to the model values. The weight that AIMS gives to the seismic contribution can be absolute (3:N), where each individual frequency has the same weight as each global constraint,

$$\chi^2_{total} = \chi^2_{freq} + \chi^2_{global}, \quad (7)$$

or relative (3:3), where all the frequencies have the same weight as all the global constraints,

$$\chi^2_{total} = \left(\frac{N_{global}}{N_{freq}} \right) \chi^2_{freq} + \chi^2_{global}, \quad (8)$$

where N_{global} and N_{freq} are the numbers of global and frequency constraints, respectively.

Cunha et al. (2021) assessed the impact of using these two different ways to consider the weight in the frequencies. The weights 3:3 synthetically inflate the uncertainties of the individual frequencies, which allows the optimisation procedure to explore more of the parameter space. However, this is not statistically correct, as explained in Cunha et al. (2021). If we want the optimisation to be statistically correct, we should instead consider 3:N weights, which use the full potential of the seismic frequencies, leading to results with smaller uncertainties. However, as discussed in Cunha et al. (2021), the use of 3:N weights is more sensitive to an incomplete or incorrect modelling of stars and can lead to results that are incompatible with the global constraints. Given the discussion in the literature around the application of weights, in this work we decided to assess the effect of using both weight options in the results (see Sect. 6.1). The properties of masses, radii, and ages inferred using Grid B are provided in Tables B.1 and C.1 for both (3:N) and (3:3) frequency weights.

Table 2. Solar properties from the optimisation process.

		M ($M_\odot$)	R ($R_\odot$)	τ (Gyr)	ρ (g cm^{-3})
Grid A	3:3	0.999 ± 0.007	0.998 ± 0.002	4.68 ± 0.22	1.416 ± 0.001
	3:N	1.007 ± 0.002	1.000 ± 0.001	4.66 ± 0.06	1.418 ± 0.001
Grid B	3:3	0.998 ± 0.007	0.998 ± 0.002	4.69 ± 0.22	1.416 ± 0.001
	3:N.	1.007 ± 0.002	1.000 ± 0.001	4.66 ± 0.06	1.418 ± 0.001

Notes. The age of the Sun used as a reference is 4.57 Gyr.

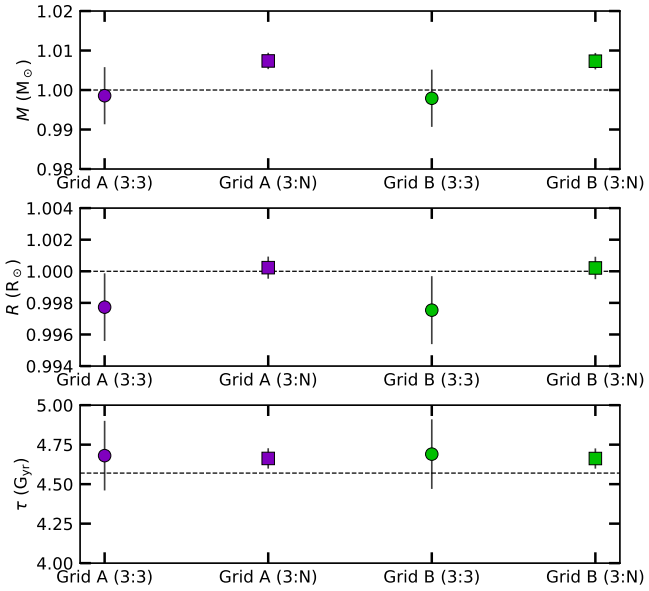

Fig. 2. Optimisation results for the Sun: for mass (top panel), radius (middle panel), and age (bottom panel). The dashed line indicates the real value of the Sun.

5. Results

5.1. The Sun

As a first test, we determined how both grids perform in the inference of the properties of the degraded Sun. This tests the accuracy of the grids in the optimisation process. The results for the Sun are shown in Table 2 and in Fig. 2 for both grids with the consideration of the relative or absolute weights in the frequencies. The results are similar for both grids when we use the same weights in the optimisation. This is expected because the physics is the same for the low-mass models of the grids. In the models of Grid B, the effect of turbulent mixing is negligible, because the convective envelope already fully homogenises the region where it should have an impact. For grid A, most of the models include atomic diffusion. Comparing the same grid but different weights in the frequencies, we see with the 3:3 weights that the true properties of the Sun are within the 1σ uncertainties, except for the radius, which is within 2σ. In contrast, for the 3:N weights, only the radius has the true value within 1σ. For the age it is within 2σ, and for the mass it is within 4σ. From a global perspective,

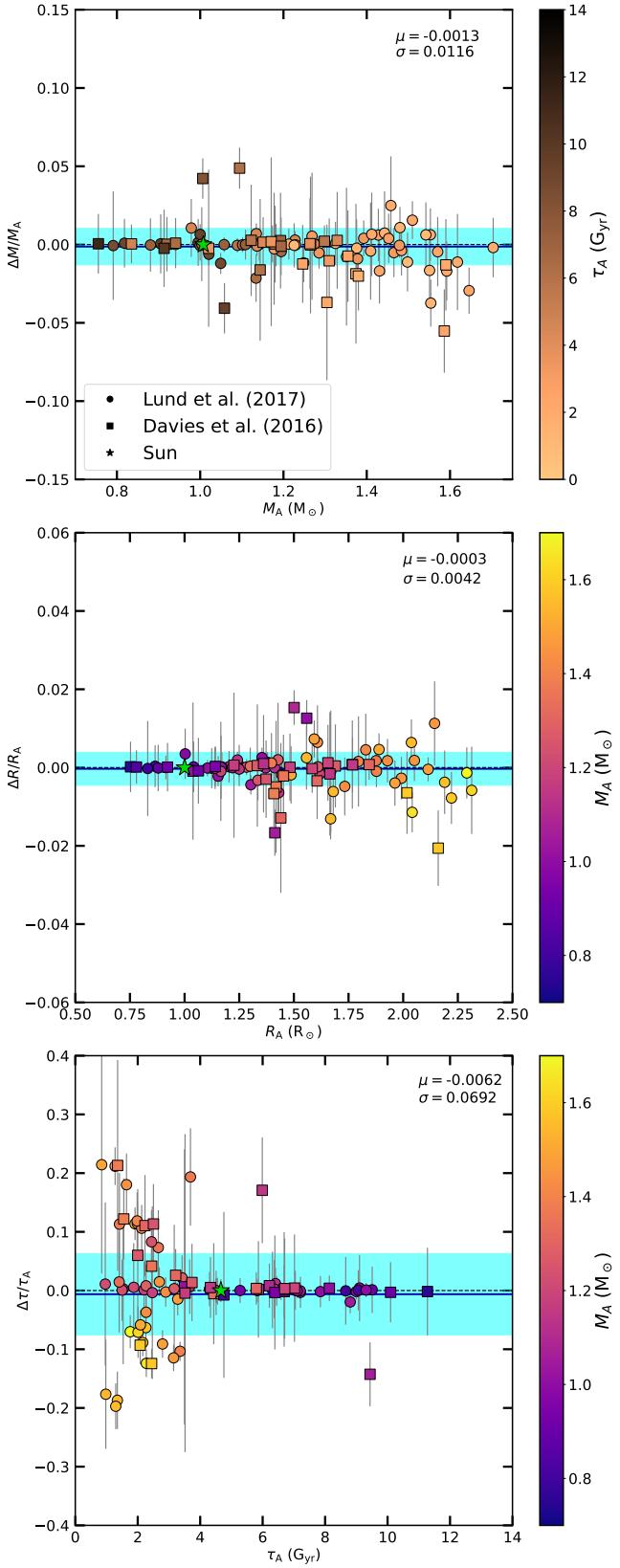

Fig. 3. Relative difference for mass (top panel), radius (middle panel), and age (bottom panel) between grids A and B, for 3:N weights. The blue solid line indicates the bias, and the blue region is the 1σ of the standard deviation. Each point is colour coded with the corresponding reference age (top panel) and mass (middle and bottom panels).

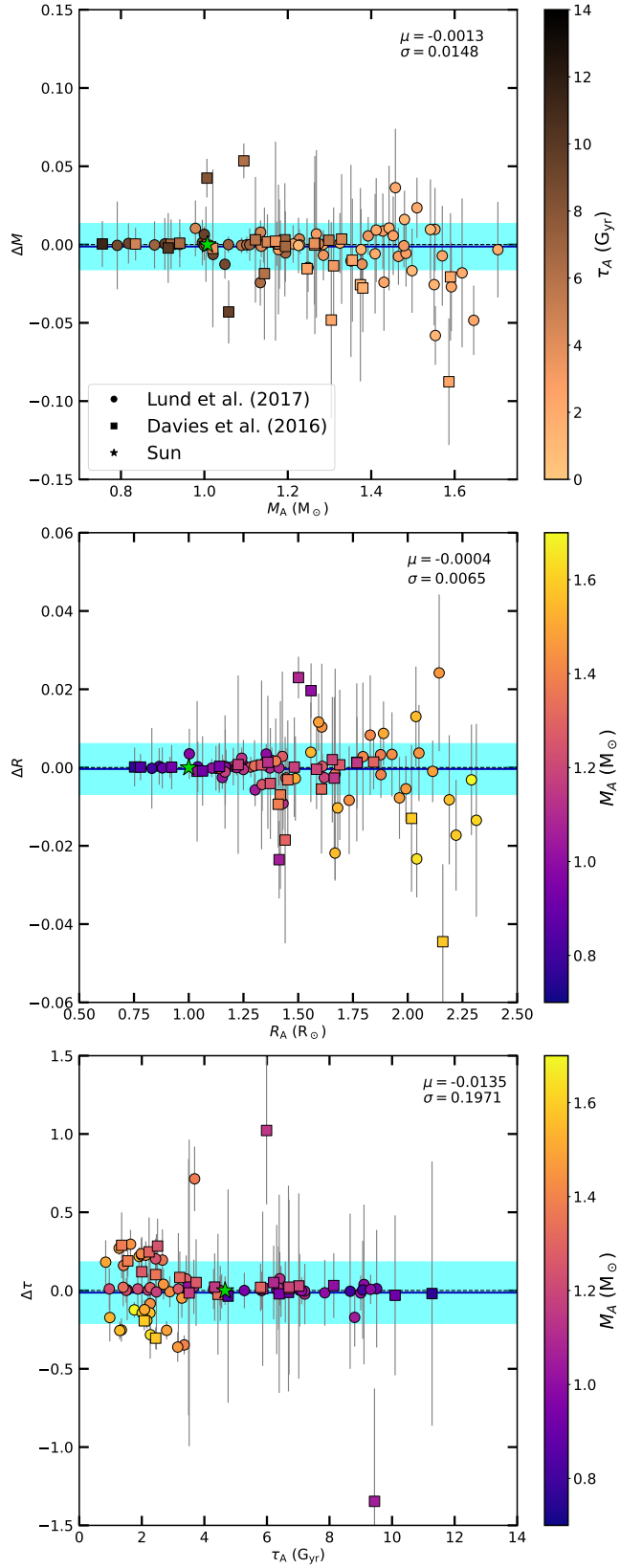

Fig. 4. Absolute difference for mass (top panel), radius (middle panel), and age (bottom panel) between grids A and B, for 3:N weights. The blue solid line indicates the bias, and the blue region is the 1σ of the standard deviation. Each point is colour coded with the corresponding reference age (top panel) and mass (middle and bottom panels).

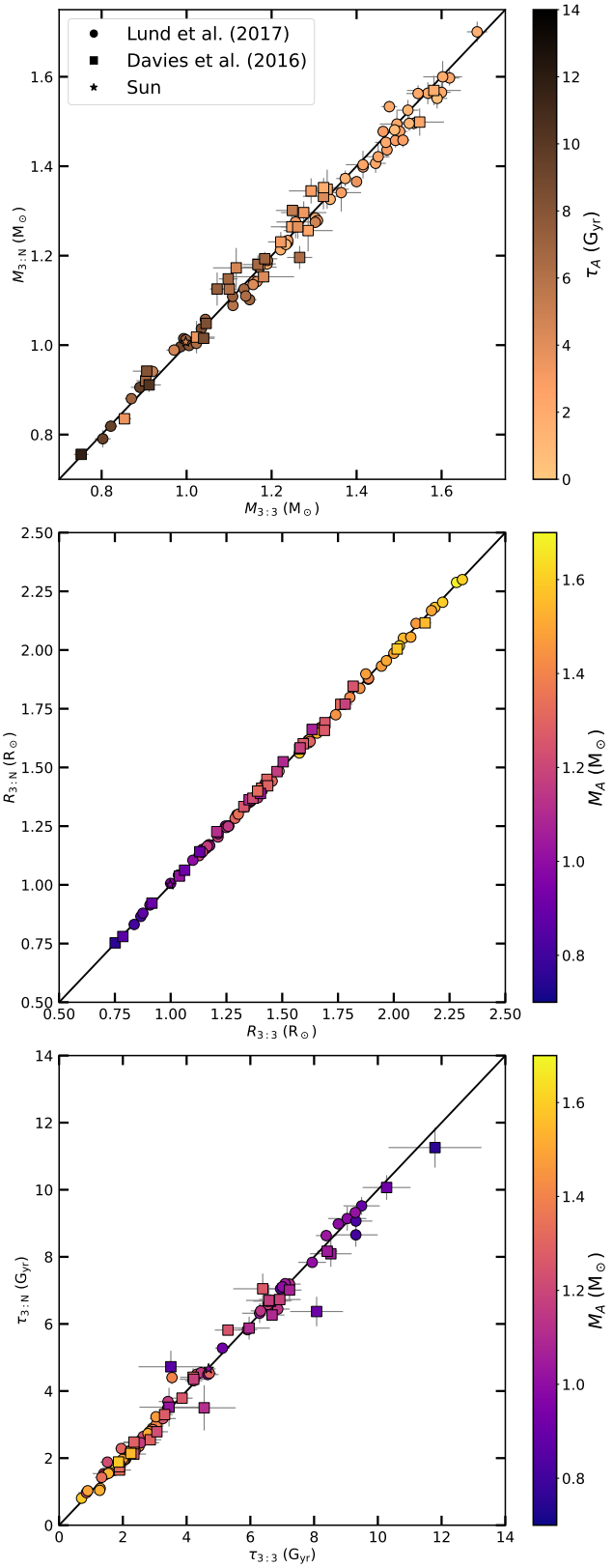

Fig. 5. Comparison of the properties inferred when using 3:N or 3:3 weights on the full sample, for mass (top panel), radius (middle panel), and age (bottom panel). Each point is colour coded with the corresponding reference age (top panel) and mass (middle and bottom panels).

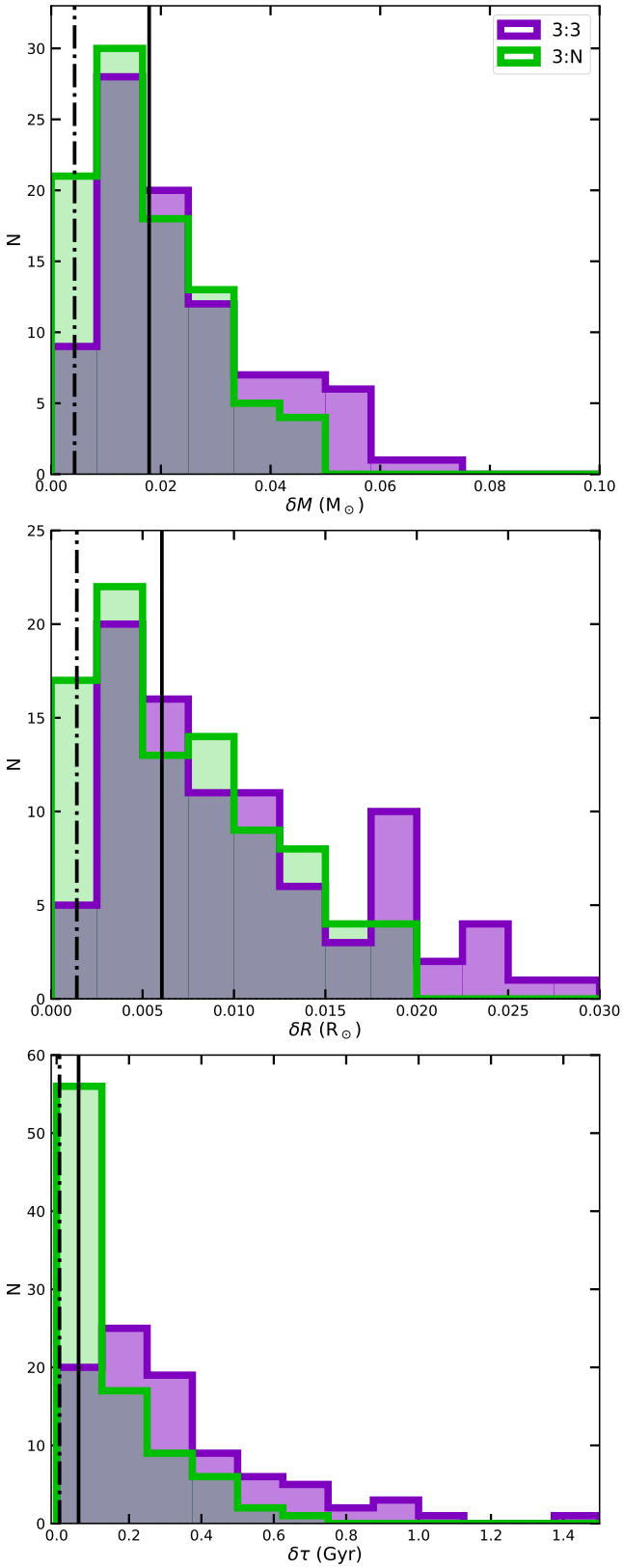

Fig. 6. Histogram of uncertainties on the inferred parameters for the full sample and two different weights: mass (top panel), radius (middle panel), and age (bottom panel). The vertical dash-dotted line marks the value of the bias and the vertical solid line marks the value of the standard deviation.

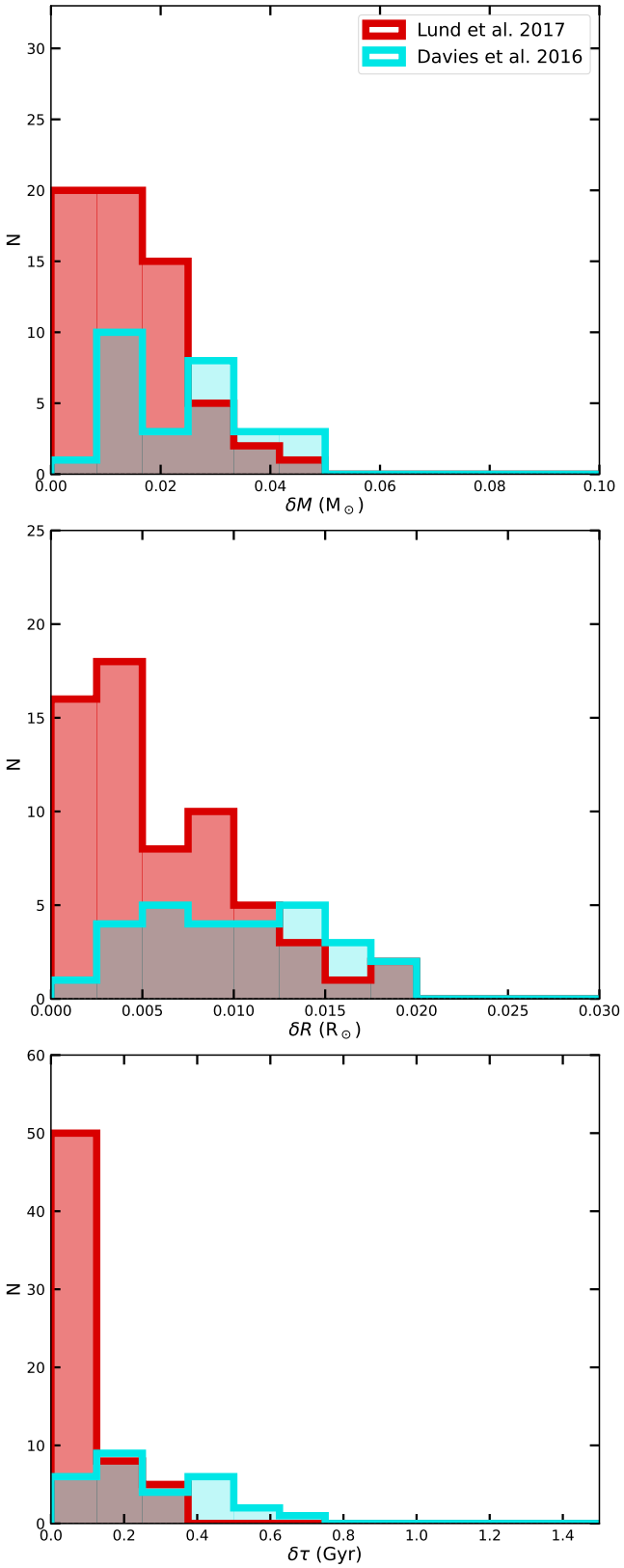

Fig. 7. Histogram of uncertainties on the fundamental properties of stars from both samples using the 3:N weights: mass (top panel), radius (middle panel), and age (bottom panel).

the results are compatible with the current Sun and are in agreement with those obtained by Silva Aguirre et al. (2017).

5.2. Grid comparison

In order to understand how the change of physics (adding turbulent mixing and atomic diffusion for the more massive stars) affects the stellar characterisation, we compare the relative and absolute differences between the fundamental properties inferred with the two grids. In both grids, the inference is made using the 3:N weights of the frequencies in the optimisation because that is the statistically correct option. We estimate the absolute difference with

$$\Delta X = X_B - X_A, \tag{9}$$

and the relative difference with

$$\frac{\Delta X}{X_A}, \tag{10}$$

where X is the parameter value that is inferred, X_B is the value obtained from grid B, and X_A is the reference value obtained from grid A. Figures 3 and 4 show the results for the relative and absolute differences for mass, radius, and age, respectively.

Globally, we see that the change in physics does not induce a significant bias in the results. Nevertheless, the mean dispersion for age can reach values of about 7%, and the maximum dispersion can reach values of greater than 20%, indicating that the changes in physics have a strong impact on the age determination for individual stars.

We also see that the dispersion in all parameters increases as the stellar mass increases, indicating that the change we made to the grid has indeed impacted the more massive stars. For the lower mass stars, both grids include atomic diffusion and the turbulent mixing prescription has no significant impact (i.e. the turbulent mixing effects are within the convective envelope of these stars).

For the more massive stars, the majority of the models of grid A do not include atomic diffusion. We expect the models with atomic diffusion (grid B) to be affected in two ways. First, the models have a different surface composition at a given age, which has an impact on the inferred stellar properties through the [Fe/H] constraint. Second, atomic diffusion changes the amount of time that the star spends on the main sequence by helping to deplete some of the hydrogen in the core. We see that this can lead to a relative difference for individual stars of greater than 5% in mass, 2% in radius, and 20% in age.

We also look at the absolute differences (Fig. 4) to decipher whether or not the dispersion we see in relative differences at smaller ages is an artefact caused by the computation of a ratio (particularly age; the small reference value in the denominator may mislead the interpretation). We find the same behaviour in the dispersion of the absolute difference, where it increases with stellar mass. The age dispersion can reach differences of more than 0.4 Gyr for the more massive stars, with much larger differences than those found for the lower masses. This leads us to the conclusion that the dispersion in the relative difference is not fully explained by the smaller ages.

In both the relative and absolute cases, we find three outliers for mass and age in low-mass stars. The large difference in these stars is caused by the way Grid A was computed. These stars encounter the border where atomic diffusion is turned off. This creates a discontinuity in the parameter space where models do and do not have atomic diffusion, which leads to greater dispersion in the results for these stars. This reveals that the current way of grid-based modelling – where atomic diffusion is cut at a certain point in the grid in order to avoid excessive variation

Table 3. Inferred properties of the stars common to the D16 and L17 samples using the individual frequencies obtained in the respective works.

KIC		Mass ($M_\odot$)		Radius ($R_\odot$)		Age (Gyr)		$[M/H]_i$		Y_i	
		D16	L17	D16	L17	D16	L17	D16	L17	D16	L17
3632418	(3:3)	1.420 ± 0.042	1.471 ± 0.013	1.917 ± 0.020	1.945 ± 0.006	2.795 ± 0.127	2.927 ± 0.121	0.159 ± 0.049	0.171 ± 0.054	0.278 ± 0.024	0.271 ± 0.022
	(3:N)	1.405 ± 0.024	1.437 ± 0.017	1.911 ± 0.011	1.931 ± 0.008	2.719 ± 0.051	2.888 ± 0.051	0.221 ± 0.023	0.228 ± 0.026	0.290 ± 0.013	0.289 ± 0.014
9414417	(3:3)	1.434 ± 0.052	1.502 ± 0.019	1.935 ± 0.025	1.967 ± 0.009	2.483 ± 0.125	2.571 ± 0.103	0.151 ± 0.052	0.152 ± 0.068	0.275 ± 0.070	0.276 ± 0.024
	(3:N)	1.455 ± 0.035	1.478 ± 0.017	1.944 ± 0.016	1.955 ± 0.008	2.380 ± 0.057	2.539 ± 0.048	0.214 ± 0.038	0.217 ± 0.040	0.281 ± 0.016	0.282 ± 0.040
10963065	(3:3)	1.111 ± 0.027	1.156 ± 0.009	1.239 ± 0.011	1.258 ± 0.003	4.211 ± 0.319	4.223 ± 0.267	0.016 ± 0.060	0.043 ± 0.062	0.262 ± 0.017	0.264 ± 0.017
	(3:N)	1.108 ± 0.013	1.135 ± 0.005	1.237 ± 0.005	1.249 ± 0.002	4.121 ± 0.095	4.307 ± 0.089	−0.044 ± 0.043	−0.054 ± 0.044	0.258 ± 0.011	0.259 ± 0.011

in chemical surface abundance – will be a source of large uncertainty. The most physically consistent approach is to consider atomic diffusion in all the stellar models whilst considering the other chemical transport mechanisms in competition.

6. Discussion

6.1. Impact of the weight of the frequencies on the inferences

In this section, only grid B is used because both grids give similar results when comparing the inference using 3:N and 3:3 frequency weight. Figure 5 shows the comparison of values inferred using Grid B for the two weight options. The results show that the impact of changing the weights is more significant for the mass and age (top and bottom panels)

The parameter uncertainties for both cases are presented in the histograms of Fig. 6 for all stars. We find that the two methods give different uncertainty distributions – in accordance with Cunha et al. (2021) – because the use of 3:3 weights is similar to synthetically inflating the uncertainties of the frequencies, as expected. We look at the statistics of the relative differences for the inferred mass, radius, and age between the two cases. The vertical lines in the histograms show the values of the bias (dash-dotted line) and the standard deviation (solid line). There is no significant bias for any of the parameters; all biases are lower than 1%. There is a large scatter in the results of 1.8%, 0.6%, and 6.1% for mass, radius, and age, respectively.

6.2. Comparison of uncertainties between L17 and D16

In this section, we compare how the quality of the seismic data affects the results, in particular the relationship between the precision of the frequencies and the inferred fundamental properties of the stars. Both L17 and D16 used the same method of seismic identification and quality assurance. The difference is that L17 uses *Kepler* observations for the stars with the highest signal-to-noise ratios, and therefore the seismic data for this sample are expected to be of better quality.

Figure 7 shows a histogram of the uncertainties for the two sets of stars regarding mass, radius, and age. The D16 sample has a more scattered histogram than the L17 sample and tends to have higher uncertainties, as expected.

There are three stars in common between the samples (KIC3632418, KIC9414417, and KIC10963065), which can be used to see how the different frequency estimates affect the inference of the results (we used the same $T_{\rm eff}$ and [Fe/H] in the inference, only changing $\nu_{\rm max}$ to be consistent with the individual frequency estimate in each work). The results obtained from the seismic data provided by D16 and L17 are presented in Table 3. For the three stars in common, D16 data tend to give smaller values of mass, radius, and age compared to L17 data, and also show a higher uncertainty for these three properties. These differences show that even a small change in the estimated individual frequencies can have a significant impact on the results derived from them. A somewhat surprising finding is that lower masses are linked to lower ages in these three stars from the D16 sample. A possible explanation for this correlation is the difference in the initial chemical compositions ($[M/H]_i$ and Y_i). For the case of D16, these three stellar models have slightly lower $[M/H]_i$ and higher Y_i, which may cause the age to be lower for lower estimated masses.

Uncertainties are expected to decrease with improved quality. This hypothesis was tested on synthetic stars in the work of Cunha et al. (2021), who found that the degraded data gave less accurate results, especially for age determination. This is in agreement with what we find for the *Kepler* data analysed here.

6.3. Comparison of our results with those of Silva Aguirre et al. (2015, 2017)

In this section, we compare the results obtained using Grid B with those of previous works. We compare our study of the L17 sample with the work of Silva Aguirre et al. (2017) and our study of the D16 sample with the work of Silva Aguirre et al. (2015). In both works, the authors used different pipelines and the grids were built with different codes and input physics. They also use different optimisation codes in each pipeline and use a relative weight for each frequency. Here we compare their results with our results derived using the same relative weight (for consistency).

6.3.1. Comparison with Silva Aguirre et al. (2017)

We compare our results for the L17 sample with the results presented in Silva Aguirre et al. (2017). Here, we show the results for only one of the seven pipelines used in their paper: namely AIMS. Similar conclusions can be drawn for all the others. This pipeline uses the same evolutionary code (MESA) to compute the stellar models as in our work, but with different physical inputs: the stellar models use Grevesse & Noels (1993) solar mixture, an Eddington grey atmosphere, no atomic diffusion, and a fixed helium enrichment ratio ($\frac{\Delta Y}{\Delta Z} = 2.0$).

Figure 8 shows the comparison of Grid B results with those from the AIMS pipeline of Silva Aguirre et al. (2017). Our results show a bias towards higher values for mass, radius, and age, with a scatter of 6%, 2%, and 24%, respectively. However, the relative difference for an individual star can be up to 15% for mass, 5% for radius, and 60% for age.

We also compared the results from Silva Aguirre et al. (2017) with those of grid A in Fig. 9; however, for most cases, we find similar significant bias and scatter as in the comparison with grid B. This suggests that the systematic effects arising from turbulent mixing are overshadowed by the different physics used between our work and Silva Aguirre et al. (2017).

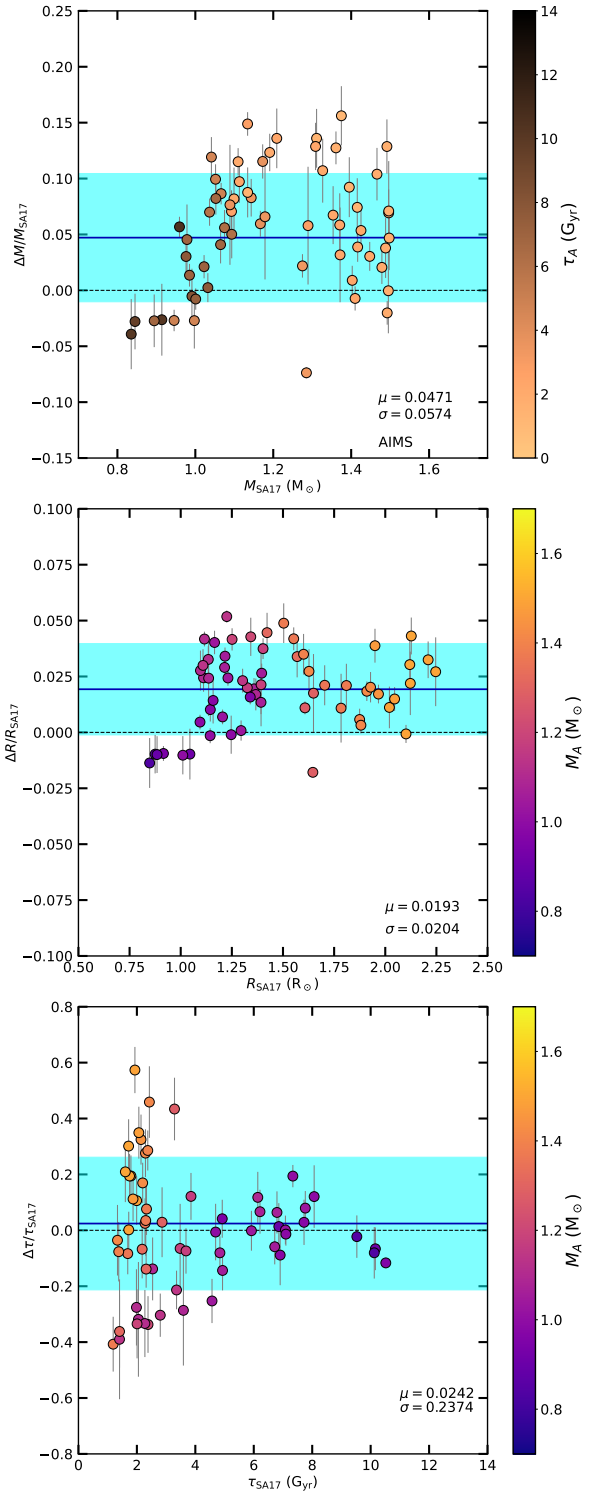

Fig. 8. Relative difference for mass (top panel), radius (middle panel), and age (bottom panel) between grid B and the results of Silva Aguirre et al. (2017) for the AIMS pipeline. The blue solid line indicates the bias, and the blue region is the 1σ deviation. Each point is colour coded according to the corresponding reference age (top panel) and mass (middle and bottom panels).

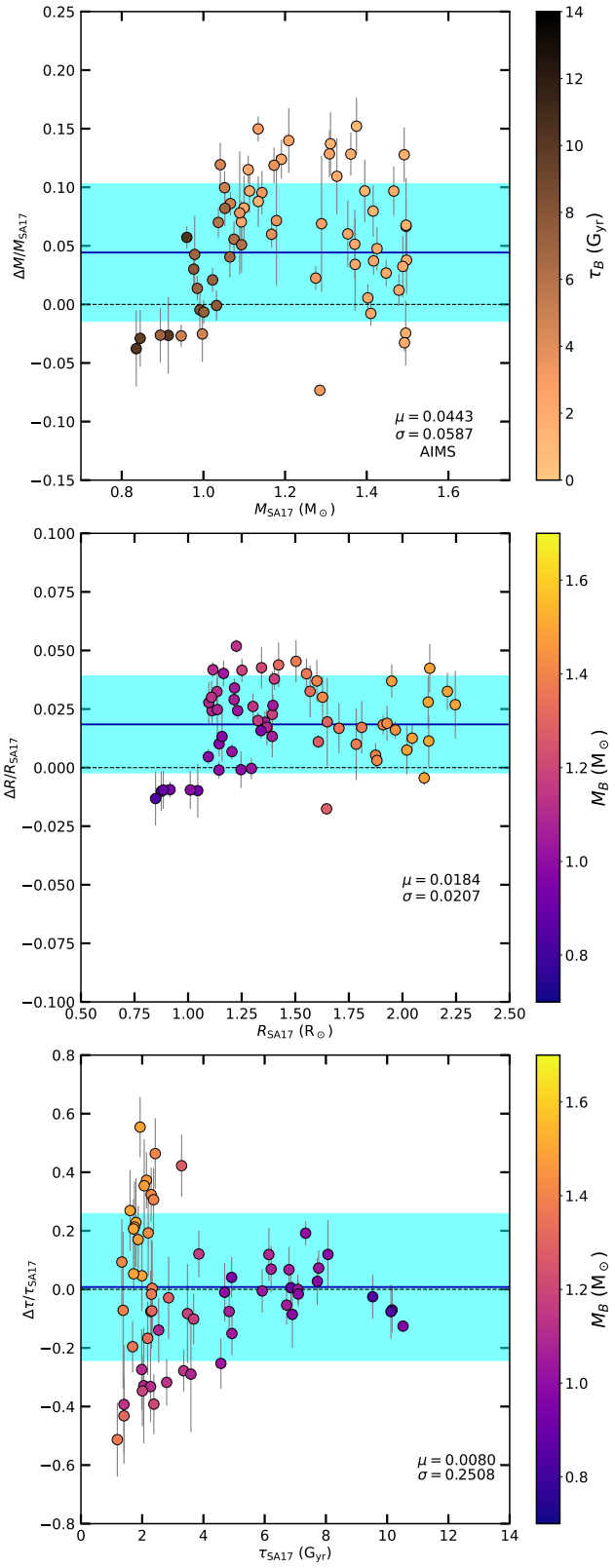

Fig. 9. Same as Fig. 8 but using our results from Grid A.

6.3.2. Comparison with Silva Aguirre et al. (2015)

We now compare our results for the stars of D16 with those presented by Silva Aguirre et al. (2015). As in the previous section, the results obtained from all the pipelines in their work were similar and led to the same conclusions. Therefore, we only present a comparison with the BASTA pipeline (Fig. 10) here.

We observe a bias towards higher masses and radii, and a bias towards younger ages, with a dispersion of 6%, 2%, and 17% for mass, radius, and age, respectively. For some individual

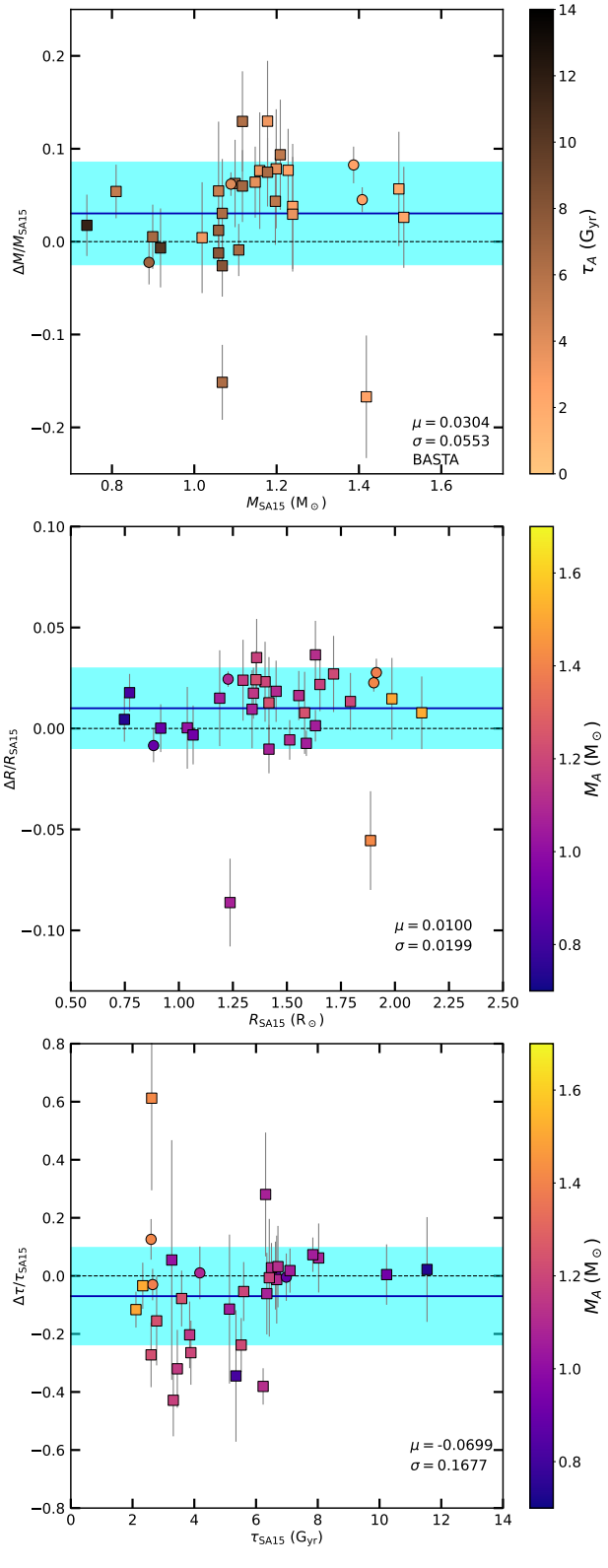

Fig. 10. Relative difference for mass (top panel), radius (middle panel), and age (bottom panel) between grid B and Silva Aguirre et al. (2015) results for the BASTA pipeline. The blue solid line indicates the bias, and the blue region is the 1σ deviation. Each point is colour coded according to the corresponding reference age (top panel) and mass (middle and bottom panels).

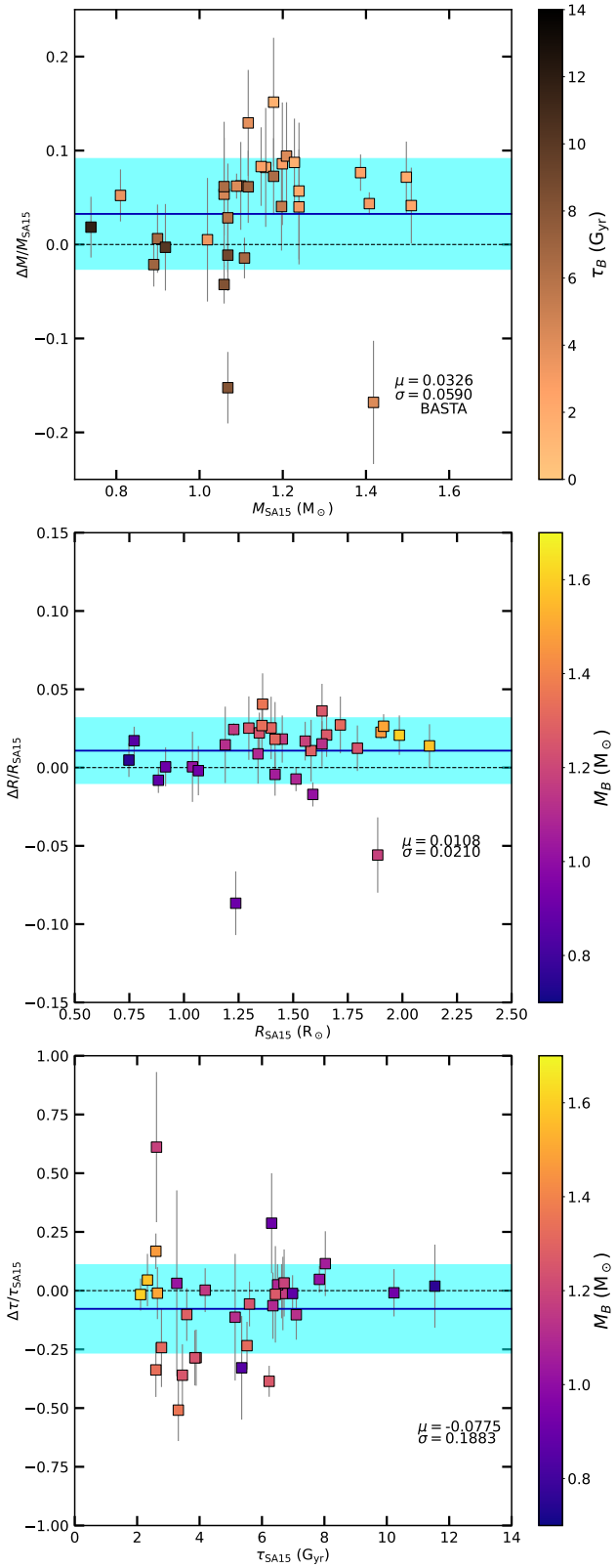

Fig. 11. Same as Fig. 10 but using our results from Grid A.

stars, the relative difference can be up to 20% for mass, 10% for radius, and 60% for age.

As before, we also compared the Silva Aguirre et al. (2015) with the results from grid A in Fig. 11. However, we identify a similar bias and scatter as in the comparison with grid B. This again shows that the systematic uncertainties we observe are a consequence of the different physics used between the two works

and are not specifically related to the incorporation of turbulent mixing in our grid B.

7. Conclusion

This work is a continuation of the study by Moedas et al. (2022). Our aim is to understand how turbulent mixing and atomic diffusion affects the stellar characterisation of F-type stars. More, precisely, our objective is to study the impact of including calibrated turbulent mixing in stellar models on the derived stellar properties. Including this mechanism allows us to also incorporate atomic diffusion in F-type stars while avoiding excessive variation in surface chemical abundances. To do this, we computed two grids from which we inferred the stellar properties of a sample of FGK-type stars. The first grid (A) neglects atomic diffusion for the F-type stars, while the second grid (B) uses our calibrated turbulent mixing, allowing the use of atomic diffusion in stellar models.

In addition to studying the impact of turbulent mixing, we tested how applying different weights to the seismic data impacts the results. Furthermore, by selecting samples from two different sources, D16 and L17, we investigated how the data quality affects the uncertainties on the properties of observed stars. Finally, we compared our results with those of previous studies that analysed the same samples of stars.

Concerning the combined inclusion of turbulent mixing and atomic diffusion, globally speaking we find no significant impact; that is, a relative bias of less than 1% for masses, radii, and ages. However, we find that there is an increase in the dispersion of the relative differences with mass caused by neglecting atomic diffusion in F-type stars. This can lead to individual relative differences of up to 5% for mass, 2% for radius, and 20% for age. This shows that including atomic diffusion is necessary if we want to avoid this source of uncertainty. We also find three stars that can be considered outliers; their best-fit models are within the limits where atomic diffusion is turned off for grid A for F-type stars. This type of discontinuity in the parameter space introduced in grids by considering models with and without diffusion (such as in our grid A) can therefore introduce significant errors in the inferred stellar properties. Our conclusion is that, in this region of the parameter space, we need the most homogeneous physics across the grid, avoiding discontinuity problems. This result shows that, in order to reduce the uncertainties, we have to consider atomic diffusion in all stellar modes in combination with other chemical-transport mechanisms to avoid unrealistic surface abundance variations. Turbulent mixing is a parameterisation of the different processes and is a step that allows us to improve stellar models and better characterise stars. Although, this improves the prediction of the evolution of iron in stellar models, we still need to take into consideration that it may not be appropriate for other elements (i.e. oxygen and calcium).

The results of other tests we performed on the inference method and data quality are consistent with what was found by Cunha et al. (2021) using synthetic stars. The use of a weight of (3:N) instead of (3:3) for the individual frequency constraints leads to results that are more sensitive to the input physics considered in the stellar models, and to smaller uncertainties, as expected. Our tests show that the better quality of the individual frequencies of L17 provides smaller uncertainties in the inferred properties compared to D16. Our results for the three stars common to both works (KIC3632418, KIC9414417, and KIC10963065) also lead us to a similar conclusion. Nonetheless, the small changes in the determination of the seismic data in these three stars lead to small differences in the inferred values of mass, radius, age, and initial chemical composition.

We compared the results of our sample with previous works. For D16, we compared with the results of Silva Aguirre et al. (2015) and for L17 with Silva Aguirre et al. (2017). We find that there are large differences in both cases, which are due to the different physics adopted in this work compared to in Silva Aguirre et al. (2015, 2017). This reinforces the need for careful consideration of the input physics.

The present work demonstrates that the calibrated turbulent mixing of Moedas et al. (2022) allows a better characterisation of observed F-type stars, even if the proposed scheme is not able to reproduce the chemical evolution of all individual elements. In order to overcome this issue, a further step could be taken, namely the implementation in MESA of the single value parameter (SVP) method (Alecian & LeBlanc 2020), which provides a good balance in efficiency between the calculation of the radiative accelerations and the computation time. Nevertheless, this calibrated turbulent mixing is a step towards a better characterisation of stars with more accurate physics (including atomic diffusion). Finally, with this work, we provide an updated characterisation in terms of the fundamental parameters (mass, radius, and age) for the D16 and L17 stars analysed.

Acknowledgements. This work was supported by FCT/MCTES through the research grants UIDB/04434/2020, DOI: 10.54499/UIDB/04434/2020, UIDP/04434/2020, DOI: 10.54499/UIDP/04434/2020, 2022.06962.PTDC., 2022.03993.PTDC, and DOI: 10.54499/2022.03993.PTDC. N.M. acknowledges support from the Fundação para a Ciência e a Tecnologia (FCT) through the Fellowship UI/BD/152075/2021 and POCH/FSE (EC). D.B. acknowledges funding support by the Italian Ministerial Grant PRIN 2022, "Radiative opacities for astrophysical applications", no. 2022NEXMP8, CUP C53D23001220006. M.C. acknowledges the support by national funds (FCT/MCTES, Portugal), through the contract CEECIND/02619/2017. We also thank Daniel Reese for providing us with the results from AIMS pipeline from Silva Aguirre et al. (2017). We thank the anonymous referee for the valuable comments which helped to improve the paper.

References

Alecian, G., & LeBlanc, F. 2020, MNRAS, 498, 3420
Asplund, M., Grevesse, N., Sauval, A. J., & Scott, P. 2009, ARA&A, 47, 481
Baglin, A., Auvergne, M., Barge, P., et al. 2006, in The CoRoT Mission Pre-Launch Status - Stellar Seismology and Planet Finding, eds. M. Fridlund, A. Baglin, J. Lochard, & L. Conroy, ESA Spec. Publ., 1306, 33
Ball, W. H., & Gizon, L. 2014, A&A, 568, A123
Borucki, W. J., Koch, D., Basri, G., et al. 2010, Science, 327, 977
Bressan, A., Marigo, P., Girardi, L., et al. 2012, MNRAS, 427, 127
Chaboyer, B., Fenton, W. H., Nelan, J. E., Patnaude, D. J., & Simon, F. E. 2001, ApJ, 562, 521
Cox, J. P., & Giuli, R. T. 1968, Principles of Stellar Structure (Gordon & Breach)
Cunha, M. S., Roxburgh, I. W., Aguirre Børsen-Koch, V., et al. 2021, MNRAS, 508, 5864
Davies, G. R., Silva Aguirre, V., Bedding, T. R., et al. 2016, MNRAS, 456, 2183
Deal, M., Alecian, G., Lebreton, Y., et al. 2018, A&A, 618, A10
Deal, M., Goupil, M. J., Marques, J. P., Reese, D. R., & Lebreton, Y. 2020, A&A, 633, A23
Dumont, T., Palacios, A., Charbonnel, C., et al. 2021, A&A, 646, A48
Eggenberger, P., Meynet, G., Maeder, A., et al. 2010, A&A, 519, A116
Eggenberger, P., Buldgen, G., Salmon, S. J. A. J., et al. 2022, Nat. Astron., 6, 788
Ferguson, J. W., Alexander, D. R., Allard, F., et al. 2005, ApJ, 623, 585
Grevesse, N., & Noels, A. 1993, Phys. Scr. Vol. T, 47, 133
Gruyters, P., Korn, A. J., Richard, O., et al. 2013, A&A, 555, A31
Gruyters, P., Nordlander, T., & Korn, A. J. 2014, A&A, 567, A72
Gruyters, P., Lind, K., Richard, O., et al. 2016, A&A, 589, A61
Herwig, F. 2000, A&A, 360, 952
Hidalgo, S. L., Pietrinferni, A., Cassisi, S., et al. 2018, ApJ, 856, 125
Iglesias, C. A., & Rogers, F. J. 1996, ApJ, 464, 943
Krishna Swamy, K. S. 1966, ApJ, 145, 174
Lund, M. N., Silva Aguirre, V., Davies, G. R., et al. 2017, ApJ, 835, 172
Michaud, G., Richer, J., & Richard, O. 2011a, A&A, 529, A60

Michaud, G., Richer, J., & Vick, M. 2011b, A&A, 534, A18
Michaud, G., Alecian, G., & Richer, J. 2015, Atomic Diffusion in Stars (Springer)
Moedas, N., Deal, M., Bossini, D., & Campilho, B. 2022, A&A, 666, A43
Morel, T., Creevey, O. L., Montalbán, J., Miglio, A., & Willett, E. 2021, A&A, 646, A78
Nsamba, B., Campante, T. L., Monteiro, M. J. P. F. G., et al. 2018, MNRAS, 477, 5052
Paxton, B., Bildsten, L., Dotter, A., et al. 2011, ApJS, 192, 3
Paxton, B., Cantiello, M., Arras, P., et al. 2013, ApJS, 208, 4
Paxton, B., Marchant, P., Schwab, J., et al. 2015, ApJS, 220, 15
Paxton, B., Schwab, J., Bauer, E. B., et al. 2018, ApJS, 234, 34
Paxton, B., Smolec, R., Schwab, J., et al. 2019, ApJS, 243, 10
Pietrinferni, A., Hidalgo, S., Cassisi, S., et al. 2021, ApJ, 908, 102
Rauer, H., Catala, C., Aerts, C., et al. 2014, Exp. Astron., 38, 249
Rendle, B. M., Buldgen, G., Miglio, A., et al. 2019, MNRAS, 484, 771
Richer, J., Michaud, G., & Turcotte, S. 2000, ApJ, 529, 338
Ricker, G. R. 2016, in AGU Fall Meeting Abstracts, P13C–01
Rogers, F. J., & Nayfonov, A. 2002, ApJ, 576, 1064
Salaris, M., & Weiss, A. 2001, A&A, 376, 955
Semenova, E., Bergemann, M., Deal, M., et al. 2020, A&A, 643, A164
Silva Aguirre, V., Davies, G. R., Basu, S., et al. 2015, MNRAS, 452, 2127
Silva Aguirre, V., Lund, M. N., Antia, H. M., et al. 2017, ApJ, 835, 173
Townsend, R. H. D., & Teitler, S. A. 2013, MNRAS, 435, 3406
Valle, G., Dell'Omodarme, M., Prada Moroni, P. G., & Degl'Innocenti, S. 2014, A&A, 561, A125
Valle, G., Dell'Omodarme, M., Prada Moroni, P. G., & Degl'Innocenti, S. 2015, A&A, 575, A12
Verma, K., & Silva Aguirre, V. 2019, MNRAS, 489, 1850
Vick, M., Michaud, G., Richer, J., & Richard, O. 2010, A&A, 521, A62
Weiss, A., & Schlattl, H. 2008, Ap&SS, 316, 99

Appendix A: Grid comparison 3:3 frequency weight

Figures A.1 and A.2 are the same as Figs. 3 and 4 but for the 3:3 weights. In this case, we can see the same behaviour as in the case of the 3:N weights. However, we can see that for the case of relative weights, there is a smaller dispersion (which we can see in the standard deviation). This is due to the fact that the use of absolute weights leads to greater sensitivity to the input physics. Nevertheless, the conclusion we obtain using the 3:N or 3:3 weights in frequencies is the same, and is simply more pronounced for the 3:N weights.

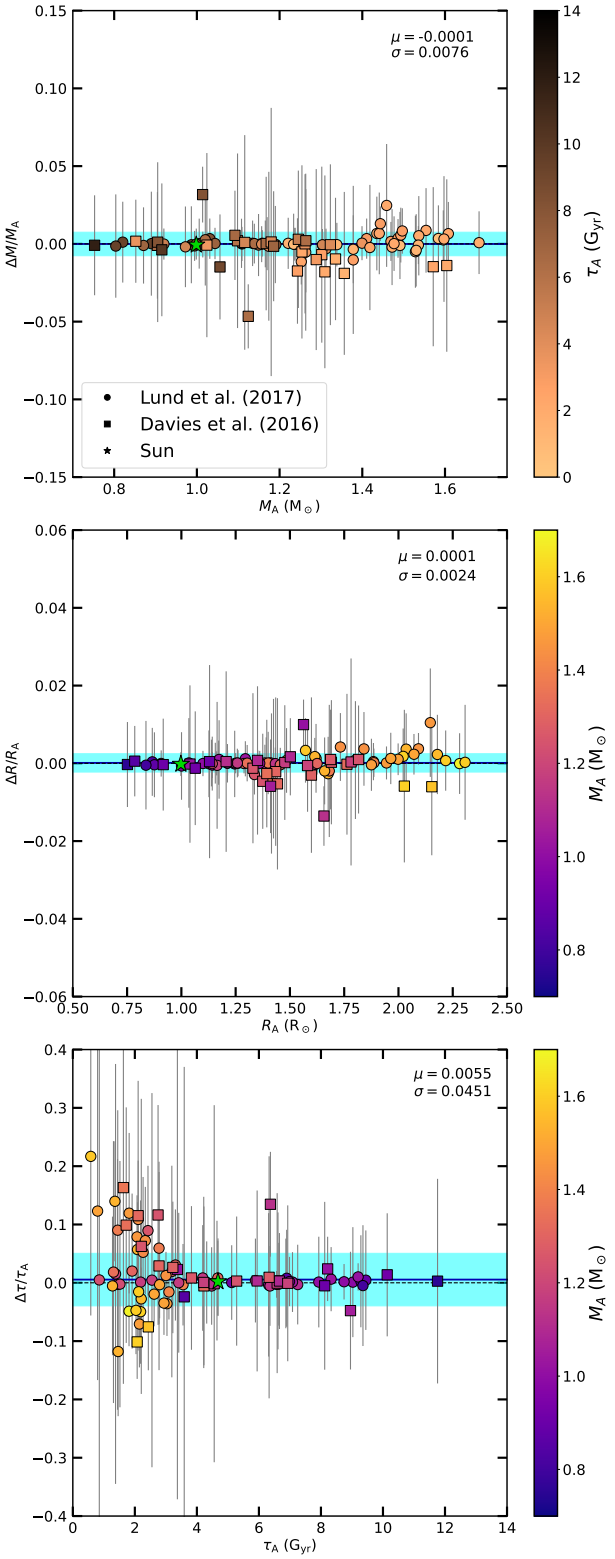

Fig. A.1. Same as Fig. 3 but using 3:3 weights for frequencies.

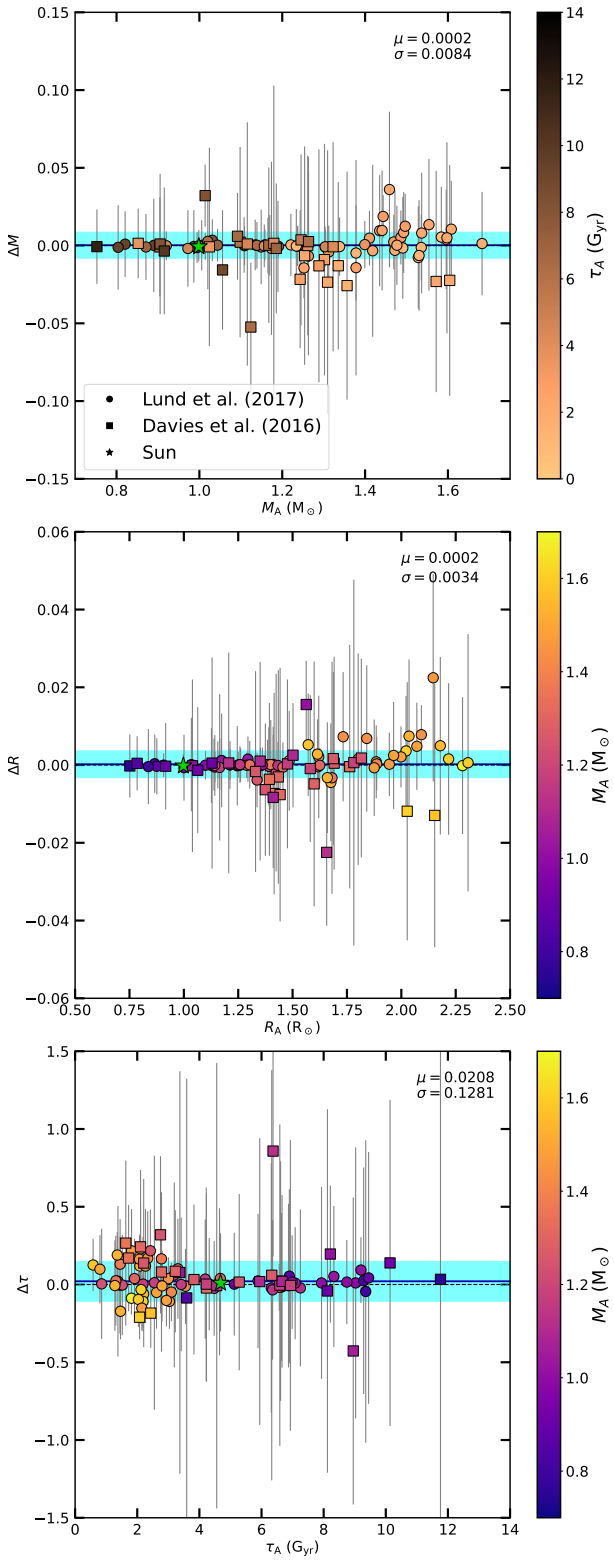

Fig. A.2. Same as Fig. 4 but using 3:3 weights for frequencies

Appendix B: Fundamental properties using 3:N frequency weighting

Table B.1. Inferred fundamental properties of the stars using 3:N frequency weighting.[4]

KIC	Mass ($M_\odot$)	Radius ($R_\odot$)	Age (Gyr)	$[M/H]_i$	Y_i
1435467	1.406 ± 0.021	1.724 ± 0.009	2.184 ± 0.044	0.251 ± 0.045	0.301 ± 0.013
2837475	1.525 ± 0.023	1.670 ± 0.009	1.096 ± 0.051	0.279 ± 0.047	0.289 ± 0.016
3427720	1.174 ± 0.010	1.140 ± 0.004	2.205 ± 0.075	0.043 ± 0.039	0.243 ± 0.003
3456181	1.563 ± 0.025	2.181 ± 0.013	2.117 ± 0.045	0.042 ± 0.050	0.258 ± 0.012
3632418	1.437 ± 0.017	1.931 ± 0.008	2.888 ± 0.051	0.213 ± 0.035	0.283 ± 0.012
3656476	1.037 ± 0.005	1.298 ± 0.002	8.634 ± 0.121	0.287 ± 0.007	0.306 ± 0.004
3735871	1.182 ± 0.011	1.124 ± 0.004	1.538 ± 0.139	0.045 ± 0.041	0.245 ± 0.005
4914923	1.126 ± 0.006	1.381 ± 0.003	6.487 ± 0.122	0.179 ± 0.025	0.280 ± 0.005
5184732	1.231 ± 0.005	1.351 ± 0.002	4.499 ± 0.065	0.415 ± 0.005	0.285 ± 0.003
5773345	1.563 ± 0.018	2.051 ± 0.008	2.131 ± 0.036	0.399 ± 0.016	0.298 ± 0.008
5950854	0.996 ± 0.011	1.250 ± 0.005	9.141 ± 0.362	-0.103 ± 0.049	0.260 ± 0.012
6106415	1.143 ± 0.005	1.244 ± 0.002	4.547 ± 0.074	0.049 ± 0.027	0.257 ± 0.006
6116048	1.089 ± 0.004	1.251 ± 0.001	5.828 ± 0.082	-0.153 ± 0.020	0.244 ± 0.003
6225718	1.284 ± 0.005	1.283 ± 0.002	2.285 ± 0.057	0.182 ± 0.019	0.243 ± 0.003
6508366	1.565 ± 0.021	2.204 ± 0.010	1.970 ± 0.037	0.243 ± 0.053	0.297 ± 0.014
6603624	1.015 ± 0.005	1.151 ± 0.002	8.982 ± 0.086	0.219 ± 0.020	0.283 ± 0.004
6679371	1.700 ± 0.023	2.288 ± 0.011	1.637 ± 0.036	0.279 ± 0.033	0.277 ± 0.013
6933899	1.189 ± 0.004	1.616 ± 0.002	6.579 ± 0.067	0.061 ± 0.009	0.250 ± 0.002
7103006	1.597 ± 0.017	2.018 ± 0.007	1.993 ± 0.040	0.389 ± 0.028	0.285 ± 0.011
7206837	1.453 ± 0.027	1.618 ± 0.011	1.936 ± 0.056	0.368 ± 0.033	0.282 ± 0.014
7296438	1.102 ± 0.004	1.371 ± 0.002	6.443 ± 0.115	0.292 ± 0.019	0.308 ± 0.003
7510397	1.398 ± 0.011	1.876 ± 0.005	3.008 ± 0.041	-0.041 ± 0.025	0.252 ± 0.007
7680114	1.109 ± 0.007	1.412 ± 0.003	7.188 ± 0.135	0.158 ± 0.035	0.279 ± 0.008
7771282	1.341 ± 0.042	1.667 ± 0.018	2.854 ± 0.116	0.070 ± 0.062	0.275 ± 0.023
7871531	0.819 ± 0.009	0.865 ± 0.003	9.067 ± 0.220	-0.107 ± 0.031	0.297 ± 0.009
7940546	1.458 ± 0.016	1.986 ± 0.008	2.787 ± 0.053	0.170 ± 0.021	0.276 ± 0.010
8006161	0.941 ± 0.006	0.914 ± 0.002	5.278 ± 0.080	0.334 ± 0.012	0.305 ± 0.004
8150065	1.275 ± 0.036	1.430 ± 0.015	3.179 ± 0.243	0.123 ± 0.062	0.265 ± 0.020
8179536	1.373 ± 0.018	1.399 ± 0.008	1.574 ± 0.082	0.150 ± 0.052	0.248 ± 0.007
8228742	1.365 ± 0.009	1.879 ± 0.005	4.402 ± 0.196	0.230 ± 0.036	0.264 ± 0.006
8379927	1.229 ± 0.004	1.159 ± 0.002	1.501 ± 0.055	0.168 ± 0.023	0.242 ± 0.002
8394589	1.142 ± 0.008	1.204 ± 0.003	3.686 ± 0.120	-0.077 ± 0.039	0.246 ± 0.005
8424992	0.906 ± 0.012	1.042 ± 0.005	9.519 ± 0.266	0.024 ± 0.052	0.296 ± 0.014
8938364	1.006 ± 0.005	1.357 ± 0.002	9.321 ± 0.079	-0.227 ± 0.019	0.245 ± 0.003
9025370	0.989 ± 0.013	1.006 ± 0.005	4.491 ± 0.121	0.059 ± 0.051	0.288 ± 0.012
9098294	0.999 ± 0.007	1.154 ± 0.003	7.836 ± 0.147	-0.096 ± 0.038	0.259 ± 0.009
9139151	1.213 ± 0.008	1.171 ± 0.003	1.881 ± 0.099	0.115 ± 0.034	0.245 ± 0.005
9139163	1.496 ± 0.014	1.605 ± 0.005	1.546 ± 0.026	0.387 ± 0.024	0.274 ± 0.007
9206432	1.552 ± 0.022	1.562 ± 0.009	0.805 ± 0.070	0.277 ± 0.054	0.253 ± 0.009
9353712	1.494 ± 0.032	2.168 ± 0.016	2.216 ± 0.052	0.085 ± 0.046	0.287 ± 0.018
9410862	1.004 ± 0.017	1.167 ± 0.007	6.319 ± 0.291	-0.213 ± 0.053	0.266 ± 0.015
9414417	1.478 ± 0.017	1.955 ± 0.008	2.539 ± 0.048	0.057 ± 0.035	0.256 ± 0.010
9812850	1.421 ± 0.027	1.837 ± 0.012	2.352 ± 0.057	0.230 ± 0.050	0.301 ± 0.015
9955598	0.880 ± 0.011	0.879 ± 0.004	7.048 ± 0.165	0.077 ± 0.037	0.287 ± 0.011
9965715	1.234 ± 0.011	1.331 ± 0.005	2.644 ± 0.090	-0.135 ± 0.031	0.243 ± 0.003
10068307	1.478 ± 0.008	2.113 ± 0.005	3.232 ± 0.065	0.168 ± 0.031	0.261 ± 0.006
10079226	1.174 ± 0.030	1.165 ± 0.010	2.458 ± 0.257	0.200 ± 0.057	0.269 ± 0.018
10162436	1.458 ± 0.016	2.055 ± 0.008	2.732 ± 0.046	0.228 ± 0.035	0.293 ± 0.010
10454113	1.326 ± 0.013	1.301 ± 0.004	1.426 ± 0.085	0.284 ± 0.044	0.260 ± 0.009
10516096	1.110 ± 0.012	1.422 ± 0.006	6.389 ± 0.223	0.102 ± 0.047	0.284 ± 0.011
10644253	1.225 ± 0.012	1.140 ± 0.004	0.971 ± 0.094	0.186 ± 0.042	0.250 ± 0.007
10730618	1.403 ± 0.031	1.798 ± 0.015	2.216 ± 0.064	0.267 ± 0.074	0.315 ± 0.017
10963065	1.135 ± 0.005	1.249 ± 0.002	4.307 ± 0.089	-0.103 ± 0.033	0.248 ± 0.006

Table B.1. Continued.

KIC	Mass ($M_\odot$)	Radius ($R_\odot$)	Age (Gyr)	$[M/H]_i$	Y_i
11081729	1.481 ± 0.020	1.484 ± 0.008	1.027 ± 0.100	0.216 ± 0.047	0.245 ± 0.005
11253226	1.496 ± 0.017	1.646 ± 0.006	1.040 ± 0.039	0.336 ± 0.039	0.308 ± 0.011
11772920	0.791 ± 0.019	0.831 ± 0.007	8.655 ± 0.353	-0.158 ± 0.079	0.306 ± 0.018
12009504	1.279 ± 0.009	1.442 ± 0.004	3.494 ± 0.091	0.017 ± 0.032	0.242 ± 0.002
12069127	1.600 ± 0.035	2.300 ± 0.018	1.868 ± 0.064	0.165 ± 0.074	0.286 ± 0.021
12069424	1.057 ± 0.004	1.218 ± 0.001	7.201 ± 0.073	0.107 ± 0.021	0.272 ± 0.004
12069449	1.012 ± 0.004	1.105 ± 0.002	7.108 ± 0.061	0.128 ± 0.023	0.279 ± 0.005
12258514	1.275 ± 0.005	1.610 ± 0.002	4.529 ± 0.068	0.026 ± 0.018	0.247 ± 0.003
12317678	1.533 ± 0.013	1.898 ± 0.005	1.965 ± 0.038	0.041 ± 0.026	0.248 ± 0.007
3425851	1.348 ± 0.044	1.411 ± 0.017	1.644 ± 0.155	0.119 ± 0.075	0.262 ± 0.018
3544595	0.920 ± 0.011	0.922 ± 0.004	6.679 ± 0.211	-0.127 ± 0.046	0.253 ± 0.010
4141376	1.018 ± 0.036	1.037 ± 0.013	3.519 ± 0.577	-0.210 ± 0.073	0.264 ± 0.021
4349452	1.265 ± 0.039	1.333 ± 0.015	2.121 ± 0.155	0.100 ± 0.069	0.270 ± 0.021
4914423	1.180 ± 0.020	1.482 ± 0.009	6.701 ± 0.461	0.108 ± 0.055	0.249 ± 0.009
5094751	1.125 ± 0.028	1.363 ± 0.012	5.875 ± 0.341	0.066 ± 0.060	0.271 ± 0.018
5866724	1.345 ± 0.028	1.449 ± 0.011	2.547 ± 0.129	0.191 ± 0.042	0.256 ± 0.014
6196457	1.333 ± 0.029	1.769 ± 0.014	4.411 ± 0.270	0.180 ± 0.064	0.262 ± 0.017
6278762	0.756 ± 0.010	0.753 ± 0.003	11.258 ± 0.596	-0.121 ± 0.045	0.265 ± 0.014
6521045	1.148 ± 0.010	1.524 ± 0.005	6.266 ± 0.164	-0.075 ± 0.037	0.250 ± 0.007
7670943	1.256 ± 0.047	1.422 ± 0.020	2.479 ± 0.129	-0.014 ± 0.071	0.275 ± 0.023
8077137	1.264 ± 0.026	1.690 ± 0.013	3.788 ± 0.173	-0.124 ± 0.058	0.260 ± 0.015
8292840	1.231 ± 0.022	1.369 ± 0.010	2.787 ± 0.114	-0.142 ± 0.051	0.250 ± 0.009
8349582	1.015 ± 0.012	1.389 ± 0.006	8.092 ± 0.391	0.202 ± 0.033	0.321 ± 0.007
8478994	0.835 ± 0.007	0.780 ± 0.002	4.723 ± 0.477	-0.195 ± 0.041	0.246 ± 0.005
8494142	1.153 ± 0.013	1.770 ± 0.009	4.351 ± 0.158	0.158 ± 0.052	0.334 ± 0.006
8554498	1.301 ± 0.009	1.846 ± 0.005	5.817 ± 0.113	0.233 ± 0.025	0.249 ± 0.006
8866102	1.352 ± 0.022	1.399 ± 0.008	1.742 ± 0.072	0.131 ± 0.038	0.253 ± 0.009
9592705	1.499 ± 0.031	2.116 ± 0.015	2.140 ± 0.046	0.344 ± 0.035	0.323 ± 0.013
10514430	1.049 ± 0.009	1.578 ± 0.005	8.167 ± 0.125	-0.190 ± 0.038	0.255 ± 0.005
10586004	1.196 ± 0.026	1.658 ± 0.011	7.048 ± 0.453	0.192 ± 0.061	0.259 ± 0.007
10666592	1.569 ± 0.033	2.005 ± 0.015	1.885 ± 0.050	0.182 ± 0.043	0.270 ± 0.016
11133306	1.173 ± 0.045	1.226 ± 0.016	3.499 ± 0.675	0.101 ± 0.076	0.260 ± 0.017
11295426	0.942 ± 0.011	1.141 ± 0.004	6.370 ± 0.439	0.044 ± 0.034	0.335 ± 0.005
11401755	1.125 ± 0.037	1.662 ± 0.019	7.010 ± 0.351	-0.094 ± 0.072	0.253 ± 0.007
11807274	1.296 ± 0.025	1.601 ± 0.011	3.298 ± 0.101	-0.043 ± 0.041	0.258 ± 0.014
11853905	1.193 ± 0.016	1.583 ± 0.007	6.727 ± 0.403	0.083 ± 0.040	0.247 ± 0.005
11904151	0.911 ± 0.016	1.062 ± 0.006	10.067 ± 0.367	-0.022 ± 0.057	0.285 ± 0.016

[4]ASCII format: https://github.com/nmoedas/Appendix_Tables.git

Appendix C: Fundamental properties using 3:3 frequency weighting

Table C.1. Inferred fundamental properties of the stars using 3:3 frequencies weight.[5]

KIC	Mass ($M_\odot$)	Radius ($R_\odot$)	Age (Gyr)	$[M/H]_i$	Y_i
1435467	1.445 ± 0.024	1.740 ± 0.011	2.336 ± 0.142	0.166 ± 0.063	0.267 ± 0.017
2837475	1.521 ± 0.025	1.672 ± 0.011	1.289 ± 0.121	0.196 ± 0.073	0.269 ± 0.019
3427720	1.170 ± 0.014	1.139 ± 0.005	2.188 ± 0.216	0.064 ± 0.047	0.249 ± 0.008
3456181	1.568 ± 0.030	2.184 ± 0.016	2.145 ± 0.085	0.039 ± 0.060	0.255 ± 0.013
3632418	1.472 ± 0.013	1.945 ± 0.006	2.927 ± 0.121	0.119 ± 0.039	0.253 ± 0.010
3656476	1.035 ± 0.009	1.296 ± 0.004	8.380 ± 0.323	0.261 ± 0.030	0.306 ± 0.009
3735871	1.189 ± 0.021	1.127 ± 0.007	1.399 ± 0.348	0.086 ± 0.053	0.249 ± 0.008
4914923	1.135 ± 0.012	1.385 ± 0.005	6.626 ± 0.334	0.107 ± 0.052	0.262 ± 0.012
5184732	1.236 ± 0.009	1.352 ± 0.003	4.319 ± 0.215	0.393 ± 0.021	0.282 ± 0.006
5773345	1.545 ± 0.028	2.043 ± 0.013	2.204 ± 0.116	0.327 ± 0.056	0.291 ± 0.017
5950854	0.986 ± 0.017	1.245 ± 0.008	9.040 ± 0.602	-0.146 ± 0.060	0.261 ± 0.016
6106415	1.158 ± 0.007	1.250 ± 0.002	4.451 ± 0.211	0.024 ± 0.026	0.247 ± 0.005
6116048	1.109 ± 0.009	1.261 ± 0.003	5.911 ± 0.299	-0.033 ± 0.033	0.248 ± 0.006
6225718	1.303 ± 0.008	1.289 ± 0.002	1.950 ± 0.178	0.198 ± 0.025	0.244 ± 0.003
6508366	1.600 ± 0.021	2.219 ± 0.012	2.090 ± 0.089	0.131 ± 0.060	0.262 ± 0.015
6603624	0.993 ± 0.007	1.142 ± 0.003	8.761 ± 0.188	0.211 ± 0.026	0.296 ± 0.007
6679371	1.684 ± 0.024	2.281 ± 0.013	1.724 ± 0.079	0.192 ± 0.063	0.265 ± 0.017
6933899	1.190 ± 0.005	1.617 ± 0.002	6.553 ± 0.107	0.053 ± 0.012	0.249 ± 0.003
7103006	1.619 ± 0.023	2.025 ± 0.010	2.078 ± 0.099	0.278 ± 0.047	0.257 ± 0.012
7206837	1.469 ± 0.025	1.622 ± 0.010	2.034 ± 0.167	0.269 ± 0.057	0.258 ± 0.014
7296438	1.148 ± 0.016	1.390 ± 0.007	6.861 ± 0.373	0.208 ± 0.049	0.267 ± 0.013
7510397	1.415 ± 0.013	1.886 ± 0.006	3.050 ± 0.104	0.001 ± 0.042	0.250 ± 0.008
7680114	1.108 ± 0.012	1.411 ± 0.005	7.229 ± 0.351	0.085 ± 0.056	0.267 ± 0.013
7771282	1.364 ± 0.047	1.678 ± 0.020	2.945 ± 0.249	0.091 ± 0.070	0.266 ± 0.020
7871531	0.822 ± 0.015	0.866 ± 0.005	9.312 ± 0.517	-0.143 ± 0.043	0.288 ± 0.014
7940546	1.492 ± 0.013	2.001 ± 0.006	2.836 ± 0.115	0.105 ± 0.034	0.251 ± 0.009
8006161	0.920 ± 0.006	0.907 ± 0.002	5.125 ± 0.232	0.300 ± 0.038	0.318 ± 0.009
8150065	1.256 ± 0.045	1.422 ± 0.018	3.254 ± 0.406	0.097 ± 0.084	0.269 ± 0.022
8179536	1.373 ± 0.021	1.400 ± 0.008	1.579 ± 0.201	0.170 ± 0.054	0.250 ± 0.009
8228742	1.400 ± 0.011	1.887 ± 0.005	3.542 ± 0.176	0.053 ± 0.040	0.248 ± 0.007
8379927	1.238 ± 0.009	1.163 ± 0.003	1.438 ± 0.219	0.230 ± 0.032	0.247 ± 0.006
8394589	1.165 ± 0.012	1.212 ± 0.004	3.415 ± 0.290	-0.019 ± 0.041	0.246 ± 0.005
8424992	0.890 ± 0.021	1.035 ± 0.008	9.490 ± 0.569	-0.059 ± 0.070	0.296 ± 0.021
8938364	1.014 ± 0.006	1.361 ± 0.003	9.292 ± 0.151	-0.204 ± 0.025	0.244 ± 0.004
9025370	0.970 ± 0.018	1.000 ± 0.006	4.665 ± 0.337	0.105 ± 0.088	0.304 ± 0.020
9098294	1.006 ± 0.011	1.156 ± 0.004	7.941 ± 0.436	-0.100 ± 0.049	0.253 ± 0.011
9139151	1.221 ± 0.014	1.172 ± 0.005	1.516 ± 0.227	0.100 ± 0.044	0.248 ± 0.007
9139163	1.534 ± 0.013	1.617 ± 0.005	1.547 ± 0.092	0.333 ± 0.040	0.250 ± 0.008
9206432	1.590 ± 0.024	1.577 ± 0.009	0.705 ± 0.100	0.353 ± 0.048	0.251 ± 0.010
9353712	1.495 ± 0.040	2.169 ± 0.021	2.234 ± 0.100	0.093 ± 0.055	0.287 ± 0.021
9410862	1.023 ± 0.021	1.175 ± 0.008	6.291 ± 0.550	-0.204 ± 0.062	0.256 ± 0.013
9414417	1.502 ± 0.019	1.967 ± 0.009	2.571 ± 0.103	0.092 ± 0.048	0.251 ± 0.010
9812850	1.451 ± 0.027	1.848 ± 0.012	2.507 ± 0.147	0.098 ± 0.064	0.264 ± 0.017
9955598	0.870 ± 0.015	0.876 ± 0.005	6.949 ± 0.404	0.043 ± 0.066	0.292 ± 0.018
9965715	1.238 ± 0.013	1.333 ± 0.005	2.640 ± 0.182	-0.122 ± 0.029	0.242 ± 0.002
10068307	1.462 ± 0.011	2.100 ± 0.006	3.041 ± 0.086	0.046 ± 0.042	0.255 ± 0.009
10079226	1.172 ± 0.040	1.164 ± 0.013	2.563 ± 0.578	0.195 ± 0.068	0.268 ± 0.020
10162436	1.509 ± 0.015	2.076 ± 0.008	2.789 ± 0.114	0.104 ± 0.042	0.252 ± 0.010
10454113	1.338 ± 0.013	1.303 ± 0.004	1.335 ± 0.206	0.221 ± 0.041	0.247 ± 0.007
10516096	1.139 ± 0.010	1.433 ± 0.004	6.322 ± 0.308	-0.007 ± 0.048	0.255 ± 0.010
10644253	1.234 ± 0.017	1.142 ± 0.006	0.858 ± 0.257	0.201 ± 0.049	0.249 ± 0.008
10730618	1.415 ± 0.040	1.803 ± 0.019	2.384 ± 0.201	0.175 ± 0.110	0.290 ± 0.026
10963065	1.156 ± 0.009	1.258 ± 0.003	4.223 ± 0.267	-0.029 ± 0.040	0.248 ± 0.007
11081729	1.490 ± 0.023	1.486 ± 0.009	0.897 ± 0.154	0.250 ± 0.056	0.251 ± 0.009
11253226	1.524 ± 0.025	1.657 ± 0.010	1.273 ± 0.108	0.173 ± 0.065	0.262 ± 0.016

Table C.1. Continued.

KIC	Mass ($M_\odot$)	Radius ($R_\odot$)	Age (Gyr)	$[M/H]_i$	Y_i
11772920	0.803 ± 0.019	0.836 ± 0.007	9.310 ± 0.687	0.037 ± 0.083	0.312 ± 0.020
12009504	1.308 ± 0.012	1.455 ± 0.005	3.409 ± 0.220	0.118 ± 0.033	0.245 ± 0.005
12069127	1.603 ± 0.046	2.307 ± 0.024	1.941 ± 0.111	0.182 ± 0.078	0.284 ± 0.024
12069424	1.044 ± 0.007	1.213 ± 0.003	7.092 ± 0.257	0.103 ± 0.039	0.280 ± 0.010
12069449	0.998 ± 0.007	1.099 ± 0.003	7.002 ± 0.208	0.098 ± 0.038	0.284 ± 0.009
12258514	1.303 ± 0.009	1.625 ± 0.003	4.714 ± 0.211	0.122 ± 0.026	0.245 ± 0.004
12317678	1.477 ± 0.018	1.875 ± 0.009	1.995 ± 0.117	0.009 ± 0.077	0.264 ± 0.018
3425851	1.331 ± 0.051	1.408 ± 0.018	1.897 ± 0.358	0.114 ± 0.079	0.262 ± 0.019
3544595	0.904 ± 0.022	0.916 ± 0.008	6.637 ± 0.548	-0.138 ± 0.064	0.265 ± 0.018
4141376	1.023 ± 0.043	1.039 ± 0.015	3.449 ± 0.929	-0.194 ± 0.084	0.265 ± 0.021
4349452	1.248 ± 0.050	1.328 ± 0.018	2.345 ± 0.383	0.077 ± 0.074	0.270 ± 0.023
4914423	1.168 ± 0.035	1.477 ± 0.015	6.585 ± 0.719	0.111 ± 0.062	0.258 ± 0.017
5094751	1.101 ± 0.044	1.352 ± 0.018	5.962 ± 0.651	0.015 ± 0.068	0.276 ± 0.025
5866724	1.293 ± 0.052	1.431 ± 0.019	2.860 ± 0.346	0.172 ± 0.061	0.270 ± 0.023
6196457	1.322 ± 0.048	1.762 ± 0.023	4.204 ± 0.408	0.215 ± 0.071	0.277 ± 0.026
6278762	0.752 ± 0.017	0.751 ± 0.006	11.794 ± 1.457	-0.220 ± 0.059	0.254 ± 0.013
6521045	1.098 ± 0.022	1.504 ± 0.011	6.682 ± 0.387	0.070 ± 0.050	0.287 ± 0.015
7670943	1.286 ± 0.058	1.435 ± 0.023	2.348 ± 0.325	0.084 ± 0.084	0.278 ± 0.026
8077137	1.262 ± 0.040	1.692 ± 0.019	3.857 ± 0.332	-0.055 ± 0.056	0.269 ± 0.022
8292840	1.222 ± 0.030	1.368 ± 0.012	3.068 ± 0.346	-0.118 ± 0.059	0.252 ± 0.011
8349582	1.040 ± 0.025	1.402 ± 0.012	8.525 ± 0.654	0.260 ± 0.052	0.312 ± 0.015
8478994	0.854 ± 0.016	0.786 ± 0.005	3.505 ± 1.014	-0.173 ± 0.044	0.245 ± 0.005
8494142	1.181 ± 0.072	1.782 ± 0.034	4.224 ± 0.438	0.135 ± 0.062	0.324 ± 0.020
8554498	1.249 ± 0.039	1.818 ± 0.018	5.298 ± 0.413	0.196 ± 0.041	0.276 ± 0.017
8866102	1.322 ± 0.037	1.390 ± 0.014	1.892 ± 0.234	0.139 ± 0.064	0.265 ± 0.019
9592705	1.548 ± 0.057	2.140 ± 0.027	2.251 ± 0.133	0.291 ± 0.061	0.293 ± 0.026
10514430	1.046 ± 0.013	1.578 ± 0.007	8.412 ± 0.317	-0.164 ± 0.049	0.256 ± 0.007
10586004	1.266 ± 0.030	1.689 ± 0.015	6.389 ± 0.924	0.281 ± 0.056	0.257 ± 0.017
10666592	1.582 ± 0.063	2.015 ± 0.028	1.865 ± 0.098	0.295 ± 0.057	0.284 ± 0.027
11133306	1.117 ± 0.054	1.207 ± 0.020	4.552 ± 0.988	0.048 ± 0.081	0.265 ± 0.020
11295426	0.906 ± 0.033	1.130 ± 0.020	8.080 ± 0.829	0.035 ± 0.046	0.332 ± 0.011
11401755	1.072 ± 0.017	1.634 ± 0.009	7.229 ± 0.379	-0.219 ± 0.033	0.257 ± 0.011
11807274	1.276 ± 0.053	1.594 ± 0.023	3.310 ± 0.254	0.027 ± 0.061	0.278 ± 0.026
11853905	1.184 ± 0.030	1.580 ± 0.013	6.924 ± 0.655	0.096 ± 0.054	0.250 ± 0.010
11904151	0.912 ± 0.028	1.063 ± 0.011	10.276 ± 0.751	-0.048 ± 0.070	0.280 ± 0.023

[5]ASCII format: https://github.com/nmoedas/Appendix_Tables.git

Appendix C

Implementing the SVP method in MESA

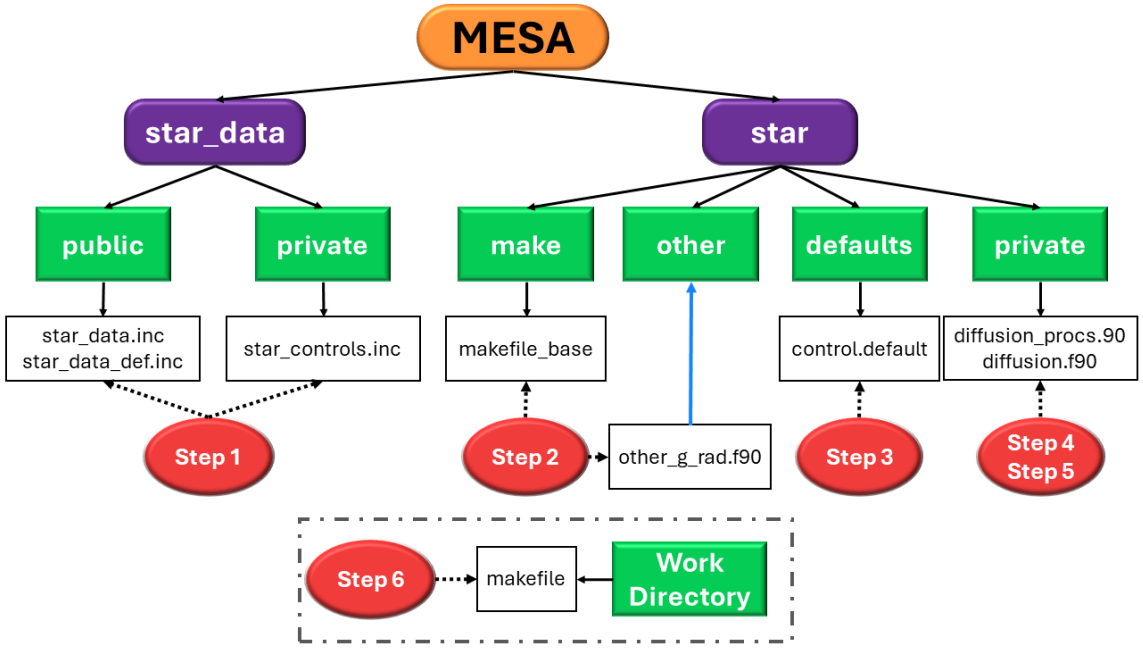

FIGURE C.1: Schematic of the MESA modules/directories and folders that need to be modified to implement SVP.

For the implementation, I took the following steps (a schematic is presented in Fig. C.1):

1. Add a new hook that creates null functions in the files *star_data.inc*, *star_data_def.inc*, and *star_controls.inc* in the *star_data* folder (see Fig. C.2);
2. Create a new hook file/module called *other_g_rad.f90* in the folder *other* and add it in the MESA *makefile_base* for compilation in the *make* folder (see Fig. C.3). All in the *star* folder of MESA;

3. Add in the *control.default* file the routine and set it off by default in MESA (see Fig. C.4);
4. In the radiative acceleration file (in *diffusion_procs.f90*), add a condition to select whether to use the hook or the default routine (see Fig. C.5);
5. Add a condition in the diffusion routine that allows us to turn the computation of the Rosseland mean opacity with monochromatic opacity on or off when using SVP (in *diffusion.f90* and *diffusion_procs.f90*). MESA by default does not allow the use of radiative accelerations if the monochromatic opacities are not used (see Fig. C.6);
6. Add a folder that contains the SVP routine, and add its directory in the *makefile* for the models;
7. Finally, recompile/reinstall MESA after making the changes.

This gives access to an "outside" hook to implement all the different functions needed to call the SVP routine, without major changes to the source code of MESA.

```
1932      ! "other" procedures
1933
1934         ! deffine as a null function
1935         procedure (other_g_rad_interface), pointer, nopass :: &
1936            other_g_rad => null()
```

```
615
616      !Creat a new hook interface
617
618         subroutine other_g_rad_interface(id, &
619            nz, nzlo, nzhi, nc, m, kmax_rad_accel, X, A, &
620            class_chem_id, net_iso, op_mono_factors, &
621            L_face, rho_face, r_face, T_face, alfa_face,&
622            min_T_for_radaccel, max_T_for_radaccel, &
623            min_Z_for_radaccel, max_Z_for_radaccel, &
624            screening, log10_g_rad, g_rad, &
625            rad_accel_face, ierr)
626
627            use const_def, only: dp
628            integer, intent(in) :: id
629            integer, intent(in) :: nz, nzlo, nzhi, nc, m, kmax_rad_accel, class_chem_id(:), net_iso(:), &
630            min_Z_for_radaccel, max_Z_for_radaccel
631            real(dp), intent(in) :: min_T_for_radaccel, max_T_for_radaccel
632            real(dp), dimension(:), intent(in) :: A, L_face, rho_face, r_face, T_face, alfa_face, op_mono_factors
633            real(dp), dimension(:,:), intent(in) :: X
634            logical, intent(in) :: screening
635            real(dp), dimension(:,:), intent(out) :: log10_g_rad, g_rad, rad_accel_face
636            integer, intent(out) :: ierr
637         end subroutine other_g_rad_interface
```

```
1418      ! Add other hook creat a new logical parameter
1419
1420         logical :: use_other_g_rad
1421         logical :: use_other_eos
```

FIGURE C.2: Code implemented in *star_data.inc* (top panel), *star_data_def.inc* (middle panel), and *star_controls.inc* (bottom panel).

```
! ************************************************************************

      module other_g_rad

      ! consult star/other/README for general usage instructions
      ! control name: use_other_g_rad = .true.
      ! procedure pointer: s% other_g_rad => my_routine



      use star_def

      implicit none


      contains

      subroutine null_other_g_rad( id, &
            nz, nzlo, nzhi, nc, m, kmax_rad_accel, X, A, &
            class_chem_id, net_iso, op_mono_factors, &
            L_face, rho_face, r_face, T_face, alfa_face, &
            min_T_for_radaccel, max_T_for_radaccel, &
            min_Z_for_radaccel, max_Z_for_radaccel, &
            screening, log10_g_rad, g_rad, &
            rad_accel_face, ierr)
         use star_def

         use const_def, only: dp
         integer, intent(in) :: id
         integer, intent(in) :: nz, nzlo, nzhi, nc, m, kmax_rad_accel, class_chem_id(:), net_iso(:), &
                                min_Z_for_radaccel, max_Z_for_radaccel
         real(dp), intent(in) :: min_T_for_radaccel, max_T_for_radaccel
         real(dp), dimension(:), intent(in) :: A, L_face, rho_face, r_face, T_face, alfa_face, op_mono_factors
         real(dp), dimension(:,:), intent(in) :: X
         logical, intent(in) :: screening
         real(dp), dimension(:,:), intent(out) :: log10_g_rad, g_rad, rad_accel_face
         integer, intent(out) :: ierr

         type (star_info), pointer :: s
         ierr = 0
         call star_ptr(id, s, ierr)
         if (ierr /= 0) return


         log10_g_rad(:,:) = -99
         g_rad(:,:) = 0
         rad_accel_face(:,:) = 0
         write(*,*) 'null_g_rad'
         return
      end subroutine null_other_g_rad
```

```
SRCS = \
   star_def.f90 \
   star_profile_def.f90 \
   star_history_def.f90 \
   star_private_def.f90 \
   other_extras.f90 \
   other_split_mix.f90 \
   other_g_rad.f90 \
   other_d_mix.f90 \
```

FIGURE C.3: New hook file *other_g_rad.f90* (top panel) and modification in *makefile_base* file (bottom panel).

```
         !### use_other_{hook}

         ! Logicals to deploy the use_other routines.

      use_other_g_rad = .false.
```

FIGURE C.4: Modification in *controls.defaults* file.

```
1039      subroutine setup_struct_info( &
1040           s, nz, nzlo, nzhi, species, nc, m, X, A, tiny_X, &
1041           dlnP_dm_face, dlnT_dm_face, dlnRho_dm_face, cell_dm, dm_in, &
1042           abar, free_e, T, lnT, rho, lnd, L_face, r_face, alfa_face, &
1043           class, class_chem_id, calculate_ionization, nsmooth_typical_charge, &
1044           min_T_for_radaccel, max_T_for_radaccel, &
1045           min_Z_for_radaccel, max_Z_for_radaccel, &
1046           screening, rho_face, T_face, four_pi_r2_rho_face, &
1047           dlnP_dr_face, dlnT_dr_face, dlnRho_dr_face, &
1048           Z, typical_charge, xm_face, &
1049           rad_accel_face, log10_g_rad, g_rad, &
1050           kmax_rad_accel, ierr)
1051
```

```
1142
1143        if (s% use_other_g_rad) then
1144           call s% other_g_rad( s% id, &
1145              nz, nzlo, nzhi, nc, m, kmax_rad_accel, X, A, &
1146              class_chem_id, s% net_iso, s% op_mono_factors, &
1147              L_face, rho_face, r_face, T_face, alfa_face, &
1148              min_T_for_radaccel, max_T_for_radaccel, &
1149              min_Z_for_radaccel, max_Z_for_radaccel, &
1150              screening, log10_g_rad, g_rad, &
1151              rad_accel_face, ierr)
1152           if (ierr /= 0) return
1153        else
1154
1155           call calc_g_rad( &
1156              nz, nzlo, nzhi, nc, m, kmax_rad_accel, X, A, &
1157              class_chem_id, s% net_iso, s% op_mono_factors, &
1158              L_face, rho_face, r_face, T_face, alfa_face, &
1159              min_T_for_radaccel, max_T_for_radaccel, &
1160              min_Z_for_radaccel, max_Z_for_radaccel, &
1161              screening, log10_g_rad, g_rad, &
1162              rad_accel_face, ierr)
1163           if (dbg) write(*,*) 'done calc_g_rad'
1164        end if
1165
1166        return
```

FIGURE C.5: Modifications in the *diffusion_procs.f90* top panel indicates the subroutine need to be modified, and the bottom panel is the modification.

```
202
203        if (T(1) <= max_T_for_radaccel .and. (.not. s% x_logical_ctrl(6)) ) then
204           if (dbg) write(*,*) 'call load_op_mono_data'
205           call load_op_mono_data( &
206              op_mono_data_path, op_mono_data_cache_filename, ierr)
207           if (dbg) write(*,*) 'done load_op_mono_data'
208           if (ierr /= 0) then
209              write(*,*) 'error while loading OP data, ierr = ',ierr
210              return
211           end if
212        end if
213
```

FIGURE C.6: Modification of the condition of the monochromatic opacities in *diffusion_procs.f90* and *diffusion.f90* files.